Stochastic dynamics of cell adhesion in hydrodynamic flow

Dissertation

zur Erlangung des akademischen Grades
„doctor rerum naturalium"
(Dr. rer. nat.)
in der Wissenschaftsdisziplin „Theoretische Physik"

eingereicht an der
Mathematisch-Naturwissenschaftlichen Fakultät
der Universität Potsdam

angefertigt am
Max-Planck-Institut für Kolloid- und Grenzflächenforschung in Potsdam

von

Christian Korn

geboren am 05. Oktober 1976 in Tübingen

Potsdam, im Januar 2007

Abstract

In this thesis the interplay between hydrodynamic transport and specific adhesion is theoretically investigated. An important biological motivation for this work is the rolling adhesion of white blood cells experimentally investigated in flow chambers. There, specific adhesion is mediated by weak bonds between complementary molecular building blocks which are either located on the cell surface (receptors) or attached to the bottom plate of the flow chamber (ligands).

The model system under consideration is a hard sphere covered with receptors moving above a planar ligand-bearing wall. The motion of the sphere is influenced by a simple shear flow, deterministic forces, and Brownian motion. An algorithm is given that allows to numerically simulate this motion as well as the formation and rupture of bonds between receptors and ligands. The presented algorithm spatially resolves receptors and ligands. This opens up the perspective to apply the results also to flow chamber experiments done with patterned substrates based on modern nanotechnological developments.

In the first part the influence of flow rate, as well as of the number and geometry of receptors and ligands, on the probability for initial binding is studied. This is done by determining the mean time that elapses until the first encounter between a receptor and a ligand occurs. It turns out that besides the number of receptors, especially the height by which the receptors are elevated above the surface of the sphere plays an important role. These findings are in good agreement with observations of actual biological systems like white blood cells or malaria-infected red blood cells.

Then, the influence of bonds which have formed between receptors and ligands, but easily rupture in response to force, on the motion of the sphere is studied. It is demonstrated that different states of motion—for example rolling—can be distinguished. The appearance of these states depending on important model parameters is then systematically investigated. Furthermore, it is shown by which bond property the ability of cells to stably roll in a large range of applied flow rates is increased.

Finally, the model is applied to another biological process, the transport of spherical cargo particles by molecular motors. In analogy to the so far described systems molecular motors can be considered as bonds that are able to actively move. In this part of the thesis the mean distance the cargo particles are transported is determined.

Zusammenfassung

In der vorliegenden Arbeit wird das Zusammenspiel zwischen hydrodynamischem Transport und spezifischer Adhäsion theoretisch untersucht. Eine wichtige biologische Motivation für diese Arbeit ist die rollende Adhäsion weißer Blutkörperchen, die experimentell in Flusskammern untersucht wird. Die spezifische Adhäsion wird durch schwache Bindungen zwischen komplementären molekularen Bausteinen vermittelt, die sich einerseits auf der Zelloberfläche, Rezeptoren genannt, andererseits auf der unteren begrenzenden Platte der Flusskammer, Liganden genannt, befinden.

Das untersuchte Modellsystem besteht aus einer festen Kugel, die mit Rezeptoren bedeckt ist und sich unter dem Einfluss einer einfachen Scherströmung, deterministischer Kräfte und der Brownschen Molekularbewegung oberhalb einer mit Liganden bedeckten Wand bewegt. Es wird ein Algorithmus angegeben, mit dessen Hilfe diese Bewegung sowie das Entstehen und Reißen von Bindungen zwischen Rezeptoren und Liganden numerisch simuliert werden kann. In der numerischen Modellierung werden die Positionen von Rezeptoren und Liganden räumlich aufgelöst, wodurch sich die Möglichkeit ergibt, die Ergebnisse auch mit Flusskammerexperimenten, in denen moderne nanotechnologisch strukturierte Substrate verwendet werden, zu vergleichen.

Als Erstes wird der Einfluss von Strömungsrate sowie Zahl und Form der Rezeptoren bzw. Liganden auf die Wahrscheinlichkeit, mit der es zu einer Bindung kommen kann, untersucht. Hierfür wird die mittlere Zeit bestimmt, die vergeht bis zum ersten Mal ein Rezeptor mit einem Liganden in Kontakt kommt. Dabei stellt sich heraus, dass neben der Anzahl der Rezeptoren auf der Kugel insbesondere der Abstand, welchen die Rezeptoren von der Oberfläche haben, eine große Rolle spielt. Dieses Ergebnis ist in sehr guter Übereinstimmung mit tatsächlichen biologischen Systemen wie etwa weißen Blutkörperchen oder mit Malaria infizierten roten Blutkörperchen.

Als Nächstes wird betrachtet, welchen Einfluss Bindungen haben, die sich zwischen Rezeptoren und Liganden bilden, aber unter Kraft auch leicht wieder reißen. Dabei zeigt sich, dass verschiedene Bewegungstypen auftreten, beispielsweise Rollen, deren Erscheinen in Abhägigkeit wichtiger Modellparameter dann systematisch untersucht wird. Weiter wird der Frage nachgegangen, welche Eigenschaften von Bindungen dazu führen können, dass Zellen in einem großen Bereich von Strömungsraten ein stabiles Rollverhalten zeigen.

Abschließend wird das Modell auf einen etwas anderen biologischen Prozess angewendet, nämlich den Transport kugelförmiger Lastpartikeln durch molekulare Motoren. In Analogie zu den bisher beschriebenenq Systemen können diese molekularen Motoren als sich aktiv bewegende Bindungen betrachtet werden. In diesem Teil der Arbeit wird ermittelt, wie weit die Lastpartikel im Mittel transportiert werden.

Contents

List of Symbols

A	x,θ-sector of the mobility matrix, Eq. (4.2) on page 57
$A(z)$	Drift term in MFPT equation, Eq. (3.1) on page 31
A_θ	Rotational drift in MFPT problem, pages 39,48
$a(i,j)$	Coefficient in solution to the simple on-off model, page 77, Eq. (4.24)
a_b	Area fraction on sphere surface carrying motors accessible to the microtubule, Fig. 5.5 on page 95
$\alpha,\beta,(\hat{\alpha},\hat{\beta})$	(Dimensionless) scalar friction functions, Sec. B.1
B	Decomposition part of mobility matrix, Eq. (2.22) on page 18
$\vec{b}$	x,θ components of velocity of a free hydrodynamic particle, page 57
C	2-dimensional matrix in linearized equation of motion, page 57
C	Concentration of receptor-ligand complexes, page 23
D	Diffusion matrix, page 18
$D, D_{\mathrm{RL}}, D_\theta, \ldots$	Diffusion constants
d	Ligand-ligand distance, pages 40, 62
δ	Step length of a processive motor protein, Tab. 5.2 on page 89
E	Concentration of encounter complexes, page 23
E^∞	Rate of strain tensor, Eq. (2.12) on page 16
E_b	Height of transition state barrier, Fig. 2.6 on page 26
$\epsilon,(\epsilon_0)$	(Unperturbed) dimensionless off-rate, chapters 4,5
$\mathcal{F},(\mathbf{f})$	Force density field (multipole representation), Eq. (2.1) on page 13
$\mathbf{F}_B, \mathbf{T}_B$	Bond force and torque, page 28 in Sec. 2.4.3
$F_{B,x}$	x-component of bond force, Eq. (4.1) on page 57
$\bar{F}^i_{B,x}, \bar{F}^i_{B,z}$	Time-averaged bond force in bin i relative to cell center (x,z-component), Eq. (4.29) on page 81
$\mathbf{F}^D$	Combined six-dimensional force/torque vector, Sec. 2.2 after Eq. (2.18)
F_d	detachment force, Eq. (2.37) on page 26
$\mathbf{F}^H, \mathbf{T}^H$	Hydrodynamic fore and torque acting on the fluid by the particle, Eq. (2.11) on page 16
$\mathbf{F}^S$	Combined shear force/torque vector, Eq. (2.13) on page 16
$\mathbf{F}_S, \mathbf{T}_S$	Shear force and torque on a spherical particle, Fig. 4.2 on page 56
F_s	Stall force for a motor protein, Eq. (5.2) on page 89
f	Dimensionless force constant in Langevin eq., Eq. (2.23) on page 19

$f_{B,x}, f_{B,z}, f_B$	Force distribution density (x, z-component, total), Eq. (4.30) on page 81
g	Earth acceleration constant ($g = 9.81$ m/s^2, [146]), page 20
$\mathbf{g}_t$	Gaussian white noise process, Eq. (2.20) on page 18
$\mathbf{g}(\Delta t)$	White noise contribution to the Euler update step, Eq. (2.26) on page 19 and Eq. (B.21) on page 114, respectively
$\dot{\gamma}$	Shear rate, page 13
H	Gap height of parallel-plate flow chamber, Fig. 1.3b on p. 4 and p. 33
h_{min}	Height of glycocalyx, Tab. 4.1 on page 62
h_{MT}	Diameter of microtubule, Fig. 5.1a on p. 88 and Tab. 5.2 on p. 89
h	Minimum distance between sphere and microtubule, Fig. 5.1a on p. 88
η	Viscosity of a Newtonian fluid, Eq. (2.1) on page 13
$k, \bar{k}$	Rate of wall encounters, p. 47 before Eq. (3.23) and p. 46, respectively
k_+, k_-	Rate of encounter formation and dissolution, respectively, page 24
$\mathbf{k}$	Normal vector on the boundary wall, Fig. 2.1 on page 14
k_B	Boltzmann's constant; we use: $k_B = 1.38 \cdot 10^{-23}$ J/K, [146]
k_f, k_r	Forward and reverse rate for receptor-ligand complex formation, p. 23
k_{on}, k_{off}	On-rate and off-rate for complex formation from encounter, Sec. 2.4.1
k_0	Unstressed off-rate, Eq. (2.36) on page 26
κ	Spring constant, Eq. (2.39) on page 28
L	Concentration of ligands, page 23
L_b	Number of *bins* for force distribution measurements, page 81
l_0	Resting length of a bond (p. 28) and of a molecular motor, Tab. 5.2
$\lambda_\pm$	Eigenvalues of 2-dimensional operator C, Eq. (4.7) on page 57
$\lambda_s, (\lambda_s^0)$	(Unloaded) stepping rate of a motor protein, p. 90 after Eq. (5.3) (Tab. 5.2)
M	Mobility matrix, Eq. (2.15) on page 16
μ	Mobility coefficient in on-off (sliding) model, Eq. (4.14) on page 75
$\mu^{tt}, \mu^{tr}, \ldots$	Mobility tensors, Eq. (2.1.1) on page 16
μ_{xx}^{tt}	xx-component of translational mobility tensor, page 90
$\mu_m := v_0/F_s$	Internal mobility coefficient of a motor head, page 90
N	Number of iterations of simulating a stochastic process, chapter 2-5
N_l	Number of ligands per μm^2, p. 63, and per contact zone, p. 71
N_m	Maximum number of bonds in (sliding) model, Sec. 4.3; maximum number of simultaneous pulling motors, Sec. 5.2.1
N_r	Number of receptors and receptor patches, respectively, chapters 3,4
N_{tot}	Total number of motor proteins attached to a bead, Tab. 5.1 on p. 87
$\bar{N}_r$	Mean number of bound microvilli, page 85
N_b	Mean number of bound motors, Eq. (5.7) on page 93
$\langle N_b \rangle_{Poisson}$	Poisson-averaged mean number of bound motors, Eq. (5.12) on page 96
ν_i	Exponent in solution to the simple on-off model, page 77 (Eq. (4.23))

ν_D	Attempt frequency (for escape over a barrier), Eq. (2.36) on page 26
$\mathbf{\Omega}, \Omega$	Angular velocity of a spherical particle, Eq. (2.2) on page 13
$\mathbf{\Omega}^\infty$	Shear vorticity vector, Eq. (2.12) on page 16
$P(\mathbf{r})$	Scalar pressure field, Eq. (2.1) on page 13
Pe	Péclet number Eq. (2.24) on page 19 and chapter 3
Pe_z	Péclet number in z-direction Eq. (2.27) on page 20 and chapter 3
P_i	Stationary probability for i-bond state, page 77
$P(k, n_b)$	Poisson distribution with mean n_b for k motors available for binding, Eq. (5.9) on page 94
π	Dimensionless on-rate, chapters 4, 5
$\pi_n = (N_b - n)\pi$	(On)-rate from n to $n+1$ bond state, page 76
$\Psi_s(z)$	Stationary probability density function for a particle diffusing in gravity field, Eq. (2.30) on page 22
$\phi, \psi, (\hat{\phi}, \hat{\psi})$	(Dimensionless) scalar friction functions, Sec. B.1
Q	Green vector for pressure field, Eq. (2.5) on page 14
R	Radius of a spherical particle, Fig. 2.1 on page 14
$\mathbf{R}$	Position vector of the center of a spherical particle, Eq. (2.2) on page 13
R	Concentration of receptors, page 23
$\mathsf{R_u}$	Friction matrix, Eq. (2.14) on page 16
$\mathbf{r}$	Position vector, Fig. 2.1 on page 14
$\hat{\mathbf{r}}$	Position vector of sphere surface point w. r. t. the sphere's center, Fig. 2.7 on p. 28, Fig. 4.2 on p. 56
$\mathbf{r}_r, \mathbf{r}_l$	Position of receptor and ligand, respectively, Fig. 2.7 on p. 28
r_0	Capture radius and height in chapter 4 and chapter 3, respectively
r_d	Ligand patch radius, Fig. 3.6a on page 40
r_p	Receptor patch size, Fig. 3.3 on page 36
r_p^{eff}	Effective receptor patch radius, Eq. (3.20) on page 45
ρ	Density of Newtonian fluid, page 20
$\rho_{sphere}, \Delta\rho$	Density of spherical particle and density difference compared to fluid density, page 20
ρ_l	Ligand density, pages 40, 44
ρ_r	Receptor density, pages 35, 42
σ_q	Standard deviation of quantity q
$\mathsf{T}, (\mathbf{T})$	Green tensor for fluid field (matrix representation.), p. 14 (p. 15)
T_0	Oseen tensor, Eq. (2.7) on page 14
T	Mean first passage time (MFPT), 31
T_{sim}	Time of a simulation run, 81
$\langle T \rangle_x$	MFPT averaged over initial configuration x, chapter 3
T_a	Ambient temperature, Eq. (2.20) on page 18
$T_{B,y}$	y-component of bond torque, Eq. (4.1) on page 57

t	Time coordinate
Δt	Numerical time step in simulations, Eq. (2.26) on page 19
θ_0	Range of possible encounter, Fig. 3.3 on page 36
θ_s	1D receptor periodicity, Fig. 3.3 on page 36
$\vec{\theta}$	Orientational degrees of freedom for a particle, page 34
θ	Rotational degree of freedom about the y-axis, Fig. 4.2 on page 56
$\mathbf{U}, U$	Translational velocity of a spherical particle (center), Eq. (2.2) on p. 13
$\mathbf{U}^\infty$	Shear velocity at position of particle's center, Eq. (2.12) on page 16
$\mathbf{u}(\mathbf{r})$	Fluid field, Eq. (2.1) on page 13
$\mathbf{u}^\infty, (\mathbf{c}^+)$	Incident shear flow field (multipole representation), page 13 (Sec. 2.1)
$v_m, (v_0)$	Mean velocity of a (unloaded) motor protein along a MT, Eq. (5.2) on page 89
$\mathcal{W}(\mathbf{x}_i\|\mathbf{x}_j)$	Transition probability per time from state $\mathbf{x}_i$ to state $\mathbf{x}_i$, page 75
$W(\mathbf{x}_i\|\mathbf{x}_j)$	Transition probability per time from i- to j-bond state, Eq. (4.16) on p. 4.16
$\mathbf{X}$	Six-dimensional position/orientation vector of a sphere, on page 17
x, y, z	Cartesian coordinates for sphere center, Fig. 2.1 on page 14
x_b	Total bond length in on-off model, Eq. (4.14) on page 75
$x_{b,i}$	Sum of the length of i closed bonds, Eq. (4.15) on page 76
x_c	Reactive compliance, Fig. 2.6 on page 26
$\langle \Delta x_b \rangle$	Mean walking distance of a bead pulled by motors, Eq. (5.8) on page 93
$\langle\langle \Delta x_b \rangle\rangle_{Poisson}$	Poisson-averaged mean walking distance of a cargo, Eq. (5.11) on p. 95
χ	Angle between bond (motor) and wall, Fig. 4.2 on page 56
$\mathsf{Z}, (\mathbf{Z})$	Grand resistance tensor (matrix representation), Eq. (2.9) on p. 15 (17)
ζ	Friction tensors, page 16

List of abbreviations

CD	cluster of differentiation, Fig. 1.2
CLA	cutaneous lymphocyte-associated antigen, Fig. 1.2
ICAM	intercellular adhesion molecule, Fig. 1.2
LFA	lymphocyte fusion-associated antigen, Fig. 1.2
(M)FPT	(mean) first passage time, Chapter 3
MT	microtubule, Chapter 5
MV	microvilli, Sec. 4.4.2
PNAd	peripheral node addressin, Fig. 4.1
PSGL	P-selectin glycoprotein ligand, Fig. 1.2
VCAM	vascular cell adhesion molecule, Fig. 1.2
VLA	very late antigen, Fig. 1.2
w. r. t.	with respect to

Chapter 1

Introduction

1.1 Specific adhesion and transport

Adhesion between opposing surfaces occurs in many different ways in biological systems, most prominently between the cells building up a multicellular organism. In contrast to adhesion in man-made systems like tape or car wheels, adhesion in biological systems is not based on non-specific interactions like the van der Waals interaction, but rather on specific interactions based on the biomolecular binding process between receptor and ligand, which complement each other like a lock and a key. A prominent example is antigen-antibody recognition, one of the key properties of our immune system, which enables it to react even to a single ligand presented by an invading pathogen.

In cell-cell adhesion, complex formation (*bonding*) between surface receptors expressed on one cell and complementary ligands expressed on another cell allows the cells to specifically adhere to each other. Cell-cell adhesion leads to a mechanically stable connection and at the same time allows the cells to communicate with each other. In order to obtain a complete picture of this process of *specific adhesion*, the understanding of physical aspects is equally important as the analysis of the chemical properties of the receptor-ligand complex. In particular, a physical *transport* process is required to bring the two binding partners to close proximity. In this context the notion of the formation of an *encounter complex*, which in turn may react to the final complex, turned out to be a very useful concept [40, 16, 141, 127]. Bonds that mediate specific adhesion are typically weak—a property that allows for quick rearrangements in response to external stimuli. Forces play a dominant role in this context as they are ubiquitous in biological systems and dramatically shorten the lifetime of receptor-ligand bonds. Transport of receptors and ligands in solution is dominated by thermally activated diffusion which is always present on the cellular and subcellular level. On the typical scales of these systems motion is quite different from what we are used to in our daily life because the influence of inertia is negligible. Consequently, the particles' velocities depend linearly on forces and once the total force on a particle is zero, the particle stops immediately [118].

Adhesion and *transport* embody two antipodes: stop and motion, respectively. In biological systems they are intertwined in various ways and define the basis for many different processes of specific adhesion. In the simplest case transport is simply required for receptor-ligand encounter, for example in the diffusion dominated process of virus docking to cell surface receptors [1, 41]. A more complex interplay of transport and adhesion exists for the *rolling adhesion* of white blood cells [144], which is one of the main motivations for the work presented here. In this case, the convective transport of white blood cells in the blood stream is slowed down and guided by specific adhesion bonds in

order to allow these cells to adhere and extravasate the vessel at very specific sites. Similar situations also arise in microbiology, when bacteria adhere to the intestinal wall [153], in malaria infection, when infected red blood cells adhere to the vessel walls [11, 105], in the initial stages of pregnancy, when the developing embryo adheres to the uterus [57], and in biotechnology, e. g., when sorting cells on microfluidic chips [54]. A somehow different, but related transport process based on specific adhesion is active transport by molecular motors. Molecular motors are proteins firmly attached to a membrane enclosed organelle or a vesicle ("cargo") that can transport this cargo along filaments once adhesion has occurred [124].

1.2 Biological systems and experimental setups

Rolling adhesion of leukocytes

One prominent example for specific adhesion combined with transport is the already mentioned *rolling adhesion* of leukocytes (white blood cells). Leukocytes are part of the immune system and play an important role in the *inflammatory response*. They circulate the body in the blood and lymph. At sites of inflammation, e. g., due to local injuries of the peripheral tissues, leukocytes can leave the blood flow through the vessel walls [61, 1]. Using intravital microscopy this process, called *extravasation*, was already observed and described in the late eighteen hundreds [95] but only recent biochemical developments allowed to shed light on the complex mechanochemical regulation processes behind this phenomenon.

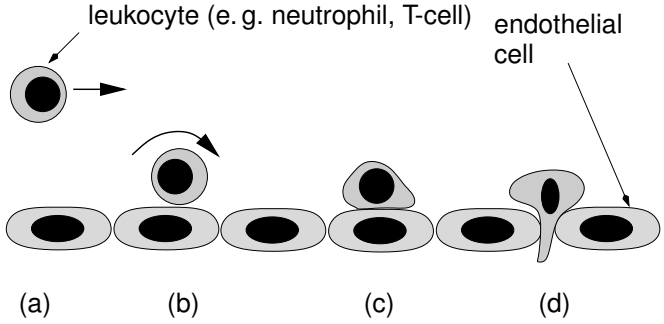

Figure 1.1: Cartoon of the extravasation cascade of white blood cells (leukocytes). (a) A leukocyte flows with blood stream. (b) Rolling on endothelial cells through labile selectin bonds. (c) Firm adhesion mediated by integrins bonds, the leukocyte starts spreading. (d) Transendothelial migration.

Extravasation of leukocytes occurs in different steps. For some subtypes of leukocytes like *neutrophils* and *T-cells* it is known that each of these steps can be independently regulated allowing for an increased specificity. This is the so-called *multistep paradigm* [144, 121]. The main steps of the extravasation cascade are depicted in Fig. 1.1. A leukocyte traveling through the blood stream (Fig. 1.1a), and getting in contact with the vessel wall can specifically adhere to the endothelial cells via *selectin bonds*. Selectin bonds are labile *tethers* that are further weakened by tensile forces, thus, the drag by the blood stream causes them to rupture. In the case that the formation of new bonds at the leukocyte's front end compensates the rupture of bonds at the leukocyte's rear end the cell rolls along the vessel wall (Fig. 1.1b). This process is called *rolling adhesion*. A main effect of rolling is a strong decrease of the leukocyte's velocity allowing for the detection of molecular signals (e. g., chemokines) that are expressed on endothelial cells as part of the inflammatory response. This leads to the activation of integrins [63] which form much stronger bonds—enabling the cell to firmly adhere (Fig. 1.1c). Subsequently, the leuko-

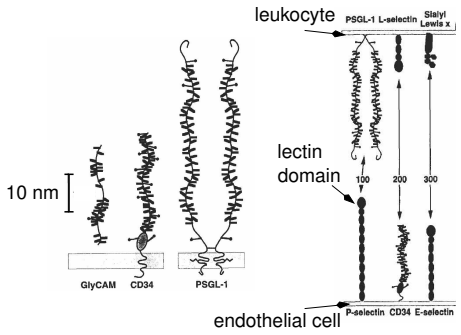

(a)

receptor	ligand
L-selectin	GlyCAM-1, CD34
E-selectin	CLA [121], PSGL-1 [61]
P-selectin	PSGL-1
Integrin LFA-1	ICAM-2
Integrin VLA-4	VCAM-1

(b)

Figure 1.2: (a) Schematic drawings of selectins and their mucin-like counter receptors (ligands) from [145]. The length of the molecules is some 10 nm, e. g., the length of P-selectin is about 40 nm that of E-selectin about 30 nm [108] (the scale bar refers to left part only). The cartoon also shows which molecules are located on the surface of the endothelial cells and which on the leukocytes. (b) Receptors of the selectin family and some of their possible ligands [121]. Some selected integrins and their ligands [145]. 'CAM' is the abbreviation of 'cell adhesion molecule'.

cyte actively deforms and migrates through the vessel wall (*transendothelial migration*, Fig. 1.1c) into the surrounding tissues where it follows chemoattractants (*chemotaxis*) towards the source of inflammation [1, 61, 121].

Extravasation preferentially occurs in postcapillary venules, i. e., at points in a vessel where the diameter is suddenly increased (swelling and dilation of vessels is part of the immune response). At these points the mean flow velocity of the blood stream is decreased and red blood cells being smaller and more flexible than leukocytes push those towards the vessel walls which increases their contact probability to the wall [95, 121].

The specific adhesion sites (*tether bonds*) mediating rolling adhesion and firm arrest of the leukocytes are complexes formed between receptor and ligand molecules complementarily located on the leukocytes and the endothelial cells, respectively. Fig. 1.2 lists some receptor-ligand pairs being important for leukocyte adhesion and shows schematic drawings of some of these molecules (taken from Ref. [145]). The selectin receptors (L-, E-, P-selectin) are glycoproteins that can bind with their lectin domain (their *binding sites*, see Fig. 1.2a) to specific carbohydrate groups of their mucin-like ligands [121, 61]. E- and P-selectins as well as the L-selectin ligand are located on the surface layer of endothelial cells (see Fig. 1.2a). Complementarily, L-selectins as well as the E- and P-selectin ligand PSGL-1 are located on the tips of small protrusions of the leukocyte surface, called *microvilli* [103, 29]. The notation in literature which of the two complementary binding parts has to be called receptor and which ligand is not unique. For the sake of simplicity, we will from now on always call the respective molecule on the leukocyte's surface *receptor*, and the counter receptor on the wall *ligand*.

Flow chamber experiments

In order to investigate the extravasation process and to determine and understand the different steps in this cascade many types of *in vitro* experiments have been established. Special focus has been given to study the interactions between receptors and ligands (see for example the reviews by Bongrand [20] and Pierres et al. [114]). Prominent examples for such *in vitro* setups include the field of *dynamic force spectroscopy*, in which the behavior

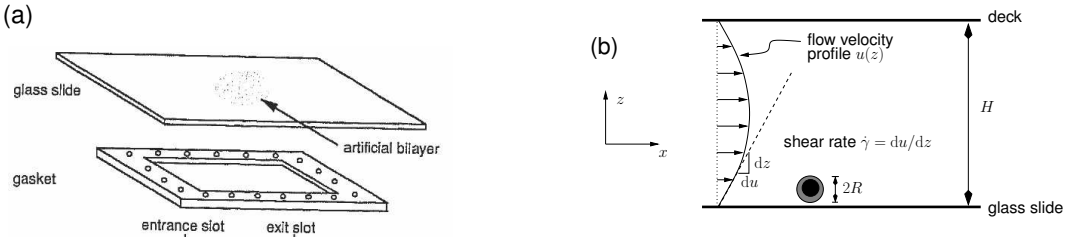

Figure 1.3: (a) Drawing of a parallel-plate flow chamber taken from [95]. (b) Sketch of the velocity profile in a parallel-plate flow chamber [95]. Cell radius R and plate distance H are not drawn to scale, typically $H \gg R$ ($H \approx 260$ μm [135]).

of receptor-ligand bonds under force is examined [45, 46], and flow chamber experiments.

In flow chamber experiments leukocytes are suspended in solution and perfused between two parallel plates (Fig. 1.3a shows an drawing of a flow chamber [95]). Leukocytes are slightly denser than the surrounding medium so that they sediment to the lower wall [104, 30], which usually is coated with an artificial lipid mono- or bilayer bearing the ligands. The adhesive interaction between cells and substrate is then observed by phase contrast microscopy along a field of view of some hundred micrometers [95]. The laminar *Poiseuille flow* between the two plates of the flow chamber approximately mimics the flow velocity profile in postcapillary venules, but not all properties of hemodynamic flow [131]. The change in flow velocity per change in distance from the wall is called *shear rate* and is highest at the wall (see Fig. 1.3b). The product of shear rate and medium viscosity defines the *shear stress*. Shear rate and shear stress are thus kinematic and dynamic quantities, respectively. The setup of a flow chamber experiment allows to separately control many of the parameters influencing the adhesion process, including salt concentration [34], wall shear rate, viscosity and shear stress [30, 39], and the type and density of ligands on the substrate [5, 3]. Furthermore, having low concentrations of leukocytes and no red blood cells suspended in the medium provides a framework that facilitates the development of theoretical models for interpreting experimental data.

One of the features that have been extensively studied using flow chamber experiments is rolling mediated by selectin bonds. In order to support rolling, these bonds must form and rupture rapidly. Moreover, it was found that rolling on L-selectin bonds is about ten times faster than rolling on E- and P-selectin bonds. In principle, rolling velocity can be regulated by intrinsic bond kinetics—via the intrinsic *on- and off-rate* for bond formation and rupture, respectively—and the *susceptibility* to applied force (called *reactive compliance*), i. e., the extend by which tensile forces weaken the bond strength. Using substrates with very diluted ligand densities that resolve single tether events, Alon and co-workers found that fast intrinsic on- and off-rates rather than the reactive compliance regulate rolling velocity [5, 3]. They also found that the susceptibility to applied force for selectin bonds is much smaller than for many other receptor-ligand complexes observed in biological systems. Both of these are distinguished properties of selectins necessary to mediate rolling over a large range of physiological shear stress.

Off-rates can directly be determined from lifetime measurements of single bonds [5]. However, the intrinsic on-rate can only be determined upon the complete knowledge of the transport process preceeding bond formation. In flow chamber experiments binding affinity is often measured as the fraction of tethered cells. Chen and Springer observed that

for P-selectin bonds this frequency first increases with increasing shear rate goes through a maximum and decreases again at large shear rates. They altered the medium viscosity by adding different weight percentages of Ficoll (a highly branched polymer of sucrose that is supposed not to alter the intrinsic bond behavior) and observed that the maximum frequency appears always at the same shear rate. This suggests initial tethering to be a purely transport and not force governed process [30]. L-selectins require wall shear rates above a certain threshold to mediate rolling [53]. Different explanations for this *shear threshold effect* have been given. Using video microscopy with high temporal resolution Dwir et al. found that L-selectin bonds are also formed at small shear rates, however, only above a critical shear rate these bonds seem to be sufficiently stabilized to support rolling [39]. This has been interpreted to be due to a transport enhanced formation of multiple bonds [129]. Another explanation suggests that L-selectins form so-called *catch bonds*, i. e., bonds whose lifetime increases with increasing tensile force [161]. This would mean that the threshold is a threshold in shear stress rather than in shear rate. Clearly, in order to decide which of these explanations is correct, a detailed understanding of the transport process that brings cell receptors and ligands to close proximity is necessary.

In principle, leukocyte deformations might play an important role during rolling adhesion. However, no visible leukocyte deformations were reported for the shear rates and ligand densities typically used in flow chamber experiments [3]. In order to check whether some of the characteristic bond properties observed for leukocytes depend on (small) viscoelastic cell deformations, experiments have also been conducted using cell-free systems. Cell-free means that instead of leukocytes, receptor-covered microspheres are perfused through the flow chamber [65, 160, 140]. Typically, these microspheres are hardly deformable. For example, the above described shear threshold effect was also observed for microspheres that were covered with a L-selectin counter-receptor and perfused over a L-selectin bearing wall [65]. The hydrodynamic drag force on a leukocyte strongly depends on the cell-radius [59], however, radii vary only slightly within one type of leukocytes. Thus, flow chamber experiments also allow to study the impact of the particle diameter to, e. g., the rolling velocity [140, 161].

For the flow chamber experiments described so far, the lower wall is covered with ligands of a certain type and density. In principle, new nanotechnological developments, e. g., by Spatz and co-workers, could be used to conduct some of these experiments also on substrates bearing a regular ligand pattern with a well defined ligand-ligand distance [8]. This would then, e. g., allow to determine the critical ligand-ligand distance that supports rolling.

Active transport by molecular motors and bead assays

Another important example that combines transport and specific adhesion is the active "cargo" transport by molecular motors in cellular systems. Molecular motors are proteins that bind with their *head*, or *motor domains*, to filaments and use energy from ATP hydrolysis (ATP = adenosine triphosphate) to *walk* along these filaments. Many types of motor proteins are known; they differ from each other, e. g., in the type of filament they bind to and their walking direction [1]. A prominent example is *conventional kinesin*, or kinesin-1, a member of the kinesin superfamily (Fig. 1.4a). Kinesin walks along a *protofilament* towards the so-called plus end of *microtubules*. These are long hollow cylindrical tubes containing several protofilaments with a certain polarity that results from an asymmetry in the subunits (i. e., tubulin) they are built of [98]. Kinesin has two head domains that can bind to special sites on these protofilaments and it walks by a so-called *hand-*

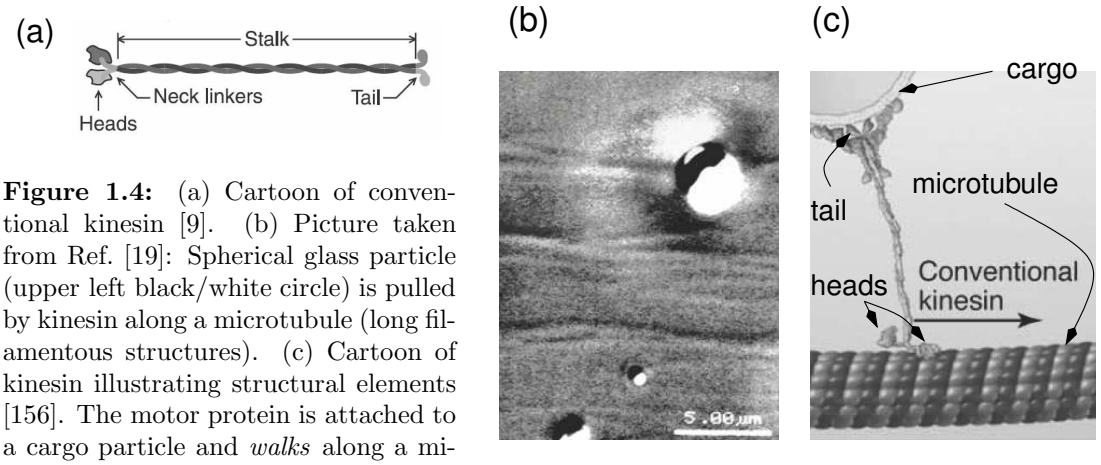

Figure 1.4: (a) Cartoon of conventional kinesin [9]. (b) Picture taken from Ref. [19]: Spherical glass particle (upper left black/white circle) is pulled by kinesin along a microtubule (long filamentous structures). (c) Cartoon of kinesin illustrating structural elements [156]. The motor protein is attached to a cargo particle and *walks* along a microtubule.

over-hand mechanism [9]. That means that each ATP hydrolysis cycle [33] is coupled to a conformational change of the protein in which the trailing head "flips" forward and becomes the leading head. Thus, the motor protein walks in discrete steps from one binding site to the next and is able to generate force. This force is used to pull a cargo particle (mainly membrane enclosed organelles, or vesicles) attached to the motor's tail domain along the microtubule through the cytoplasm (Fig. 1.4c).

Two types of assays are often used to investigate the transport properties of kinesin *in vitro*, gliding assays and bead assays. In gliding assays motors are fixed with their tails to the substrate and microtubules are moved. A bead assay is a flow chamber where microtubules are immobilized to the bottom wall and motor-coated beads (e. g., spherical glass, or polystyrene particles) are added to the fluid filling the chamber (however, usually no flow is applied) [19]. Then, using light microscopy walking motor proteins can be investigated by tracking the beads to which they are attached to (Fig. 1.4b).

An important property of conventional kinesin is its *processivity*, which means that after initial binding kinesin makes many steps before it unbinds. From experiments with beads pulled by a single motor it was found that kinesin walks on average for about one second (> 100 steps) before it unbinds. During that time it transports its cargo by about one micrometer. Much longer walking distances are achieved when several motors can pull on the cargo particle [19]. Then, walking is only interrupted if all motors unbind simultaneously from the microtubule [83].

So far, we introduced two fairly different biological systems: leukocytes that roll driven by the blood stream and cargo particles that are actively transported by molecular motors. However, these two systems bear some analogies. Both, rolling and cargo transport are mediated by very specific molecules, i. e., receptor-ligand complexes (bonds) and molecular motors, respectively. From a conceptual point of view motor proteins include some properties of receptors (e. g., binding and force-dependent unbinding [126]), and the specific binding sites on the protofilament of microtubule correspond to ligands. As mentioned, both of these systems are *in vitro* observed using flow chambers. Thus, the analogies pointed out allow to model leukocytes and receptor-covered microspheres rolling in flow chambers on the one hand and motor-coated spheres moving in bead assays on the other hand, within the same theoretical framework.

1.3 Physical aspects and previous theoretical work

For a complete theoretical modeling of the described systems one must consider various aspects from different fields. These include hydrodynamics, elasticity theory, the theory of stochastic processes and reaction kinetics. In order to reveal certain effects it can be also useful to consider some of these aspects separately, although they all contribute to the total observed behavior of the system.

A dimensionless key number of hydrodynamics is the *Reynolds number* Re which measures the relative strength of inertial and viscous contributions to the flow due to a moving particle. Given a typical length scale L, a typical particle velocity U and the viscosity and density of the fluid medium η and ρ, respectively, the Reynolds number reads $Re = \rho U L/\eta$ [115]. For a cell in a flow chamber we have typically $Re \approx 10^{-2} \ll 1$ (with $\eta = 10^{-3}$ Pa s, $\rho = 10^3$ kg/m^3, $L = 10$ μm, and $U = 1$ mm/s), thus viscous effects dominate and the inertia of the cells can be neglected (*Stokes regime*). It is one of the characteristics of the Stokes regime that the particle's velocity is linearly related to forces acting on the particle. This linear relation can be expressed via the so-called *friction matrix*. In an anisotropic fluid the friction matrix depends on the position of the particle. In 1967 Goldman et al. measured with finite element methods the friction matrix for a rigid sphere in linear shear flow above a planar wall [59, 60]. In many flow chamber experiments the gap height between the two plates is large compared to the size of the cells (cf. Fig. 1.3b). Then, the shear rate does hardly change within some cell diameters above the wall. As leukocytes are slightly denser than the surrounding fluid they sediment [104, 30] and experience an approximately constant shear rate in the vicinity of the lower wall. Therefore, the classical work by Goldman et al. is typically cited in the context of leukocyte rolling in flow chambers in order to give an estimate for the shear force on rolling cells (e. g., [95, 66, 3, 129]). A disadvantage of the Goldman data is that the friction matrix and shear force was only tabulated for some selected height values. In the 1990s Jones and co-workers presented a numerical scheme that allows to accurately calculate the same quantities but at arbitrary heights [111, 31]. The validity of the one-wall approximation for the friction matrix close to the bottom wall of a parallel plate flow chamber has been investigated by Jones. He showed that for the gap height between the two plates being only slightly larger than the sphere diameter the one-wall approximation strongly deviates from the exact solution. For a gap height that is about five times larger than the sphere diameter the proper two-wall friction matrix can be approximated by a superposition of the one-wall results [75]. At even larger relative gap heights this superposition is indeed governed by the contribution from the bottom wall.

Due to its small size (μm range) a cell in solution is subject to thermal fluctuations which results in additional random movements known as *Brownian motion*. This randomness requires a statistical description of the cell's trajectory. Brownian motion is a *Markov process* [157] and the evolution of the cell's phase space distribution function is determined by a *Fokker-Planck equation*. As mentioned above inertial effects can be neglected in the Stokes regime; in regard to Brownian motion this means that the distribution of momenta relaxes much more rapidly to its equilibrium distribution than the distribution of positions. Times larger than the time scale of momentum relaxation are referred to as the diffusion regime [44]. In the diffusion regime the time evolution of the particle's configuration space distribution function is described by the *Smoluchowski equation* [36]. An alternative approach to the statistical properties of the particle motion is based on the *Langevin equation*. The integration of this equation provides sample trajectories and statistical quantities are obtained by averaging over many trajectories. In 1978 Ermak and

McCammon derived—based on a Langevin equation—a *Brownian dynamics* algorithm for the computation of the configuration space trajectories of M colloidal particles including only simple hydrodynamics [44]. Ten years later Brady and Bossis presented a review where they described a similar method that includes an improved treatment of hydrodynamic interactions. They gave this method the name *Stokesian dynamics* to emphasize the proper treatment of hydrodynamic interactions in the Stokes limit (hydrodynamic interactions occur between particles but also between a particle and a boundary). In their terminology Brownian dynamics is a special case of Stokesian dynamics [21].

According to the *Einstein relation* the hydrodynamic friction matrix is related to the diffusion matrix via the temperature of the fluid. This relation was used to experimentally verify theoretically computed friction coefficients by measuring the particle's diffusion, e. g., for a microsphere between two parallel plates [37].

Particles that tend to easily deform when shear stress is applied cannot in general be treated as spherical objects. Shape and motion of these particles in hydrodynamic flow are non-trivially coupled to each other. Both must then be determined from the balance of hydrodynamic and mechanical forces on the particle's surface. The latter depend on the particular properties of the particle. For vesicles (i. e., closed bilayers formed from phospholipids) these are determined, e. g., by the bending rigidity of their incompressible fluid membrane. The shape of vesicles in shear flow in an unbounded fluid was numerically computed by Kraus et al. [92]. Later Pozrikidis performed similar simulations including also shear elasticity of the membrane in order to model red blood cells [116]. The problem of a vesicle in shear flow above a wall was analytically treated by Seifert [133] and numerically by Sukumaran and Seifert [147]. In the latter paper it was found that the deformations of the vesicle lead to a lift force proportional to the applied shear rate that pushes the vesicle away from the wall. Gravity counteracts this lift and the vesicle moves at a stationary height above the wall. They also explored the effect of unspecific adhesion by introducing a wall potential and found that unbinding occurs at a critical shear rate proportional to the adhesion strength [147].

In contrast to vesicles or red blood cells, deformations of leukocytes also depend on the structural properties of the cell body. However, at typical shear rates used in flow chambers no crucial deformations are expected [130]. This agrees with observations by Alon and co-workers who did not detect visible deformations at shear rates they applied [3]. Therefore, the assumption of leukocytes being rigid spheres seems reasonable for the shear rate and ligand densities commonly used in experiments. At very close contact to the wall the fluid layer between cell and substrate may also induce deformations (*lubrication forces*) that lead to lift forces in response to applied shear flow [134, 142].

A key property of the adhesion processes described above is their specificity mediated by receptor-ligand bonds. The interplay between membrane fluctuations and specific adhesion via anchored *stickers* have been investigated by Lipowsky [99]. Often, membrane adhesion is induced by competing receptor-ligand pairs of different lengths. Depending on the concentrations of receptor-ligand bonds membrane bending (which occurs to compensate the length mismatch) can induce a lateral phase separation between the different receptor-ligand bonds [10]. The process of rolling adhesion, however, is governed by fast position changes. Then, initial bond formation and rupture behavior of bonds play a dominant role. Formation of specific receptor-ligand bonds are preceeded by a transport process leading to receptor-ligand encounter. This transport has been studied in different contexts, e. g., by Berg and Purcell [16] and Berg [15] for the encounter of soluble ligands to cell surface receptors. For rolling leukocytes, both, receptors and ligands are attached

to surfaces and the receptor transport is connected to the transport of the whole cell. In contrast to bond formation, bond rupture is strongly affected by force as described above. In a seminal work, Bell (1978) proposed an empirical model for bond rupture according to which the bond dissociation rate increases exponentially with applied tensile bond force. Later on, this model has been rationalized (e. g., [47, 138]) in the framework of Kramers theory for escape over an energy barrier [90]. Recently, also so-called catch bond models [35] were discussed, which predict a decrease of rupture rate at small tensile forces [46, 12, 109].

In an early study of cell adhesion in flow by Hammer and Lauffenburger the conditions of firm adhesion in terms of shear force, receptor and ligand density, and binding affinity were examined. They treated the *contact area* (between cell and substrate) as a homogeneous region rather than spatially resolving single bonds [67]. In order to numerically simulate rolling adhesion of leukocytes, Hammer and Apte (1992) setup an algorithm in which leukocytes are modeled as rigid spheres, bonds form and dissociate with certain rates and existing bonds behave as harmonic springs [66] (the article appeared in *Biophys. J.*, Vol. 63; in the same volume of this journal Tözeren and Ley presented a very similar model [155]). One of the achievements of the Hammer and Apte model (known as *adhesive dynamics*) is the spatial resolution of single bonds. The adhesive dynamics method was applied to study various aspects of leukocyte adhesion in flow chambers, e. g., stationary types of motion [28, 25] or detachment of adherent cells under the action of flow [26, 93, 81]. The numerical results of Ref. [66] revealed that leukocytes roll in the physical sense (i. e., they do not slip over the substrate) due to the action of labile bonds. Depending on the parameters different distinct types of motion can be observed form simulation data. Accordingly, Hammer and co-workers defined different states of motion (mainly based on the mean translational cell velocity) and displayed the appearance of these states in state diagrams for different planes of the multi-dimensional parameter space. This resulted, e. g., in a state diagram for the plane spanned by the *unstressed off-rate* (i. e., the dissociation rate when no tensile force is applied to the bond) and the *reactive compliance* [28, 107], and a state diagram for two different types of receptor-ligand pairs expressing the dependence on their respective densities [17]. In a semi-analytic approach Krasik and Hammer calculated also the occurrence of the states rolling and firm adhesion depending on the *on-rate* (i. e., rate of bond formation) and the unstressed *off-rate* [91].

The approach of modeling rolling adhesion by the Hammer group mentioned so far is based on a single rigid sphere. Others have focused on the effects of deformations in leukocyte adhesion. For example, N'Dri et al. performed a numerical study in which the cell was modeled as a compound drop with *nucleus* and *cytoplasm* being fluids characterized by their surface tension and viscosities. For high bond density their simulations revealed tether-like deformations at the trailing end of rolling leukocytes [106]. Similar observations were obtained by Khismatullin and Truskey who modeled the cell as a compound *viscoelastic* drop [78]. At high cell densities rolling adhesion is also affected by cell-cell interactions (i. e., collisions and hydrodynamic interactions). Using a multiparticle version of adhesive dynamics King and Hammer found that cell-cell interactions in flow chambers results in an increased stability of rolling velocity [80, 82] and an enhancement of initial binding [79]. Munn et al. studied the effect of leukocyte rolling in vessels and postcapillary venules. They reported a supporting effect to rolling and initial binding by red blood cells passing the leukocyte [102, 148].

Models for the simulation of active transport by molecular motors in *in vitro* assays including effects of hydrodynamic interactions and thermal noise have been developed

mostly for gliding assays. Gibbons et al. described such an algorithm with which they, e. g., studied the velocity of microtubules attached to many motors [58]. Recently, Kraikivski et al. numerically studied the enhancement of nematic microtubule ordering due to molecular motors pulling on the microtubules [89]. During recent years, theoretical models have also been developed for the pulling out of membrane tethers from adhering vesicles by molecular motors walking on adhering microtubules [87, 97]. In this experiments, tether pulling is only possible if several motors work together. The transport of cargo by several motors has recently been described theoretically by Klumpp and Lipowsky [83].

1.4 Overview

To properly interprete experimental data obtained in flow chamber experiments, a well-founded understanding of the physical aspects involved is required. In this thesis, we focus on the transport properties of a spherical particle in hydrodynamic flow which can bind to a boundary wall through specific adhesion. We address these topics using a theoretical model system which combines methods from hydrodynamics and stochastic dynamics.

Close to the bottom wall of a parallel-plate flow chamber, whose gap height between the two plates is much larger than a typical cell radius, the laminar flow profile is approximately linear and the mobility is hardly influenced by the presence of the upper wall [75]. In addition, it was reported that at typical shear rates no visible elastic cell deformations occur [3]. Thus, the model system we consider is basically a single rigid spherical particle covered with receptors that moves in linear shear flow above a ligand-coated wall (the situation is illustrated by the cartoon shown in Fig. 1.5a). The details of this model are explained in Chapter 2. There, we start by introducing the relevant concepts from hydrodynamics at small Reynolds numbers, in particular the mobility matrix and the shear force resulting from the Stokes equation for a rigid sphere above a wall [31]. In order to account for Brownian motion that arises from thermal forces on the sphere we include concepts of stochastic processes and arrive at a Langevin equation with a non-trivial multiplicative noise term [21]. The latter one results from the presence of the boundary wall that in turn results in an anisotropy in vertical direction. We then illustrate the effects of deterministic and thermal forces by considering the example of a sphere in linear shear flow subject to gravity. In fact, cells and microspheres used in flow chamber experiments are slightly denser than the surrounding medium [30]. Together with other forces pushing the sphere towards the bottom wall (e. g., electric forces, or hydrodynamic or contact interactions with other particles) this drift ensures that a sufficient number of spheres in a flow chamber experiment can interact with wall ligands. For conceptual simplicity, in Chapters 3 and 4 we consider only a constant gravitational drift.

The second part of Chapter 2 deals with formation and rupture of specific bonds between receptors and ligands. For both processes appropriate rates are introduced. In particular, using the notion of encounter complexes the process of bond formation can be spitted into a transport and an intrinsic reaction step. Rates are then defined for the two sub-steps and the overall process. Throughout this thesis we consider the rates of bond formation to be force independent. In contrast, bond dissociation is modeled by employing the famous Bell equation [13], which states that the rupture rate increases exponentially with applied tensile bond force. We close Chapter 2 by introducing an adhesive dynamics algorithm. This algorithm combines the Langevin dynamics with rules for bond kinetics, and functional bonds are modeled as harmonics springs. In addition to previous versions of this algorithm (e. g., [66]) we allow for spatially resolved receptors and ligands, and Brownian motion of the sphere. This opens up the perspective to apply our

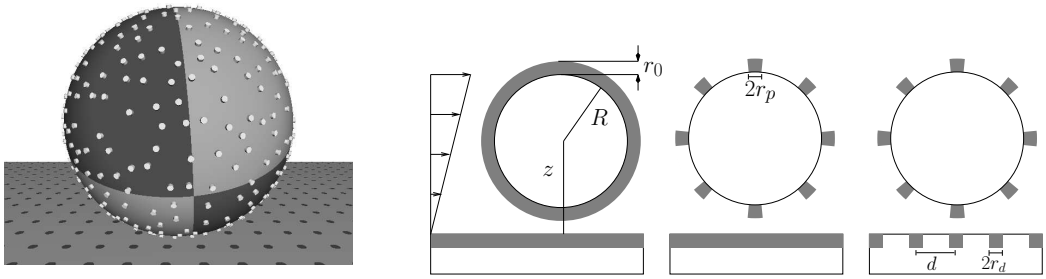

Figure 1.5: (a) Illustration of a sphere covered with receptor patches above a wall covered with a regular ligand pattern. (b) From left to right: Series of increasing complexity for receptor-ligand encounters as investigated in Chapter 3. The receptors are modeled as patches of radius r_p and height r_0, ligands as patches with radius r_d and mutual distance d.

simulations to experiments with regularly patterned ligand distributions based on recent nanotechnological developments [8].

In Chapters 3-5 we apply this model to describe several generic aspects of "receptor-ligand systems" experimentally observed in flow chambers. In Chapter 3 we model receptors as spherical patches of a certain height on the surface of the sphere and ligands as spherical patches on the boundary wall (cf. Fig. 1.5) and investigate the efficiency of initial binding (encounter complex formation) in terms of the number of receptors, the patch geometry, the ligand density, and the flow parameters. An encounter complex is identified with the first overlap of any pair of receptor and ligand patches. In the language of stochastic dynamics the formation of a receptor-ligand encounter is a (mean) first passage time problem and the inverse of the mean first passage time defines the rate of encounter formation. In order to solve the mean first passage time problem, we employ both analytical and numerical methods. Numerically, we calculate the mean first passage time by repeatedly integrating the Langevin equation upon the first occurrence of a receptor-ligand encounter for a series of increasing complexity (illustrated in Fig. 1.5b). We start with the case of homogeneous receptor and ligand coverage. This simplest case can also be solved exactly and provides a favorable test for the numerical treatment. In the context of homogeneous coverage we discuss the influence of gravity and what difference it makes when considering both a top and a bottom wall as a boundary instead of a bottom wall only. In the following parts of this chapter we explore how the mean first passage time for encounter formation is modified by non-homogeneous coverage. There, we focus on the one hand on the influence of flow rate and on the other hand—for zero flow rate, i. e., for purely diffusive motion—on the influence of the receptor geometry defined by the number of receptor patches, their height and lateral dimension [85, 86]. Using a mean-field approach (by using average values for the diffusion and drift terms) allows us to obtain some of the results also analytically and to derive scaling laws for some limiting cases. Our results reveal that the receptor height has an important influence on initial binding efficiency and we discuss this finding in the context of biological systems of interest.

In Chapter 4 we investigate the motion of a sphere under the influence of labile tether bonds as occurring in rolling adhesion experiments with leukocytes or microspheres. First, we apply an analytical treatment in order to examine how the motion of cells in shear flow close to the bottom wall changes due to bonds. Then, we present a new classification for five distinct stationary states of cell motion (e. g., rolling) based on the *translational*

and *angular* cell velocities. By extensive use of the adhesive dynamics algorithm we identify the different stationary states of motion for many different sets of parameters and summarize the results in state diagrams that display the occurrence of the different states with respect to the rate of bond formation (i. e., *on-rate*) and dissociation (i. e., *unstressed off-rate*). Furthermore, we define and analytically solve a simple model system based on a one-step master equation. The analysis of this simple model helps to understand some general effects revealed by our adhesive dynamics simulations. In the remaining part of this chapter we use the adhesive dynamics algorithm to determine how bond forces of a stationarily rolling cell are distributed relative to the cell center. In addition, we address the robustness of rolling against an increase of shear rate. According to the Bell model, at large shear forces bond strength is fairly reduced, therefore, bonds may become too weak to further support rolling. We show that tether bonds with an increased elasticity nevertheless are able to support rolling even at large shear rates.

In Chapter 5 we extend the scope of our model and consider a different system that is also often studied in flow chamber-like assays, namely the active transport of beads by molecular motors—like kinesin—along filaments that are immobilized to the bottom wall of the chamber. We treat molecular motors connecting a bead with the filament as bonds similar to receptor-ligand complexes and describe how bead transport can be simulated using an extended version of the adhesive dynamics algorithm that accounts for the active steps of the motor proteins. We then apply the algorithm to compute the mean run length of beads and compare our results with results obtained from an analytical model by Klumpp and Lipowsky [83]. We work out the impact of effects that were neglected in the analytical model but are accounted for by our algorithm.

Chapter 2

Model and theoretical background

In this chapter we present a detailed description of our model system: a hard sphere covered with receptors moving in linear shear flow above a planar ligand-coated wall. We also give a brief summary of the underlying theory. In the first part we discuss the solution of the hydrodynamic one-body problem by hydrodynamic scattering theory. We then setup a proper *Langevin equation* that allows us to correctly incorporate *Brownian motion*. This Langevin equation is then applied to a sphere falling due to gravity. In the second part we consider the process of bond formation and dissociation. These processes are translated into rules defining an *adhesive dynamics algorithm*.

2.1 Stokes equation and one-body problem

At low Reynolds numbers a particle moving in a Newtonian fluid with viscosity η is described by the Stokes equation (linearized Navier-Stokes equation) and the continuity equation [125]

$$\eta\nabla^2\mathbf{u}(\mathbf{r}) - \nabla P(\mathbf{r}) = -\mathcal{F}(\mathbf{r}), \qquad \nabla\cdot\mathbf{u}(\mathbf{r}) = 0, \tag{2.1}$$

where $\mathbf{u}(\mathbf{r})$ is the fluid velocity field, $P(\mathbf{r})$ is the pressure field and $\mathcal{F}(\mathbf{r})$ is the force density on the fluid by the particle. Here, we use the induced force picture, i. e., the fluid equations of motion Eq. (2.1) are extended to the interior of the particle and the particle is replaced by an appropriate force density $\mathcal{F}(\mathbf{r})$ acting on the fluid [48].

The unperturbed flow field has to satisfy the homogeneous version of Eq. (2.1) as well as no-slip boundary conditions at the wall. In this thesis, we use linear shear flow, $\mathbf{u}^\infty = \dot\gamma z\mathbf{e}_x$. This is the simplest possible but non-trivial flow. In addition, it provides a good approximation to flow chamber velocity profiles close to the bottom wall.

The solution of Eq. (2.1) for the flow field in the region occupied by the rigid sphere reads [31]:

$$\mathbf{u}(\mathbf{r}) = \left(\mathbf{U} + \boldsymbol{\Omega}\times(\mathbf{r}-\mathbf{R})\right)\Theta(R - \|\mathbf{r}-\mathbf{R}\|)\ , \tag{2.2}$$

where $\mathbf{U}, \boldsymbol{\Omega}$ are the translational and angular velocities of the sphere, respectively. $\mathbf{R}$ is the position of its center (see Fig. 2.1), R the sphere radius and Θ the theta step-function.

As the Stokes equation (2.1) is linear in $\mathbf{u}$ and P it can be solved using the method of

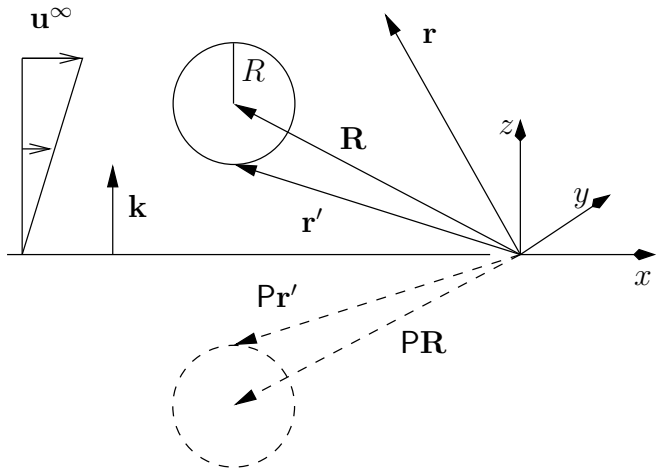

Figure 2.1: Illustration of a sphere in linear shear flow $\mathbf{u}^\infty$ above a planar wall. The normal on the wall pointing into the fluid is denoted by $\mathbf{k} = (0, 0, 1)$. The sphere is located at $\mathbf{R} = (x, y, z)$. $\mathbf{r}'$ denotes a position on the sphere's surface. At $z = R$ the sphere touches the wall. Due to the presence of the wall the Green tensor includes singularities from an image sphere located at $\mathsf{P}\mathbf{R} = (x, y, -z)$.

Greens functions (cf. e. g., [115, 49, 31]). This leads to the solution

$$\mathbf{u}(\mathbf{r}) = \mathbf{u}^\infty(\mathbf{r}) + \int \mathsf{T}(\mathbf{r}, \mathbf{r}')\mathcal{F}(\mathbf{r}')\mathrm{d}\mathbf{r}', \tag{2.3}$$

$$P(\mathbf{r}) = P^\infty(\mathbf{r}) + \int \mathsf{Q}(\mathbf{r}, \mathbf{r}')\mathcal{F}(\mathbf{r}')\mathrm{d}\mathbf{r}', \tag{2.4}$$

where T is the Green tensor for the fluid field and Q is the Green vector function for the pressure field which satisfy

$$\eta\nabla^2\mathsf{T}(\mathbf{r}, \mathbf{r}') - \nabla\mathsf{Q}(\mathbf{r}, \mathbf{r}') = -\mathbf{b}\delta(\mathbf{r} - \mathbf{r}'), \qquad \nabla\mathsf{T}(\mathbf{r}, \mathbf{r}') = 0, \tag{2.5}$$

i. e., $\mathbf{u}_i(\mathbf{r}) = \mathsf{T}_{ij}(\mathbf{r}, \mathbf{r}')\mathbf{b}_j$ and $P(\mathbf{r}) = \mathsf{Q}_j(\mathbf{r}, \mathbf{r}')\mathbf{b}_j$ are the solutions to (2.1) for a point force density located at position $\mathbf{r}'$ and strength and direction given by $\mathbf{b}$. T can be written in the form

$$\mathsf{T}(\mathbf{r}, \mathbf{r}') = \mathsf{T}_0(\mathbf{r} - \mathbf{r}') + \Delta\mathsf{T}(\mathbf{r}, \mathbf{r}'), \tag{2.6}$$

where T_0 is called Stokeslet or the Oseen or Oseen-Burgers tensor (cf. [115]), the Green tensor for the unbounded fluid and $\Delta\mathsf{T}$ is the correction due to the presence of a boundary. The correction term $\Delta\mathsf{T}$ is regular both in $\mathbf{r}$ and $\mathbf{r}'$ [31], while the singularity of the Green tensor T at $\mathbf{r} = \mathbf{r}'$ is contained in the Oseen tensor. Explicitly the Oseen tensor and Q_0 are given by

$$\mathsf{T}_{0ij}(\mathbf{x}) = \frac{1}{8\pi\eta}\left(\frac{\delta_{ij}}{\|\mathbf{x}\|} + \frac{x_i x_j}{\|\mathbf{x}\|^3}\right), \qquad \mathsf{Q}_0 = \frac{1}{4\pi}\frac{\mathbf{x}}{\|\mathbf{x}\|^3}. \tag{2.7}$$

For a planar boundary wall at $z = 0$ (cf . Fig. 2.1) with normal vector $\mathbf{k} = (0, 0, 1)$ pointing into the fluid, Blake (1971) found that $\Delta\mathsf{T}(\mathbf{r}, \mathbf{r}')$ can be written as the sum of image singularities located below the wall. So for $\mathbf{r}, \mathbf{r}' \in \{(x, y, z) \in \mathbb{R}^3 | z > 0\}$, $\Delta\mathsf{T}(\mathbf{r}, \mathbf{r}')$ reads ([115, 31]):

$$\Delta\mathsf{T}(\mathbf{r}, \mathbf{r}') = -\mathsf{T}_0(\mathbf{r} - \mathsf{P}\mathbf{r}') + 2z'^2\bar{\mathsf{D}}(\mathbf{r} - \mathsf{P}\mathbf{r}') - 2z'\bar{\mathsf{S}}(\mathbf{r} - \mathsf{P}\mathbf{r}'), \tag{2.8}$$

with the reflection operator $\mathsf{P} = \mathbb{1} - 2\mathbf{kk}$, $(x_1, x_2, x_3) \equiv (x, y, z)$ and the operators

$$\bar{\mathsf{D}}_{ij}(\mathbf{x}) := \frac{1}{8\pi\eta} \sum_{l=1}^{3} \mathsf{P}_{jl} \frac{\partial}{\partial x_l} \frac{x_i}{\|\mathbf{x}\|^3},$$

$$\bar{\mathsf{S}}_{ij}(\mathbf{x}) := x_3 \bar{\mathsf{D}}_{ij}(\mathbf{x}) + \frac{1}{8\pi\eta} \sum_{l=1}^{3} \mathsf{P}_{jl} \frac{\delta_{l3} x_i - \delta_{i3} x_l}{\|\mathbf{x}\|^3}.$$

Thus, the one-body problem of a sphere above a wall is solved by the integral in Eq. (2.3), when the induced force density $\mathcal{F}(\mathbf{r})$ is known. Due to the linearity of the Stokes equation, the force density $\mathcal{F}(\mathbf{r})$ can be linearly expressed in terms of the incident flow field $\mathbf{u}^\infty$ and the rigid body motion of the sphere $\mathbf{u}$ through the so-called grand resistance operator Z [125, 31]

$$\mathcal{F}(\mathbf{r}) = -\int \mathsf{Z}(\mathbf{r}, \mathbf{r}')(\mathbf{u}^\infty(\mathbf{r}') - \mathbf{u}(\mathbf{r}'))\mathrm{d}\mathbf{r}'. \tag{2.9}$$

The support of $\mathsf{Z}(\mathbf{r}, \mathbf{r}')$ is on the surface of the sphere [110]. The operator Z is symmetric in the sense that $\mathsf{Z}_{\alpha\beta}(\mathbf{r}, \mathbf{r}') = \mathsf{Z}_{\beta\alpha}(\mathbf{r}', \mathbf{r})$, which follows from Lorentz' reciprocity theorem [115, 49].

Eq. (2.3) and Eq. (2.9) both relate the incident flow $\mathbf{u}^\infty$ and the total flow $\mathbf{u}$ to the force density $\mathcal{F}$. Eq. (2.3) can be interpreted as the sum of an incident flow and a (scattered) flow field due to the presence of the force density $\mathcal{F}$. Eq. (2.9) tells us what force density is caused by the driving flow, which is the difference between real and unperturbed flows. This interpretation is better elucidated by writing equations (2.3) and (2.9) in matrix notation, which then leads to a formalism called hydrodynamic scattering theory [50]. This formalism was worked out, e. g., by Cichocki, Felderhof, Jones, and Schmitz and is described in a series of papers [125, 50, 49, 110]. The basic idea is that one can find two basis sets of solutions of the homogeneous Stokes equation appropriate to the spherical symmetry of the unbounded problem. These sets are built up of the vector spherical harmonics [49] and can be found, e. g., in [51, 49, 110]. One of these sets is complete for expanding a solution of the homogeneous Stokes equation that is regular everywhere [110]. Thus, the incident flow-field $\mathbf{u}^\infty$ and the rigid body motion Eq. (2.2) can be expanded in this set and we denote their (countable infinite) coefficient vectors by $\mathbf{c}^+$ and $\mathbf{c}^u$, respectively. The second set is complete for expanding a solution of the homogeneous Stokes equation that is singular at the origin but regular elsewhere and vanishes at infinity. It turns out that the second term in Eq. (2.3) can be expanded in this set and we denote the corresponding coefficient vector by $\mathbf{c}^-$. In this analysis also the force density $\mathcal{F}$, the grand resistance operator Z and the Green tensor T can be represented in vector and matrix form, respectively [125]. We denote these representations as $\mathbf{f}, \mathbf{Z}$, and $\mathbf{T}$, respectively. Then, equations (2.3) and (2.9) are rewritten in the form

$$\mathbf{c}^- = \mathbf{T}\mathbf{f}, \qquad \mathbf{f} = -\mathbf{Z}(\mathbf{c}^+ - \mathbf{c}^u), \tag{2.10}$$

where total flow is given as $\mathbf{c}^+ + \mathbf{c}^-$. This depicts the definition of force multipoles exerted on the fluid by the particle and shows how the Green tensor propagates these multipoles.

2.1.1 Friction and mobility matrices

We turn now to Cartesian multipole moments of the force density and the driving field. The total force and torque the sphere exerts on the fluid follow from the force density as

$$\mathbf{F}^H = \int \mathcal{F}(\mathbf{r})\mathrm{d}\mathbf{r}, \quad \mathbf{T}^H = \int (\mathbf{r}-\mathbf{R}) \times \mathcal{F}(\mathbf{r})\mathrm{d}\mathbf{r} \; . \tag{2.11}$$

Because we consider a rigid object, higher (Cartesian) moments of the force density are not required in our context. For the unperturbed flow at the mid-point of the sphere, we make the following definitions:

$$\mathbf{U}^\infty = \mathbf{u}^\infty(\mathbf{R}), \quad \mathbf{\Omega}^\infty = \frac{1}{2} \nabla \times \mathbf{u}^\infty(\mathbf{r})\Big|_{\mathbf{r}=\mathbf{R}}, \quad \mathsf{E}^\infty_{ij} = \frac{1}{2}\left(\partial_i u^\infty_j(\mathbf{r}) + \partial_j u^\infty_i(\mathbf{r})\right)\Big|_{\mathbf{r}=\mathbf{R}}, \tag{2.12}$$

where the vector $\mathbf{\Omega}^\infty$ is called vorticity and the tensor E^∞ *rate of strain tensor*. Because we restrict ourselves to linear shear flow, all higher moments of the unperturbed flow vanish.

The linear relationship between the force density $\mathcal{F}(\mathbf{r})$ and the driving flow, given in Eq. (2.9) can be specified for the first Cartesian moments of the force density [125]. It leads to the following relation, which defines the friction matrix $\mathsf{R_u}$ and the (six-dimensional) shear force $\mathbf{F}^S$ [31]:

$$\begin{pmatrix} \mathbf{F}^H \\ \mathbf{T}^H \end{pmatrix} = -\mathsf{R_u} \begin{pmatrix} \mathbf{U}^\infty - \mathbf{U} \\ \mathbf{\Omega}^\infty - \mathbf{\Omega} \end{pmatrix} - \mathbf{F}^S, \tag{2.13}$$

where $\mathbf{F}^S = \mathsf{R_E} : \mathsf{E}^\infty$ with $\mathsf{A} : \mathsf{B} = \mathrm{tr}\ \mathsf{AB}^\mathsf{T}$. The shear force $\mathbf{F}^S$ results from the perturbation of the flow by the presence of the wall and vanishes for free flow. The two matrices $\mathsf{R_u}$ and $\mathsf{R_E}$ are conveniently written as

$$\mathsf{R_u} := \begin{pmatrix} \zeta^{tt} & \zeta^{tr} \\ \zeta^{rt} & \zeta^{rr} \end{pmatrix}, \qquad \mathsf{R_E} := \begin{pmatrix} \zeta^{td} \\ \zeta^{rd} \end{pmatrix}, \tag{2.14}$$

where ζ denote the *friction tensors* and the superscripts t, r and d stand for translational, rotational and dipolar, respectively. In order to obtain the translational and rotational velocities of the sphere as a function of the hydrodynamic forces and torques, we have to invert Eq. (2.13):

$$\begin{pmatrix} \mathbf{U} \\ \mathbf{\Omega} \end{pmatrix} = \begin{pmatrix} \mathbf{U}^\infty \\ \mathbf{\Omega}^\infty \end{pmatrix} + \mathsf{M}\left[\begin{pmatrix} \mathbf{F}^H \\ \mathbf{T}^H \end{pmatrix} + \mathbf{F}^S\right] \; . \tag{2.15}$$

The symmetric matrix $\mathsf{M} = {\mathsf{R_u}}^{-1}$ is called *mobility matrix*. It is convenient to define the mobility tensors through

$$\mathsf{M} = {\mathsf{R_u}}^{-1} = \begin{pmatrix} \mu^{tt} & \mu^{tr} \\ \mu^{rt} & \mu^{rr} \end{pmatrix}, \qquad {\mathsf{R_u}}^{-1}\mathsf{R_E} = \begin{pmatrix} \mu^{td} \\ \mu^{rd} \end{pmatrix} \; . \tag{2.16}$$

The symmetry of $\mathsf{R_u}$ and its inverse M follows from the symmetry of the grand resistance operator Z mentioned above. In order to calculate the friction and *mobility tensors* μ for the special case of a sphere in linear shear flow above a wall, we follow the procedure from Ref. [31]. The friction tensors ζ introduced in Eq. (2.14) and the mobility tensors

μ introduced in Eq. (2.16) are expressed in terms of scalar functions together with irreducible tensors formed form the Kronecker symbol δ_{ij}, the Levi-Civita symbol ϵ_{ijk} and the normal vector $\mathbf{k} = \mathbf{e}_z$. The scalar friction functions are given by elements of the matrix representation $\mathbf{Z}$ of the grand resistance operator which was introduced in Eq. (2.10) [110, 111]. For the unbounded fluid the matrix $\mathbf{Z}_0$ can be obtained from the solution of the flow problem which is found in [125]. In the presence of a wall the required elements of $\mathbf{Z}$ are not known analytically. As explained by Perkins and Jones [110], the elements of the matrix representation $\mathbf{Z}$ can be determined by iteration of

$$\mathbf{Z} = \mathbf{Z}_0 - \mathbf{Z}_0 \Delta\mathbf{T}\mathbf{Z}, \tag{2.17}$$

where $\Delta\mathbf{T}$ is the matrix representation of the image Green tensor Eq. (2.8). The iteration of (2.17) expresses $\mathbf{Z}$ in terms of the resistance matrix for the unbounded fluid $\mathbf{Z}_0$ and a series of terms of increasing powers of $\Delta\mathbf{T}$. This series is called reflection series [110] and is a series in powers of $s = R/z \in [0, 1]$ as $\Delta\mathbf{T}$ depends on the distance from the wall. In the limit $s \to 0$, that is far away from the wall, this series converges rapidly [31]. In the other limit $s \to 1$, that is close to the wall, the series convergence is bad but analytical results for the scalar friction functions can be obtained with lubrication theory[1]. In order to cover the whole interval, the two limit solutions are matched using a Padé summation scheme. More details of this implementation are given in Appendix B.1.

2.2 Langevin equation

The motion of a particle subject to thermal, hydrodynamic and direct external forces like gravity is called *Stokesian Dynamics* [21]. In this section we derive the corresponding stochastic differential equation (*Langevin equation*). The Langevin equation will allow us to base our statistical treatment on the repeated simulation of individual trajectories. Because we are interested in the over-damped (Stokes) limit, we can neglect inertia in Newton's second law:

$$-\mathbf{F}^H + \mathbf{F}^D + \mathbf{F}^B = 0, \tag{2.18}$$

where $-\mathbf{F}^H$, $\mathbf{F}^D$ and $\mathbf{F}^B$ are hydrodynamic, direct and thermal forces acting on the sphere. An analogous balance exists for the torques. For the following treatment, forces and torques as described above are united in one symbol. For example, if not explicitly said differently, from now on the symbol $\mathbf{F}$ denotes $(\mathbf{F}, \mathbf{T})$, a six-dimensional vector comprising force $\mathbf{F}$ and torque $\mathbf{T}$, and $\mathbf{U}$ denotes the six-dimensional particle translational/angular velocity vector.
In the absence of Brownian forces, $\mathbf{F}^B = 0$ and $\mathbf{F}^D = \mathbf{F}^H$. Inserting this into Eq. (2.15) then gives

$$\mathbf{U} = \mathbf{U}^\infty + \mathsf{M}(\mathbf{F}^D + \mathbf{F}^S) \tag{2.19}$$

and the particle trajectory can be found with a simple Euler algorithm as $\mathbf{X}(t + \Delta t) = \mathbf{X}(t) + \mathbf{U}\Delta t + \mathcal{O}(\Delta t^2)$.

In the presence of Brownian motion, the situation is more complex, because thermal noise leads to terms of the order $\Delta t^{1/2}$ and special care has to be taken to include all terms

[1] Lubrication theory deals with flows close to boundaries. Such flows can be approximated to be unidirectional which means that the flow profile is assumed to depend only on the local pressure gradient and the geometry of the domain of flow [115].

up to order Δt. Due to the fluctuation-dissipation theorem, for our problem Gaussian white noise reads

$$\langle \mathbf{g}_t \rangle = 0, \qquad \langle \mathbf{g}_t \mathbf{g}_{t'} \rangle = 2k_B T_a \mathsf{M} \delta(t - t') \ , \tag{2.20}$$

with T_a ambient temperature and Boltzmann constant k_B. Here, the subscript t corresponds to the fact that the thermal force $\mathbf{g}$ is a random process. According to the *Einstein relation* the diffusion matrix of the sphere is $\mathsf{D} = k_B T_a \mathsf{M}$. To fulfill Eq. (2.20), the mobility matrix and therefore also the diffusion matrix have to be positive definite. This is indeed the case as the viscous flow about a sphere represents a dissipative system [32].

The left part of Eq. (2.20) states that the forces on the particles exerted by the fluid are equally distributed in all directions so there is no net drift due to thermal fluctuations. The right part of Eq. (2.20) states that forces at different times are not correlated, which is a good approximation because the diffusive forces act on a much faster time scale than the hydrodynamic forces. Because the mobility matrix M is position-dependent, we deal with so-called *multiplicative noise*. Since the δ-correlation in Eq. (2.20) can be considered to be the limit of a process with an intrinsic time scale for thermal relaxation, which is much faster than the time scale of hydrodynamic movement, the Stratonovich interpretation of the stochastic process is appropriate [157, 71]. This means that for each time step, the mobility functions have to be evaluated at $\mathbf{X}(t+(1/2)\Delta t)$ (rather than at $\mathbf{X}(t)$ as in the Itô interpretation). The Stratonovich interpretation also implies that the rules for integration and coordinate transformation are the same as for the Riemann integral in non-stochastic calculus.

The presence of the thermal noise Eq. (2.20) converts the position function $\mathbf{X}(t)$ into a random process $\mathbf{X}_t$. Multiplicative noise can result in additional drift terms. We therefore write the Langevin equation as

$$\partial_t \mathbf{X}_t = \mathbf{U}^\infty + \mathsf{M}(\mathbf{F}^D + \mathbf{F}^S) + k_B T_a \mathbf{Y} + \mathbf{g}_t^S, \tag{2.21}$$

where in comparison to the deterministic equation Eq. (2.19) we have added both the Gaussian white noise $\mathbf{g}_t^S$ (to be interpreted in the Stratonovich sense) and some drift term $\mathbf{Y}$. The drift term $\mathbf{Y}$ can be derived by requiring Eq. (2.21) to be equivalent to the appropriate Smoluchowski equation. The details of these calculations are given in Appendix B.2. The result is

$$\mathbf{Y} = \mathsf{B}\nabla\mathsf{B}^T, \qquad \mathsf{M} = \mathsf{B}\mathsf{B}^T, \qquad Y_i = \mathsf{B}_{ik}(\partial_l \mathsf{B}_{lk}), \qquad \mathsf{M}_{ij} = \mathsf{B}_{ik}\mathsf{B}_{jk} \ . \tag{2.22}$$

For additive noise, that is for position-independent mobility functions, the additional drift term would vanish. In the case of position-dependent mobility matrices, the noise term $\mathbf{g}_t^S$ alone would lead to a drift of the particle towards regions of lower mobility (that is towards the wall, where mobility vanishes due to the no-slip boundary condition) [36]. This drift, however, is exactly compensated by the additional term $\mathbf{Y}$. The limit of vanishing mass, i. e., the limit of no inertia, is a singular limit [64]. The appearance of the drift term $\mathbf{Y}$ can also be derived by a proper treatment of this limit [44, 64].

For the following, it is useful to non-dimensionalize Eq. (2.21). For length, the natural scale is sphere radius R. For time, it is convenient to use $6\pi\eta R^3/k_B T_a$, which is the time needed to diffuse the distance R. For force, we use $6\pi\eta R^2\dot{\gamma}$, the Stokes force at velocity $R\dot{\gamma}$, that is in linear shear flow a distance R away from the wall. The scalar friction and mobility functions appearing in M, R_E and R_u, also become dimensionless as explained in

Appendix B.1. The Langevin equation Eq. (2.21) now reads

$$\partial_t \mathbf{X}_t = Pe\left(\mathbf{U}^\infty + \mathsf{M}(f\mathbf{F}^D + \mathbf{F}^S)\right) + \mathsf{B}\nabla\mathsf{B}^T + \mathbf{g}_t^S, \tag{2.23}$$

where the *Péclet number*

$$Pe = \frac{6\pi\eta R^3\dot{\gamma}}{k_B T_a} \tag{2.24}$$

measures the relative importance of deterministic to Brownian motion. In the limit $Pe \to 0$ the particle only exhibits diffusive motion and in the limit $Pe \to \infty$ it is no longer subjected to diffusion. The second dimensionless parameter $f = \|\mathbf{F}^D\|/6\pi\eta R^2\dot{\gamma}$ measures the relative importance of direct forces/torques versus the shear force/torque ($\mathbf{F}^D$ in Eq. (2.23) is now a unit vector pointing in the direction of the deterministic force/torque vector). Measuring the time in units of the diffusive time scale is appropriate for Péclet numbers of order ten or less for which diffusion effects are important. In this thesis we will use the above given choice of time and force scale for the computation of mean first passage times in Chapter 3 (the same scales are used in the next section 2.3, where for illustrative reasons the Stokesian dynamics algorithm is applied to a simple example). For simulations with larger Péclet numbers as carried out in Chapter 4 it is more suitable to scale time with the inverse shear rate $\dot{\gamma}^{-1}$. This has the effect of dividing Eq. (2.23) by Pe. For the simulations done in Chapter 5 which include motor dynamics we use internal scales of the motor protein as force and time scale, respectively. In Appendix A.1 a synopsis of all three choices for time and force scales used in this thesis is given, together with the respective form of the dimensionless Langevin equation.

In order to solve Eq. (2.23) numerically, it has to be discretized with respect to time. The appropriate Euler algorithm can be derived by rewriting Eq. (2.23) in the Itô-version, which adds another drift term to the equation. As explained in Appendix B.3, the two drift terms together lead to the result

$$\partial_t \mathbf{X} = Pe\left(\mathbf{U}^\infty + \mathsf{M}(f\mathbf{F}^D + \mathbf{F}^S)\right) + \nabla\mathsf{M} + \mathbf{g}_t^I \ . \tag{2.25}$$

Its discretized version is simply

$$\Delta\mathbf{X} = \left[Pe\left(\mathbf{U}^\infty + \mathsf{M}(f\mathbf{F}^D + \mathbf{F}^S)\right)\Big|_t + \nabla\mathsf{M}|_t\right]\Delta t + \mathbf{g}(\Delta t) + \mathcal{O}(\Delta t^2) \ . \tag{2.26}$$

This final result has been derived before in a different way by Brady and Bossis [21]. For vanishing shear flow, it also agrees with the classical result by Ermak and McCammon [44]. In Appendix B.3, we describe the algorithms used to implement Eq. (2.26), in particular the algorithm to generate the thermal forces $\mathbf{g}(\Delta t)$ and the update rule for the orientation of the sphere. Furthermore, we explicitly give the update steps for the six degrees of freedom in Eq. (B.23) (three translational and three rotational degrees of freedom).

In Chapters 3 and 4 we deal with two versions of this algorithm. Using the full version Eq. (2.26), involving all six degrees of freedom we refer to 3D simulations. In some simulations we use a pseudo-2D projection which is referred to as 2D algorithm. In this version translational motion is restricted to the (xz)-plane and rotations are restricted to rotations about the y-axis, thus resulting in only three degrees of freedom. The 2D version is much faster not only due to the decreased dimension, but also due to the fact that the rotational degree of freedom (in the following chapters denoted by θ) can then be treated as a Cartesian coordinate which simplifies the update rule (cf. Sec. B.3). Physically, the 2D situation can be realized, e. g., if the sphere has a magnetic moment $\mathbf{m}$ and moves in

a magnetic field $\mathbf{B} = B\mathbf{e}_y$. Then, the resulting torque $\mathbf{T}_m = B\mathbf{m} \times \mathbf{e}_y$ [72] acts to align the moment with the external field (for alignment, i. e., $\mathbf{m} \parallel \mathbf{e}_y$, the torque vanishes).

2.3 Sphere falling in shear flow

If the density of the sphere ρ_{sphere} is different from that of the surrounding fluid ρ, then the sphere is subject to a buoyant force that is proportional to the density difference $\Delta\rho := \rho - \rho_{sphere}$. Thus, if the sphere density is larger than that of the fluid $\Delta\rho < 0$ a constant drift force towards the wall exists. As we will see later, this drift ensures that on average the receptor covered sphere will bind to the ligand-coated wall in finite time. The two independent parameters defined in Eq. (2.23) for this model system are Pe and $f = (2R\Delta\rho g)/(9\eta\dot{\gamma})$, with the earth acceleration constant $g = 9.81\ \mathrm{m/s^2}$. For the considerations done in Chapter 3, it is convenient to introduce also the parameter

$$Pe_z = f\ Pe = \frac{4\pi\Delta\rho R^4 g}{3k_B T_a}, \tag{2.27}$$

which we call the *Péclet number in z-direction*. Pe and Pe_z represent the strengths of the hydrodynamic and gravitational forces in respect to the thermal force, respectively. It must be noted that out of the three parameters Pe, f and Pe_z, only two are independent (because $f = Pe_z/Pe$).

We first consider the path of a sphere falling in shear flow after it has been dropped at some initial height z_0 at time t_0. Fig. 2.2 illustrates the effect of the Péclet number by showing some representative simulation trajectories (more precisely, only the projections onto the (x, z)-plane is shown, i. e., $z(x)$ and $\theta(x)$). For $Pe = \infty$ the motion of the sphere is purely deterministic and only governed by the parameter f (see Fig. 2.2a). In the diffusive limit $Pe = 0$, the sphere makes a pure random walk (except for the drift in z-direction due to the gravitational force, see Fig. 2.2d).

As the mobility matrix does only depend on the height of the sphere above the wall (cf. Appendix B.1), the motion in the z-direction is independent of the position in the (x, y)-plane and the orientation of the sphere. Therefore, it can be treated separately. In the deterministic regime the equation of motion in z direction is obtained from Eq. (2.25) by dividing the z-component by Pe, and taking the limit $Pe \to \infty$. We then get the following differential equation

$$\dot{z} = -f\hat{\alpha}^{tt}(1/z), \tag{2.28}$$

with the scalar mobility function $\hat{\alpha}^{tt}$ defined in Appendix B.1. Using the approximation $\alpha^{tt}(1/z) \approx 1 - 1/z$, which is valid in the proximity to the wall (cf. page 111), Eq. (2.28) can be integrated to provide

$$z(t - t_0) = 1 + \mathrm{plog}\ e^{-f(t-t_0)+z_0-1+\ln(z_0-1)},$$

with the product logarithm $x = \mathrm{plog}\ a$ defined as the solution to the equation $xe^x = a$, and $\mathrm{plog}\ a = 0$ only if $a = 0$. Thus, the sphere does not reach the wall in finite time, only if $t \to \infty$ the height approaches the limit $z \to 1$. In Fig. 2.3 translational and angular velocities $U = \dot{x}$ and $\Omega = \dot{\theta}$, respectively, are shown over a large range of heights. When $z \to 1$ the mobility vanishes and therefore both translational and angular velocity approach zero (no-slip boundary conditions). At large distance from the wall the sphere moves like a particle in unbound fluid with $U = z\dot{\gamma}$ and $\Omega = \frac{1}{2}\dot{\gamma}$. It has been shown by Goldman

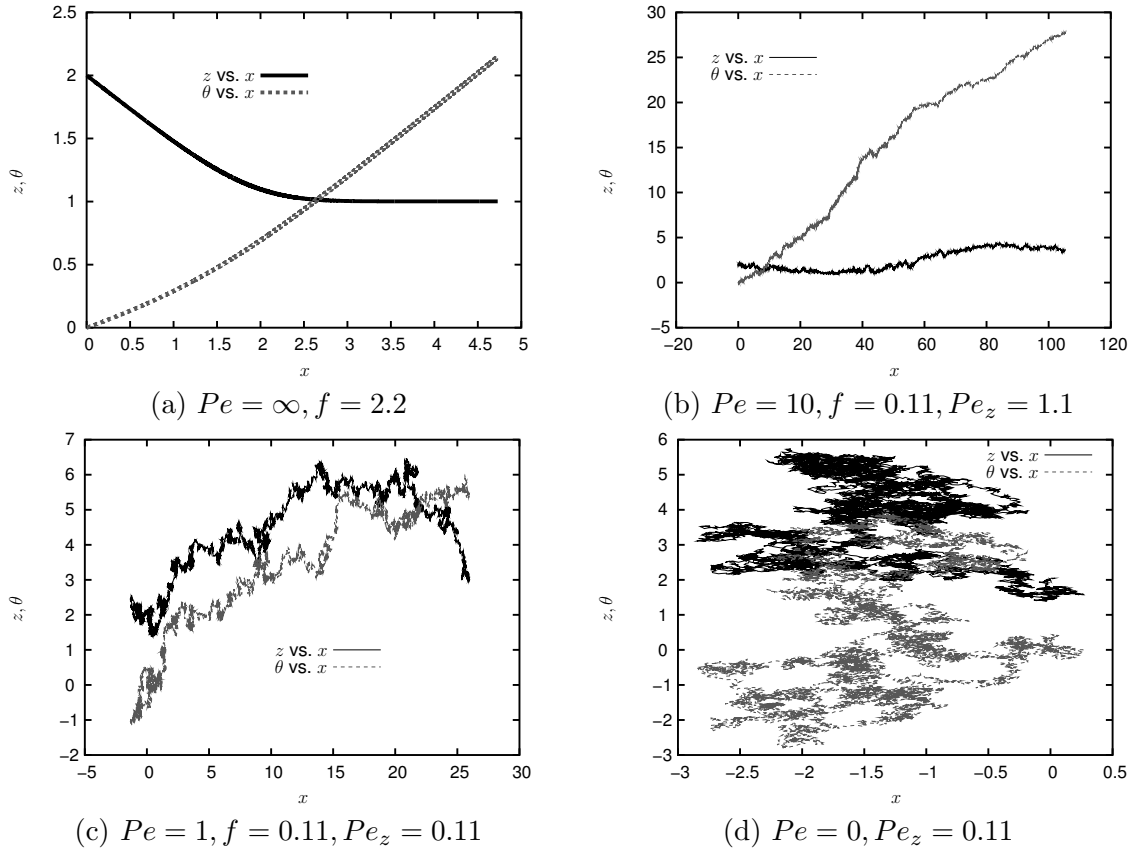

(a) $Pe = \infty, f = 2.2$ (b) $Pe = 10, f = 0.11, Pe_z = 1.1$

(c) $Pe = 1, f = 0.11, Pe_z = 0.11$ (d) $Pe = 0, Pe_z = 0.11$

Figure 2.2: Falling sphere in shear flow. For different values of the shear rate (represented by the Péclet number Pe) and the driving force (represented by f or Pe_z). The z-coordinate and the orientation angle θ are plotted versus the x-coordinate (with initial conditions $z = 2, \theta = 0$ and length scale R).

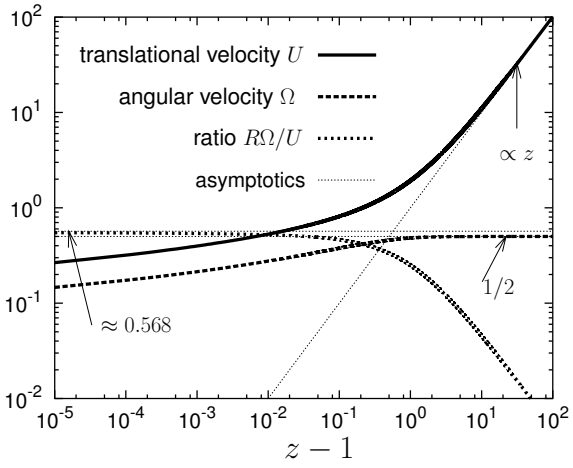

Figure 2.3: 2D motion in the limit $Pe \to \infty$. Translational and angular velocity $U = \dot{x}$ and $\Omega = \dot{\theta}$, respectively, and their ratio $R\Omega/U$ are shown as a function of the height above the wall $z - 1$. The thin lines depict the asymptotic behavior for $z \to 1$ and $z \to \infty$, respectively. U and Ω are plotted in units of $R\dot{\gamma}$ and $\dot{\gamma}$, respectively.

et al. that the ratio $R\Omega/U$ has a definite limit for $z \to 1$, which is $R\Omega/U \approx 0.5676$ [60] (this value can be obtained using the coefficients of the lubrication expansion tabulated in Tab. B.1). As can be seen from Fig. 2.3 the ratio $R\Omega/U$ increases monotonically with decreasing height. But it never comes close to rolling which is defined by $R\Omega/U = 1$. In

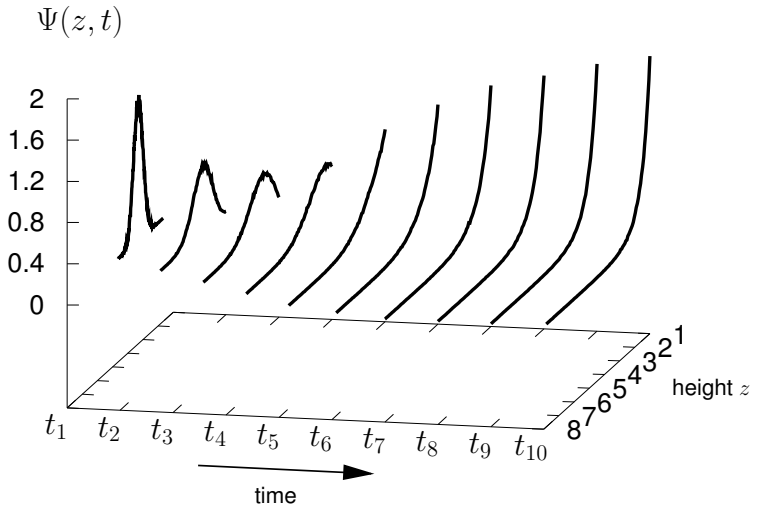

Figure 2.4: Probability distribution function $\Psi(z,t)$ numerically obtained from $N = 10^5$ sample paths for ten consecutive points in time. The initial distribution was $\Psi(z,t_0) = \delta(z-3)$ at $t = t_0$, $Pe_z = 2$. For large times the distribution function approximates the a stationary shape given by Eq. (2.30).

Fig. 2.2a this ratio appears as the slope of the $\theta(x)$ curve (as $R\partial\theta/\partial x = R\dot{\theta}/\dot{x}$). There again, it can be seen that the ratio $R\dot{\Omega}/U$, i. e., the slope of the $\theta(x)$-curve, increases while the sphere approaches the wall.

In the non-deterministic limit, i. e., for finite Pe, the height of the sphere is described by a probability density function Ψ. The probability density $\Psi(z,t)$ for the sphere being at height z at time t is the solution to a one-dimensional Smoluchowski equation

$$\partial_t \Psi(z,t) = -\partial_z J_z, \;\; J_z = -\mathsf{M}_{zz}(\partial_z \Psi + Pe_z \Psi). \tag{2.29}$$

This equation cannot be solved analytically as the mobility function M_{zz} is not known in closed form. In Fig. 2.4 we show numerical solutions obtained by simulating the equivalent Langevin equation. One clearly sees that first the δ-function at $t = 0$ is broadened due to diffusion and then develops into a stationary solution which has its maximum at the wall. This stationary solution has a simple analytical form which follows from Eq. (2.29) by integrating $J_z = 0$:

$$\Psi_s(z) = Pe_z e^{-Pe_z(z-1)} \; . \tag{2.30}$$

Thus, the stationary solution is simply the barometric formula, as it should be for thermodynamic reasons. We also find that the first two moments (mean and variance) are the same:

$$\langle z-1 \rangle = \sqrt{\langle z^2 \rangle - \langle z \rangle^2} = \frac{1}{Pe_z} \; . \tag{2.31}$$

In the limit of vanishing gravitational force ($Pe_z \to 0$), the probability distribution becomes flat and the probability of finding the sphere does not peak at the wall anymore.

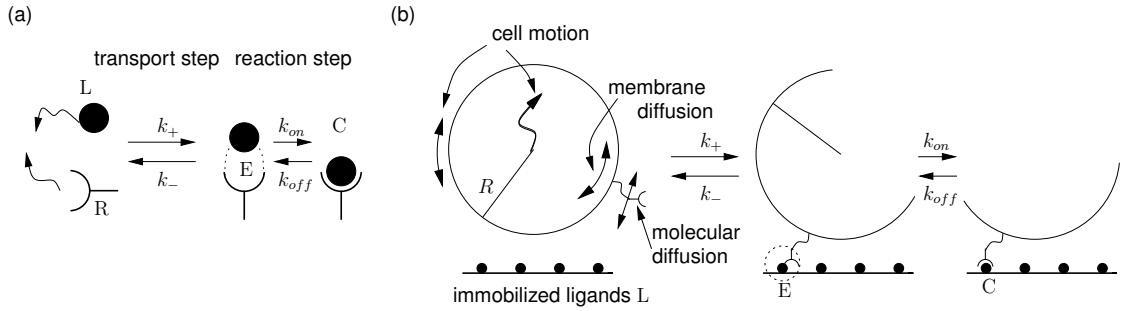

Figure 2.5: Illustration of separating the overall receptor-ligand complex formation into a transport and a reaction step. (a) Receptors and ligands free in solution. Bond formation is separated in a transport step by diffusion with rates k_+, k_- and a reaction step which is characterized by the intrinsic rates k_{on}, k_{off} (figure based on a figure from Lauffenburger and Linderman [94]). (b) Immobilized ligands on a wall and receptors attached to a sphere. The encounter step is now defined by transport of cell receptor to the proximity of a wall ligand. The on- and off-rate k_{on}, k_{off} might then still depend on membrane and molecular diffusion of the receptor.

2.4 Dynamics of receptor-ligand complexes

The main focus of this thesis is the interaction of cells with the wall by specific bonds. Here we discuss the process of formation and dissociation of such bonds.

2.4.1 Bond formation

Considering receptors R and ligands L with mutual affinity in solution their interactions can be described by the following reaction equation [94]

$$\mathrm{R} + \mathrm{L} \underset{k_r}{\overset{k_f}{\rightleftharpoons}} \mathrm{C},$$

where C denotes the receptor-ligand complex and the rate constants k_f and k_r account for the forward and reverse reaction, respectively, and define reaction kinetics according to

$$\frac{\mathrm{dC}}{\mathrm{d}t} = k_f \mathrm{RL} - k_r \mathrm{C}.$$

Here R,L,C are the concentrations of receptors, ligands and complexes, respectively, given in M = mol/l (mole per liter). Thus, the forward reaction rate is given in units of 1/(Ms) and the reverse rate is given in units of 1/s ≡ Hz. In general, a chemical reaction of at least second order is always preceded by a diffusional encounter process [40]. Thus, it is convenient to consider the receptor-ligand complex formation as a two-step process, according to (see e. g.,[40, 20] and Fig. 2.5a)

$$\mathrm{R} + \mathrm{L} \underset{k_-}{\overset{k_+}{\rightleftharpoons}} \mathrm{E} \underset{k_{off}}{\overset{k_{on}}{\rightleftharpoons}} \mathrm{C}.$$

Thus, in the first step a physical transport process (mainly diffusion) brings receptor and ligand to close proximity to form the encounter complex E. The rates for formation and dissolution of the encounter complex are given by k_+ and k_-, respectively. The second step is the actual reaction step with the *intrinsic* rates k_{on}, k_{off}. The notion of encounter complexes has a long tradition and was first introduced to study reactions between ions, e. g., Smoluchowski 1917 ("Koagulationskinetik" [143]). In the 1970s this concept was also discussed in the context of biological reactions by Eigen [40] and Berg and Purcell [16]. Using again the principles of mass action kinetics the equations for the time change of E and C read

$$\frac{\mathrm{dE}}{\mathrm{d}t} = k_+\mathrm{RL} + k_{off}\mathrm{C} - (k_- + k_{on})\mathrm{E},$$
$$\frac{\mathrm{dC}}{\mathrm{d}t} = k_{on}\mathrm{E} - k_{off}\mathrm{C} = k_f\mathrm{RL} - k_r\mathrm{C}.$$

These equations define the units of the rates k_-, k_{on}, k_{off} to be 1/s, and k_+ to be measured in 1/(M s). The encounter concentration can be approximated to be in quasi-steady state $\mathrm{dE}/\mathrm{d}t = 0$ [40, 141]. Then, the overall rates k_f, k_r can be expressed in terms of $k_+, k_-, k_{on}, k_{off}$ via

$$k_f = \frac{k_+ k_{on}}{k_- + k_{on}}, \qquad k_r = \frac{k_{off} k_-}{k_- + k_{on}}. \tag{2.32}$$

From the preceeding relation two limiting cases for the mutual efficiency of diffusion and intrinsic reaction can be derived. If the decay of the encounter complex is much slower than the formation of the actual complex C, i. e., $k_- \ll k_{on}$, then

$$k_f \approx k_+, \qquad k_r \approx k_- \frac{k_{off}}{k_{on}} \tag{2.33}$$

and the overall process is diffusion controlled. Reversely, if the reactional association is much slower than the dissolution of the encounter complex, i. e., $k_- \gg k_{on}$, the process is reaction controlled, leading to

$$k_f \approx k_{on} \frac{k_+}{k_-}, \qquad k_r \approx k_{off}. \tag{2.34}$$

The notion of encounter complex is closely related to that of capture radius r_0. The capture radius defines the critical distance to which the two reactants have to approximate each other in order to undergo their reaction, thus it defines at which distance encounter occurs. When solving the diffusion equation with the boundary condition of fixed ligand concentration c_0 at infinity and an absorbing boundary on a sphere (with radius given by the capture radius r_0) around the receptor's position, the number of ligands absorbing per c_0 can be identified with the rate k_+ (Smoluchowski: "probability of adsorption per time" [143]). On the other hand, solving the diffusion equation with the boundary condition that the concentration on the capture sphere is constant and a perfect sink exists at infinity, the resulting flux of ligands reaching infinity can be identified with the rate k_-. For example for ligands and receptors diffusing freely in solution, with total diffusion constant $D_{\mathrm{RL}} = D_{\mathrm{R}} + D_{\mathrm{L}}$, these rates are [40, 13]:

$$k_+ = 4\pi D_{\mathrm{RL}} r_0, \qquad k_- = 3D_{\mathrm{RL}}/r_0^2. \tag{2.35}$$

Thus, the equilibrium constant for the encounter step is $k_+/k_- = 4\pi r_0^3/3$, i. e., given by the volume of the encounter sphere.

The rates k_f, k_r for ligands free in solution can be determined from affinity measurements (e. g., from BIAcore experiments [159]). Then, using Eq. (2.32) and Eq. (2.35) the intrinsic rates k_{on}, k_{off} can be calculated. It was noted by Bell, that in addition knowing similar expressions as in Eq. (2.35) for a different geometry, i. e., surface bound receptors and ligands, the overall reaction rates k'_f, k'_r for that geometry can be calculated using again Eq. (2.32) [13] (provided that geometry does not affect the intrinsic rates).

For the systems under investigation in this thesis, receptors are attached to the surface of a sphere that moves in hydrodynamic flow and ligands are attached to a boundary wall. Thus, basically three kinds of motion for the receptors (or more precisely their binding sites) can be determined (illustrated in Fig. 2.5b): i) convective and diffusive motion of the sphere on which the receptors are attached, ii) diffusion of the anchorage point of the receptor in the cell membrane, in the case the sphere represents a cell, and iii) molecular diffusion of the receptor endpoint (binding site). It is important to note that these types of transport are not of the same importance. Close receptor-ligand proximity, which provides a necessary condition for encounter, can only be reached by means of the first transport mechanism mentioned. The two others complement each other. Therefore, we consider the end of the transport step to be the encounter of a receptor molecule with an immobilized ligand molecule rather than the encounter of their respective binding sites. In Chapter 3 we will calculate the mean time T for such encounters. In order to conceptually match this quantity to the above explained theory, the expression R defining the receptor concentration must be replaced by the number of cells. Then, k_+, k_f are given in units of $1/(\text{s } \# \text{ of cells})$ and the encounter rate, i. e., the inverse of the mean encounter time T can be identified with k_+.

In this approach, applied in the following, the on-rate k_{on} does not denote the intrinsic reaction rate, as it still depends on membrane and molecular diffusion of the receptor (relative to the ligand). The diffusion constant of membrane attached molecules in lymphocytes is of the order 10^{-10} cm^2/s [13], which is the same order as for the diffusion constant of the lymphocyte itself $\sim k_B T_a/(6\pi\eta R)$ ($R \approx 5$ μm). The molecular diffusion of the binding site (which marks the end of a polymeric chain), however, is faster than the diffusion of the cell due to its three orders of magnitude smaller size. Forces along the receptor/cell-center direction due to external shear flow which might influence the motion of the receptor head turn out to be fairly weak ($< 10^{-3}$ pN) [136]. Thus, besides contributions from the overall motion of the cell, the receptor motility is dominated by the molecular diffusion of its binding site. Indeed, in a very recent study on leukocyte capture (by L-selectin) in flow chambers it was found that an increased molecular diffusivity of receptors leads to an increased adhesion probability [162]. Here, their effect will be neglected.

2.4.2 Bond dissociation

A receptor-ligand complex between surface attached receptor and ligand represents a bond. In biological systems these bonds are generally based on weak non-covalent interactions, allowing for quick rearrangements [128]. For example the fast processes occurring in rolling adhesion were not possible if adhesion was due to (strong) covalent bonds. Here, we will briefly discuss how bond dissociation can be treated as thermally activated escape over a transition state barrier in the framework of Kramers theory and how the dissociation rate (off-rate) is influenced by a force acting on the bond (a more detailed overview to

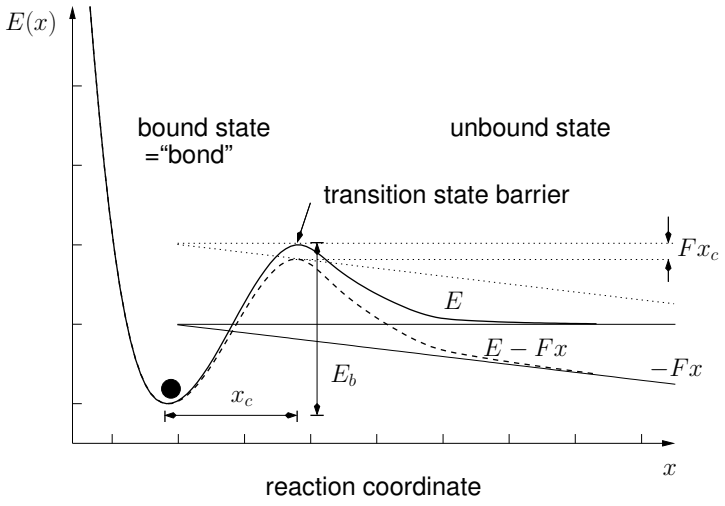

Figure 2.6: Schematic energy landscape $E(x)$ for the receptor-ligand interaction along a reaction coordinate x. The bound state is separated from the unbound state by a transition state barrier of height E_b a distance x_c (reactive compliance) away from the bound state minimum. By applying a force F along the reaction coordinate the energy landscape is tilted and the barrier height is reduced.

this issue can be found in [42]). The specific structure of the binding site (pocket) of a receptor determines the pathway for the ligand while bond formation and rupture, respectively, occurs. Usually it is assumed that this pathway can be well described as a one-dimensional potential energy landscape along a reaction coordinate x, representing the distance between receptor and ligand (such energy landscape is schematically drawn in Fig. 2.6). The bound state is represented by a deep minimum of the potential energy $E(x)$ and separated by a sharp transition state barrier of height E_b. The distance between the bound state minimum and barrier's maximum x_c is called reactive compliance. Kramers' assumption was that x undergoes Brownian motion in the potential $E(x)$. Considering the system in a quasi-stationary state, the bond dissociation rate follows from the inverse mean first passage time for x to escape over the barrier [157, 90, 68] (the original work by Kramers [90] has been reviewed by Hänggi et al. [68]). Regarding the limit of over-damped motion, and sharp and large barrier, the off-rate k_0 (escape rate) for no external force is approximately [157, 90, 68]

$$k_0 = \nu_D e^{-E_b/k_B T_a}, \tag{2.36}$$

with ν_D the frequency of attempts to cross the barrier. The attempt frequency ν_D depends on the product of curvatures of the potential $E(x)$ at its minimum and maximum position, in a way that the frequency is the larger the sharper the extrema are. Each attempt to escape is suppressed by the Arrhenius factor $e^{-E_b/k_B T_a}$ built from the barrier height E_b. Typically values for biomolecular bonds are $\nu_D \simeq 10^9$ Hz and $E_b = 20 k_B T_a$ [128], thus the off-rate is of the order of Hz, which is much smaller than the attempt frequency ν_D.

In the case the bond is subject to force, the off-rate is supposed to change. In a seminal paper, Bell proposed a model for bond rupture under force that was adopted from the rupture mechanics of solids [13]

$$k_{off}(F) = k_0 \exp(F/F_d), \tag{2.37}$$

with the detachment force F_d. This empirical relation can be rationalized in the framework of Kramers theory. When the force F acts along the reaction coordinate x an additional term $-Fx$ is added to the potential energy landscape to become $E(x) - Fx$ (see Fig. 2.6). Thus, the transition state barrier in the presence of force is $E_b(F) \approx E_b - Fx_c$. Inserting

this expression for E_b into Eq. (2.36) leads to the Bell equation Eq. (2.37). Moreover, it relates the detachment force F_d to the reactive compliance x_c via $F_d = k_B T_a / x_c$. Actually, force also slightly affects the position of the barrier height and the shape of the potential. This leads to corrections in the force-dependence of the barrier height and the attempt frequency ν_D [47, 138] (the latter one as it depends on the shape of the potential). But, the by far dominating effect of force is the exponential increase of the off-rate given in Eq. (2.37). A typical value for the reactive compliance is $x_c = 1$ nm, with this it follows for the detachment force, providing a typical force scale for bond dynamics, $F_d = k_B T_a / x_c \approx 4$ pN (with $k_B T_a = 4.1$ pN nm being the thermal energy at room temperature) [13, 128].

The results Eq. (2.36) and Eq. (2.37) from Kramers theory are based on the assumption that the system is in quasi-stationary state. Therefore, for time-dependent forces $F(t)$ the Bell equation (2.37) does only apply in the so called *adiabatic approximation*. For the adiabatic approximation it is assumed that the escape process and equilibration of the system is much faster than changes occurring in the potential. Shillcock and Seifert could show for the case of linear loading by comparing exact mean first passage time results for the escape in the presence of time-dependent forces with results obtained in the adiabatic approximation that the latter one works fairly well over a wide range of loading rates [138]. The adiabatic approximation has been applied before, e. g., to study adhesion clusters subject to a linear increased force [43] or the analysis of *dynamic force spectroscopy* experiments [47]. In this thesis we will apply this approximation to model bond-dissociation by using the Bell equation Eq. (2.37) in the presence of time-dependent forces that occur, e. g., in rolling adhesion.

It was suggested by Dembo et al. to call a bond whose life-time decreases in the presence of force as in Eq. (2.37) a slip bond and a bond that strengthens up with force a catch bond [35]. Having been an academic issue for a long time, only recently catch bond behavior could be directly observed for P-selection-PSGL-1 bonds by Marshall and co-workers. Using both, flow chambers and atomic force microscopy they showed that the lifetime of P-selection-PSGL-1 bonds first increases with increasing force and then decreases with even further increasing applied force [101]. Recent theoretical studies gave explanations for this effect in the framework of Kramers theory assuming an at least two-dimensional energy landscape in which the unbinding pathway is determined by the amount of applied force [46, 12, 109].

2.4.3 Adhesive dynamics algorithm

We now discuss how the algorithm Eq. (2.26) which defines the position/orientation update of a sphere can be extended to include the probabilistic nature of bond formation and rupture. Such rules have been setup by Hammer and co-workers [66] and been refined several times (e. g., [28, 80, 25]) to model various aspects of leukocyte rolling. The collection of these rules are now known as *adhesive dynamics*. Detailed descriptions of this algorithm can be found for example in Refs. [66, 26]. In the following we list these rules in the way we have implemented them in routines, which were used for the numerical simulation experiments explained in Chapters 4 and 5.

The sphere's motion is described by Eq. (2.21). If no bond between the sphere receptors and wall ligand exist, we take only gravity into account for the deterministic force in Eq. (2.21), i. e., the six-dimensional force/torque vector is given by $\mathbf{F}^D = (-\Delta m g \mathbf{e}_z, \mathbf{0})$ (cf. 2.3). Functional bonds lead to additional contributions to both the force- and momentum-part of $\mathbf{F}^D$. More precisely, a (functional) bond between a ligand located at $\mathbf{r}_l$ (the z-component of this vector is zero) and a receptor located at $\mathbf{r}_r$ on the sphere's surface pulls

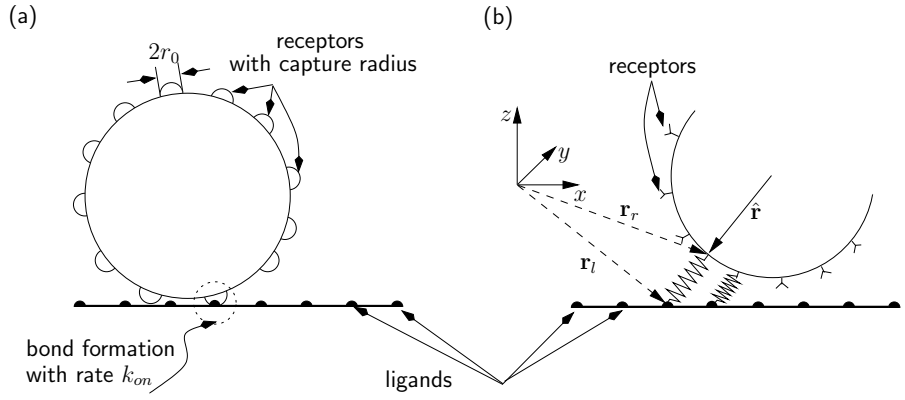

Figure 2.7: Adhesive dynamics. (a) Each receptor is represented as a capture-ball of radius r_0. During encounter with a wall ligand, bond formation occurs with rate k_{on}. (b) Closed (stretched) bonds are modeled as harmonic springs (capture ball is not drawn).

with a force

$$\mathbf{F}_B = \hat{\mathbf{r}}_b F(r_b), \qquad \hat{\mathbf{r}}_b := \frac{\mathbf{r}_l - \mathbf{r}_r}{\|\mathbf{r}_l - \mathbf{r}_r\|}, \qquad r_b := \|\mathbf{r}_l - \mathbf{r}_r\|. \tag{2.38}$$

$F(x)$ is the force extension curve that describes by what force the bond must be pulled to stretch it up to a total length x. Here, we mainly consider the bonds to be semi-harmonic springs (cable model)

$$F(x) = \kappa(x - l_0)\Theta(x - l_0), \qquad \Theta(x) := \begin{cases} 1, & x > 0 \\ 0, & \text{else} \end{cases}, \tag{2.39}$$

with l_0 the resting length and κ the spring constant. The cable model is the simplest model for polymeric tethers. In the cable model a bond behaves as a spring only if it is stretched (extension larger than the resting length), otherwise the bond exerts no force on the sphere. Treating the receptor-ligand complex as a harmonic spring works fine in the small extension regime [56]. For large extensions the force extension curve for polymers is supposed to grow much faster than linear, and when the bond extension approaches the total contour length of the receptor-ligand complex it even diverges (strain stiffening). However, as described before typical bonds are weak and their rupture probability increases exponentially with force. Therefore, we expect bond extensions to be restricted to the linear regime. As the bond force pulls on the sphere's surface also a torque results

$$\mathbf{T}_B = \hat{\mathbf{r}} \times \mathbf{F}_B(\mathbf{r}_b),$$

where $\hat{\mathbf{r}}$ is the connection vector from the center of the sphere to the point on its surface where the receptor is attached (see Fig. 2.7). Thus, the total force/torque contribution to $\mathbf{F}^D$ by the bonds is

$$\kappa \sum_{i=1}^{N_r} q_i F(r_b^i) \left(\hat{\mathbf{r}}_b^i, \hat{\mathbf{r}}^i \times \hat{\mathbf{r}}_b^i\right), \tag{2.40}$$

with N_r the total number of receptors and $q_i = 1$ if the ith receptor forms a bond and zero otherwise. The $q_i, i = 1, \ldots, N_r$ are stochastic variables. Thus, the contribution Eq. (2.40)

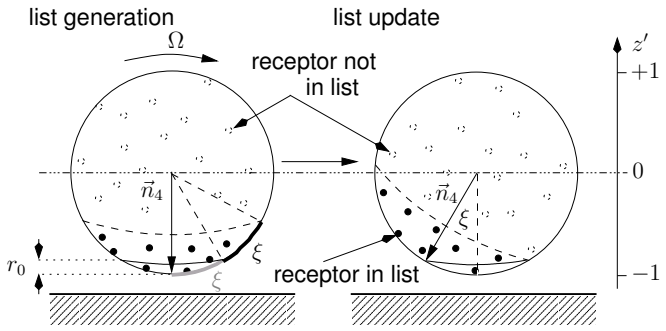

Figure 2.8: Only receptors close enough to the wall will be considered in the adhesive dynamics algorithm. Therefore, all receptors with a maximum arclength distance 2ξ from the lowest point of the sphere are put into a list. The list is updated when the vector $\vec{n}_4$ has turned by the angle ξ. z' defines a position in vertical direction relative to the sphere center.

lets the "deterministic force" $\mathbf{F}^D$ also become a stochastic variable.

With this at hand we can now define the *adhesive dynamics* rules, applied in each update step Δt (cf. Fig. 2.7):

- The sphere's position and orientation is updated according to Eq. (2.26) (for an explicit description see Appendix B.3).
- The receptor positions in the flow chamber coordinate system are calculated.
- Each inactive receptor is represented by a capture ball with radius $r_0 \ll 1$.
- (*) If the distance between a receptor and any ligand is $\leq r_0$ a bond is established with probability $p_{on} = 1 - \exp(-\Delta t \cdot k_{on})$, then the resting length of the bond is set to the receptor-ligand distance at the instance of bond-formation (i. e., the bond force at the moment of bond formation is zero) and is stored together with the ligand position. A bond can only be formed if the corresponding receptor and ligand are not already part of another bond.
- For each active bond, the contribution to $\mathbf{F}^D$ is calculated.
- Each existing bond dissociates with a rate given by the Bell equation Eq. (2.37). Thus, each bond ruptures with probability $p_{off} = 1 - \exp(-\Delta t \cdot k_{off}(F))$, where F is the instantaneous force acting along this bond.

When a bond has ruptured, both the receptor and the ligand can form a new bond in the next time step according to the rule (*). As the resting length of a bond is always smaller than $r_0 \ll 1$, modeling bonds as harmonic springs in both the extension and compression regime would not make much difference to the results that are obtained by the cable model. Given the probability for bond formation or rupture p_{on} or p_{off}, respectively, a standard *Monte-Carlo technique* is used to decide whether the action happens or not: Using a pseudo-random number generator a random number *rand* from the uniform distribution in the interval $[0, 1]$ is drawn. If then $p_{on/off} > rand$ the respective action takes place, otherwise not.

The position update of the receptors is quite costly and only the positions of those receptors close enough to the wall are needed. So, to save time we store the *relevant*

receptors in a list, and consider only those. The list is created in the following way (see Fig. 2.8): The z-coordinates relative to the center of the sphere z_r' is calculated for all receptors, if $z_r' < -1 + 4r_0$ or a receptor is part of a bond it is marked as relevant. Simultaneously, a vector relative to the sphere's center $\vec{n}_4 = (0, 0, -1)^T$ is introduced. The vector $\vec{n}_4$ is fixed relative to the sphere and updated at each time step (cf. Sec. B.3). If the third component of $\vec{n}_4$ has become larger than $-1 + r_0$ the list is updated. By construction the list always includes all the receptors that can encounter a ligand, i. e., those for which $z_r' \leq -1 + r_0$ is true. The arclength ξ between the lowest point of the sphere and a receptor at $z_r' = -1 + r_0$ is $\xi = \arccos(1 - r_0) \approx \sqrt{2r_0}$. Allowing for $\vec{n}_4$ a maximum deviation ξ with respect to its original orientation, all receptors whose arclength from the lower apex of the sphere is maximally 2ξ must be taken into account. These fulfill $z_r' < -(1 - \cos(2\xi)) \approx -1 + 4r_0$ (the described method is similar to the *Verlet list* of a single particle in molecular dynamics simulations [55]). The smaller the angular velocity of the sphere Ω the less often a list update is necessary and therefore, the more this method is efficient.

The two main differences between our implementation of adhesive dynamics and the original version of Hammer are: i) we explicitly resolve the ligand positions in space; ii) we account for Brownian motion of the cell via the Langevin equation Eq. (2.26). Without incorporating diffusive motion the use of spatially resolved receptors and ligands could lead to numerical artefacts. For example at low densities of receptors and ligands purely deterministic motion of the cell could be such that a receptor-ligand encounter never occurs. Thus, the algorithm explained above opens up the perspective to apply adhesive dynamics simulations to flow chamber experiments using substrates with regular ligand patterns.

Chapter 3

Mean first passage times for receptor-ligand encounter

Interactions mediated between receptors and ligands are highly specific. For these interactions to occur a physical transport process bringing receptor and ligand molecules to close proximity is required. For receptor-coated cells with ligands attached to a substrate this transport is mainly governed by the transport of the cell itself. In this chapter we consider the general case of a receptor coated sphere being subject to gravity and moving in linear shear flow above a ligand bearing wall, thus, mimicking flow close the bottom wall of flow chambers. For this setup we numerically compute the mean first passage times (MFPT) for receptor-ligand encounters for a series of situations of increasing complexity. We first consider homogeneous receptor and ligand coverage and show that the MFPT can be calculated exactly. We then consider spatially resolved receptor patches and finally also spatially resolved ligand patches for both movement in 2D and 3D. In an analytical approach to the MFPT problem we treat the appearing position-dependent diffusion and drift terms in a mean-field like manner which allows us to correctly predict the asymptotic behavior of the MFPT for some limiting cases.

3.1 First contact with homogeneous coverage

If the sphere and the wall are homogeneously covered with receptors and ligands, respectively, an encounter complex is established whenever the sphere comes sufficiently close to the wall. The mean time which elapses after the sphere is set free at some initial position until an encounter complex is established is then identical with the mean first passage time (MFPT) for a sphere dropped at initial height z_0 to reach the height z_1. Note again that the motion in z-direction is independent of the values of the other coordinates. For a particle diffusing in an interval $[z_1, b]$, with z_1 being an absorbing boundary and b a reflective boundary, the MFPT T to reach z_1 when started at $z \in [z_1, b]$ is the solution to the following ordinary differential equation [157]

$$A(z)\partial_z T(z|z_1) + D(z)\partial_z^2 T(z|z_1) = -1, \quad T(z_1|z_1) = 0, \quad \partial_z T(z|z_1)|_{z=b} = 0. \tag{3.1}$$

In our case, $b = \infty$. The drift term $A(z) = -Pe_z \hat{\alpha}^{tt}(1/z) + \partial_z \hat{\alpha}^{tt}(1/z)$ and the diffusive term $D(z) = \mathsf{M}_{zz} = \hat{\alpha}^{tt}(1/z)$ follow from Eq. (2.25), where $\hat{\alpha}^{tt}(1/z)$ is a scalar mobility function as explained in Appendix B.1. Pe_z is the Péclet number in z-direction defined

in Eq. (2.27). The general solution to Eq. (3.1) is [157]

$$T(z_0|z_1) = \int_{z_1}^{z_0} \mathrm{d}z \frac{1}{\Phi(z)} \left(\int_z^\infty \mathrm{d}y \frac{\Phi(y)}{D(y)} \right), \qquad \Phi(z) = \exp\left(\int^z \mathrm{d}x \frac{A(x)}{D(x)} \right). \tag{3.2}$$

This can be reduced up to an integral over $\hat{\alpha}^{tt}(1/z)$:

$$T(z_0|z_1) = \frac{1}{Pe_z} \int_{z_1}^{z_0} \mathrm{d}z \frac{1}{\hat{\alpha}^{tt}(1/z)}. \tag{3.3}$$

Thus, the dependence of $T(z_0|z_1)$ on Pe_z, the only parameter in this problem, is obtained exactly. It is important to note that the compact form for the MFPT in Eq. (3.3) is a result of the constant vertical force. For a more general vertical potential force $F_\perp = -\partial_z V(z)$ with a potential V, the drift term reads $A(z) = -\partial_z V(z)\hat{\alpha}^{tt}(1/z) + \partial_z \hat{\alpha}^{tt}(1/z)$ and Eq. (3.2) can be reduced to

$$T(z_0|z_1) = \int_{z_1}^{z_0} \frac{dz}{\hat{\alpha}^{tt}(1/z)} \int_z^\infty dy e^{V(z)-V(y)} \ . \tag{3.4}$$

This equation shows that the potential must satisfy the condition $\lim_{y\to\infty}(V(z)-V(y)) \to -\infty$ for the MFPT to be finite. This holds true, e. g., for the gravitational force studied here or for the interaction of a charged object with an oppositely charged wall, but not, e. g., for a Lennard-Jones potential.

The integral Eq. (3.3) over the scalar mobility function $\hat{\alpha}^{tt}$ can easily be calculated numerically as $\hat{\alpha}^{tt}$ behaves well in the full range of z. In fact, close to the wall $\hat{\alpha}^{tt}(s)$ can be approximated by $\hat{\alpha}^{tt}(s) \approx 1 - s$ (cf. page 111). We then find

$$T(z_0|z_1) \approx \frac{1}{Pe_z} \left[z_0 - z_1 + \ln\left(\frac{z_0 - 1}{z_1 - 1} \right) \right]. \tag{3.5}$$

A numerical analysis shows that the approximation Eq. (3.5) deviates only by a few percent from the exact solution Eq. (3.3). Thus, $T(z_0|z_1)$ is logarithmically divergent if the absorbing point is close to the wall, $z_1 \to 1$, and linearly divergent if the starting point is at infinite height, $z_0 \to \infty$.

For a sphere homogeneously covered with receptors each having a capture radius r_0, the mean time for forming an encounter complex is $T(z_0|1 + r_0)$. This time will serve as a useful limiting result in some of the considerations presented in the next sections. The exactly known result Eq. (3.3) provides also a good test for the algorithm we implemented. In Fig. 3.1a the MFPT obtained from simulation experiments and from quadrature of Eq. (3.3) are compared. The two results agree very well (see Appendix C for a discussion of the statistical and systematic errors of the simulation results). In Fig. 3.1b we show the numerically obtained distribution of first passage times (FPT). One clearly sees that the larger Pe_z, the stronger they peak around the mean. As typical for first passage time problems [70], the standard deviations of the FPT distributions are of the same order of magnitude as the mean value. For small Pe_z one finds that the standard deviations are somewhat larger than the mean value. At large Pe_z we find the reverse result.

As already mentioned, the fact that the drift towards the wall does not vanish at $z \to \infty$, i. e., $Pe_z > 0$ for a constant drift, ensures that the MFPT is finite. For no such

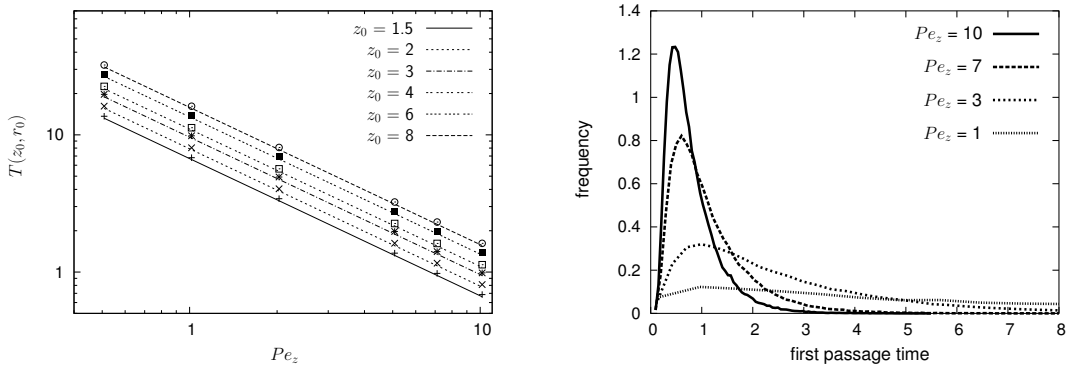

Figure 3.1: Results of first passage time simulations with encounter radius $r_0 = 10^{-3}$. (a) Mean first passage time T as a function of the vertical drift Pe_z for different starting heights z_0. Dots are the results from simulations with $N = 10^4$ runs and time step $\Delta t = 10^{-5}$. Lines are the results from quadrature of (3.3). (b) Distribution of first passage times for different values of Pe_z (numerical parameters $N = 10^5, \Delta t = 10^{-5}$.).

drift the sphere might diffuse with finite probability away from the wall and return only after an infinite long time. However, in a flow chamber the MFPT is always finite as an upper boundary for the sphere exists. Therefore, for the moment, we suppose that the sphere moves between two parallel plates with the bottom one still at $z = 0$ and the top one at height $H \gg R$. If the upper wall is not covered with ligands it acts as a reflective boundary and the MFPT $T_{2W}(z_0|z_1)$ to reach the height z_1 when started at height z_0 is

$$T_{2W}(z_0|z_1) = \int_{z_1}^{z_0} \mathrm{d}z \frac{1}{\hat{\alpha}^{tt}_{2W}(z)} \int_{z}^{H-1} e^{Pe_z(z-y)} \mathrm{d}y = \frac{1}{Pe_z} \int_{z_1}^{z_0} \frac{\mathrm{d}z}{\hat{\alpha}^{tt}_{2W}(z)} \left(1 - e^{-Pe_z(H-1-z)}\right), \tag{3.6}$$

where $\hat{\alpha}^{tt}_{2W}(z)$ is the dimensionless scalar mobility function governing translational motion in z-direction for the two-wall geometry. For large wall separations, i. e., $H \gg R$ the two-wall mobility function can be approximated by a superposition of the single-wall mobility functions. It has been shown by Jones that this approximation agrees up to a few percent already at a wall-wall distance of $H = 10$ [75]. In terms of $\hat{\alpha}^{tt}(1/z)$ this superposition reads

$$\frac{1}{\hat{\alpha}^{tt}_{2W}(z)} = \frac{1}{\hat{\alpha}^{tt}(1/z)} + \frac{1}{\hat{\alpha}^{tt}(1/(H-z))} - 1, \tag{3.7}$$

where the unbounded fluid result is subtracted to avoid double counting. Typically $z_1 < z_0 \ll H$, so the dependence of the exponential in Eq. (3.6) on z is negligible. Furthermore, for the two-wall mobility function $\hat{\alpha}^{tt}_{2W}(z) \approx \hat{\alpha}^{tt}(1/z)$ for $z \ll H$ holds. Thus, as long as $Pe_z > 0$, the MFPT $T_{2W}(z_0|z_1)$ is

$$T_{2W}(z_0|z_1) \approx T(z_0|z_1) \left(1 - e^{-Pe_z H}\right). \tag{3.8}$$

From this we conclude that the perturbation of the MFPT due to the presence of a second wall at $H \gg 1$ is small, as long as the drift towards the bottom wall is not too small, i. e.,

$Pe_z > 1$. In the case that $Pe_z = 0$ the MFPT is

$$T_{2W}(z_0|z_1) = \int_{z_1}^{z_0} \mathrm{d}z \frac{H-1-z}{\hat{\alpha}^{tt}_{2W}(z)} \approx H \int_{z_1}^{z_0} \frac{\mathrm{d}z}{\hat{\alpha}^{tt}(1/z)}. \tag{3.9}$$

Thus, T_{2W} depends linearly on the gap height H between the two walls. Hence, compared to the MFPT in the case of a constant drift $Pe_z > 1$ the MFPT is a factor $Pe_z H$ larger in the case of no drift.

We conclude the case of homogenous coverage by noting that in order to obtain dimensionalized results, one has to multiply the MFPT by the diffusive time scale $6\pi\eta R^3/k_B T_a$. This result does not depend on shear rate $\dot{\gamma}$ because vertical and horizontal motion are decoupled and rotational motion is not relevant here. However, it depends on viscosity η, which sets the time scale for vertical motion. If one switched off thermal fluctuations, the falling time would be exactly the same as the MFPT from Eq. (3.3), but this is a special result for constant force and not true in general. If one removed the wall, the translational symmetry in z-direction would not be broken and the MFPT would be $T = (z_0 - z_1)/Pe_z$, that is the logarithmic term in Eq. (3.5) would be missing.

3.2 Effect of initial height

We now turn to spatially resolved receptor and ligand coverage. The MFPT $T(\vec{\theta}, \vec{x}|C)$ now will depend on the initial position $\vec{x} = (x, y, z_0)$ and the initial orientation $\vec{\theta}$ as well as on the absorbing boundary C in diffusion space. The latter is given by the special receptor and ligand geometry. In an experimental setup with linear shear flow it is possible to measure only particles which have been initially at a certain height. This is due to the fact that their average velocity as obtained from the solution of the Stokes equation Eq. (2.15) depends on their height in a unique way [30]. However, it is almost impossible to prepare a certain initial orientation $\vec{\theta}$ or (x, y)-position relative to the ligands. Therefore, the quantity of interest to us will be a MFPT which is averaged over all possible initial orientations $\vec{\theta}$ and all initial positions (x, y), which will be denoted as $\langle T(\vec{\theta}, \vec{x}|C)\rangle_{\vec{\theta},(x,y)}$. The dependence

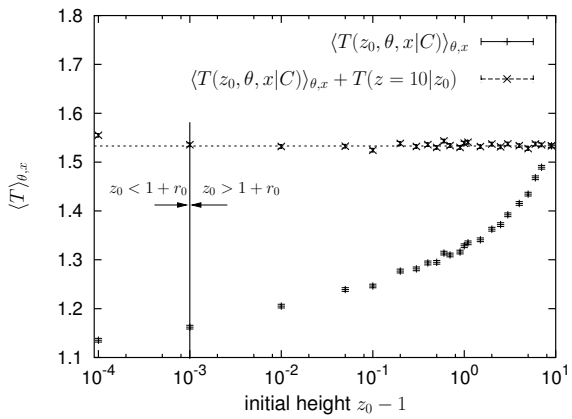

Figure 3.2: The dependence of the MFPT $\langle T(z_0, \theta, x|C)\rangle_{\theta,x}$ averaged over the sphere's initial position x and initial orientation θ on the initial height z_0 in two dimensions. The sphere is covered with $N_r = 10$ receptor patches and the ligand density is $\rho_l = 0.01$. We plot $\langle T(z_0, \theta, x|C)\rangle_{\theta,x}$ (+) and $\langle T(z_0, \theta, x|C)\rangle_{\theta,x} + T(z = 10|z_0)$ (×) as a function of z_0, where $T(z = 10|z_0)$ is obtained from Eq. (3.3). For $z_0 > 1 + r_0$ the latter curve is constant at the value $\langle T(z = 10, \theta, x|C)\rangle_{\theta,x}$ as predicted by the addition theorem Eq. (3.11). (Numerical parameters: $N = 10^5, \Delta t = 10^{-5}$.)

of $\langle T(\vec{x}, \vec{\theta}|C)\rangle_{\vec{\theta},(x,y)}$ on the initial height for $z_0 > 1 + r_0$ can be derived exactly. For

homogeneous ligand coverage the quantity of interest is

$$\langle T(\vec{\theta}, z_0|C)\rangle_{\vec{\theta}} = \frac{1}{V_{\vec{\theta}}} \int_{\vec{\theta}} d^3\vec{\theta}\, T(\vec{\theta}, z_0|C),$$

where C is the absorbing hyper-surface in $(\vec{\theta}, z)$-space and $V_{\vec{\theta}}$ a normalization constant. Absorption is only possible if $z < 1 + r_0$, thus, if we look at some intermediate height $z_0 > z_m > 1 + r_0$, then

$$T(\vec{\theta}, z_0|C) = T(\vec{\theta}, z_0|z_m) + \int d^3\vec{\theta}_m\; p(\vec{\theta}_m|\vec{\theta}) T(\vec{\theta}_m, z_m|C), \tag{3.10}$$

where $p(\vec{\theta}_m|\vec{\theta})$ is the conditional probability to pass the height z_m with the orientation $\vec{\theta}_m$ when starting with the initial orientation $\vec{\theta}$ at z_0. $T(\vec{\theta}, z_0|z_m)$ is independent of the initial orientation and can be calculated by means of Eq. (3.3). Now averaging Eq. (3.10) over the initial orientation gives

$$\begin{aligned}\langle T(\vec{\theta}, z_0|C)\rangle_{\vec{\theta}} &= T(z_0|z_m) + \frac{1}{V_{\vec{\theta}}} \int d^3\vec{\theta}_m \left[\int d^3\vec{\theta}\; p(\vec{\theta}_m|\vec{\theta})\right] T(\vec{\theta}_m, z_m|C) \\ &= T(z_0|z_m) + \frac{1}{V_{\vec{\theta}}} \int d^3\vec{\theta}_m\; T(\vec{\theta}_m, z_m|C) = T(z_0|z_m) + \langle T(\vec{\theta}_m, z_m|C)\rangle_{\vec{\theta}_m}.\end{aligned} \tag{3.11}$$

The term in square brackets being 1 follows from the spherical symmetry. Thus, if the orientation-averaged MFPT is known for some initial height $z_0 > 1 + r_0$, then the MFPT for any other initial height $z_0' > 1 + r_0$ can be calculated by means of equations Eq. (3.11) and Eq. (3.3). A similar expression can be obtained for the average over the initial x, y positions. In Fig. 3.2, this result is verified by simulations for the two-dimensional case, that is the sphere can only move in the (x, z)-plane and rotate only around the y-axis (compare Fig. 2.1 and page 19). Due to the decomposition Eq. (3.11), the initial height is not essential. In the following, we therefore will always use the value $z_0 = 2$, that is the sphere has to fall by one radius until it hits the substrate for the first time.

3.3 Movement in two dimensions

3.3.1 Dependence on receptor number

We now study the effect of shear rate for heterogeneous receptor distribution if the sphere is restricted to move only in two dimensions (cf. page 19). We consider a sphere which is covered by N_r receptor patches. For the moment being, the wall is still considered to be homogeneously covered with ligands. Shear rate is basically expressed by the Péclet number Pe that was introduced in Eq. (2.24). The receptor patches can be equidistantly distributed over the circumference as illustrated in Fig. 3.3. Each receptor patch has a capture height of r_0 and a width of $2r_p$. The 2D receptor density is then $\rho_r = N_r r_p/\pi$. Orientation is now represented by a single angle θ. The absorbing boundary C is illustrated in Fig. 3.3. For each receptor patch, binding can occur over a range $2\theta_0$, which consists of two parts. The inner part is valid already for $r_p = 0$ and reflects the overlap due to a finite r_0. The outer part is results from a finite r_p. Together this leads to $\theta_0(z) = \arccos(z/(1 + r_0)) + r_p$. The receptor patches establish a periodicity with period $\theta_s = 2\pi/N_r$. As the number of receptor patches grows, this period decreases and one finally achieves overlap. Then, encounter becomes possible for all values of θ, that is we are back to the case of

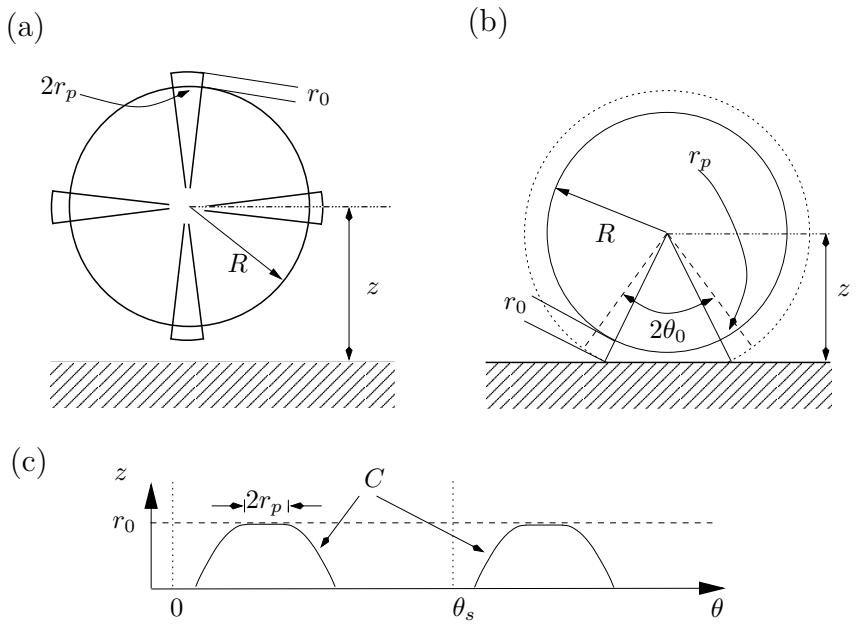

Figure 3.3: (a) Example of a sphere restricted to move in two dimensions and covered with $N_r = 4$ receptor patches, which are regularly distributed over the circumference. (b) Illustration of the range of θ in which encounter occurs. This range is given by $2\theta_0$ with $\theta_0(z) = \arccos(z/(1+r_0)) + r_p$. (c) The absorbing boundary C in the (z, θ)-plane is periodic w. r. t. θ with period $\theta_s = 2\pi/N_r$.

homogeneous receptor coverage. In our case of non-homogeneous coverage, the MFPT depends on Pe, Pe_z, N_r, r_0, r_p and z_0. For the following simulations $r_p = r_0 = 10^{-3}$, $Pe_z = 50$ and $z_0 = 2$ is chosen unless other values are explicitly mentioned.

Fig. 3.4a shows the MFPT as a function of the Péclet number Pe. Note that in the log-log plot, an apparent plateau appears at small value of Pe, although in a linear plot there would be strictly monotonous decay. Three regimes can be distinguished. For $Pe \approx 0$ (*diffusive limit*) the transport by the imposed shear flow is negligible and only diffusive transport is present. For very large values of Pe, $\langle T \rangle_\theta$ plateaus at the value given by Eq. (3.3) independent of N_r. In this limit the time for rotation to any certain orientation is negligible compared to the mean time to fall down close to the wall, therefore, the result for rotational symmetry is recovered. Between these two limits the MFPT decreases monotonically with increasing Pe. Fig. 3.4b shows the data from Fig. 3.4a plotted as a function of the receptor density $\rho_r \propto N_r$. The larger Pe the less pronounced is the dependence of $\langle T \rangle_\theta$ on N_r. For $Pe \approx 0$, however, $\langle T \rangle_\theta$ strongly depends on N_r. The latter relation is better illustrated in Fig. 3.4c. There, at $Pe \approx 0$, $\langle T \rangle_\theta$ is shown for a wide range of N_r. The simulations were done for fixed patch size r_p but for four different values of the capture radius r_0 (cf. Fig. 3.3). For $\rho_r \to 1$, $\langle T \rangle_\theta$ reaches the value given by Eq. (3.3). As described by Eq. (3.3), $\langle T \rangle_\theta$ is the smaller the larger r_0 is. An increase in the number of receptor patches N_r leads to a strong decrease for the MFPT, however, no special scaling behavior can be observed. It is remarkable that the limiting value for the case of homogeneous receptor coverage is already reached for $\rho_r \approx 10^{-2}$. The larger the capture radius r_0 the more pronounced is this effect. This can be understood by observing that the effective patch size as given by the angle $\theta_0 \geq r_p$ (see Fig. 3.3) is monotonically increasing with increasing r_0.

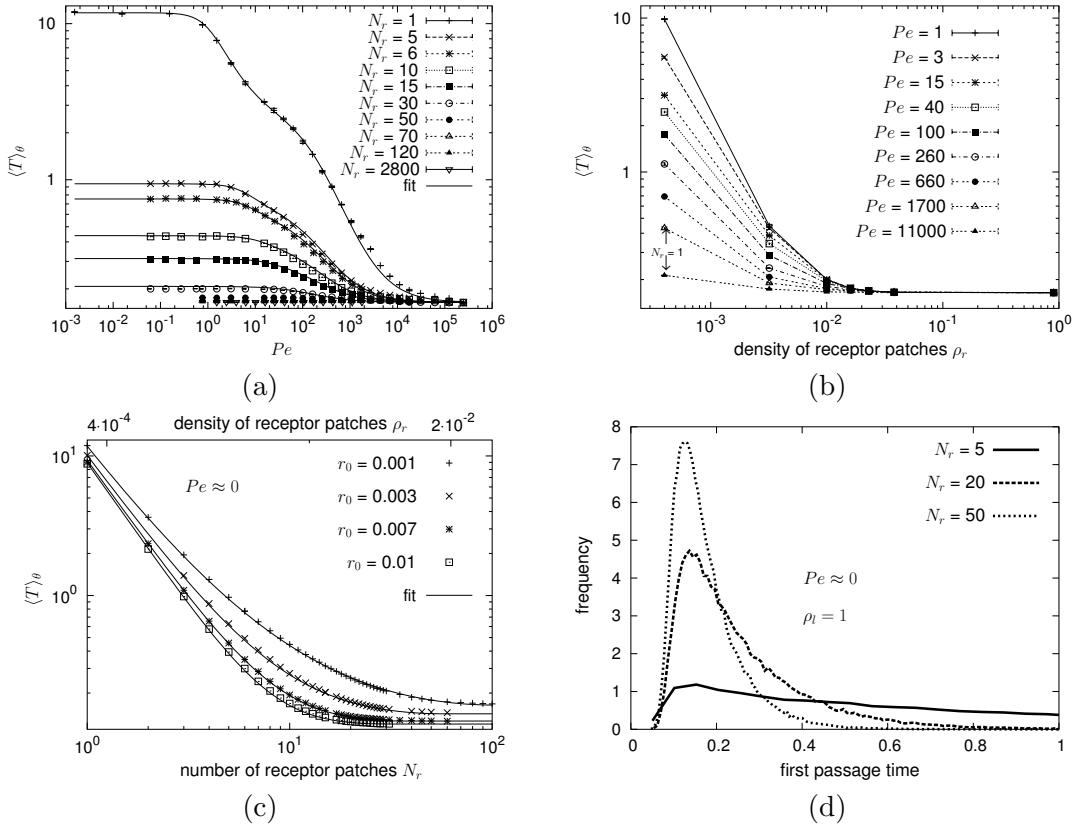

Figure 3.4: The MFPT averaged over the initial orientation $\langle T \rangle_\theta$ (log-log plots). (a) Plotted as a function of the Péclet number Pe for different numbers of receptor patches N_r. (b) $\langle T \rangle_\theta$ is plotted as a function of the receptor density $\rho_r \propto N_r$ for different values of Pe. (c) $\langle T \rangle_\theta$ as a function of N_r in the diffusive regime ($Pe \approx 0$) for different values of the capture height r_0, but fixed value of the patch radius $r_p = 0.001$. (d) The distribution of θ-averaged first passage time is shown for $N_r = 5, 20, 50$ receptor patches. (Numerical parameters for each data point: $N = 10^5, \Delta t = 10^{-5}$.) In (a,c) also fits to the numerical results are shown. In Sec. 3.5.1 it is explained how these fits are obtained.

We next try to qualitatively understand the effect of shear rate for the simulation results shown in Fig. 3.4a. In general, it is very hard to separate the effects of diffusion and convection. The time for binding at $Pe \approx 0$ is determined purely by diffusion and will be denoted by T_D. As shear flow increases, the rotation of the sphere is increasingly dominated by convection. We now derive a convection time T_F which competes with the diffusion time T_D at large Péclet numbers. For very large Péclet number, we expect the MFPT to be the sum of the homogeneous result from Eq. (3.5) plus this additional time T_F. An important question then is, at which Pe the convection time T_F becomes smaller than the diffusion time T_D.

In order to estimate T_F, we note that the main effect of increased shear rate is faster rotation in the direction of flow. Once a receptor has rotated such that it opposes a ligand on the substrate, there is some probability p that the sphere is at the correct height that an encounter can occur. If no encounter occurs with the complementary probability $1-p$, the sphere has to rotate about another angle $\theta_s = 2\pi/N_r$ until the next receptor points downwards. Supposing the time, $2t_0$, to rotate about the angle θ_s is large enough that

there is no correlation between the height of the sphere before and after the rotation, then an encounter occurs again with probability p (therefore, this analysis also does not hold at very large Pe). Thus, the mean time T_F for encounter is

$$\begin{aligned} T_F &= pt_0 + (1-p)(p3t_0 + (1-p)(p5t_0 + (1-p)(\ldots))) \\ &= pt_0 \sum_{i=0}^{\infty} (2i+1)(1-p)^i = t_0 \frac{2-p}{p} \approx \frac{2t_0}{p} \ , \end{aligned} \tag{3.12}$$

where the series has been summed up by means of the geometric formula. In the last term we assumed that the probability p for the proper height is small due to a small capture distance r_0. It follows from the stationary probability distribution $\Psi_s(z)$ given by Eq. (2.30):

$$p = \int_1^{1+r_0} dz \Psi_s(z) = 1 - e^{-Pe_z r_0} \approx Pe_z r_0 \ . \tag{3.13}$$

The time t_0 to rotate about half of the angle θ_s is approximately $t_0 = \theta_s / Pe$. Therefore, we get

$$T_F \approx \frac{4\pi}{N_r Pe Pe_z r_0} \ . \tag{3.14}$$

In this analysis, the convection time T_F scales inversely with the number of receptor patches N_r and the Péclet number Pe. As Pe increases, T_F gets smaller than T_D and then dominates the overall outcome. Comparing Eq. (3.14) to the simulation data for $Pe \approx 0$ shows that this crossover occurs in the range $Pe \approx 10^1 - 10^2$ and that the corresponding value of Pe increases with increasing receptor number N_r, exactly as observed in the simulation data over the full range of Pe. However, the exact scaling of this data is not $\sim 1/N_r$ for large Pe as predicted by Eq. (3.14). In practice, the decay is somehow slower due to correlations between the height of the sphere at two successive instances of a receptor pointing downwards, which we have neglected in our analysis.

Dependence on Pe_z and limit of large Pe_z

We now turn to the effect of the downward driving force, that is Pe_z. Above we have found that in two cases, homogeneous coverage from Eq. (3.3) and convection-dominated rotation from Eq. (3.14), the MFPT scales inversely with Pe_z. In Fig. 3.5 $\langle T \rangle_\theta$ is plotted as a function of Pe_z for $N_r = 10$ and $Pe \approx 0$. Again, we find the inverse scaling for small Pe_z. However, for very large values of Pe_z the mean first passage time approximates a constant value. The reason is that the larger Pe_z, the smaller the mean time to fall below the height $z = 1 + r_0$. As indicated by Eq. (2.30), then the sphere stays below this height until an encounter occurs. This implies that in this limit, the MFPT depends only on rotational motion and the falling motion is irrelevant. We therefore can identify it with the MFPT for θ to reach one of the boundaries of the interval $[\mathcal{L} := \theta_0, \mathcal{R} := \theta_s - \theta_0]$ (cf. Fig. 3.3). The length of this interval is denoted by $\Delta\theta := \mathcal{R} - \mathcal{L} = \theta_s - 2\theta_0$. For the following derivation of this time we assume that the rotation occurs with constant drift A_θ and constant diffusion D_θ though both quantities depend on z, as does θ_0. But average

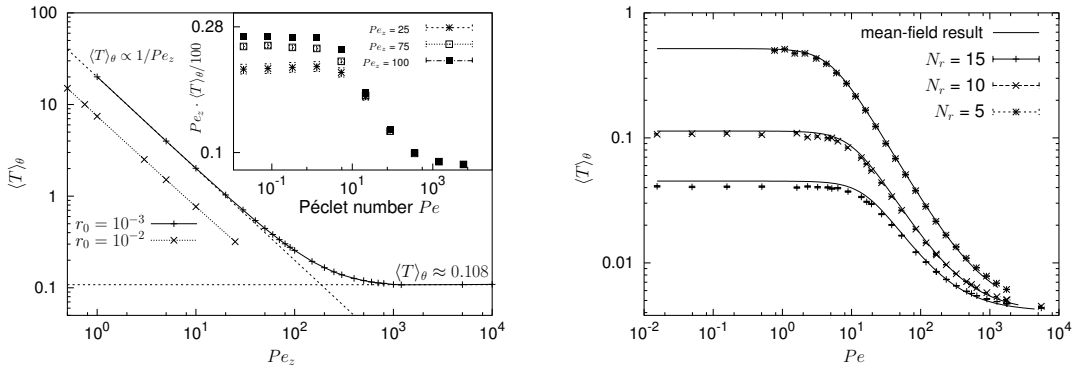

(a) (b)

Figure 3.5: (a) MFPT $\langle T\rangle_\theta$ is shown as a function of vertical drift Pe_z with $Pe \approx 0, N_r = 10$ for the two capture heights $r_0 = 0.001, 0.01$. For small Pe_z, $\langle T\rangle_\theta$ scales as $1/Pe_z$, for large Pe_z a constant value is reached (only shown for $r_0 = 0.001$). In the inset $\frac{Pe_z}{100}\langle T(N_r = 10)\rangle_\theta$ is plotted as function of the Péclet number Pe for $Pe_z = 25, 75, 100$ (numerical parameters: $\Delta t = 10^{-5}, N = 10^5$, inset: $\Delta t = 10^{-4}, N = 10^4$). (b) MFPT $\langle T\rangle_\theta$ as a function of Pe for three different numbers of receptor patches N_r. Comparison between simulation results (dots) and the estimate Eq. (3.18) at $Pe_z = 2000$ (numerical parameters: $N = 10^4, \Delta t = 10^{-7}$).

quantities can be obtained by using the stationary solution:

$$\bar{A}_\theta = \int_1^\infty \Psi_s(z) A_\theta(z) dz, \quad \bar{D}_\theta = \int_1^\infty \Psi_s(z) D_\theta(z) dz, \quad \bar{\theta}_0 = \frac{\int_1^{1+r_0} \Psi_s(z)\theta_0(z) dz}{1 - e^{-Pe_z r_0}} \tag{3.15}$$

(at later usage of these averages we will omit the bar). Although $\theta_0 = 2r_p$ for $z > 1 - r_0$, there is no proper meaning for θ_0 for these heights. Therefore, we use the conditional probability that the sphere is below $1 + r_0$ for the average of θ_0 (for Pe_z large, the denominator becomes approximately one). Drift and diffusion as a function of z follow from the definitions made in Appendix B.1 as $A_\theta(z) = Pe/2(1 - \hat{\beta}^{dr}(1/z))$ and $D_\theta(z) = 3/4\hat{\beta}^{rr}(1/z)$. Far away from the wall, they approach $A_\theta = Pe/2$ and $D_\theta = 3/4$ (the latter value results because time is scaled with the translational rather than rotational diffusion constant). If there are only few small receptor patches, then $\Delta\theta \approx \theta_s = 2\pi/N_r$. The probability $\pi_{\mathcal{R}/\mathcal{L}}$ to reach the left or the right boundary is then the solution to [157]

$$A_\theta \partial_\theta \pi_{\mathcal{R}/\mathcal{L}} + D_\theta \partial_\theta^2 \pi_{\mathcal{R}/\mathcal{L}} = 0, \;\; \pi_{\mathcal{R}}(\mathcal{R}) = 1, \; \pi_{\mathcal{R}}(\mathcal{L}) = 0, \; \pi_{\mathcal{L}}(\mathcal{R}) = 0, \; \pi_{\mathcal{L}}(\mathcal{L}) = 1. \tag{3.16}$$

The mean first passage time $T_{\mathcal{R}/\mathcal{L}}(\theta)$ to reach the left/right boundary can then be obtained from the differential equation for the product quantity $\vartheta_{\mathcal{R}/\mathcal{L}} := \pi_{\mathcal{R}/\mathcal{L}} T_{\mathcal{R}/\mathcal{L}}$ which reads

$$A_\theta \partial_\theta \vartheta_{\mathcal{R}/\mathcal{L}} + D_\theta \partial_\theta^2 \vartheta_{\mathcal{R}/\mathcal{L}} = -\pi_{\mathcal{R}/\mathcal{L}}, \qquad \vartheta_{\mathcal{R}/\mathcal{L}}(\mathcal{R}) = 0, \qquad \vartheta_{\mathcal{R}/\mathcal{L}}(\mathcal{L}) = 0. \tag{3.17}$$

Regarding the initial condition, we have to take an average over all possible angles between 0 and θ_s, including the intervals $[0, \mathcal{L}]$ and $[\mathcal{R}, \theta_s]$ in which binding is immediate. We then find:

$$\langle T\rangle_\theta = \frac{1}{\theta_s} \int_0^{\theta_s} \mathrm{d}\theta (\vartheta_{\mathcal{R}} + \vartheta_{\mathcal{L}}) = \frac{A_\theta \Delta\theta^2 \coth(\frac{A_\theta \Delta\theta}{2D_\theta}) - 2D_\theta \Delta\theta}{2A_\theta^2 \theta_s}. \tag{3.18}$$

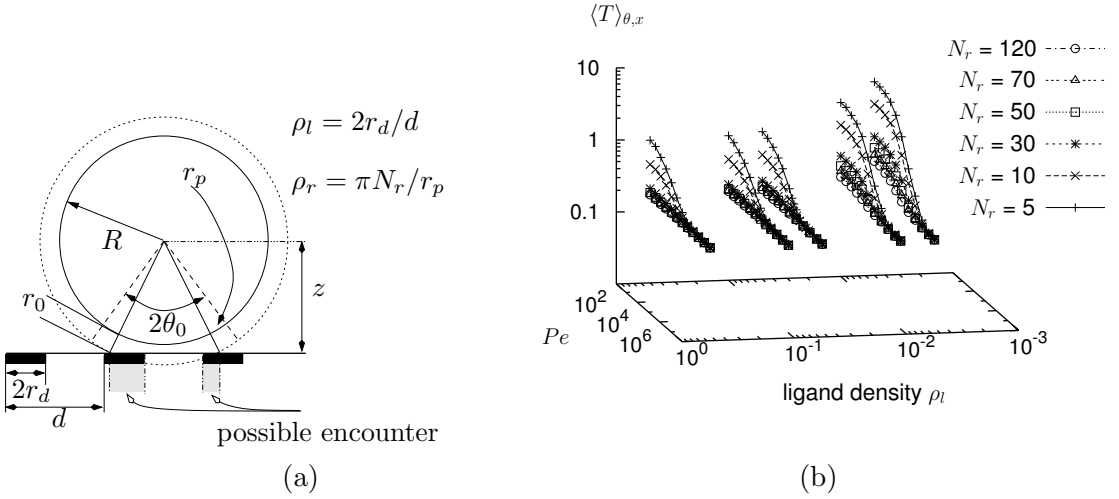

Figure 3.6: (a) Illustration of the situation with a density of receptor patches ρ_r as well as a density of ligands ρ_l. The first passage time is now determined by an overlap of a receptor patch with a ligand patch. (b) $\langle T\rangle_{\theta,x}$ as a function of the Péclet number Pe and the ligand density ρ_l for different numbers of receptor patches N_r (numerical parameters: $\Delta t = 5 \cdot 10^{-6}, N = 10^4$).

In the general case, one can numerically obtain average values for the drift and diffusion constants as defined in Eq. (3.15) and use them in Eq. (3.18). For $Pe_z = 2000$ and $N_r = 10$, this gives $\langle T\rangle_\theta = 0.11$, which fits quite well to the value $\langle T\rangle_\theta = 0.108$ obtained from Fig. 3.5a. In the limit of large Pe_z also the quantitative agreement regarding the dependence on Pe between Eq. (3.18) and our simulation results is rather good, as illustrated in Fig. 3.5b. There, the simulation results for $Pe_z = 2000$ are compared with the results obtained from the sum of the falling time Eq. (3.3) and the rotational MFPT time Eq. (3.18) using the average values defined in Eq. (3.15). Only the diffusive limit for the MFPT is somewhat overestimated by Eq. (3.18) compared to the simulation results. The latter observation reveals the fact that the determination of the average values in Eq. (3.15) by use of the stationary height distribution obviously becomes the less appropriate the smaller the MFPT is (for small times the sphere, or better the ensemble of spheres over which the first passage times are averaged, is not in equilibrium).

For completeness, we also mention that the extreme case $Pe_z \to \infty$ is somehow pathological because in this case, the sphere is always found attached to the wall, and therefore it is no longer able to rotate due to the no-slip boundary condition. Therefore, for values of Pe_z much larger than in Fig. 3.5 $\langle T\rangle_\theta$ is again increasing. In practice, there will always be some repulsive (colloidal) interaction which keeps the sphere from making perfect contact with the wall.

3.3.2 Dependence on ligand density

We now introduce spatially resolved ligands into the 2D-model. Fig. 3.6a shows the model definition: the ligand patches are considered to have the same radius $r_d = r_p$ as the receptor patches and they are located at a distance d from each other. This results in a one-dimensional ligand density given by $\rho_l = 2r_d/d$. The mean first passage time will now also depend on the initial x-position, $T = T(z_0, \theta, x|C)$, where C is the hypersurface in (z, θ, x) space where a receptor patch touches a ligand patch. But similarly as in the above

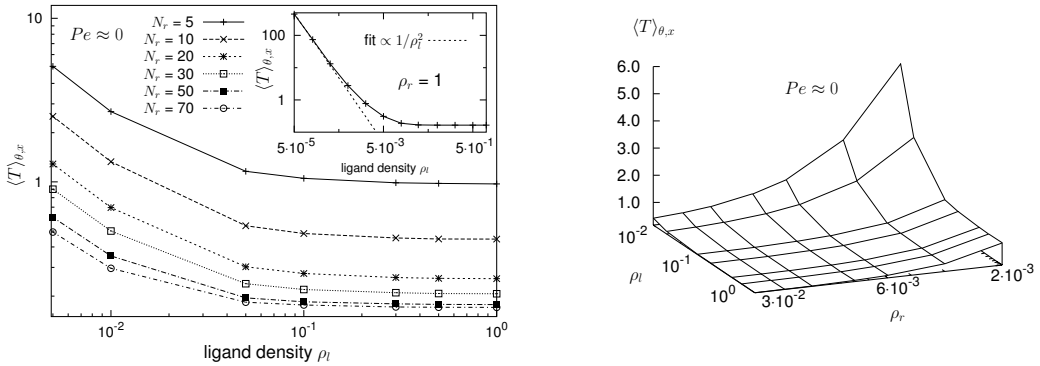

Figure 3.7: (a) The MFPT $\langle T\rangle_{\theta,x}$ is shown in the diffusion limit (i. e., at $Pe \approx 0$) as a function the ligand density ρ_l for different numbers of receptor patches N_r. Inset (plot for $\rho_r \approx 1$): The mean first passage time scales as $\langle T\rangle_{\theta,x} \propto 1/\rho_l^2$ (numerical parameters: $\Delta t = 10^{-5}, N = 10^5$). (b) Dependence of $\langle T\rangle_{\theta,x}$ in the diffusive limit ($Pe \approx 0$) on ρ_r, ρ_l, where the receptor density ρ_r has been varied by changing N_r at fixed r_p (numerical parameters: $\Delta t = 10^{-5}, N = 10^5$).

section in regard to initial orientation, the dependence on the initial x-position is of minor interest, and therefore we will discuss the MFPT averaged over the initial position and orientation, denoted by $\langle T\rangle_{\theta,x}$. Fig. 3.6b shows that by varying the Péclet number we can identify the same three regimes for all ligand-densities as before. For $Pe \to 0$ in the limit of pure diffusive transport, $\langle T\rangle_{\theta,x}$ approaches a finite value, depending on ρ_r and ρ_l. With increasing Pe, $\langle T\rangle_{\theta,x}$ decreases monotonically and finally, for $Pe \to \infty$, reaches the value of the MFPT in the limit of homogeneous receptor and ligand coverage. In contrast to the above case, however, in this limit the shear flow not only restores rotational invariance of the sphere, but in addition also translational invariance of the substrate.

Fig. 3.7a provides more details for $\langle T\rangle_{\theta,x}$ as a function of ρ_l in the diffusive limit ($Pe \approx 0$). We find that in the range $0.1 < \rho_l < 1$ the MFPT is almost not affected by ligand concentration: as long as the ligand patches are sufficiently close to each other, a receptor patch touching the wall will most probably find a ligand before diffusing away again. The situation changes completely with small ligand density. For $\rho_l \ll 1$ the averaged mean first passage time $\langle T\rangle_{\theta,x}$ scales with the ligand density ρ_l as $\langle T\rangle_{\theta,x} \propto 1/\rho_l^2 \propto d^2$. This can be understood by calculating the position-averaged MFPT $\langle T\rangle_x$ for a particle diffusing in an interval $[0, d]$ with diffusion constant D, which gives $\langle T\rangle_x = d^2/12D$. This suggests that the quadratic scaling with d results from the diffusive motion between adjacent ligand patches. Fig. 3.7b summarizes our results for the dependence of the 2D MFPT $\langle T\rangle_{\theta,x}$ on ligand density ρ_l and receptor density ρ_r in the diffusive limit. It can be clearly seen that there exists a large plateau around the value for the case of homogeneous coverage $\rho_r = \rho_l = 1$. This implies that if ligand and receptor patches are not too strongly diluted, the mean encounter time is still close to the optimum value given by Eq. (3.3). On the other hand if the number of receptor and/or ligand patches is highly reduced the mean encounter time is strongly increased.

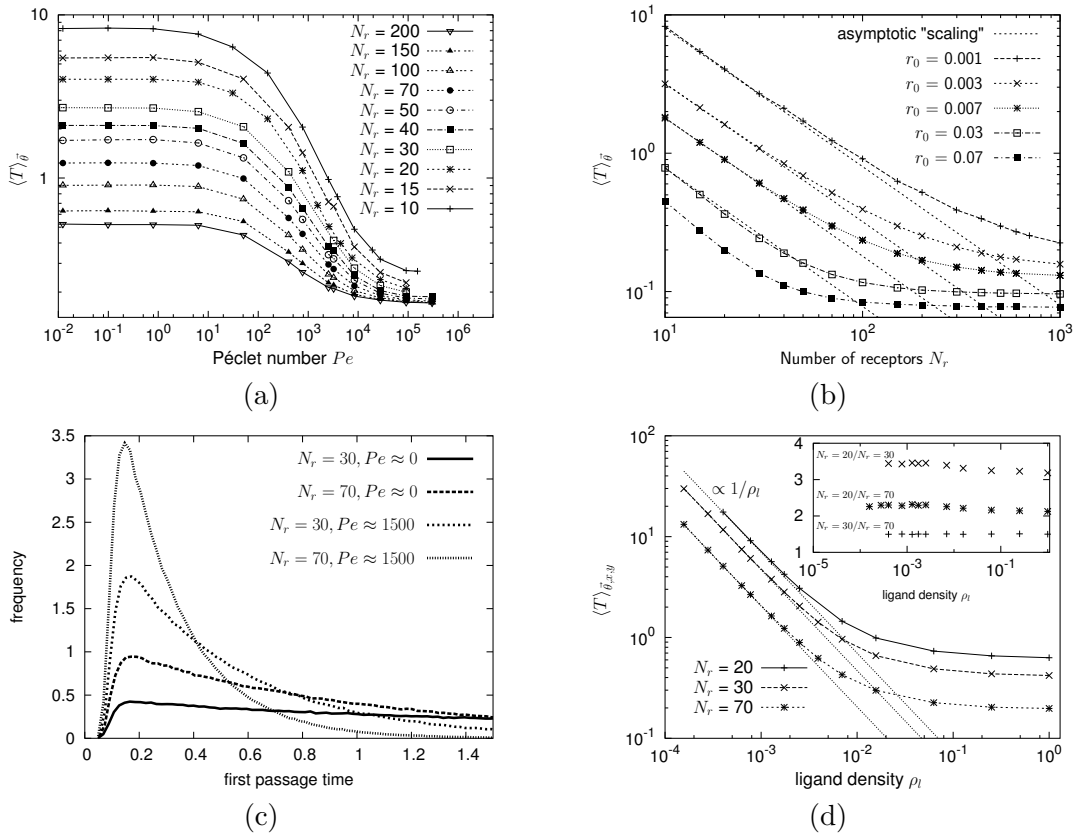

Figure 3.8: (a) The MFPT $\langle T \rangle_{\vec{\theta}}$ was calculated as a function of the Péclet number Pe in the limit of homogeneous ligand coverage for different values of the number of receptor patches N_r. (b) The dependence of the MFPT on N_r for different values of the capture height r_0. Lines show the scaling with $1/N_r$. (c) First passage time distribution for $N_r = 30, 70$ and $Pe \approx 0, 1500$ ($N = 7 \cdot 10^5$). (d) Dependence of $\langle T \rangle_{\vec{\theta},x,y}$ on the 2D ligand density ρ_l in the diffusive limit $Pe \approx 0$. For $\rho_l \ll 1$ the mean first passage time is proportional to $1/\rho_l$ (dotted lines). In the inset the mutual ratios of the averaged MFPTs are plotted for $N_r = 20, 30, 70$, showing that the dependence on the ligand density is nearly independent on N_r (numerical parameters for (a,b,d): $\Delta t = 5 \cdot 10^{-5}, N = 10^5, r_p = 10^{-3}$, $r_0 = 10^{-3}$ for (a,c); $r_0 = r_d = 10^{-2}$ for (d)).

3.4 Movement in three dimensions

We finally turn to the full 3D-situation, that is the sphere may diffuse about all three axes as described by Eq. (2.26) and Eq. (B.24). Receptors are located in spherical patches which are randomly distributed over the sphere. Each receptor patch has a radius r_p and a height (capture length) r_0. That is the appropriate generalization of the situation shown in Fig. 3.3 for the 2D-case. Thus, for N_r receptor patches the receptor density is $\rho_r = 2\pi N_r(1 - \cos(r_p))/4\pi \approx N_r r_p^2/4$ (for $r_p \ll 1$). In contrast to the preceeding sections where the receptor patches could be regularly distributed over the circumference, this is no longer possible on the surface of a sphere. Therefore, we distribute the patches randomly over the sphere with equal probability for each position, with a hard disk overlap algorithm making sure that no two patches overlap [66]. One has to bear in mind that then for small N_r two different distributions may have slightly different binding properties. This effect becomes weaker for larger N_r. Therefore, in the following we will only use $N_r \geq 10$. The

quantity we measure in our simulations is now $\langle T \rangle_{\vec{\theta}}$ in the case of homogeneous ligand coverage and $\langle T \rangle_{\vec{\theta},(x,y)}$ in the case that the ligands are located in spherical patches on a 2D-lattice. Thus, we average the MFPT over the initial orientations and positions as explained above.

In order to explore the dependence of $\langle T \rangle_{\vec{\theta}}$ on N_r and Pe the receptor-ligand encounter in the case of homogeneous ligand coverage $\rho_l = 1$ was simulated. The average over the initial positions was obtained by starting each run with a randomly chosen initial orientation. After 100 runs a new receptor distribution was generated, thus averaging out the effect of different receptor distributions, too. Typically 100,000 runs were used, in order to achieve reasonable statistics. The results are shown in Fig. 3.8a. Again, we find three different regimes as a function of the Péclet number Pe. This proves that qualitatively the basic results of the 2D-treatment remain valid in 3D. However, in detail there are important differences. In contrast to the 2D results presented above, $\langle T \rangle_{\vec{\theta}}$ in the limit $Pe \to \infty$ is diffusion-limited and no longer given by Eq. (3.3) if N_r is small. That is due to the fact that for $Pe \to \infty$ the receptor patches effectively behave as ring-like structures. The rotation of such a ring about the x- or y-axis is not affected by Pe and thus still depends on diffusion. For large N_r the rings cover the whole sphere and for $Pe \to \infty$ $\langle T \rangle_{\vec{\theta}}$ is again given by Eq. (3.3). In order to obtain proper results also for the case of large Péclet numbers the algorithm must be designed with special care. With increasing Pe also the mean rotation about the y-axis at each numerical time step increases. Thus, at large enough Pe it happens that the sphere rotates by more than θ_0 during time step Δt and therefore an encounter may be missed by the algorithm. This failure can of course be avoided by using a numerical time step that decreases with increasing Pe, i. e., $\Delta t \propto 1/Pe$ for $Pe > 1$. As argued before diffusive motion is still important in the high Pe limit and therefore the MFPT in this limit has to be determined using a large number of trajectories as for $Pe \approx 0$. Based on these requirements it turns out that the computation time explodes using a decreasing time step (we found that this procedure took a month and more per data point when checked on a 2 GHz processor). Thus, this solution is not applicable to explore the full range of Péclet numbers. To circumvent this dilemma we keep the time step constant but check for encounter also along the receptors' trajectories (for receptors located on the lower half of the sphere), that are obtained by interpolation between the receptor positions at two successive time steps. Thus, accounting for both the deterministic nature of rotations about the y-axis and the purely diffusive motion about the other two axis.

In Fig. 3.8b we plot the $Pe \to 0$ limit of $\langle T \rangle_{\vec{\theta}}$ as a function of the number of receptor patches N_r, for different values of the capture radius r_0. The fitted straight line for $r_0 = 10^{-3}$ shows that $\langle T \rangle_{\vec{\theta}}$ approximately behaves like $\langle T \rangle_{\vec{\theta}} \propto 1/N_r$. Neglecting effects of curvature, the average distance between two receptors patches is $d \propto (4\pi/N_r)^{1/2}$ and the mean time to diffuse that distance is $t_d \propto d^2 \propto 1/N_r$. This provides a simple explanation for the observed scaling behavior. For high N_r, the MFPT reaches a plateau value, given by Eq. (3.3). This plateau value depends on r_0 and is the smaller the larger r_0. Also the crossover from the asymptotic behavior at small N_r to the plateau at large N_r is shifted with increasing capture height r_0 towards smaller N_r.

In Fig. 3.8c the effect of Péclet number and number of receptors on the distributions of first passage times is shown for four combinations of Pe and N_r. As already observed before, the FPT-distribution is the broader the larger the MFPT is. For the standard deviations σ_T of the FPT distributions corresponding to the MFPT shown in this section the following qualitative statement can be made: If the MFPT is large compared to the limiting value for homogeneous coverage (e. g., for $Pe \approx 0$, N_r small) the standard

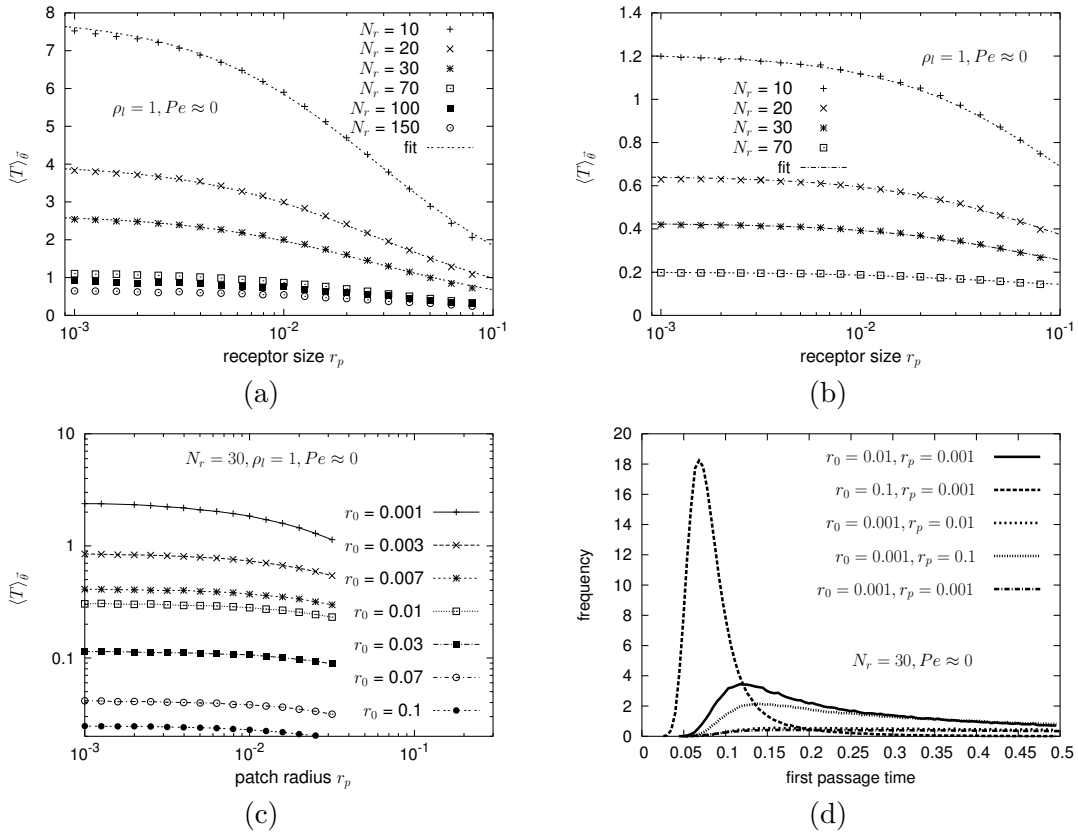

Figure 3.9: (a, b) Dependence of the MFPT $\langle T \rangle_{\vec{\theta}}$ on the receptor patch radius r_p ($Pe \approx 0$). The dotted lines are fits of $a/(b+r_p)$ to the simulation results. (a) Capture height $r_0 = 0.001$, (b) $r_0 = 0.01$ (numerical parameters: $N = 1-3 \cdot 10^5, \Delta t = 5 \cdot 10^{-5}$). (c) For $N_r = 30$ receptor patches the dependence on r_p is shown for different values of r_0. For better comparison the r_0-dependent part of the MFPT as given by Eq. (3.3) was subtracted. (d) Some first passage time distributions for the diffusive limit, $Pe \approx 0$ and $N_r = 30$, showing the effect of the receptor patch parameters r_0, r_p ($\Delta t = 5 \cdot 10^{-5}, N = 7 \cdot 10^5$).

deviation of the FPT distribution is within a few percent given by the MFPT itself. If on the other hand the MFPT T is close to the limit of homogeneous coverage T is larger (by 50 % or more) than the respective standard deviation σ_T.

In Fig. 3.8d we show the effect of finite ligand density ρ_l at $Pe \approx 0$. For the simulations we distributed the ligands in circular patches of radius $r_d = 0.01$ on a quadratic lattice with lattice constant d, thus resulting in a ligand density $\rho_l = \pi r_d^2/d^2$. In our implementation, the intersection between the receptor patch and the wall is approximated by an appropriate circle, because it is easy to check if this circle overlaps with the ligand patch. The fits given in Fig. 3.8d show that for small ρ_l, the MFPT scales as $\langle T \rangle_{\vec{\theta},(x,y)} \propto 1/\rho_l \propto d^2$. Because the curves for different N_r appear to be rather similar, in the inset we plot the ratio of different pairs of these curves. As this results in approximately constant plateaus, we conclude that the scaling with ligand density is hardly effected by N_r. As in 2D, the inverse scaling with ligand density can be understood in simple terms by noting that the MFPT to diffusional capture scales like d^2. At a coverage around 0.01, saturation occurs as it did for receptor coverage.

We finally discuss the influence of the receptor geometry described by the parameters

r_0 and r_p. Because Pe changes the MFPT in a monotonous way, it is sufficient to study the diffusive limit $Pe \approx 0$. Fig. 3.9a and b show $\langle T \rangle_{\vec{\theta}}$ as a function of r_p for $r_0 = 0.001$ and $r_0 = 0.01$, respectively. In order to obtain smooth curves, in this case only one receptor distribution was used for all runs. We find that the curves can be fitted well to the function

$$\langle T(r_p) \rangle_{\vec{\theta}} = \frac{a}{b + r_p} + T(z_0 = 2 | z_1 = 1 + r_0), \tag{3.19}$$

where the second term is the homogeneous result from Eq. (3.3). This means that even for vanishing receptor size $r_p \to 0$ the MFPT remains finite. This makes sense because above we have shown that the effective patch size is determined both by r_p and r_0. In detail, Fig. 3.3 showed that capture occurs over the solid angle $2\theta_0$ with $\theta_0(z) = \arccos(z/(1 + r_0)) + r_p$. For small r_0 and r_p, this allows us to define an effective patch size

$$r_p^{eff} = \arccos(\langle z \rangle / (1 + r_0)) + r_p \approx \arccos(1 - \frac{1}{2} r_0) + r_p \approx \sqrt{r_0} + r_p, \tag{3.20}$$

where we have used $\langle z \rangle = 1 + r_0/2$. Suppose now that the sphere diffuses over the time t_d until a receptor patch points downwards, then it may encounter a ligand with a probability p that is given by the normalized area of one effective receptor patch:

$$p = \frac{1}{2}(1 - \cos(r_p^{eff})) \approx \frac{1}{4}(\sqrt{r_0} + r_p)^2 \approx \frac{1}{2}\sqrt{r_0}(\frac{1}{2}\sqrt{r_0} + r_p). \tag{3.21}$$

If no encounter occurs, the sphere has to diffuse again over a time t_d until the next encounter can occur. This leads to the mean encounter time $T = t_d/p$. Putting everything together gives Eq. (3.19) with $a = 2t_d/(\sqrt{r_0})$ and $b = \frac{1}{2}\sqrt{r_0}$. If checked against our simulation results, we indeed find that the fit parameter b is an increasing function of r_0, but varies only slightly with N_r (cf. Tab. 3.1). The fit parameter a scales approximately

r_0	$N_r = 10$	$N_r = 20$	$N_r = 30$
0.001	$a = 0.216, b = 0.028$	$a = 0.105, b = 0.0274$	$a = 0.065, b = 0.026$
0.01	$a = 0.12, b = 0.11$	$a = 0.05, b = 0.095$	$a = 0.025, b = 0.081$

Table 3.1: Results for the fit parameters a, b from Eq. (3.19), for different values of capture height r_0 and number of receptor patches N_r. For the fit the gnuplot fit-routine was used.

as $\sim 1/N_r$ and varies with r_0, also consistent with the above analysis. In Fig. 3.9c $\langle T \rangle_{\vec{\theta}}$ is plotted as a function of r_p for several values of r_0 and $N_r = 30$. One clearly sees that increasing r_p has a much smaller impact on $\langle T \rangle_{\vec{\theta}}$ than a comparable increase in r_0, which is qualitatively well described by the preceeding analysis. The FPT distributions shown in Fig. 3.9d for $N_r = 30, Pe \approx 0$ further illustrates the strong impact of the capture height r_0 (for the sake of comparison the FPT distribution for $N_r = 30, Pe \approx 0, r_0 = 0.001, r_p = 0.001$ which is shown in Fig. 3.8c is also shown in Fig. 3.9d). In the scale of Fig. 3.9d the difference between the $r_p = 0.001$ and $r_p = 0.01$ curves (both for $r_0 = 0.001$) is hard to identify. In contrast, the $r_p = 0.001$ curve with capture height $r_0 = 0.1$ exhibits a fairly sharp maximum at small first passage times.

In Fig. 3.9a and b the receptor density is varied over almost four orders of magnitude by changing r_p, but the largest measured decrease for $\langle T \rangle_{\vec{\theta}}$ is only by a factor four. In contrast, an increase of the receptor density by one order of magnitude due to ten-fold

more receptor patches leads to a decrease of $\langle T \rangle_{\vec{\theta}}$ by almost also one order of magnitude. However, this is only true as long as N_r is not too large, as for large N_r $\langle T \rangle_{\vec{\theta}}$ saturates at the limiting value of homogeneous receptor coverage (cf. Fig. 3.8b). The crossover from the $1/N_r$ behavior to the saturation should take place when the average distance between two receptor patches $d' \sim (4\pi/N_r)^{1/2}$ becomes comparable to the size of one receptor patch. This corresponds to $r_p^{eff} \sim (4\pi/N_r)^{1/2}$ or $N_r \sim 4\pi/(\sqrt{r_0} + r_p)$. This estimate predicts that the crossover takes place between several tens to several hundreds of receptor-patches, depending on r_0, in agreement with the data shown in Fig. 3.8b.

3.5 Mean-field analysis for the MFPT

In this section we consider reaction-diffusion equations to obtain quantitative estimates for the MFPT. From these we are able to derive the proper scaling for different limiting regimes of the Péclet numbers and the number of receptor patches.

3.5.1 MFPT for homogeneous ligand coverage in 2D

In Sec. 3.2 we have shown that the angle averaged MFPT can be decomposed into periods of falling and rotation. As motion in z-direction is not coupled to changes in the other degrees of freedom the falling time could be solved exactly providing Eq. (3.3). In contrast, the exact determination of the rotational MFPT is much more complicated as two degrees of freedom are involved (translational motion in z and rotations in θ) and the drift and diffusion coefficients depend via z on the configuration. As shown in Sec. 3.3, the latter problem can be solved in a mean-field like approach by using drift and diffusion coefficients that are obtained from the stationary averages of the corresponding quantities (cf. Eq. (3.15)). If then Pe_z is large enough so that the probability of the sphere to be above capture height $z > 1 + r_0$ is negligible, movements in z-direction become unimportant and the calculation of rotational MFPT becomes effectively an one-dimensional problem with solution given in Eq. (3.18). Indeed, as shown in Fig. 3.5b the sum of falling time Eq. (3.3) and time for rotation is in good quantitative agreement with simulation results. For arbitrary Pe_z this sum does not quantitatively predict the correct MFPT as illustrated by Fig. 3.10a. In the following we show, that much better results can be obtained, taking the point of view that the sphere rotates by diffusion and convection and whenever a receptor patch points downwards absorption (i. e., an encounter) occurs only with a certain rate k. Including the stationary probability distribution Eq. (2.30) to derive an expression for the rate k accounts then for the translational motion in z-direction. Mathematically, the MFPT of such a system is obtained form a reaction-diffusion-(convection) equation (which got its name as it is commonly used to model chemical reactions between diffusing reactants [119]).

Reaction diffusion equation

For the diffusive limit (i. e., $A_\theta = 0$) the equation for the MFPT with reactive term on the interval $]-\theta_s/2, \theta_s/2]$[1] reads

$$D_\theta \partial_\theta^2 T(\theta) - \bar{k}(\theta) T(\theta) = -1, \qquad \bar{k}(\theta) = \begin{cases} \bar{k}, & |\theta| < \theta_0 \\ 0, & \text{else} \end{cases} . \tag{3.22}$$

[1] For the solution of Eq. (3.18) we considered the interval $]0, \theta_s]$ which is equivalent to the interval used here due to the periodicity in θ.

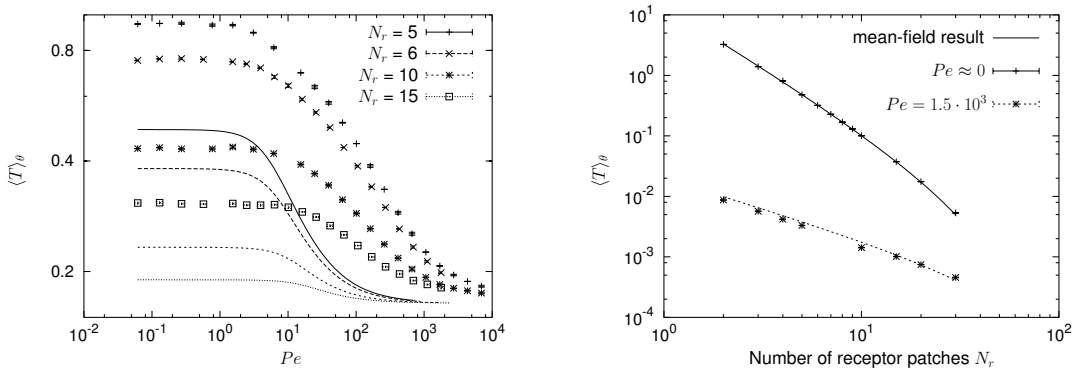

(a) (b)

Figure 3.10: (a) MFPT $\langle T \rangle_\theta$ as a function of Péclet number Pe for different values of the number of receptor patches N_r. Comparison between the sum of the estimates from Eq. (3.3) and Eq. (3.18) (lines) with the full simulation results (dots). Péclet number in z-direction $Pe_z = 50$. (b) At $Pe_z = 1000$ simulation results for $\langle T \rangle_\theta$ as a function of receptor patches N_r minus the falling time $T(z_0 = 2|z_1 = 1.001)$ (cf. Eq. (3.3)) for both $Pe \approx 0$ and $Pe = 1.5 \cdot 10^3$ are shown (dots). The lines are fits to these data according to Eq. (3.28) for $Pe \approx 0$ and Eq. (3.29) for $Pe = 1.5 \cdot 10^3$, respectively (numerical parameters: $N = 10^5$, and $\Delta t = 10^{-6}$ for $Pe \approx 0$ and $\Delta t = 10^{-7}$ for $Pe \approx 1.5 \cdot 10^3$).

Here, we set the rate $\bar{k}$ to a finite but constant value within the interval $]-\theta_0, \theta_0[$, i. e., when the receptor patch is pointing downwards, and zero outside. The rate $\bar{k}$ is measured in units of inverse time. Eq. (3.22) can be solved piecewise with $T^{(1)}(\theta)$ on $]-\theta_s/2, -\theta_0]$, $T^{(2)}(\theta)$ on $]-\theta_0, \theta_0[$ and $T^{(3)}(\theta) = T^{(1)}(\theta - \theta_s)$ on $[\theta_0, \theta_s/2]$, leading to

$$T^{(3)}(\theta) = -\frac{\theta^2}{2D_\theta} + a_1\theta + a_2, \quad T^{(2)}(\theta) = \frac{1}{\bar{k}} + a_3 e^{\sqrt{\frac{\bar{k}}{D_\theta}}\theta} + a_4 e^{-\sqrt{\frac{\bar{k}}{D_\theta}}\theta},$$

where the four constants a_1, a_2, a_3, a_4 are obtained by demanding that T has a continuous derivative at $\theta = \pm\theta_0$. The MFPT averaged over all initial orientations is then

$$\langle T \rangle_\theta = \frac{1}{\theta_s} \int_{-\theta_s/2}^{\theta_s/2} d\theta T(\theta) = \frac{\bar{k}(\theta_s - 2\theta_0)^3 + 24D_\theta(\theta_s - \theta_0) + 6\sqrt{D_\theta \bar{k}}(\theta_s - 2\theta_0)^2 \coth(\sqrt{\frac{\bar{k}}{D_\theta}}\theta_0)}{12D_\theta \bar{k}\theta_s}.$$

Using a rate $\bar{k}$ to account for the probability of the sphere to be in binding range $z < 1 + r_0$, implies that the height of the sphere at two consecutive times is independent of each other. As the sphere moves on a continuous path this cannot be true. Therefore, this model only makes sense in the limit of a small reactive interval, (i. e., $\theta_0 \ll \theta_s$) when the period of time of a receptor pointing downwards is small. Thus, defining a new rate $k = 2\theta_0\bar{k}$ and taking the limit $\bar{k} \to \infty, \theta_0 \to 0$ while keeping k constant, we obtain for the MFPT $\langle T \rangle_\theta$

$$\langle T \rangle_\theta = \frac{\theta_s^2}{12D_\theta} + \frac{\theta_s}{k}. \tag{3.23}$$

The newly defined rate k is measured in units of angle per time.

The result given in Eq. (3.23) can also be obtained from

$$D_\theta \partial_\theta^2 T(\theta) - k\delta(\theta)T(\theta) = -1, \tag{3.24}$$

i. e., taking the limit $\bar{k} \to \infty, \theta_0 \to 0$ already in the setup of Eq. (3.22). Using the δ-function approximation simplifies the underlying calculations and allows to obtain transparent results for non-vanishing drift, too.

Reaction-diffusion-convection equation in δ-approximation

In the derivation of Eq. (3.23) we neglected one subtlety regarding the initial height of the sphere. When separating the MFPT in falling and rotation time, the initial height condition in the calculation of the rotation time is $z = 1 + r_0$. Therefore, when averaging over the initial orientation, the MFPT is zero for $\theta \in [-\theta_0, \theta_0]$. So, in the following we consider Eq. (3.24) including a drift A_θ due to a finite Péclet number on the interval $]-\Delta\theta/2, \Delta\theta/2]$, with $\Delta\theta := \theta_s - 2\theta_0$

$$D_\theta \partial_\theta^2 T(\theta) + A_\theta \partial_\theta T(\theta) - k\delta(\theta)T(\theta) = -1. \tag{3.25}$$

The solution is again obtained by first solving Eq. (3.25) piecewise with $T^{(1)}(\theta)$ on $]-\Delta\theta/2, 0-[$ and $T^{(2)}(\theta)$ on $]0+, \Delta\theta/2]$ leading to

$$T^{(1)} = -\frac{\theta}{A_\theta} + \frac{D_\theta}{A_\theta^2}\left(1 - a_1 e^{-\frac{A_\theta}{D_\theta}\theta}\right) + a_2, \;\; T^{(2)} = -\frac{\theta}{A_\theta} + \frac{D_\theta}{A_\theta^2}\left(1 - a_3 e^{-\frac{A_\theta}{D_\theta}\theta}\right) + a_4.$$

The four constants a_1, a_2, a_3, a_4 are now obtained by demanding that the solution is periodic, i. e., $T^{(1)}(-\Delta\theta/2) = T^{(2)}(\Delta\theta/2), T^{(1)\prime}(-\Delta\theta/2) = T^{(2)\prime}(\Delta\theta/2)$ and continuous at $\theta = 0$, i. e., $T^{(1)}(0) = T^{(2)}(0)$. The fourth condition follows from integration of Eq. (3.25) from $-\varepsilon$ to ε with some $\varepsilon > 0$ and then considering the limit $\varepsilon \to 0$. This leads to $T^{(2)\prime}(0+) - T^{(1)\prime}(0-) = \frac{k}{D_\theta} T^{(2)}(0+)$. For the average over all initial orientations including some for which MFPT is zero, we then get

$$\langle T \rangle_\theta = \frac{1}{\theta_s} \int_{-\Delta\theta/2}^{\Delta\theta/2} d\theta T(\theta) = \frac{A_\theta \Delta\theta^2 \coth(\frac{A_\theta \Delta\theta}{2D_\theta}) - 2D_\theta \Delta\theta}{2A_\theta^2 \theta_s} + \frac{\Delta\theta^2}{k\theta_s}. \tag{3.26}$$

Before we can compare Eq. (3.26) with the simulation results from Sec. 3.3, we must specify the rate k. The following estimate is again based on the assumption that $\theta_0 \ll \theta_s$. Then, applying the stationary probability distribution Eq. (2.30) for the sphere's height, the probability for an encounter while a receptor passes the interval $[-\theta_0, \theta_0]$ is $p_z = 1 - e^{-Pe_z r_0}$. On the other hand if τ is the mean time the receptor is pointing downwards, then, the probability for encounter is $p_{\bar{k}} = 1 - e^{-\bar{k}\tau}$, involving the rate $\bar{k}$. In the discussion above we saw that k is related to $\bar{k}$ via $k = 2\theta_0 \bar{k}$. In the diffusive limit ($A_\theta = 0$), a good estimate for the time τ is the mean first passage time to reach the boundary of $[-\theta_0, \theta_0]$ when starting at $\theta = 0$. This time is given by $\tau = \theta_0^2/2D_\theta$ [15]. For A_θ very large, we expect $\tau \sim 1/A_\theta$, these two limits may be combined to provide $1/\tau = 2D_\theta/\theta_0^2 + A_\theta/2\theta_0$. Demanding that $p_z = p_{\bar{k}}$, we obtain as an estimate for k

$$k = Pe_z r_0 \frac{2\theta_0}{\tau} = Pe_z r_0 \left(\frac{4D_\theta}{\theta_0} + A_\theta\right). \tag{3.27}$$

r_0	D_θ	A_θ/Pe	$2\theta_0$	k estimated in Eq. (3.27)	k used in the plot Fig. 3.4a,c
10^{-3}	0.35	0.28	0.06	$2.33 + 0.014Pe$	$2.51 + 0.014Pe$
$3 \cdot 10^{-3}$	0.35	0.28	0.107	$3.93 + \ldots$	$5.79 + \ldots$
$7 \cdot 10^{-3}$	0.35	0.28	0.165	$5.94 + \ldots$	$11.86 + \ldots$
$10 \cdot 10^{-3}$	0.35	0.28	0.2	$7 + \ldots$	$21.75 + \ldots$

Table 3.2: Comparison between the values for k obtained by fit with its estimation. For the fit the Marquardt-Levenberg algorithm implemented in gnuplot was used.

Now, using the average quantities for drift and diffusion coefficient, A_θ and D_θ, respectively, given in Eq. (3.15), we can calculate the 2D MFPT for homogeneous ligand coverage by means of Eq. (3.26) and Eq. (3.27). It turns out that this predicts the results shown in Fig. 3.4a and Fig. 3.4c quite well for $r_0 = 10^{-3}$.

However, the larger r_0 the larger θ_0, so that the assumption $\theta_0 \ll \theta_s$ becomes less appropriate. Indeed, our predictions match the curves in Fig. 3.4c for $r_0 \geq 3 \cdot 10^{-3}$ only qualitatively. Therefore, instead of using the estimate given by Eq. (3.27), we consider k as a fit parameter for Eq. (3.26) to the curves in Fig. 3.4c. The resulting values for k together with the average quantities from Eq. (3.15) and the estimate Eq. (3.27) are listed in Tab. 3.2. The resulting fits are the solid lines in Fig. 3.4a,c. Especially, in Fig. 3.4a the estimates fit quite well for all N_r, although only one fit parameter was used for all curves together.

Scaling limits

The favorable agreement between our estimate Eq. (3.26) and the simulation results for the MFPT allows us to derive scaling laws from Eq. (3.26) for certain limits.

For a large driving force onto the wall $Pe_z \gg 1$ the rate defined in Eq. (3.27) becomes large. Thus, Eq. (3.26) effectively reduces to Eq. (3.18) which was derived for motion in an interval between two absorbing boundaries. Then, the two limits in regard to Pe give different scaling in regard to N_r. For small Pe, we get (with $\Delta\theta = \theta_s - 2\theta_0$)

$$\langle T \rangle_\theta = \frac{(\Delta\theta)^3}{12\theta_s D_\theta} \approx \frac{4\pi^2}{9N_r^2} \; . \tag{3.28}$$

For large Pe, we get

$$\langle T \rangle_\theta = \frac{\Delta\theta^2}{2\theta_s A_\theta} \approx \frac{4\pi}{N_r Pe} \; . \tag{3.29}$$

The validity of these expressions is explicitly verified in Fig. 3.10b. There, the MFPT is shown as a function of N_r obtained from simulations for $Pe \approx 0$ and $Pe \approx 1.5 \cdot 10^3$ (denoted by + and $\times$, respectively). The solid lines refer to Eq. (3.28) and Eq. (3.29) for the low and high Péclet limit, respectively. For $A_\theta, D_\theta, \theta_0$ the average quantities according to Eq. (3.15) are used (at $Pe_z = 1000$ these are $D_\theta = 0.226, A_\theta = 0.2Pe, \theta_0 = 0.067$). The predicted curve Eq. (3.29) matches even better to the simulation results when using slightly smaller values for θ_0. This reflect the fact that the MFPT for high values of Pe is smaller than in the diffusive limit. Therefore, for large Pe the sphere is on average less close to the wall, resulting in a smaller mean-field value for θ_0 than given in Eq. (3.15).

In the limit of small driving forces $Pe_z \sim 1, Pe \approx 0$ the absorption rate Eq. (3.27) is

small and the second term in Eq. (3.26) becomes dominant. Then, the MFPT scales as $1/Pe_z$ in regard to the strength of drift in z-direction. This was verified in Fig. 3.5a. In Tab. 3.3 the derived scalings (including the result Eq. (3.3)) are summarized.

limit	$N_r \gg 1, \quad Pe_z \sim 1$	$N_r < 10$ and $Pe_z \gg 1$	
		$Pe \ll 1$	$Pe \gg 1$
$\langle T \rangle_\theta$	$1/Pe_z$	$1/N_r^2$	$1/(N_r Pe)$

Table 3.3: Scaling behavior of the 2D MFPT for some asymptotic limits (in the limit of homogeneous ligand coverage).

3.5.2 Reaction-diffusion equation for the 3D diffusive limit

To estimate the MFPT in the 3D diffusive limit is much more difficult than for 2D. For example, if one considers only rotational diffusion of the sphere, it turns out that it is not isotropic due to the presence of the wall (cf. Ref. [76] and Appendix B.3). In addition, the "space of free diffusion", which in the previous section was given as the interval located between two receptor patches, is now the surface of the sphere except the receptor patches, i. e., the boundary is the joint but unconnected boundary of all receptor patches. To nevertheless get at least a qualitative estimate for the MFPT in the 3D diffusive limit, we will use an approximation proposed by Berg and Purcell [16]. They were looking for the mean first passage time of a ligand moving on a cell surface to find an immobilized cell surface receptor. For that they considered diffusion on a ring between two concentric circles. The outer one with radius $R' \propto 1/\sqrt{N_r}$ and the inner one with radius $r' := r_p^{eff}$ (cf. Eq. (3.20)) representing the receptor patch (see Fig. 3.11). In our case the sphere has to move towards the ligands and not the other way round, nonetheless, we can adopt this

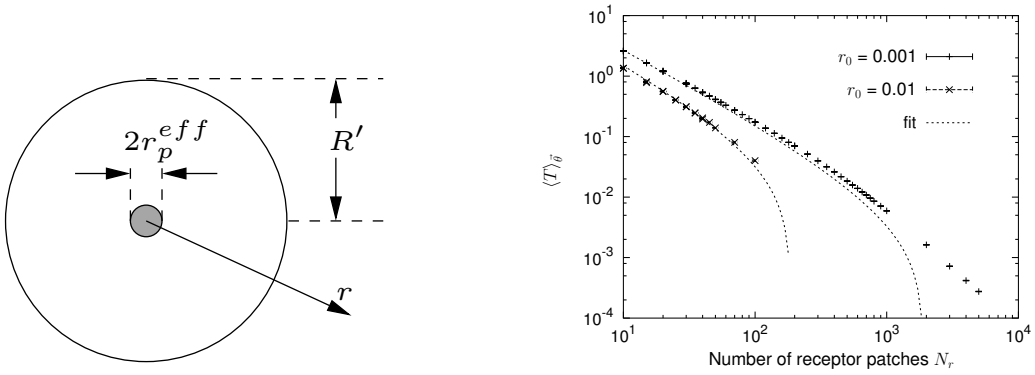

(a) (b)

Figure 3.11: (a) Illustration of the approximation used by Berg and Purcell: a receptor patch with effective radius r_p^{eff} inside a disk of radius R'. (b) MFPT $\langle T \rangle_{\vec{\theta}}$ as a function of the number of receptor patches N_r for homogeneous ligand coverage in the 3D diffusive limit. The data shown is the MFPT for an initial height $z_0 = 2$ (subtracted by the MFPT in the limit of homogeneous receptor coverage Eq. (3.3)) for the two receptor heights $r_0 = 0.001, 0.01$. The data is compared to a fit according to Eq. (3.33). For the fit the Marquardt-Levenberg algorithm of gnuplot was used.($Pe_z = 2000, r_p = 0.001, N = 10^4, \Delta t = 10^{-6}$).

approximation to our problem. In addition, we have to incorporate the possibility that the sphere is not close enough to the wall and therefore a receptor-ligand encounter is not possible, although the sphere is in the right orientation. We do this in a similar fashion as in the 2D case by considering a reaction rate k. It turns out that now the limit $r' \ll R'$ cannot be obtained by replacing the reactive patch with a δ function. Therefore, we use so called *radiation boundary conditions*, similar to the work done in Ref. [152]. The equation for the MFPT then reads (assuming azimuthal symmetry)

$$D\partial_r^2 T - \frac{D}{r}\partial_r T = -1, \tag{3.30}$$

with the boundary conditions $\partial_r T|_{r=R'} = 0$ (reflective boundary), and $\partial_r T|_{r=r'} = k/D_\theta T(r')$ (radiation boundary). The reactive rate k is again measured in units of "length"(angle) per time. The solution to Eq. (3.30) for the given boundary conditions is given in Ref. [152]. Integrating it over the whole circle and assuming that the MFPT for being initially inside the reactive patch is zero we get

$$\langle T\rangle = \frac{R'^2}{2D}\left(\ln\frac{R'}{r'} - \frac{3}{4} + \frac{r'^2}{R'^2} - \frac{r'^4}{4R'^4}\right) + \frac{(R'^2 - r'^2)^2}{2R'^2 r' k}. \tag{3.31}$$

Using the same arguments as in the previous section we note that the approximation considered here makes only sense in the limit $R' \gg r'$. Then, Eq. (3.31) reduces to

$$\langle T\rangle = \frac{R'^2}{2D}\left(\ln\frac{R'}{r'} - \frac{3}{4}\right) + \frac{R'^2}{2r'k}. \tag{3.32}$$

If the rate k is infinity, i. e., "reaction" occurs with probability 1 when the reactive patch is reached, the second term in Eq. (3.32) is zero and we have the result derived by Berg and Purcell [16] to approximate the MFPT of ligands to immobile receptors on a spherical surface.

Here, we like to utilize Eq. (3.32) as an estimate for the MFPT $\langle T\rangle_{\vec{\theta}}$ in the diffusive limit computed in Sec. 3.4 (in the case of homogeneous ligand density). First, we notice that an average rotational diffusion constant as in Eq. (3.15) can be calculated for rotations about all three axes. As rotations about the z-axis do not change the height of the receptor patches we take only rotation about the x- and y-axis into account. For the two latter ones the mobilities are equal (azimuthal symmetry). So we set $D = 2D_\theta$, with D_θ from Eq. (3.15). We already defined the effective patch radius r' as $r' = r_p^{eff} = \sqrt{r_0} + r_p$ which approximates θ_0 quite well for large Pe_z. For the rate we postulate $k \propto Pe_z$. For the radius R' we expect $R' = a_1/\sqrt{N_r}$ with a constant a_1. In the following we fit Eq. (3.32) for a_1 to our simulation results. To reduce the uncertainties included in the estimate of k we consider large vertical driving force, i. e., $Pe_z \gg 1$. Putting everything together our estimate for $\langle T\rangle_{\vec{\theta}}$ in the limit of large Pe_z is

$$\langle T\rangle_{\vec{\theta}} = \frac{a_1^2}{4D_\theta N_r}\left(\ln a_1 - \frac{1}{2}\ln N_r - \ln r' - \frac{3}{4}\right). \tag{3.33}$$

In Fig. 3.11b simulation results for the MFPT $\langle T\rangle_{\vec{\theta}}$ as a function of N_r for both $r_0 = 0.001$ and $r_0 = 0.01$ are shown. A fit of Eq. (3.32) for a_1 at the $r_0 = 0.001$ results gives $a_1 \approx 2.92$. With this value for a_1 the estimate Eq. (3.33) for $r_0 = 0.01, 0.001$ (without any extra fit for $r_0 = 0.01$) is plotted in Fig. 3.11b, too. It can be seen that for small N_r, i. e., $N_r < 1000$

and $N_r < 100$ for $r_0 = 0.001$ and $r_0 = 0.01$, respectively, the accordance between Eq. (3.33) and the simulation results is quite well. At large numbers of receptor patches the analytic estimate fails, as for $N_r \gg 1$ Eq. (3.33) becomes negative, which is obviously unphysical. The reason is that then the assumption made for the derivation Eq. (3.33), i. e., $R' \gg r'$, is no longer fulfilled. Indeed, at $N_r = 1000$ we have $R' \approx 0.09$ which is of the same order of magnitude as $r' \approx 0.03$ (for $r_0 = 0.001$).

$2R'$ is interpreted as to be the "mean distance" (measured on the surface of the sphere) between two receptor patches. For $N_1 = 1$ the fitted value for a_1 suggests $2R' \approx 6$ which is slightly less than the circumference of a great circle on the sphere. In Ref. [16] the authors gave an estimate of $R' = \sqrt{\pi/N_r} \Rightarrow a_1 \approx 1.8$, which is smaller but of the same order of magnitude as the value obtained from our fit.

Using Eq. (3.32) as the base to determine the proper asymptotic behavior of the MFPT in regard to $N_r \to 1$ we obtain $\langle T \rangle_{\vec{\theta}} \propto \ln(const/N_r)/N_r$ for the limit $Pe_z \gg 1$. For $r'k \ll D_\theta$ the second term in Eq. (3.32) becomes dominant and we have $\langle T \rangle_{\vec{\theta}} \propto 1/N_r$. Supposing for k again the estimate Eq. (3.27), we have $r'k = 8D_\theta Pe_z r_0 r'/\theta_0 \propto Pe_z r_0$. Thus, at intermediate values for Pe_z, the capture height r_0 determines whether the MFPT behaves rather as $\propto \ln(const/N_r)/N_r$ (large r_0) or rather as $\propto 1/N_r$ (small r_0). In Fig. 3.8b we actually were able to approximately determine $\langle T \rangle_{\vec{\theta}} \propto 1/N_r$ for $r_0 = 0.001$. But for $r_0 = 0.07$ the increase in the MFPT for $N_r \to 1$ is steeper than $1/N_r$.

3.6 Summary and discussion

In this chapter we presented the results for the mean first passage times (MFPT) for initial encounter between spatially resolved receptors on a spherical Brownian particle in linear shear flow and spatially resolved ligands on the boundary wall for both, motion restricted to 2D and motion in 3D. The main results were obtained by repeated simulations of the discretized Langevin equation Eq. (2.26). Each data point shown corresponds to at least 100,000 simulation runs. It is important to note that these simulations are very time consuming because we resolve objects of the size of 10^{-3} R, that is for μm-sized particles we resolve the nm-scale. The simulation results were interpreted further by an analytical analysis based on reaction-diffusion equations. For the 2D case, the MFPT could be solved in a mean-field like approach resulting in the correct asymptotic limits in regard to the two dimensionless numbers characterizing the motion of the particle, the Péclet number Pe and the Péclet number in z-direction Pe_z, respectively.

In general, we found that the MFPT was always monotonically decreased when the Péclet number was increased. That means that a particle which is covered with receptors in a way that it binds well to ligands already in the diffusive limit is even better suited to initiate binding at finite shear rates. In our simulations we modeled the receptor geometry using three parameters: the number of receptor patches N_r, the radius of the receptor patches r_p, and the capture radius r_0. The efficiency of binding is mainly increased by N_r, but only up to a saturation value of the order of hundred. An increase of r_p leads only to a weak enhancement of binding efficiency. The influence of r_0 to the MFPT is threefold: i) it reduces the mean falling time, ii) it increases the effective patch size, and iii) according to the stationary probability distribution for the z-direction, it becomes more probable for the sphere to be within the encounter zone when r_0 is increasing. An additional but more indirect effect of receptor protrusions is that the further the cell is away from the wall, the faster it can rotate (even in the diffusive limit) due to the larger mobility. As shown by Eq. (3.11) rotations play a role only within binding range, i. e., for $z < 1 + r_0$. Therefore, a large r_0 lets the cell also benefit from faster rotations. Summarizing our findings in regard

to receptor geometry, we conclude that the most efficient design for particle capture under flow is to cover the particle with hundreds of receptor patches (N_r above threshold), each with a rather small area (small r_p), but formed as a protrusion (large r_0).

Indeed, this strategy seems to be used by white blood cells, which have evolved intriguing mechanisms both on the molecular and cellular scale in order to adhere effectively to the endothelium under the conditions of hydrodynamic flow. The typical size of white blood cells is $R \approx 5$ μm and they are covered with a few hundreds of protrusions (*microvilli*) with the receptors (most notably L-selectin) localized to the microvilli tips [103, 29]. In general, the microvilli of white blood cells are much more complex than the parameter r_0 in our model: they are rather long (typical length 350 nm, that is $R/15$) and have their own physical properties (e. g., very flexible in the transverse direction and viscoelastic in the longitudinal direction) [137]. Nevertheless, it is striking that elevation of the receptors above the main cell surface seems to be a major design principle for white blood cells. In fact, the same strategy appears to be used also by malaria-infected red blood cells, which are known to develop a dense coverage with elevated receptor patches (*knobs*) on the cell surface [11, 105, 6]. A typical value for the cell radius is 3.5 μm [149]. The knobs have a typical height of 20 nm, a radius of about 90 nm and a distance of 200 nm (for red blood cells infected by single parasites) [105]. This dense and elevated coverage suggests that like the white blood cells, the malaria-infected red blood cells also function in the regime of homogeneous coverage.

In order to discuss the motion of white blood cells in more detail, it is instructive to consider the parameters for a typical flow chamber experiment. In aqueous solution and at room temperature, $\rho = 1$ g/cm^3, $\eta = 10^{-3}$ Pa s, and $T_a = 293$ K. Then, the dimensionless parameters determining cell motion become

$$Pe = 4.67\ R^3\dot{\gamma}, \qquad Pe_z = 10.16\ R^4\Delta\rho, \qquad \Delta t = \frac{Pe}{\dot{\gamma}} = 4.67\ R^3 s, \tag{3.34}$$

where R is given in μm, $\Delta\rho$ in units of g/cm^3 and the shear rate $\dot{\gamma}$ in units of 1 per second; Δt is the diffusive time scale. For leukocytes in flow chambers we typically have $R = 5$, $\dot{\gamma} = 100$ and $\Delta\rho = 0.05$, thus for the two Péclet numbers we get $Pe = 6 \times 10^4$ and $Pe_z = 317$, respectively. Then, $f = Pe_z/Pe = 0.005$ (cf. Sec. 2.3), that is the effect of hydrodynamic deterministic motion will be very strong. The experimental time scale is given by the time for transversing the field of view, which is about 3 s at a shear rate of 100 Hz and length of 650 μm. The diffusive time scale Δt for leukocytes is about 600 s (10 min), which reflects their large size and shows that diffusive motion is by far not sufficient to initiate binding. Binding becomes more favorable in the presence of convection. For a start height of one radius above the wall ($z_0 = 2$), our calculations give a MFPT of about 5 s, that is much less than the diffusive time. However, this is still much larger than the experimental time scale. This proves that only those cells have a chance to bind that flow very close to the wall, exactly as observed experimentally. Therefore, *in vivo* white blood cells depend also on other mechanisms driving them onto the substrate, including contact and hydrodynamic interactions with other cells. These effects have been studied in detail before. For example, Munn and coworkers have shown that adhesion of leukocytes close to the vessel wall in post-capillary venules is enhanced by red blood cells passing them [148]. King and Hammer have shown, using an algorithm capable of simulating several cells, that already adherent leukocytes can recruit other leukocytes via hydrodynamic interactions [79]. The results presented here, when specified to leukocytes, show that indeed these mechanisms are crucial for effective leukocyte capture under flow.

Our results also suggest that leukocytes are sufficiently large that thermal fluctuations are not dominant. This changes when studying smaller particles, e. g., receptor-covered spheres with $R \approx 1$ μm, whose binding also has been investigated with flow chambers [113, 112]. Eq. (3.34) shows that the Péclet numbers scale strongly with particle radius R, therefore, these beads are subject to much stronger thermal fluctuations than leukocytes. In Ref. [112] it has been verified that indeed in equilibrium such particles obey the barometric distribution Eq. (2.30) calculated in Chapter 2. In Ref. [113] it was found that the adhesion probability p_{ad} is proportional to the ligand density, $p_{ad} \sim \rho_l$. With $p_{ad} \sim 1/T$ it follows that $T \sim 1/\rho_l$ as found by our simulations in the limit of low ligand densities.

In this chapter we have mainly considered the generic case of a constant downward acting force due to a density difference between the sphere and the surrounding fluid. Applying our work to a more specific context it might be interesting to examine also other forces which can easily be done in the framework presented here. As the addition formula Eq. (3.11) for falling and rotational MFPT was not derived under the assumption of a specific force, it is also true for non-constant forces. For general potential forces the falling time Eq. (3.3) has then to be replaced by Eq. (3.4). Also the rotational MFPT is influenced by a vertical force via the stationary height distribution. In Sec. 3.1 we showed that neglecting gravitational force and considering only short-ranged forces like van der Waals or electrostatic forces would result in infinite MFPTs for the setup of the halfspace. With an additional wall as an upper boundary the MFPT turned out to be finite also in the no-drift case. Nevertheless, we showed that already a slight density difference of some percent for a micron-sized sphere fairly reduces the MFPT. Hence, in flow chamber experiments designed to reveal any kind of sphere-wall interactions, a non-vanishing gravitational drift is important to obtain appreciable statistics.

Throughout this thesis, we use the model of a rigid sphere. For cells, elastic deformations might be relevant. For free flow, a simple scaling estimate shows that the critical value for the shear rate leading to substantial deviations from the spherical shape is $(Eh)/(\eta R)$ [130], where $E = 100$ Pa and $h = 100$ nm are Young modulus and thickness of the cellular envelope, respectively. The fact that the Young modulus E appears here indicates that cells tend to passively deform less than vesicles, whose elasticity is characterized rather by the bending rigidity [132, 147]. The scaling estimate leads to a critical shear rate of 10^3 Hz, which is above the value of a few 10^2 Hz (corresponding to $Pe \approx 10^5$ for white blood cells) which often provides an upper limit in flow chamber experiments. When the cell closely approaches the wall lubrication forces arise which tend to asymmetrically deform the cell resulting in an additional lift force [23, 134]. This effect is of second order in shear rate and strongly scales with the distance to the wall. Using an estimate for the lift force from Ref. [134] it turns out that for minimum cell wall distances typically for leukocytes lift force becomes relevant for shear rates only above the order of 10^2 Hz.

In Sec. 2.4.1 the process of bond formation between a receptor-covered particle and a ligand-covered wall was separated into an encounter and a reaction step. For the MFPTs calculated in this chapter we showed that the mean values and the standard deviations of the corresponding first passage time distributions are of the same order of magnitude. Hence, the inverse of the MFPT for encounter can be identified with the encounter rate k_+ defined in Sec. 2.4.1. For many receptor-ligand pairs the duration of each encounter should be sufficiently long for the formation of an adhesion contact in the limit of zero shear rate (i. e., the dwell time for receptor-ligand contact is expected to be much larger than the inverse on-rate $1/k_{on}$). In that case formation of an adhesion contact is diffusion limited and according to Eq. (2.33) the inverse MFPT for encounter should be a good approximation for the mean adhesion time $1/k_f$ with the forward reaction rate k_f.

Chapter 4

Rolling adhesion of leukocytes

So far we focused on free *hydrodynamic* motion of a spherical particle up to the first occurrence of a receptor-ligand encounter. If these encounters are converted into functional receptor-ligand bonds, then, the motion of a receptor carrying cell is substantially changed. In this chapter, we classify different types of motion and analyze their appearance according to the association and dissociation rates in the context of flow chamber experiments with leukocytes. We perform this analysis by use of the Stokesian dynamics algorithm including bond-formation and -dissociation processes. In addition, we show that the basic features of the different types of motion can already be derived from a master equation approach that essentially reduces the cell-motion to one degree of freedom. Furthermore, we numerically measure the distribution of force due to bonds below the moving cell. And we investigate how robust rolling can be with respect to the applied shear rate.

4.1 Rolling in experiment and simulation

The data of a rolling cell obtained in a flow chamber experiment and the data obtained in a numerical simulation of leukocyte motion is plotted in Fig. 4.1. In Fig. 4.1a the translational velocity U of a rolling leukocyte for some period of time is shown as experimentally measured by Alon and co-workers [3]. The rolling state is identified by a strong decrease of the cell velocity compared to the velocity of a free moving cell. Fig. 4.1b shows besides the translational velocity also the angular velocity $R\Omega$ of a receptor-covered sphere above a ligand bearing wall (the data is obtained by 2D simulations, cf. Sec. 2.2). As Brownian motion is included in the simulation, the velocity of the cell $U(t)$ is not its instantaneous velocity, because for the trajectory of a Brownian particle (modeled as a Wiener process) the limit $\lim_{\delta t\to 0}(X(t+\delta t)-X(t))/\delta t$ is not a well-defined quantity [71]. The velocities plotted in Fig. 4.1b are rather obtained as the difference quotient $U(t) := (X(t+\Delta t)-X(t))/\Delta t$ with some time interval Δt. Here and throughout this chapter, we choose $\Delta t = 0.02$ s which experimentally corresponds to a camera resolution of 50 Hz. At $t = 2.9$ s the first bond is formed and the cell starts rolling which can again be seen from the sudden decrease in velocity. In addition, the simulation reveals that the $R\Omega$ and U curves collapse onto one curve as soon as the cell starts rolling. Before initial binding, the cell slips over the substrate with $R\Omega/U \approx 0.57$ as explained in Sec. 2.3. This observation motivates us to define "rolling" by $R\Omega/U \to 1$ in regard to simulations which is also the common definition for rolling in mechanics. This is in contrast to simulations were usually only U is measured, and therefore rolling is defined by a strong decrease in U.

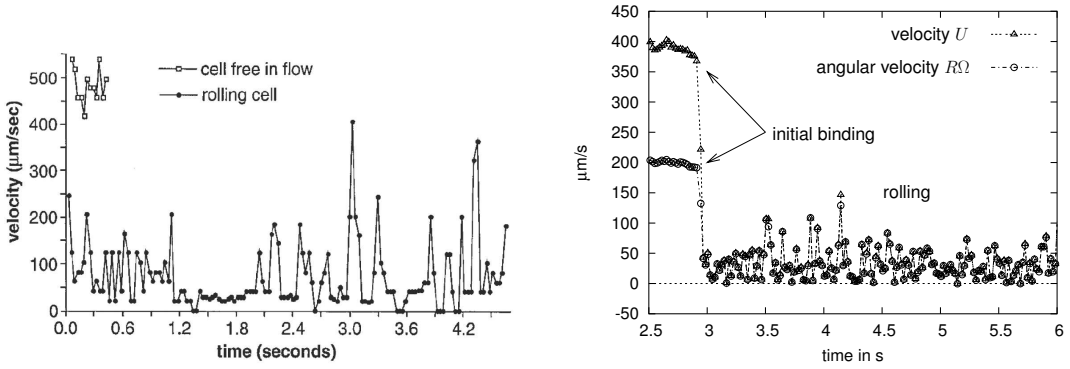

(a) (b)

Figure 4.1: Snapshots of leukocyte motion. (a) Velocity of a leukocyte (neutrophil) rolling on L-selectin ligand PNAd with 60 sites per μm^2 [3, Fig. 1A]. (b) Translational and angular velocity (U and $R\Omega$, respectively) of a sphere with radius $R = 4.5$ μm in a 2D simulation at the same ligand density (with on-rate $k_{on} = 35$ Hz and unstressed off-rate $k_0 = 6.8$ Hz).

4.1.1 The stopping-process: emergence of rolling

A molecular bond can only be formed in a contact zone, which is much smaller than the cell itself. The contact zone is the region on the cell surface which is less than a distance r_0 away from the wall. After a functional bond is formed the cell slows down under the action of this bonds. Eventually the cell will arrest unless the bond dissociates. In the following we will examine this stopping process. In the course of this analysis we will see, how the existence of bonds facilitate in rolling motion of the cell.

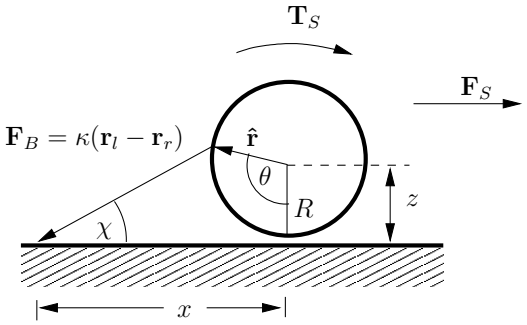

Figure 4.2: A cell is stopped by a tether force $\mathbf{F}_B$. $\mathbf{r}_l$ and $\mathbf{r}_r$ are ligand and receptors position, respectively. x, θ define two degrees of freedom, χ the angle between the bond and the wall. In equilibrium (i. e., $\dot{x} = \dot{\theta} = 0$) the shear force $\mathbf{F}_S$ and the shear torque $\mathbf{T}_S$ are balanced by the tether force and its respective torque. Not shown are gravitational force and repulsive forces from the substrate that compensate all downward acting forces.

Deterministic equations

As the Péclet number of leukocytes at typical shear rates is large we will neglect Brownian motion of the cell in the following. Furthermore, we reduce our analysis to the pseudo two-dimensional case introduced in Sec. 2.2. Assuming that the cell moves at constant height above the wall ($\dot{z} = 0$), we are left with only two degrees of freedom x, θ. In the following we fix $z = R + r_0$, that is, z is only slightly larger than R for a typical value of the capture radius.

Reducing Eq. (2.15) for these two variables we obtain the following equations for the

translational velocity $\dot{x} \equiv U$ and angular velocity $\dot{\theta} \equiv \Omega$ in dimensionless form:

$$\begin{pmatrix} \dot{x} \\ \dot{\theta} \end{pmatrix} = \mathsf{A} \begin{pmatrix} F_{B,x} \\ T_{B,y} \end{pmatrix} + \vec{b}, \tag{4.1}$$

with $F_{B,x}$ the x-component of the bond force and $T_{B,y}$ the y-component of the torque which is due to the tether bond. For a concise notation we introduced the following abbreviations

$$\mathsf{A} := \begin{pmatrix} \hat{\beta}^{tt}(s) & \frac{3}{4}\hat{\beta}^{tr}(s) \\ \frac{3}{4}\hat{\beta}^{tr}(s) & \frac{3}{4}\hat{\beta}^{rr}(s) \end{pmatrix}, \qquad \vec{b} := \begin{pmatrix} \frac{1}{t} - \frac{1}{2}\hat{\beta}^{dt}(s) \\ \frac{1}{2}(1 - \hat{\beta}^{dt}(s)) \end{pmatrix}, \tag{4.2}$$

based on the scalar mobility functions $\hat{\beta}(s)$ (with $s \equiv R/z$) introduced in Appendix B.1. If no tether exists $\dot{x} = b_1 := (\vec{b})_1$. In literature this *free* velocity is sometimes referred to as the *hydrodynamic velocity* of the cell. From Fig. 4.2 we read off tether force $\mathbf{F}_B$ and tether torque $\mathbf{T}_B$

$$\mathbf{F}_B(t) = \kappa \begin{pmatrix} -x(t) + R\sin(\theta(t)) \\ 0 \\ R\cos(\theta(t)) - z \end{pmatrix}, \quad \mathbf{T}_B(t) = \hat{\mathbf{r}} \times \mathbf{F}_B, \quad \hat{\mathbf{r}} = \begin{pmatrix} -R\sin(\theta(t)) \\ 0 \\ -R\cos(\theta(t)) \end{pmatrix}. \tag{4.3}$$

In this analysis we assume the resting length of the bond to be zero, therefore, at $t = 0$ already a small bond force in z-direction exists (but no torque). Briefly after bond formation the cell has not moved significantly and $x/R, \theta \ll 1$ holds. Thus, the quantities $F_{B,x}, T_{B,y}$ can be approximated as

$$F_{B,x} = \kappa(R\theta - x) + \mathcal{O}(\theta^3), \qquad T_{B,y} = \kappa(Rx - zR\theta) + \mathcal{O}(\theta^3) + \mathcal{O}(x\theta^2). \tag{4.4}$$

Reinserting these approximate expressions into Eq. (4.1), we obtain a first order linear differential equation for x, θ

$$\begin{pmatrix} \dot{x} \\ \dot{\theta} \end{pmatrix} = \mathsf{C} \begin{pmatrix} x \\ \theta \end{pmatrix} + \vec{b}, \qquad \mathsf{C} := \mathsf{A}\mathsf{X}, \qquad \mathsf{X} := \kappa \begin{pmatrix} -1 & R \\ R & -zR \end{pmatrix}, \tag{4.5}$$

which can readily be solved with the proper boundary conditions. In our case $x(0) = \theta(0) = 0$, resulting in

$$\begin{pmatrix} x(t) \\ \theta(t) \end{pmatrix} = (\mathsf{E} - \exp(\mathsf{C}t)) \begin{pmatrix} x_\infty \\ \theta_\infty \end{pmatrix}, \qquad \begin{pmatrix} x_\infty \\ \theta_\infty \end{pmatrix} := -(\mathsf{C})^{-1}\vec{b}, \tag{4.6}$$

where E is the unit matrix. The matrix $\exp(\mathsf{C}t)$ can be expressed in terms of its eigenvalues and eigenstates. The two eigenvalues of C are

$$\lambda_\pm = \frac{\mathrm{tr}\mathsf{C}}{2}\left(1 \pm \sqrt{1 - \frac{4\det\mathsf{C}}{(\mathrm{tr}\mathsf{C})^2}}\right). \tag{4.7}$$

The determinant $\det\mathsf{C} = \det\mathsf{A}\det\mathsf{X} = \kappa^2 \det\mathsf{A}R(z-R)$ is positive as A is part of the positive definite mobility matrix (cf. Sec. 2.1.1) and $z \gtrsim R$. Furthermore, the trace $\mathrm{tr}\mathsf{C}$ is negative (it holds true that $\mathrm{tr}\mathsf{C} = 2R\mathsf{A}_{12} - \mathsf{A}_{11} - Rz\mathsf{A}_{22} < 0$ for all heights z as the diagonal elements of A are notedly larger than A_{12}). As $z - R \ll R$ one can expand the square root in Eq. (4.7) in terms of $(4\det\mathsf{C})/(\mathrm{tr}\mathsf{C})^2$ and we obtain the following approximate expression

for the eigenvalues $\lambda_\pm$: $\lambda_+ \approx \mathrm{tr}\mathsf{C} < 0$ and $\lambda_- \approx \det\mathsf{C}/\mathrm{tr}\mathsf{C} < 0$. Thus, the matrix C is negative definite and $\lim_{t\to\infty}\exp(\mathsf{C}t) = 0$. Finally, expressing Eq. (4.6) explicitly in terms of the eigenvalues $\lambda_\pm$ and the corresponding eigenstates of C we obtain:

$$\begin{pmatrix} x(t) \\ \theta(t) \end{pmatrix} = \begin{pmatrix} 1 \\ \frac{\lambda_+ - (\mathsf{C})_{11}}{(\mathsf{C})_{12}} \end{pmatrix} \frac{b_1 - \lambda_- x_\infty}{\lambda_+ - \lambda_-} \left(1 - e^{\lambda_+ t}\right) - \begin{pmatrix} 1 \\ \frac{\lambda_- - (\mathsf{C})_{11}}{(\mathsf{C})_{12}} \end{pmatrix} \frac{b_1 - \lambda_+ x_\infty}{\lambda_+ - \lambda_-} \left(1 - e^{\lambda_- t}\right). \tag{4.8}$$

Discussion and asymptotic behavior

The two eigenvectors $\lambda_\pm$ represent two different time scales as $|\lambda_+| \gg |\lambda_-|$. Shortly after bond formation, $t \ll 1/|\lambda_+|$, $\exp(\lambda_+ t) \approx 0$ and the time development of x, θ is governed by the second term in Eq. (4.8). The initial velocities are the free hydrodynamic velocities with $R\dot{\theta}(0)/\dot{x}(0) \approx 0.5$ so that x and θ do not increase at the same speed (see Fig. 4.3a). At intermediate times t_{int} with $1/|\lambda_+| \ll t_{int} \ll 1/|\lambda_-|$ the velocities are approximately given by

$$\begin{pmatrix} \dot{x} \\ \dot{\theta} \end{pmatrix} \approx \lambda_- \begin{pmatrix} 1 \\ \frac{\lambda_- - (\mathsf{C})_{11}}{(\mathsf{C})_{12}} \end{pmatrix} \frac{b_1 - \lambda_+ x_\infty}{\lambda_+ - \lambda_-} e^{\lambda_- t_{int}}. \tag{4.9}$$

Expanding $R\dot{\theta}/\dot{x}$ in powers of $(z-R)/R$ we obtain $R\dot{\theta}/\dot{x} = 1 + \mathcal{O}((z-R)/R)$ (i. e., rolling). Thus, by the action of force and torque resulting from the tether bond translational and angular velocity of the cell are adjusted, and the cell starts rolling a short time after the first bond is formed. This can be seen in Fig. 4.3a, there the two velocities $\dot{x}, \dot{\theta}$ are plotted as a function of time. In order to visualize the initial period of adjustment a logarithmic scale for the time axis is applied there.

For large times $t \gg 1/\lambda_-$ Eq. (4.6) predicts that the cell asymptotically reaches the position $(x_\infty, \theta_\infty)$ at which it stops. In Fig. 4.3a the cell velocities as predicted form the time derivative of Eq. (4.6) is compared to the velocities which are obtained when Eq. (4.1) is numerically integrated. We see that for short times the approximation works quite well, until the cell has reached its rolling state (i. e., $R\Omega/U \approx 1$). At long time scales the approximate solution provides only a qualitative prediction of the stopping process. The figure shows that the higher order terms contributing to the bond force/torque leads to a much faster stopping than predicted by the approximation of these quantities with respect to first order in x, θ (see Eq. (4.4)). Also shown in Fig. 4.3a is the stopping process in the case that the height $z - R$ of the cell above the wall is equal to the resting length of the tether bond[1]. In that case the spring constant in Eq. (4.3) is replaced by $\kappa \to \kappa(1 - (z-R)/\|\mathbf{r}_l - \mathbf{r}_r\|)$ (see Fig. 4.2). The leading order term in the power series of $F_{B,x}$ is then of second order in x, θ. So, the linear approximation of the equations of motion cannot be applied in this case. Nevertheless, the qualitative behavior is very similar to the case of zero bond resting length. Fig. 4.3a shows that at short times the cell moves on with almost unchanged velocities, then, the velocities adjust to $R\dot{\theta} \approx \dot{x}$ (for some time even $R\dot{\theta} > \dot{x}$) and finally the cell stops after about the same time as in the case with zero bond resting length.

The mechanism that leads to cell rolling can best be understood from the time dependence of the torque that is exerted by the tether, see Fig. 4.3b. The torque is approximately

[1] That is the case in the adhesive dynamics algorithm which is used to simulate the cell motion in the presence of tether bonds. There, the initial length of the bonds is always chosen to be zero. Thus, the bond may have a resting length of $\leq r_0$ (cf. Sec. 2.4.3)

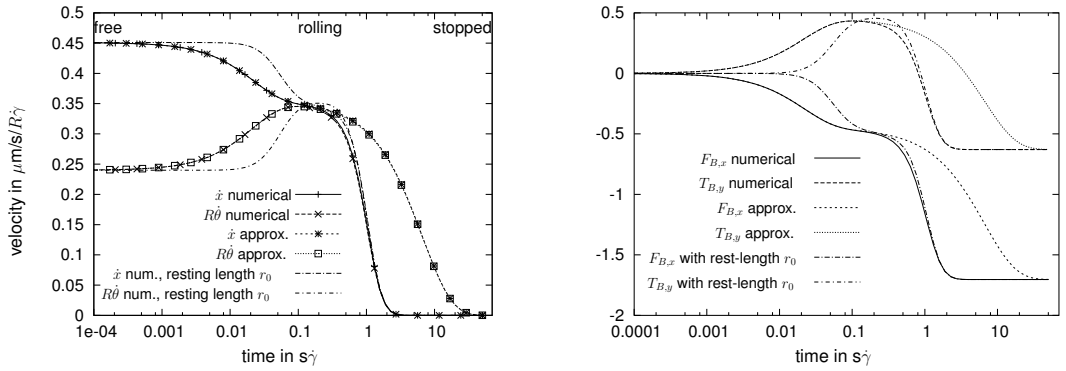

(a) (b)

Figure 4.3: Comparison of the approximate solution Eq. (4.8) with values obtained from numerical integration of Eq. (4.1) ($z = 1.01R$). All plotted quantities are in dimensionless form, i. e., force is expressed in terms of $6\pi\eta R^2\dot{\gamma}$, torque in terms of $6\pi\eta R^3\dot{\gamma}$, velocity in $\dot{\gamma}R$, and time in $1/\dot{\gamma}$. For the dimensionless spring constant $\kappa = 10^2$ was used. For a set of typical parameter values: $R = 5$ μm, $\dot{\gamma} = 100$ Hz, $\eta = 10^{-3}$ Pa s, $\kappa = 1$ corresponds to 10^{-5} N/m. (a) Plot of the (angular) velocity $\dot{x}$ ($\dot{\theta}$) as a function of time for three different calculations: from numerical integration of Eq. (4.1), from analytical derivative of Eq. (4.8), and from numerical integration of Eq. (4.1) under the assumption that the initial bond length r_0 is the resting length of the bond $l_0 = r_0$. For the time axis a logarithmic scale is used. (b) The same for the bond force (torque) $F_{B,x}$ ($T_{B,y}$).

given as $T_{B,y} = \kappa(Rx - zR\theta)$ (see Eq. (4.4)). Initially, x increases faster than $R\theta$ and as $z \approx R$ the torque is positive, i. e., it supports the shear torque and the cell starts turning faster. At the same time the force $RF_{B,x} \approx -T_{B,y}$ slows the translational motion of the sphere down. The maximum torque $\dot{T}_{B,y} = 0$ is reached when $z\dot{\theta} = \dot{x}$, i. e., when the cell is approximately rolling. From that time on x and θ increase at approximately the same speed and eventually the torque will become negative (if $x < z\theta$) and will act against the shear torque. Similar arguments hold when discussing the exact result of the torque given in Eq. (4.3). It should be noted that this analysis in the linear approximation works only, if $z > R$. The case $z = R$ is not applicable as the scalar mobility functions vanish at this height due to the no-slip boundary conditions (even if mobility was not vanishing at $z = R$ the linear approximation applied to this height would fail and instead of an asymptotic stop it would predict a state in which the cell rolls at constant velocity).

Force and torque balance at mechanical equilibrium

When the cell is at rest, shear force (torque) is balanced by tether force (torque), see Fig. 4.2

$$-F_{S,x} = F_{B,x}(\infty) := F_\infty, \qquad -T_{S,y} = T_{B,y}(\infty) := T_\infty, \tag{4.10}$$

the limiting values for force and torque can be inferred from Eq. (4.1) as

$$\begin{pmatrix} F_\infty \\ T_\infty \end{pmatrix} = \mathsf{A}^{-1}\vec{b}.$$

At a height $z = 1.01\ R$, these quantities are $F_\infty = -1.7 \cdot 6\pi\eta R^2$ and $T_\infty = -0.63 \cdot 6\pi\eta R^3$. The determination of the geometrical values x, θ and χ (see Fig. 4.2) from the approximation Eq. (4.6) provides suitable results only in the limit of very large spring constants κ. Otherwise, these quantities have to be determined numerically or geometrically from Fig. 4.2. From the force and torque balance equations the following two relations for the angle χ can be derived

$$\|\mathbf{F}_B\| R\cos\chi = \|\mathbf{T}_S\|, \qquad \|\mathbf{F}_B\| x\sin\chi = \|\mathbf{T}_S\| + R\|\mathbf{F}_B\|. \tag{4.11}$$

From this it follows that $\tan\chi = R/x\ (|T_{S,y}/RF_{B,x}| + 1)$ which can easily be evaluated knowing the proper spring constant. On the other hand these relations can be used to estimate the spring constant of the tether, when the lever arm x is known. Alon and coworkers actually measured the lever arm x by the following experiment [3]: they perfused neutrophils on a wall covered with P-selectin and the direction of motion was reversed every few seconds. Thus, a tethered cell was moving a distance of twice the lever arm length x during flow reversal. Together with $\|\mathbf{r}_l - \mathbf{r}_r\| = \ell - \sqrt{\ell^2 - x^2},\ \ell := R\sin\chi + x\cos\chi$ the tether length in the rest position can be calculated. The experiment was performed at different shear rates ($30 - 80$ Hz) and no significant dependence of x on the shear rate was detected. With a measured value $x \approx 3.06 \pm 0.53\ \mu$m and values for force and torque given above it follows then: $\|\mathbf{r}_l - \mathbf{r}_r\| \approx 1\ \mu$m and $\chi \approx 62°$ [3]. Thus, a lower limit for the spring constant is given by

$$\kappa = \frac{|F_{S,x}|}{\cos\chi(\|\mathbf{r}_l - \mathbf{r}_r\| - l_0)} > \frac{|F_{S,x}|}{\cos\chi\|\mathbf{r}_l - \mathbf{r}_r\|} \approx 10^{-4}\ \text{N/m, at } \dot\gamma = 80\ \text{Hz}, \tag{4.12}$$

where l_0 is the resting length of the tether bond. The independence of the bond length on $\dot\gamma$ in the range of measurement in Alon's experiment could either mean that the spring constant of the tether bond is much larger than the lower limit given above (e. g., if the microvillus length strongly contributes to the total tether length), or that the tether is stretched beyond the linear elastic regime of the bond. The estimate Eq. (4.12) has not been given in the original work. But from different measurements (measuring the force dependence of the off-rate, and fitting the results to the *Hookean spring model* [66]) they derived an upper limit of 7.1 N/m for the tether bond spring constant of L-selectin bonds. Due to the five orders of magnitude between the two limits these measurements don't provide a reliable estimate for the spring constant (which has neither been an aim of Ref. [3]).

Multiple bonds

Above, we found that rolling ($\dot x \approx R\dot\theta$) is a consequence of the way in which tether force and torque are acting on the cell. When multiple bonds exist (each one is formed while the corresponding receptor passes the contact zone), the total force (torque) in the small angle approximation is given as

$$\begin{pmatrix} F_B \\ T_B \end{pmatrix} = \mathsf{X}\sum_{i=1}^{n}\begin{pmatrix} x^i \\ \theta^i \end{pmatrix} = \mathsf{X}_n\begin{pmatrix} x \\ \theta \end{pmatrix} - \mathsf{X}\sum_{i=1}^{n}\begin{pmatrix} x_0^i \\ \theta_0^i \end{pmatrix}, \quad x^i = x^1 - x_0^i, i = 1, \ldots, n.$$

Here, n is the total number of bonds, $\mathsf{X}_n := n\mathsf{X}$ and $x = x^1, \theta = \theta^1$ is the position of the left-most (oldest) bond and x_0^i, θ_0^i are the positions of the left-most bond at the time the ith bond is formed. The eigenvalues $\lambda_\pm^n$ of the matrix $\mathsf{C}_n := \mathsf{A}\mathsf{X}_n$ are $n\lambda_\pm$, therefore, the

process of stopping becomes the faster, the more bonds exist. The solution of the equation of motion after the formation of the nth bond or the dissociation of one of the previously existing $n+1$ bonds (at time $t = t_0^n$) is then given by

$$\begin{pmatrix} x(t-t_0^n) \\ \theta(t-t_0^n) \end{pmatrix} = (\mathsf{E} - \exp(\mathsf{C}_n(t-t_0^n))) \begin{pmatrix} x_{n,\infty} \\ \theta_{n,\infty} \end{pmatrix} + \exp(\mathsf{C}_n(t-t_0^n)) \begin{pmatrix} x_0^n \\ \theta_0^n \end{pmatrix}. \tag{4.13}$$

The rest configuration $(x_{n,\infty}, \theta_{n,\infty})$ of the n-bond state

$$\begin{pmatrix} x_{n,\infty} \\ \theta_{n,\infty} \end{pmatrix} := -(\mathsf{C}_n)^{-1} \left(\vec{b} - \mathsf{C} \sum_{i=1}^{n} \begin{pmatrix} x_0^i \\ \theta_0^i \end{pmatrix} \right),$$

depends on the history of bond formation via $x_0^i, \theta_0^i, i = 1, \ldots, n$. The time derivative of Eq. (4.13) gives the velocities in the n-bond state

$$\begin{pmatrix} \dot{x}(t-t_0^n) \\ \dot{\theta}(t-t_0^n) \end{pmatrix} =$$
$$\lambda_-^n \begin{pmatrix} 1 \\ \frac{\lambda_-^n - (\mathsf{C}_n)_{11}}{(\mathsf{C}_n)_{12}} \end{pmatrix} \frac{((\mathsf{C}_n)_{11} - \lambda_+^n)(x_{n,\infty} - x_0^n) + (\mathsf{C}_n)_{12}(\theta_{n,\infty} - \theta_0^n)}{\lambda_+^n - \lambda_-^n} e^{\lambda_-^n (t-t_0^n)}$$
$$- \lambda_+^n \begin{pmatrix} 1 \\ \frac{\lambda_+^n - (\mathsf{C}_n)_{11}}{(\mathsf{C}_n)_{12}} \end{pmatrix} \frac{((\mathsf{C}_n)_{11} - \lambda_-^n)(x_{n,\infty} - x_0^n) + (\mathsf{C}_n)_{12}(\theta_{n,\infty} - \theta_0^n)}{\lambda_+^n - \lambda_-^n} e^{\lambda_+^n (t-t_0^n)}.$$

Now, a similar discussion as for the one bond case applies. At times t very close to t_0^n the cell might slip again. After a time $t \ll 1/|\lambda_+^n|$ the second term in the above equation is approximately zero. Furthermore, at these times $R\dot{\theta}/\dot{x} = (\mathsf{C}_n)_{12}/(\lambda_-^n - (\mathsf{C}_n)_{11}) = 1 + \mathcal{O}((z-R)/R)$ is independent of the number of closed bonds and the cell is again rolling.

We summarize this analysis by noting that bonds lead to a synchronization of translational and angular velocities (*rolling*) which mathematically corresponds to $R\Omega/U \approx 1$. Rolling might be interrupted for small periods of time due to the association of a new bond or the dissociation of an existing one.

4.2 State diagram of leukocyte motion

4.2.1 Relevant parameters

All (thirteen) parameters appearing in our model are summarized in Tab. 4.1. For the adhesive dynamics simulations carried out in this chapter we non-dimensionalize all quantities using the radius of the cell R as length scale, the wall shear rate $\dot{\gamma}$ as time scale $1/\dot{\gamma}$ and $6\pi\eta R^2\dot{\gamma}$ as force scale. This results in ten dimensionless parameters also listed in Tab. 4.1. The proper non-dimensionalized Langevin equation for this choice of scale is given in Sec. A.1. The parameters $R, T_a, \dot{\gamma}, \eta, \Delta\rho$ influence the flow properties and besides shear rate and viscosity we keep these parameters fixed. For the ambient temperature T_a we choose room temperature $T_a = 293$ K. Sometimes experiments are done at body temperature $T_a = 310$ K. However, this difference has only little influence to the cell's motion as Brownian motion for leukocytes in flow chambers is not the dominant factor as indicated by large Péclet numbers (cf. Sec. 3.6). The radius of leukocytes depends on the specific type, e. g., neutrophils which are often used in flow chamber experiments to study

Parameter → non-dimensionalized	typical value (dimensionless)	meaning	reference
$R \to 1$	$4.5 \ldots 5$ μm	radius	[154, 3]
$\dot{\gamma} \to 1$	$50 \ldots 150$ Hz	shear rate	[30]
T_a	$293 \ldots 310$ K	ambient temperature	
η	$1 \ldots 3$ Pa s	viscosity	[30]
$Pe = 6\pi\eta R^3\dot{\gamma}/k_B T_a$	$(10^3 \ldots 10^5)$	Péclet number	cf. Sec. 2.2
$\Delta\rho$	50 kg/m^3	density difference	[104]
$2Rg\Delta\rho/9\eta\dot{\gamma}$	$(1 \ldots 10 \cdot 10^{-3})$	relative grav. force	cf. Sec. 2.3
κ	$10^{-5} \ldots 10^{-2}$ N/m	bond spring constant	[56, 137, 66]
$\to \kappa/6\pi\eta R\dot{\gamma}$	$(10^{-1} \ldots 10^3)$		
k_{on}	$10^3 \ldots 10^4$ Hz	on-rate	[39]
$\to \pi = k_{on}/\dot{\gamma}$	$(7. \ldots 200)$		
k_0	$0.5 \ldots 300$ Hz	unstressed off-rate	[3, 39, 129]
$\to \epsilon_0 = k_0/\dot{\gamma}$	$(6 \cdot 10^{-3} \ldots 6)$		
r_0	50 nm	capture radius	
$\to r_0/R$	(10^{-2})		
d	$0.1 \ldots 1$ μm	ligand-ligand distance	[3]
$\to d/R$	$(0.02 \ldots 0.2)$		
x_c	$2 \ldots 4 \cdot 10^{-11}$ m	reactive compliance	[3]
$\to 6\pi\eta R^2\dot{\gamma}x_c/k_B T_a$	$(0.1. \ldots 0.6)$		
N_r	$50 \ldots 5000$	Number of receptors	[84, 66, 29]
h_{min}	15 nm	minimum cell height	[14]
$\to h_{min}/R$	$(3 \cdot 10^{-3})$		

Table 4.1: Parameters used for the adhesive dynamics simulations. If no extra symbol for the dimensionless quantity is defined we use the same symbol for both the dimensional and dimensionless representation of this quantity.

rolling adhesion have a radius of about $R = 4.25$ μm [154]. For the effective hydrodynamic radius, i. e., the radius that appears in the Stokes drag coefficient $6\pi\eta R$, also the microvilli contribute, which are about 300 nm in length [137]. For the simulations in this section, we therefore use the value $R = 4.5$ μm.

The N_r receptor patches are randomly distributed on the cell surface (the random distribution is in both the 2D and the 3D version of the algorithm; in 2D, however, the receptors are only distributed on the great circle that lies in the plane whose surface normal is the y-axis). The receptor patches might be identified with cell microvilli. The range of microvilli on a leukocyte varies from several hundreds [29] up to 10,000 [84, 66]. In our 3D simulations, we use N_r up to 5,000. In our 2D simulations the values used for N_r are typically one order of magnitude smaller. Although, usually several receptors can be found on the microvilli tips, we allow only one bond per receptor patch, i. e., N_r is also the total number of receptors. Receptors and ligands are small polymers whose binding sites (that have an extension in the nm-range) diffuse constantly within some region around their linkage (cf. Sec. 2.4.1). As the diffusion constant of a nm-sized object is about three orders of magnitude larger than that of the cell itself, it would be very costly to explicitly resolve the binding sites of receptor and ligand. In the algorithm we solve this problem by introducing a capture sphere with capture radius $r_0 = 50$ nm, which is about the combined length of ligand and receptor [108, 14].

The on-rate k_{on} for bond formation from a receptor-ligand encounter in Tab. 4.1 is given in units of Hz. Experimentally, it is very difficult to determine this rate directly. As was discussed in Sec. 2.4.1, this rate can be estimated using the notion of encounter complex from the forward reaction rate k_f. Following Schwarz and Alon a forward reaction rate $k_f = 10^5$ 1/Ms can be inferred from BIAcore data of L-selectin. For a three-dimensional diffusion constant of 10^{-6} cm^2/s they then conclude that receptor-ligand binding in solution is reaction-limited, and therefore the on-rate is approximately $k_{on} = k_f k_-/k_+ = 3/(4\pi r_0^3)k_f$ (cf. Eq. (2.34)). For a capture radius of 1 nm this leads to k_{on} of the order of 10^4 Hz for L-selectin receptors [129]. As argued above the capture radius used in our algorithm is larger than 1 nm (1 nm the typical encounter distance for the *binding-sites* of ligand and receptor). Accordingly, not every encounter of receptor and ligand molecules includes an encounter of their respective binding sites. Therefore, 10^4 Hz defines an upper limit for the on-rates used in our simulations.

We consider ligands that are distributed on a square lattice with lattice constant d. Here, d is obtained from $d = \sqrt{1/N_l}$ and N_l is the average number of ligands per μm^2. In experiments done by Alon et al., N_l typically varies between $(1 - 100)/\mu$m^2 [5, 3]. When considering ligand density instead of discrete ligands, as done in simulations by the Hammer-group (e. g., [25]), the appropriate on-rate is determined by the forward reaction-rate for surface attached molecules (units of μm^2/s) multiplied with the ligand density (units of $1/\mu$m^2). Furthermore, the forward reaction rate becomes a function of the relative motion of the cell with respect to the wall, as was shown by Chang and Hammer by calculating the forward reaction rate based on the MFPT approach from a reaction-diffusion equation [27]. In our adhesive dynamics algorithm we explicitely resolve receptors and ligands in space as well as encounter duration in time. In addition, we use the approximation that both receptors and ligands are fixed at their positions (i. e., we neglect membrane diffusion, see Sec. 2.4.1). Thus, k_{on} is independent of the relative motion of the cell to the wall.

For the force dependent off-rate we have the two Bell parameters k_0, F_d, where the detachment force is $F_d = k_B T_a/x_c$ with reactive compliance x_c (cf. Sec. 2.4.2). Both, unstressed off-rate k_0 and reactive compliance x_c have been measured for different selectin bonds [5, 3]. The reactive compliance for L-selectin bonds is $x_c = 2 \cdot 10^{-11}$ m [3], this corresponds to a detachment force of 200 pN.

For closed bonds we use the linear force extension curve (cable model) explained in Sec. 2.4.3 with spring constant κ. In previous simulations of leukocyte rolling by the Hammer group values of up to 0.1 N/m have been used. For the P-selectin-PSGL-1 complex Fritz et al. [56] measured a value of $\kappa_{RL} = 5.3 \cdot 10^{-3}$ N/m. Recently, also the role of microvilli elasticity was discussed [25]. Shao et at. determined the spring constant of microvilli in the low force regime to be $\kappa_{mv} = 4.3 \cdot 10^{-5}$ N/m [137]. The total spring constant $\kappa = \kappa_{mv}\kappa_{RL}/(\kappa_{mv} + \kappa_{RL})$ of the microvilli/bond series would then be dominated by the microvilli spring constant.

Besides the bond forces, we include only the buoyant force due to the small density difference $\Delta\rho$ between the cell and the surrounding medium (cf. Sec. 2.3). Other non-specific repulsion forces arising from electrostatic and steric stabilization forces are only taken into account during the simulations in the sense that the cell can only approach the wall up to a distance of $h_{min} = 15$ nm which is about the thickness of the glycocalyx [14].

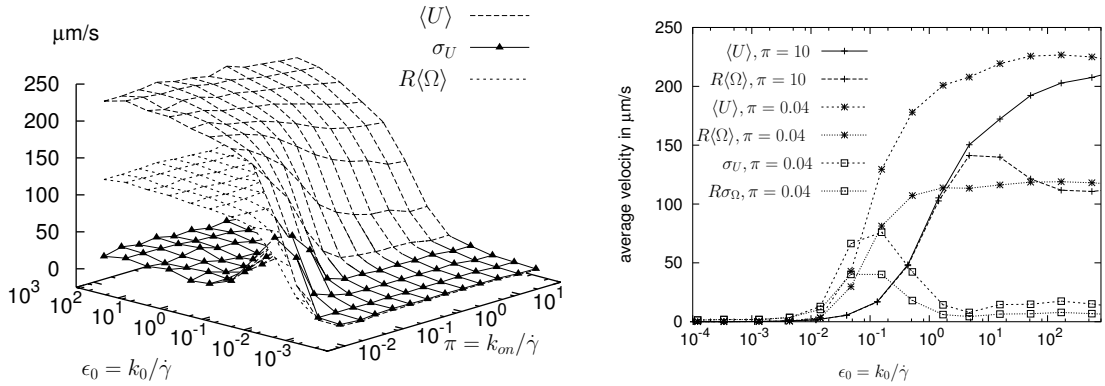

(a) (b)

Figure 4.4: (a) Mean velocity $\langle U\rangle$, its standard deviation σ_U, and mean angular velocity $R\langle\Omega\rangle$ as functions of the dimensionless rates π, ϵ_0 (in log-scale for the two horizontal axes). (b) $\langle U\rangle, R\langle\Omega\rangle, \sigma_U, \sigma_{R\Omega}$ as functions of the off-rate ϵ_0 for two different on-rates π. Parameters used for these 2D-simulations: $R = 4.5 \cdot 10^{-6}$ m, $T = 293$ K, $\dot\gamma = 100$ Hz, $\Delta\rho = 0.05 \cdot 10^3$ kg/m^3, $\eta = 1.002 \cdot 10^{-3}$ Pa s, $\kappa = 1 \cdot 10^{-3}$ N/m, $r_0 = 1.0 \cdot 10^{-2}R$, $d = 2.9 \cdot 10^{-2}R$, $N_r = 500$, $x_c = 2 \cdot 10^{-11}$ m. The average was obtained over three runs of 10 s duration.

4.2.2 Classification of states of motion

In the following the impact of some of the parameters defined in Tab. 4.1 is examined. Whether a cell is able to roll or not depends on the one hand on *external* parameters like ligand-density, shear rate and viscosity. On the other hand it depends also on the *internal* parameters of the single receptor-ligand complex which in our model are the on-rate k_{on}, the off-rate k_0 and the detachment force F_d. Fig. 4.4a shows the mean translational and angular velocity, and the standard deviation of the translational velocity $\sigma_U := \sqrt{\langle U^2\rangle - \langle U\rangle^2}$ (here the average is an average over time and an ensemble of cells) in a large range of values for the dimensionless on- and off-rate (π, ϵ_0). To further illustrate the dependence of the kinetic quantities on the on- and off-rate, in Fig. 4.4b the ϵ_0-dependence at fixed on-rate π is replotted. At $\pi = 10$, one nicely sees that with decreasing ϵ_0 translational- and angular velocities first approximate each other, i. e., U decreases and $R\Omega$ increases and then tend to zero at very low off-rates. At smaller on-rates (in the figure $\pi = 0.04$) both U and $R\Omega$ monotonically decrease with decreasing off-rate and $R\Omega \approx U$ occurs only when both quantities are close to zero. The standard deviations of the velocities $\sigma_U, \sigma_{R\Omega}$ are small for very low and very high off-rates. In between, they pass through a maximum at range of ϵ_0 where the transition from unperturbed motion to cell arrest ($U \approx R\Omega \approx 0$) occurs.

In the following we summarize these observations by defining five different classes of stationary states of cell motion (see also Tab. 4.2).

Free motion: For U_{hd} being the speed of a sphere close to the wall that moves driven by linear shear flow, but is not influenced by any non-hydrodynamic sphere-wall interaction, we call a cell to move freely if its speed is larger than 0.95 U_{hd} (an example is shown in Fig. 4.6(1)). As mentioned already in Sec. 4.1.1, the velocity in this state is often referred to as the *hydrodynamic velocity*. Free motion implies no bonds at all, however the definition given by us allows also for bonds with a very fast dissociation rate (off-rate)

state	definition
free motion	$\langle U\rangle > 0.95\ U_{hd}$
rolling adhesion	$R\langle\Omega\rangle/\langle U\rangle > 0.8$ AND $0.95 > \langle U\rangle/U_{hd} > 0.01$
firm adhesion	$\langle U\rangle < 0.01\ U_{hd}$
transient adhesion I	$0.01 < \langle U\rangle/U_{hd}$ AND $R\langle\Omega\rangle/\langle U\rangle < 0.8$ AND $\sigma_U/\langle U\rangle < 0.5$
transient adhesion II	$0.01 < \langle U\rangle/U_{hd}$ AND $R\langle\Omega\rangle/\langle U\rangle < 0.8$ AND $\sigma_U/\langle U\rangle > 0.5$

Table 4.2: Five stationary states of leukocyte motion.

or very small detachment forces. In this case existing bonds dissociate before they are stretched enough to apply forces that slow down the mean velocity of the cell below 95 % of the hydrodynamic velocity. As the hydrodynamic velocity at a given shear rate also depends on the height of the cell above the wall we determine U_{hd} at the minimal height, $z_{min} = R + h_{min}$, of the cell.

Firm adhesion (arrest): If the mean (translational) velocity is less than 1 % of the hydrodynamic velocity (Fig. 4.6(2)). This allows for small jumps due to rare dissociation events. Besides that tether bonds compensate shear force and torque (cf. Sec. 4.1.1).

Rolling adhesion: The ratio $R\langle\Omega\rangle/\langle U\rangle$ is larger than 0.8. As was shown in Sec. 2.3 this is well above the asymptotic maximum of this ratio in the limit $z \to R$ (i. e., when the cell touches the wall). Fig. 4.6(5) and Fig. 4.6(6) show two examples of numerical leukocyte rolling.

Transient adhesion: If none of these criteria applies we define the state as being transient. Within this category we distinguish two sub-classes according to the standard deviation σ_U. By $\sigma_U/\langle U\rangle < 0.5$ the first sub-class (*transient I*) is defined, otherwise the cell's motion is in the sub-class *transient II*. 'Transient I' occurs if bonds form and rupture permanently, so that they reduce the (translational) velocity considerably below the hydrodynamic velocity. But the bonds do not last long enough to increase the ratio $R\Omega/U$ above 0.8. Fig. 4.6(4) shows an example for this kind of motion. 'Transient II' is characterized by alternating periods of arrest and free motion which is illustrated in Fig. 4.6(3).

As the kinetic quantities $\langle U\rangle, \langle\Omega\rangle, \sigma_U$ vary continously with respect to π and ϵ_0, the classification given above is not unique. But it allows to clearly distinguish these states in an *on-off state diagram*, i. e., the states are in general not degenerated. Other classifications of leukocyte states have been given before. For example, in the first paper on adhesive dynamics by Hammer and Apte also five states of motion were classified [66]. But in contrast to our definition their classification is only qualitative. Later on Hammer and co-workers defined states of motion, like *free, rolling, firm adhesion*, based on the mean translational velocity only [91, 25].

4.2.3 2D state diagrams

In this section we apply the above given classification of stationary states of motion to 2D simulations of leukocyte motion. At a given set of parameter values we let the cell start at a height $z = R + r_0$. Due to the gravitational force, which drives the cell even closer to the wall, the wall ligands will be immediately be within the capture range of the cell-receptors. Then, as shown in Chapter 3, the mean time for receptor-ligand encounter is close to zero for typical ligand and receptor densities found for leukocytes. Therefore, cell-wall interactions arising from bonds are assumed to influence the cell motion for the

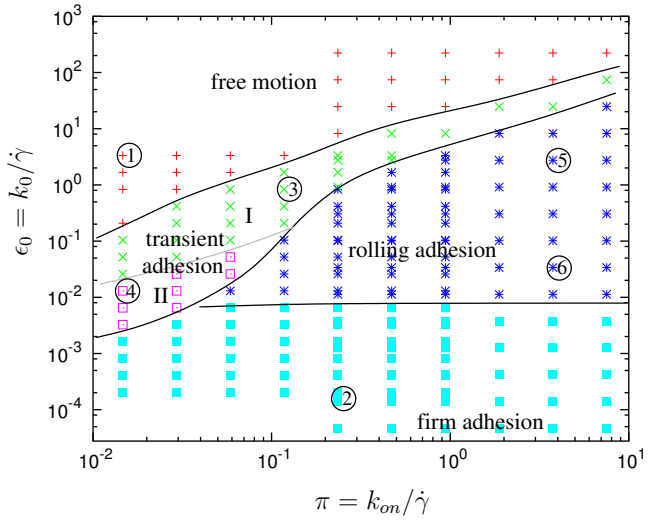

Figure 4.5: The on-off state diagram displays different stationary states of leukocyte motion obtained by 2D-simulations. The ordinate shows the dimensionless unstressed off-rate ϵ_0, the horizontal axis the dimensionless on-rate π. Snapshots for the cell velocities at the (π, ϵ_0) paramter values marked by numbered circles are shown in Fig. 4.6. Parameters used: $R = 4.5 \cdot 10^{-6}$ m, $T_a = 293$ K, $\dot{\gamma} = 150$ Hz, $\Delta\rho = 0.05 \cdot 10^3$ kg/m^3, $\eta = 1.002 \cdot 10^{-3}$ Pa s, $\kappa = 1 \cdot 10^{-2}$ N/m, $r_0 = 1.0 \cdot 10^{-2}$ R, $d = 2.9 \cdot 10^{-2}$ R, $N_r = 500$, $x_c = 2 \cdot 10^{-11}$ m.

complete run of the simulation. To nevertheless rule out any initialization effects the mean values and variances for U, Ω are only calculated for times greater than 1.8 s. The total run length of each simulation is at least 10 s. To ensure proper classification of the state of motion, the run time is extended to up to 50s if the standard deviation σ_U is large. Furthermore, each simulation run is repeated up to ten times (each time with another randomly chosen receptor distribution) and each run contributes to the mean values $\langle U \rangle, \langle \Omega \rangle$ and their standard deviations σ_U, σ_Ω. The numerical time step was chosen to be between $10^{-5} - 5 \cdot 10^{-4}$ (at a typical shear rate of $\dot{\gamma} = 100$ Hz these numerical time steps corresponds to real time steps down to 10^{-7} s. The smaller range of time steps is chosen when low ligand densities or stiff bonds (large κ) are considered (see also discussion about the time step in Sec. A.2). Keeping the other parameters fixed and varying the rates π, ϵ_0 on a grid in double logarithmic scale, we can determine the different types of leukocyte motion in an *on-off state diagram*.

Fig. 4.5 shows an example of such a state diagram. The parameters used there are listed in the figure caption (as we keep the parameters $R, T_a, \Delta\rho, r_0$ fixed for all the diagrams shown in this section, they are not explicitly listed for the following state diagrams). All five states can be identified in Fig. 4.5 and in Fig. 4.6(1-6) example trajectories for each of these phases are shown. In the limit of very large off-rates ϵ_0 the cell moves freely, i. e., no matter how frequently bonds are formed, it results from an immediate dissociation that no force on the cell can build up. At very small off-rates the cell is in the state of firm adhesion, i. e., once a bond is formed it lasts long enough to stop the cell and to allow further bonds to be formed which stabilize the cell in its rest position. In between these two limiting cases for the off-rate we find the other three states. From these the rolling state appears only for on-rates π above a certain threshold. Thus, the fast association/dissociation kinetics is responsible for some receptors (in co-operation with their ligands) to support rolling adhesion [3]. Fig. 4.5 shows the state 'transient I' over the full range of probed

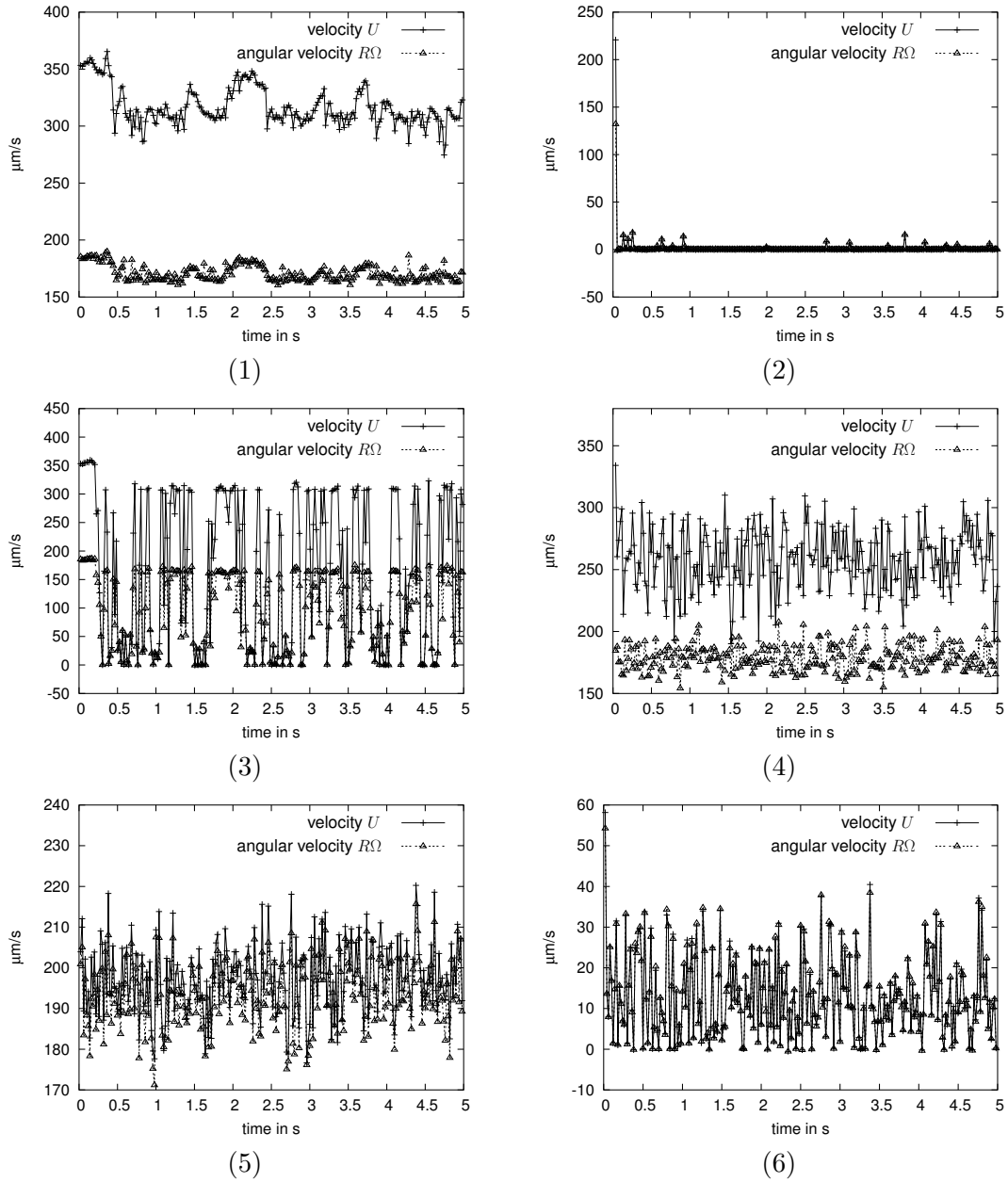

Figure 4.6: Translational and angular velocities U and $R\Omega$, respectively, that give examples of the different states of leukocyte motion defined in this section. The labels (1-6) refer to the numbered points in the state diagram shown in Fig. 4.5. (1) Free motion, (2) firm adhesion, (3) 'transient II', (4) 'transient I', (5,6) rolling adhesion.

on-rates. The off-rates at which it occurs are too large to support rolling but still too small to allow for free motion. When both on- and off-rates are small the cell is in state 'transient II'. In this state the cell stops most likely, whenever a bond is formed due to the small off-rate. This results in periods of firm adhesion. The small on-rate, however, makes it rather unlikely that bonds are formed, as can be seen in periods of free motion.

How the different parameters involved influence the border lines between the different states of motion is shown and discussed in the following. To follow the experimental

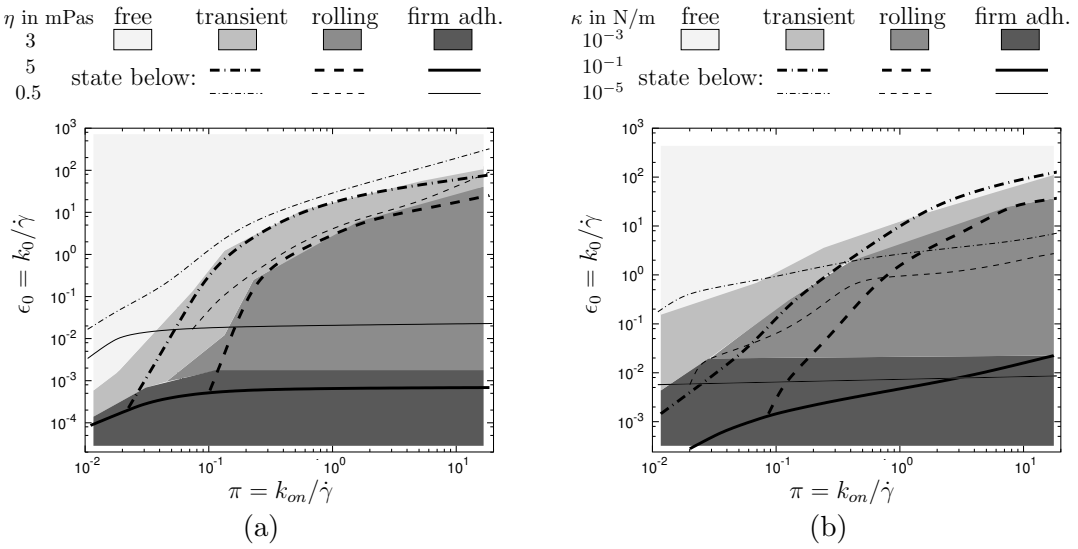

Figure 4.7: (a) On-off state diagrams for different viscosities η. The filled areas define the states of motion as determined from simulations at a reference viscosity $\eta = 3$ mPa s. The lines denote the borders between the states of motion at a lower and a higher viscosity than the reference viscosity. The thin (thick) lines refer to a viscosity $\eta = 0.5$ mPa s (5 mPa s). The figure legend tells which state is found below the corresponding line. (b) States of motion at different spring constants κ. The filled areas are the states of motion for the intermediate spring constant $\kappa = 10^{-3}$ N/m. The thin (thick) lines refer to $\kappa = 10^{-5}$ N/m ($\kappa = 10^{-1}$ N/m). (Other parameters used for simulations in both (a) and (b): $N_r = 400$, $\dot{\gamma} = 100$ Hz, $d = 2.9 \cdot 10^{-2}\ R$, $x_c = 2 \cdot 10^{-11}$ m; in (a): $\kappa = 10^{-2}$ N/m; in (b): $\eta = 1$ mPa s.)

situation we consider the effect of the original dimensional parameters and not the dimensionless parameters which appear in the algorithm. For example, we vary the viscosity which leads to a change in Pe, f, the dimensionless spring constant κ, and the value of the dimensionless detachment force F_d. But we do not vary, e. g., Pe and keep the other dimensionless parameters fixed.

The *impact of viscosity* is illustrated in Fig. 4.7a. There, the on-off diagrams for the fluid viscosities $\eta = 0.5, 3, 5$ mPa s (the viscosity of the standard medium in which leukocytes are usually perfused through flow chambers is about 1 mPa s) are shown. The border lines between different states are obtained as demonstrated by Fig. 4.5: the leukocyte motion is simulated on a grid in double logarithmic scale in the (π, ϵ_0) parameter space (for Fig. 4.7a, a $(11, 13)$-grid is used). For each point the state is then determined according to the rules given in Tab. 4.2. Finally, the lines separating two states is drawn by hand. For $\eta = 3$ mPa s the states of motion (the two transient states are treated as one state) are distinguished by areas filled with different grey scales. For $\eta = 0.5, 5$ mPa s only the border lines between two states are shown. The figure legend explains which state can be found below a given line. For the sake of clarity, the original simulation grids for the three diagrams are omitted.

Fig. 4.7a clearly shows that the main effect of increasing the viscosity is the increase in the range where rolling is possible. More precisely, the larger the viscosity, the lower the off-rate ϵ_0 at which firm adhesion sets in. This effect results from the Bell model for bond dissociation. The shear stress ($\eta\dot{\gamma}$) and the maximum force in a tether bond are

proportional to the viscosity η [2]. Therefore, an increase in viscosity increases the off-rate like

$$\epsilon = \epsilon_0 \left[\exp(F_{B,0}/F_d)\right]^{(\eta/\eta_0)},$$

with $F_{B,0}$ the bond force at viscosity η_0. Using a rough estimate for the bond force $F_{B,0} \approx \|\mathbf{F}_S\|/\cos\chi$ at the parameters used here (see Fig. 4.2 for the definition of $\mathbf{F}_S, \chi$; for the angle we estimate $\chi \approx 65°$, see discussion in Sec. 4.1.1), we have $F_{B,0}/F_d \approx 0.4$ at $\eta_0 = 0.5$ mPa s. Thus, if at some viscosity η firm adhesion occurs for off-rates smaller than a certain value ϵ_0^{firm}, i. e., for $\epsilon_0 < \epsilon_0^{firm}$, then, we expect firm adhesion for η_0 to exist at the same rate ϵ. For η_0 this rate is estimated to be $\epsilon_0^{firm} \exp(F_{B,0}/F_d)^{\eta/\eta_0 - 1}$. With $\eta/\eta_0 = 10$, we therefore expect rolling at η_0 for $\epsilon_0 > \epsilon_0^{firm}(\eta_0) \approx 30\epsilon_0^{firm}(\eta)$. A factor of 30 is indeed roughly the factor between the off-rates at the border between rolling and firm adhesion for $\eta = 5$ mPa s and $\eta_0 = 0.5$ mPa s which can be read off from Fig. 4.7a. The estimates done here suggest that the rolling state disappears at even smaller viscosities (one or two magnitudes smaller than that of water) than used in Fig. 4.7a. This is indeed observed for simulations (not shown) in this viscosity range. But one has to be very careful with predictions for this (very) low viscosity regime as the assumption of a small Reynolds number is no longer fulfilled there.

Impact of spring-constant. Fig. 4.7b shows the state diagrams for three different spring constants $\kappa_{stiff}, \kappa_{int}, \kappa_{soft} = 10^{-1}, 10^{-3}, 10^{-5}$ N/m. The intermediate spring constant κ_{int} is of the same order of magnitude as the spring constant of the P-selectin/ligand bond [56]. The softest spring constant κ_{soft} mimics the effect of soft microvilli [137]. From Fig. 4.7b we first notice that the firm adhesion state for κ_{stiff} occurs at smaller off-rates than in the case of the intermediate spring constant κ_{int}. This is most pronounced in the small on-rate region. A closer view identifies two effects that are responsible for this observation. First, the stiffness of the bond results in a small elongation which then leads to an obtuse bond-wall angle (the angle χ in Fig. 4.2). The more obtuse this angle is, the more the bond must be loaded to compensate the shear force. In addition the transport of the cell and thus also the bond extension is governed by the shear rate $\dot{\gamma}$. A stiffer bond is therefore loaded faster. Both the faster loading [43] and the larger bond force result in an effective increase of the off-rate ϵ. At larger on-rates the fast dissociation is compensated by fast binding of new bonds and rebinding of just dissociated bonds. Second, the softer the bond, the more the tethers can be elongated. Thus, bonds can exist also beyond the contact area (if they are stretched to be larger than the capture radius r_0) effectively increasing the number of receptors. On the other hand, when we compare the intermediate spring-constant κ_{int} with the soft one, κ_{soft}, we notice that the firm adhesion regions for κ_{soft} is again shifted to smaller ϵ_0. This effect results from our definition of the firm adhesion state: the bonds which basically resist the shear stress to keep the cell at rest are at the rear end of the cell (see, Sec. 4.4.1). If they dissociate they cannot rebind, as the receptor (due to the soft bond) is already far beyond the contact zone. The lack of rebinding results necessarily in a forward movement during which the remaining bonds are loaded to compensate the shear force. The length of this forward motion increases with decreasing spring constant. Thus, at the same rupture frequency the cell with the softer bonds translates slightly faster than the cell with bonds of intermediate stiffness.

In Fig. 4.8 the impact of *receptor number* and *ligand-ligand distance* is shown. In Fig. 4.8a the state diagram is given for $N_r = 50, 200, 1000$ receptors. To understand the influence of receptor number we first estimate the mean number of receptors within

[2] The maximum force is the force which holds the cell at rest, see Sec. 4.1.1.

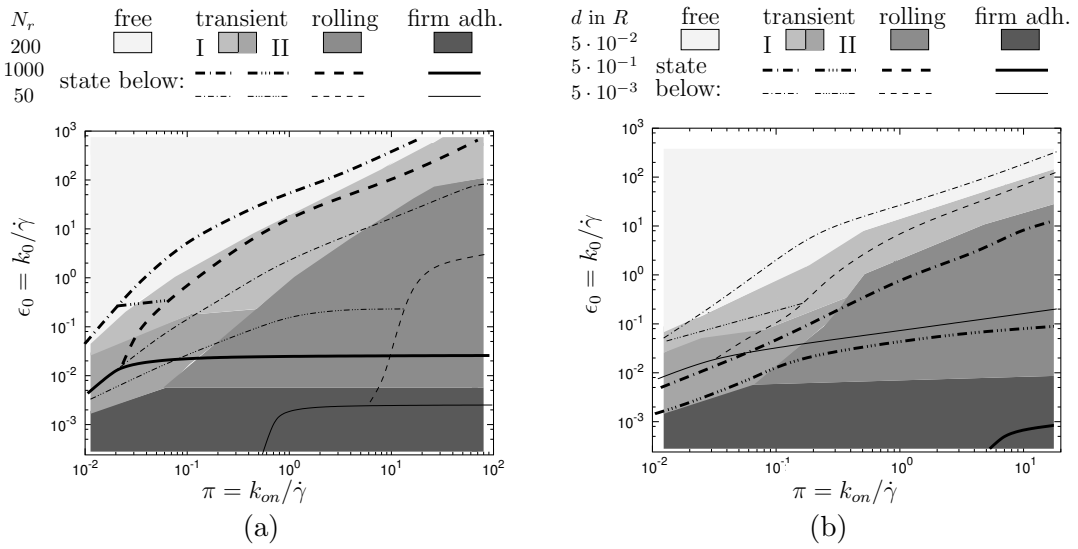

Figure 4.8: (a) On-off state diagrams for different numbers of receptors N_r. $N_r = 50$ (thin lines) $N_r = 200$ (filled areas) and $N_r = 1000$ (thick lines). (b) State diagrams for different ligand-ligand distances d. $d = 5 \cdot 10^{-3}\ R$ (thin lines) $d = 5 \cdot 10^{-2}\ R$ (filled areas) and $d = 5 \cdot 10^{-1}\ R$ (thick lines). (Other parameters used for simulations in both (a) and (b): $\kappa = 10^{-2}$ N/m, $x_c = 2 \cdot 10^{-11}$ m, $\eta = 1$ mPa s; in (a): $\dot{\gamma} = 75$ Hz, $d = 2.9 \cdot 10^{-2}$ R; in (b): $\dot{\gamma} = 100$ Hz, $N_r = 400$.)

the contact zone, which is a line in 2D. The angle 2ξ that spans this line is obtained from $2R\cos\xi = 2(R - r_0)$. As $r_0 \ll R$, one can approximate $2\xi \approx \sqrt{8r_0/R}$. Thus, the average number of receptors in the contact region is $N_{r,contact} = N_r\sqrt{2r_0/R}/\pi \approx 0.045\ N_r$. On the other hand we use $d = 2.9 \cdot 10^{-2}\ R$ for the ligand-ligand distance in Fig. 4.8a, i. e., $2R\sin\xi \approx \sqrt{8Rr_0}/d \approx 10$ ligands in the contact zone. Thus, at large receptor numbers bond formation is limited by the number of possible ligand binding sites. For $N_r = 1000$ we have $N_{r,contact} \approx 45$ and a mean receptor-receptor distance of 0.63 r_0, i. e., the capture spheres already overlap. Thus, the cell is saturated with receptors and no further enhancement of bond coupling to the wall is expected from larger receptor numbers. Indeed, measuring the mean number of bonds in the rolling region gives values around ten in accordance with the maximum number of available ligands. For $N_r = 200$ we have $N_{r,contact} \approx 9$ which is close to the number of available binding sites. However, in comparison to the $N_r = 1000$ case the regions of rolling and firm adhesion are shifted to lower off-rates. This becomes clear when noticing that the mean receptor-receptor distance is now about three times the capture radius, and therefore not every ligand is in match with a receptor (the mean number of bonds in the rolling state is five or less, i. e., only every second receptor is able to form a bond). For $N_r = 50$ we have $N_{r,contact} \approx 2.3$ and the number of bonds is limited by the number of receptors. In Fig. 4.8a we see that the states of rolling and firm adhesion are shifted to smaller off-rates and higher on-rates. Furthermore, the range in which leukocyte motion is transient is much larger than at higher N_r. The large (π, ϵ_0)-range for the transient states is a signature of few bonds being at work as we will see again when discussing the influence of ligand-ligand distance. Single tethers slow the cell down (depending on the off-rate they may either arrest the cell some while, resulting in state 'transient II', or just decelerate them resulting in state 'transient I'), but after dissociation it is unlikely that the current state of motion is supported by

further bonds. However, as long as at least two bonds are possible this effect is partly compensated at large on-rates when the probability for receptor-ligand encounter to result in a bond is high.

In Fig. 4.8b state diagrams for fixed $N_r = 400$ and three different ligand-ligand distances $d = 5 \cdot 10^{-3}\ R, 5 \cdot 10^{-2}\ R, 5 \cdot 10^{-1}\ R$ are shown. Using the same considerations as before to estimate the number of ligands $N_{l,contact}$ and receptors in the contact zone, we get $N_{l,contact} \approx 0.6, 6, 60$ for the respective d and $N_{r,contact} \approx 18$. Thus, only in the case of the smallest d the maximum number of bonds is limited by the number of receptors. In addition, the border line between the rolling and firm arrest state in this latter case is slightly tilted to go to larger ϵ_0 with increasing π. This fact emphasizes that firm adhesion may result on the one hand from small ϵ_0 and on the other hand from a large number of bonds. When firm adhesion results from a small off-rate, existing bonds keep the cell long enough at rest that new bonds can be formed, even at comparable small on-rates. At larger off-rates firm adhesion may result from a large number of bonds but only if the on-rate is large enough to compensate bond dissociation. In the extreme case, $d = 5 \cdot 10^{-1}\ R$, where ligands are diluted to be less than one in the contact zone, we notice a large increase of the (π, ϵ_0) range in which cell motion is transient similar to the above discussed case of diluted receptors. Firm adhesion is only possible for receptor-ligand pairs with a very high π and low ϵ_0. The rolling state has completely disappeared which proofs that stationary rolling is only possible by the interplay of two or more bonds.

4.2.4 3D simulations

The results shown so far are computed using the 2D version of the Stokesian dynamics algorithm (cf. Sec. 2.2). We now turn to 3D simulations. 3D simulations are of much higher computational costs for three reasons: i) In 3D we have six degrees of freedom compared to three in 2D. ii) The number of receptors and ligands in the 3D contact zone must be larger than in the 2D contact line to allow for rolling. This point will be discussed in more detail in this section. iii) In 2D it is often enough to average the velocity of a cell at a fixed set of parameters over only one run in order to determine the state of motion. In contrast, in 3D the randomly chosen receptor distribution has a much larger influence to the cell's rolling behavior than in 2D. Therefore, in general the average over more than one run (each with a different receptor distribution) is needed. Here, we choose between four and ten runs, more for large variances and less for small variances of the translational velocity, respectively.

In Fig. 4.9a the mean velocity $\langle U \rangle$, its standard deviation σ_U and the mean angular velocity $R\langle \Omega \rangle$ are shown as functions of the dimensionless on- and off-rate π and ϵ_0, respectively. The parameters for Fig. 4.9 are the same as for the analog 2D plot, Fig. 4.4, except here, for the number of receptors $N_r = 5000$ is chosen. As explained in Sec. 4.1 velocity is only well defined within a finite time interval Δt. Here, for $U\Delta t$ the sum of the projections of the sphere's movements (within each update step) on the direction of the shear flow (x-axis) is taken. Similarly, $\Omega\Delta t$ is the sum of the y-components of the angles by which the sphere is turned in each update step of the algorithm during time step Δt [3].

Despite the geometrical difference Fig. 4.4a,b and Fig. 4.9a,b look very similar. A closer look reveals some slight differences: For example at $\pi = 0.04$ the maxima of the standard deviations of the velocities in Fig. 4.9b are slightly larger than the respective values in Fig. 4.4b. For $\pi = 10$ it can be seen (Fig. 4.9b) that rolling in the sense

[3] It must be noted that $\Omega\Delta t$ is in general not equal to the y-component of the total angle by that the sphere has turned during time Δt. The difference between these angles is of the order $\mathcal{O}(\Delta t)$.

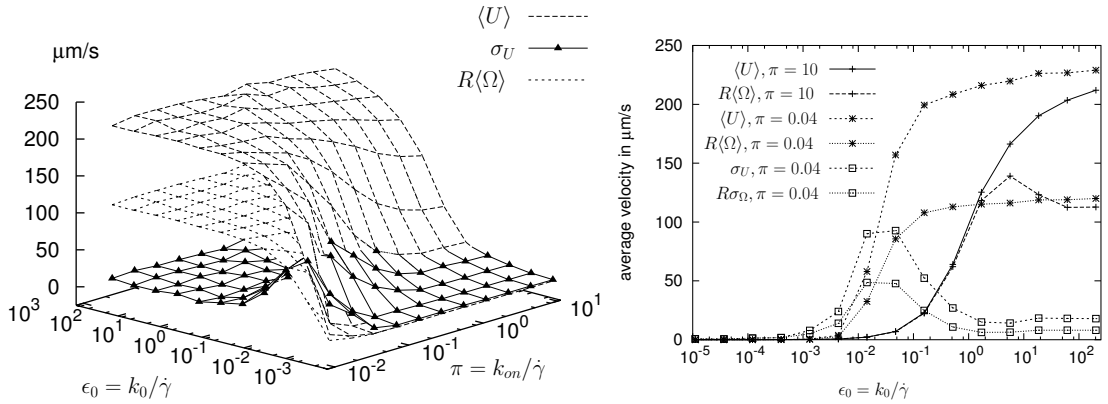

(a) (b)

Figure 4.9: 3D simulations with parameters as for the 2D simulations in Fig. 4.4, except for the number of receptors on the cell a value $N_r = 5000$ was used. (a) Mean velocity $\langle U \rangle$, its standard deviation σ_U, and mean angular velocity $R\langle\Omega\rangle$ as functions of the dimensionless rates π, ϵ_0.(b) $\langle U \rangle, R\langle\Omega\rangle, \sigma_U, \sigma_{R\Omega}$ as functions of the unstressed off-rate ϵ_0 for two different on-rates π. The average was obtained over ten runs of 20 s duration.

$R\langle\Omega\rangle/\langle U\rangle \to 1$ for off-rates smaller than a critical value occurs in 3D, too. But the approximation $R\langle\Omega\rangle/\langle U\rangle \to 1$ is somewhat more pronounced in the 2D case (Fig. 4.4b) than in the 3D case (Fig. 4.4b). This is due to the fact that in 3D tether bonds might also be located left or right of the cell's center and therefore causing rotations about an axis different from the y-axis.

Due to the similarity between 2D and 3D simulation results demonstrated by the comparison between Fig. 4.4 and Fig. 4.9, we repeat here only the discussion of the impact of *receptor number* and *ligand-ligand* distance, as these parameters strongly correlate with the considered dimension. It can easily be derived that the mean number of receptors in the contact zone is now $N_{r,contact} = N_r\ r_0/2$. The radius of the projection of the contact zone on the sphere's surface to the wall is given by the value derived for the contact line in the last section. Then, we get for the number of ligands in the contact zone $N_{l,contact} = 2\pi R r_0/d^2$. In Fig. 4.10a we have $N_r = 1000, 2500, 5000$ and $d = 5 \cdot 10^{-2} R$, i. e., in the contact zone $N_{r,contact} \approx 5, 12.5, 25$ and $N_{l,contact} \approx 25$. Therefore, the number of receptors limits the maximum number of bonds in all three cases. In addition, using the estimate for the receptor patch density on the sphere given in Sec. 3.4, $\rho_r = r_0^2 N_r/4$, we have $\rho_r < 0.125$, i. e., even for $N_r = 5000$ receptor patches, they do not cover the contact zone completely. So, not every receptor encounters a ligand, and therefore the number of tether bonds is even less than $N_{r,contact}$. In the rolling state, we actually measure an average number of 1.5, 3, 4 for $N_r = 1000, 2500, 5000$, respectively. Fig. 4.10a shows that the smaller N_r, the more are the states *rolling* and *firm adhesion* shifted to larger on-rates and smaller off-rates. Also, similar to the 2D case, the (π, ϵ_0)-range in which the cell is in the state *transient adhesion* grows with decreasing N_r.

To demonstrate the impact of ligand-ligand distance, Fig. 4.10b shows the state diagrams for $d = 5 \cdot 10^{-3}\ R, 1 \cdot 10^{-2}\ R, 5 \cdot 10^{-2}\ R$ and $N_r = 1000$. Thus, the number of ligands in the contact zone is $N_{l,contact} \approx 2500, 100, 25$ and the number of receptors $N_{r,contact} \approx 5$. Again, the number of receptors in binding range is an upper bound for the maximum number of possible bonds. From Fig. 4.10b we see that the increase of $N_{l,contact}$ from 100 to

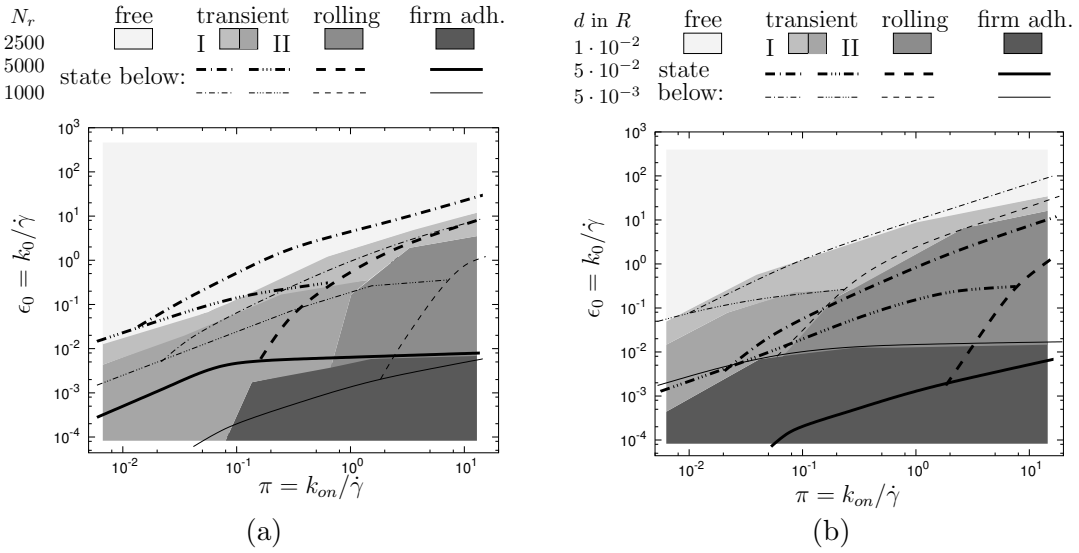

Figure 4.10: 3D on-off state diagrams. (a) For different numbers of receptors N_r. $N_r = 1000, 2500, 5000$ (thin lines, filled areas, thick lines) and $d = 5 \cdot 10^{-2}\ R$. (b) For different ligand-ligand distances d. $d = 5 \cdot 10^{-3}\ R, 1 \cdot 10^{-2}\ R, 5 \cdot 10^{-2}\ R$ (thin lines, filled areas, thick lines) and $N_r = 1000$. Other parameters for both (a) and (b): $\dot{\gamma} = 100$ Hz, $\kappa = 10^{-3}$ N/m, $x_c = 2 \cdot 10^{-11}$ m, $\eta = 1$ mPa s.

2500 has only very little influence on the state diagram, indicating that at $d = 1 \cdot 10^{-2}\ R$ the number of ligands have already reached a saturation level for $N_r = 1000$. For the average number of bonds in the *rolling state* we measure a value of about eight for both $d = 1 \cdot 10^{-2}\ R$ and $d = 5 \cdot 10^{-3} R$. The fact that this number is larger than $N_{r,contact}$ is due to the elasticity of the tethers, which allows bonds to be moved outside the contact zone. Reducing the number of ligands below the saturation level shifts the states *rolling* and *firm adhesion* to larger on- and smaller off-rates, which can be seen for $d = 5 \cdot 10^{-2}\ R$ (the configuration $N_r = 1000, d = 5 \cdot 10^{-2}\ R$ appears in both Fig. 4.10a and Fig. 4.10b).

We close this section with a general comment about a further difference between 2D and 3D simulations. Due to the dimension perpendicular to the flow direction and the wall normal it is in principle possible that two or more tethers are equally loaded in 3D as was suggested in Refs. [129]. Consequently, they share the load and thus the force enhancement of the off-rate as given by the Bell equation Eq. (2.37) is reduced. This effect stabilizes rolling against increasing shear forces. However, for the ligand densities and receptor numbers discussed here, we measure an average number of tether bonds of less than ten. At this small number it is not very likely that two tethers are actually located such that they can equally share the shear force. So this effect becomes more important at higher ligand and receptor densities.

4.3 A simple on-off model for the state diagram

The mean translational velocity $\langle U \rangle$ as a function of the rates π, ϵ_0 shows qualitative agreement in both 2D and 3D simulations (cf. Fig. 4.4a and Fig. 4.9a). Moreover, the state diagrams show a certain generic appearance over a large range of parameters. In this section we introduce and solve a simple model which demonstrates how bond dynamics results in these phases.

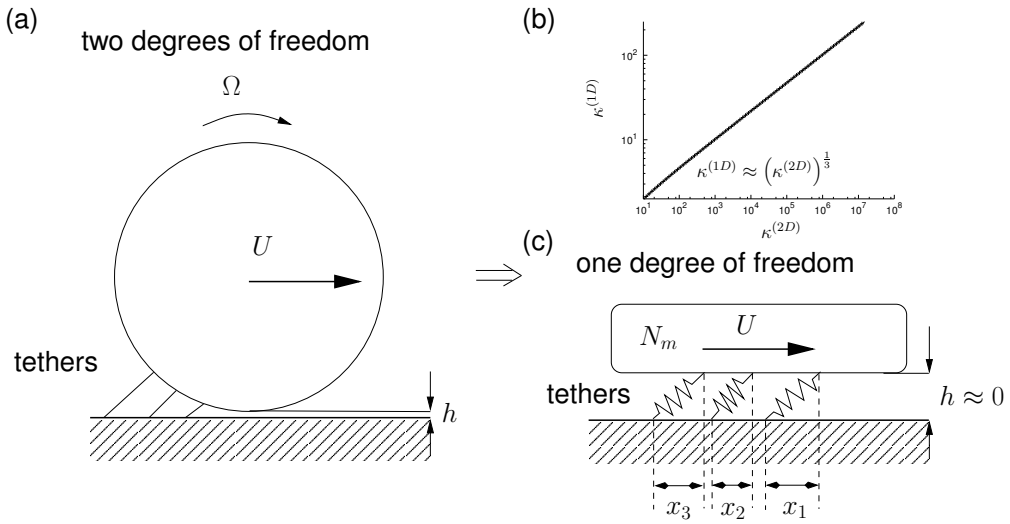

Figure 4.11: Reduction from two degrees of freedom illustrated in (a) with velocities U and Ω to one degree of freedom in (c). (c) Shows the model we use for the setup of a master equation: An object that moves in horizontal direction with velocity U. Spring-like bonds (N_m at maximum) reduce U. (b) The plot shows, how the (dimensionless) spring constant of the simple model ($\kappa^{(1D)}$) is related to the spring constant used in the simulations ($\kappa^{(2D)}$).

4.3.1 Model definition

Neglecting contributions from Brownian motion the translational and angular velocities of the cell at given height z and shear rate $\dot{\gamma}$ are completely determined by the tether forces as given by Eq. (2.15). Considering the 2D projection and the harmonic bond model, the tether force itself is determined by tether extension and tether angle relative to the wall (cf. Fig. 4.2). On a more abstract level the current states of all receptors determine the state of motion of the cell. The state of a receptor is either "off" or "on", where the receptor's on-state is specified by a pair of numbers (x_b, χ) for the bond extension x_b and the tether to wall angle χ, respectively. Given the joint probability density function for all receptors being in a certain state would then provide a solution to our problem, as the velocities could then be calculated as expectation values with respect to this probability distribution.

We will now calculate such probability density functions. However, we do not do this in the context of our original model which involves two degrees of freedom for each receptor, but in a simplified *on-off model* with only one degree of freedom per receptor. The on-off model under consideration is inspired by work of Urbakh et al. [52] and illustrated in Fig. 4.11. Ref. [52] describes sliding friction between two parallel plates, one moving relative to the other due to a driving force. There, sliding friction is modeled by dynamical formation and rupture of molecular bonds, and the relative motion between the plates is numerically simulated. Besides the work of Urbakh et al., there is a large tradition on such sliding friction models returning back to the 1960s, e. g., by Schallamach [122, 123].

As shown in Fig. 4.11c, in our model we consider an object moving with velocity U parallel to the wall. Bonds between this object and the wall can be formed which slow the object down. We assume that the height of the object above the wall h is small against a typical bond extension. Then, the force exerted by the ith closed bond is $F_B^i = -\kappa x_i$. When the maximum number of bonds is N_m the object's velocity in the over-damped

limit, with mobility coefficient μ, is

$$U(x_b) = U_0 - \mu\kappa x_b, \qquad x_b = \sum_{i=1}^{N_m} q_i x_i, \tag{4.14}$$

where q_i is one if the respective bond is closed and zero otherwise.

It must be noted that Eq. (4.14) cannot be inferred from Eq. (4.1) by projection on the translational degree of freedom. In fact, if we fix $R\theta = \phi x, \phi \in]0,1[$ (with initially $x = \theta = 0$) the first component of Eq. (4.1) reads ($z \approx R$)

$$\dot{x} = b_1 - \kappa(1-\phi)(\mathsf{A}_{11} - R\mathsf{A}_{12})x - \kappa\left(\frac{\phi}{6}\mathsf{A}_{11} + R\mathsf{A}_{12}\frac{\phi^2}{2}\left(1-\frac{\phi}{3}\right)\right)\frac{x^3}{R^2} + \mathcal{O}(x^4).$$

As we have shown in Sec. 4.1.1 most of the time during rolling process $\phi \approx 1$ and the term $\propto x^3$ becomes dominant in contrast to the proposed form of Eq. (4.14). In order to provide nevertheless some comparability with the original model shown in Fig. 4.11a we use an effective spring constant $\kappa^{(1D)}$, which is obtained in the following way: for a given spring-constant $\kappa^{(2D)}$ we numerically integrate Eq. (4.14) until the cell is stopped by a single bond and measure x_∞, F_∞. Then, we define the spring constant for our on-off model as $\kappa^{(1D)} = F_\infty/x_\infty|_{\kappa^{(2D)}}$. In other words we linearly interpolate the force-extension curve in the stop-process between the start and the end point. The correspondence is shown in Fig. 4.11b, it turns out that for the dimensionless quantities $\kappa^{(1D)} \approx (\kappa^{(2D)})^{1/3}$ holds. Furthermore, we use $\mu = \mu^{tt}_{xx}$ for the mobility coefficient (cf. Eq. (2.16)).

We nondimensionalize time by U_0/R, length by R. The model consists then of four dimensionless parameters $\hat{\mu} = \mu\kappa R/U_0, \hat{\pi} = \pi R/U_0, \hat{\epsilon} = \epsilon R/U_0$, and N_m. In the following we skip the hat for non-dimensionless quantities, Eq. (4.14) reads then $U(x_b) = 1 - \mu x_b$.

Master equation and transition rates

The state of the system is characterized by the number of closed bonds and the respective extensions of these bonds. In the following we set up a master equation for the probability density functions $p_i(x_1, \ldots, x_i)$ of the system to have i closed bonds with extensions $x_1, \ldots, x_i$. As the four parameters of our model do not change with time the system will reach a stationary state. After some initialization, the probability density functions will therefore not explicitly depend on time and the stationary master equation for the probability density function of the j-bond state reads [157]

$$\sum_{i=0}^{N_m} \int d\mathbf{x}'_i \left[\mathcal{W}(\mathbf{x}_j|\mathbf{x}'_i)p_i(\mathbf{x}'_i) - \mathcal{W}(\mathbf{x}'_i|\mathbf{x}_j)p_j(\mathbf{x}_j)\right] = 0,$$

with $\mathbf{x}_i := (x_1, \ldots, x_i)$ and $j = 0, \ldots, N_m$. $\mathcal{W}(\mathbf{x}_i|\mathbf{x}_j)$ is the transition probability per unit time from j-bond state $\mathbf{x}_j$ to i-bond state $\mathbf{x}_i$. In our model two kinds of transitions exist: i) discrete transition form j to i due to bond formation and rupture, respectively, and ii) a drift with velocity $U(x_1 + \ldots + x_j)$ for each closed bond. In the following we separate these two transitions by defining a transition rate $W(\mathbf{x}_i|\mathbf{x}'_j)$ through

$$\mathcal{W}(\mathbf{x}_i|\mathbf{x}'_j) = W(\mathbf{x}_i|\mathbf{x}'_j) + \delta_{ij}U(x'_1 + \ldots + x'_j)\sum_{k=1}^{j}\frac{\partial}{\partial x'_k}\delta^{(j)}(\mathbf{x}'_j - \mathbf{x}_i),$$

with δ_{ij} the Kronecker symbol and $\delta^{(i)}(\mathbf{x}_i)$ the i-dimensional Dirac delta function. The master equation then becomes

$$\sum_{k=1}^{j} \partial_k \left[U(x_{b,j}) p_j(\mathbf{x}_j)\right] = \sum_{i=0}^{N_m} \int d\mathbf{x}_i' \left[W(\mathbf{x}_j|\mathbf{x}_i') p_i(\mathbf{x}_i') - W(\mathbf{x}_i'|\mathbf{x}_j) p_j(\mathbf{x}_j)\right], \tag{4.15}$$

with the shorthand notations $\partial_k := \frac{\partial}{\partial x_k}$ and $x_{b,j} := x_1 + \ldots + x_j$. Next, we specify the transition rates $W(\mathbf{x}_i|\mathbf{x}_j')$. The probability for one transition event within a short time interval Δt is of order $\mathcal{O}(\Delta t)$, whereas the probability for two or more transition events is of the order $\mathcal{O}(\Delta t^2)$. Such a process is called a "one-step process" [157]. Therefore, the transition rates are only different from zero for transitions between two adjacent states, i. e., for either one bond formation or one rupture event. From the i-bond state to the j-bond state the transition rate is given by

$$W(\mathbf{x}_i|\mathbf{x}_j') = \delta_{ij-1} \sum_{k=1}^{j} \epsilon(x_k') \delta^{(i)}(\mathbf{x}_i - \mathbf{x}_{j,-k}') + \delta_{ij+1} \frac{\pi_j}{i} \sum_{k=1}^{i} \delta^{(i)}(\mathbf{x}_i - \mathbf{x}_{j,+k}'), \tag{4.16}$$

with the shorthand notation $\mathbf{x}_{j,-k} := (x_1, \ldots, x_{k-1}, x_{k+1}, \ldots, x_j)$ and $\mathbf{x}_{j,+k} := (x_1, \ldots, x_{k-1}, 0, x_k, \ldots, x_j)$. The first term in Eq. (4.16) expresses rupture transitions where for now we allow for an off-rate $\epsilon(x)$ that is force (κx) dependent like in the Bell model Eq. (2.37). The second term in Eq. (4.16) expresses bond formation events. The on-rates are $\pi_i := (N_m - i)\pi$, i. e., all non-closed receptors may form a bond with equal probability per time. The normalized sum $1/i \sum_{k=1}^{i}$ stands for formal reasons and ensures that the probability densities will be symmetric under bond permutations, e. g., $p_2(x_1, x_2) = p_2(x_2, x_1)$. The δ-functions in Eq. (4.16) ensure that i) the bond's initial extension after formation is always zero, and ii) transition events change only one bond at a time.

Inserting the transition rates Eq. (4.16) into the master equation Eq. (4.15) we get a set of N_m differential equations and one algebraic equation for the probability density functions $p_i(\mathbf{x}_i), i = 0, \ldots, N_m$:

$$0 = -\pi_0 p_0 + \int dx_1 \epsilon(x_1) p_1(x_1), \tag{4.17}$$

$$\sum_{k=1}^{i} \partial_k \left[U(x_{b,i}) p_i(\mathbf{x}_i)\right] = -\left(\pi_i + \sum_{k=1}^{i} \epsilon(x_k)\right) p_i(\mathbf{x}_i) + \sum_{k=1}^{i+1} \int dx_k \epsilon(x_k) p_{i+1}(\mathbf{x}_i, x_k), \quad i = 1 \ldots N_m - 1, \tag{4.18}$$

$$\sum_{k=1}^{N_m} \partial_k \left[U(x_{b,N_m}) p_{N_m}(\mathbf{x}_{N_m})\right] = -\sum_{k=1}^{N_m} \epsilon(x_k) p_{N_m}(\mathbf{x}_{N_m}). \tag{4.19}$$

The support of the probability density functions $p_i(\mathbf{x}_i), i = 1, \ldots, N_m$ is the simplex $S_i = \{\mathbf{x} \in \mathbb{R}^i | x_j > 0, j = 1, \ldots, i; x_1 + \ldots + x_i < x_{b,max}\}$. Here $x_{b,max}$ is the maximum possible total bond extension, which can be obtained from $U(x_{b,max}) = 0$. In the form written, Eq. (4.18) and Eq. (4.19) are partial differential equations. However, as all closed bonds drift by the same amount per time, there is only one independent dynamical variable and one can perform a coordinate transformation, that transforms Eq. (4.18) and Eq. (4.19) into N_m first order ordinary differential equations, which can be solved by standard methods (see Sec. D.1).

The probability that i closed bonds exist is $P_i := \int d\mathbf{x}_i p_i(\mathbf{x}_i)$. The stationary state, we are focusing on, is characterized by

$$\pi_i P_i = \sum_{k=1}^{i+1} \int d\mathbf{x}_i \int dx_k \epsilon(x_k) p_{i+1}(\mathbf{x}_i, x_k), \qquad i = 0, \ldots, N_m - 1, \tag{4.20}$$

i. e., the average number of rupture events is equal to the number of bond formations per unit time. The N_m conditions Eq. (4.20) together with the normalization condition

$$\sum_{i=0}^{N_m} P_i = 1, \tag{4.21}$$

provide N_m+1 boundary conditions needed to solve Eqs. (4.17 - 4.19) for $p_i, i = 0, \ldots, N_m$.

4.3.2 Solution for constant off-rates

In Appendix D.1 it is shown, how the general solution to Eqs. (4.18 - 4.19) with force dependent off-rates can be integrated. It turns out that using the Bell model (or even the linear approximation to the Bell equation), the formal integral solutions can only be evaluated with high numerical effort. This masks the mechanism at work leading to the typical appearance of the on-off state diagrams discussed in Sec. 4.2. Therefore, we discuss here only the solution for the simplest case of force independent off-rates: $\epsilon(x) \equiv \epsilon_0$. In the Bell model this corresponds to the limit of large detachment forces: $F_d \gg \kappa x$.

For the solution of the i-bond state we then make the following ansatz

$$p_i(\mathbf{x}_i) = \sum_{j=0}^{N_m - i} a(i,j) \left[\prod_{k=0}^{i-1} \mu(\nu_{i+j} + j + k) \right] (U(x_{b,i}))^{\nu_{i+j} - 1 + j}, \tag{4.22}$$

with the constants $a(i,j), i = 1, \ldots, N_m,\ j = 0, \ldots, N_m - i$ and $\nu_i, i = 1, \ldots, N_m$ that have to be determined by inserting the ansatz into Eqs. (4.18 - 4.19). As shown in the Appendix D.2 this leads to

$$\nu_i = \frac{\pi_i + i\epsilon_0}{i\mu}, \qquad i = 1, \ldots, N_m \tag{4.23}$$

and for $i = 1, \ldots, N_m; j = 0, \ldots, N_m - i$:

$$a(i,j) = a(i+j,0) \prod_{k=0}^{j-1} \frac{(i+1+k)\epsilon_0}{\mu(i+k)(\nu_{i+k} + k - j - \nu_{i+j})}, \text{ if } \forall j \ \ \nu_{i+j} + j \neq \nu_i, \tag{4.24}$$

otherwise, if a j exists such that $\nu_{i+j} + j = \nu_i$, one has to set $a(i-k, j+k) \equiv 0$ for $k = 0, \ldots, j-1$. So far, only the coefficients $a(i,0), i = 1, \ldots, N_m$ are undetermined. In the representation, Eq. (4.22), the total probability for the i-bond state reads

$$P_i = \sum_{j=0}^{N_m - i} a(i,j) = \sum_{j=0}^{N_m - i} a(i+j,0) \prod_{k=0}^{j-1} \frac{(i+1+k)\epsilon_0}{\mu(i+k)(\nu_{i+k} + k - j - \nu_{i+j})}. \tag{4.25}$$

These are N_m equations expressing the coefficients $a(i,0), i = 1, \ldots, N_m$ in terms of the N_m total i-bond state probabilities P_i which itself are determined from the stationary

state and normalization condition Eq. (4.20) and Eq. (4.21), respectively. The latter lead to

$$P_0 = \left[1 + \sum_{i=0}^{N_m-1} \prod_{j=0}^{i} \frac{\pi_j}{(j+1)\epsilon_0}\right]^{-1} = \left(\frac{\epsilon_0}{\epsilon_0+\pi}\right)^{N_m},$$
$$P_i = P_0 \prod_{j=0}^{i-1} \frac{\pi_j}{(j+1)\epsilon_0} = \frac{\binom{N_m}{i}\epsilon_0^{N_m-i}\pi^i}{(\epsilon_0+\pi)^{N_m}}. \tag{4.26}$$

The linear system of equations Eq. (4.25) is already in triangular form. Therefore, it is straightforward to solve it for $a(i,0), i = 1,\ldots,N_m$ in a recursive manner starting with $a(N_m,0)$.

Expectation values for the moments of velocity

With these results at hand we can now follow our original intention, i. e., the computation of the mean velocity and its standard deviation. Using the representation Eq. (4.22) we obtain for the mth moment of the velocity:

$$\langle U^m\rangle = P_0 + \sum_{i=1}^{N_m} \int d\mathbf{x}_i\, p_i(\mathbf{x}_i)(U(x_{b,i}))^m = P_0 + \sum_{i=1}^{N_m}\sum_{j=0}^{N_m-i} a(i,j) \prod_{k=0}^{i-1} \frac{\nu_{i+j}+j+k}{\nu_{i+j}+j+k+m}.$$

Using Eq. (4.24) and the inversion of Eq. (4.25) it is then straightforward to explicitly evaluate this expression. For the case of one receptor, $N_m = 1$, we have

$$\langle U^m\rangle_{N_m=1} = \left(P_0 + \frac{\nu_1}{\nu_1+m}P_1\right) = \left(P_0 + \frac{\epsilon_0}{\epsilon_0+\mu m}P_1\right) = \frac{\epsilon_0}{\pi+\epsilon_0}\left(1+\frac{\pi}{\epsilon_0+\mu m}\right).$$

For $N_m = 2$ the mth velocity moment reads:

$$\langle U^m\rangle_{N_m=2} = \frac{\epsilon_0}{(\epsilon_0+\pi)^2}\left[\epsilon_0 + \frac{2\pi(\epsilon_0+\pi)}{\epsilon_0+\pi+\mu m} + \pi^2\frac{(\epsilon_0+\mu)(\epsilon_0+\pi+\mu m) - 2m\mu(\epsilon_0+\mu m)}{(\epsilon_0+\pi+\mu m)(\epsilon_0+\mu+\mu m)(\epsilon_0+\mu m)}\right].$$

So, we obtain the mean velocity $\langle U\rangle$ for $m = 1$, and its variance $\sigma_U^2 = \langle U^2\rangle - \langle U\rangle^2$ for $m = 1, 2$.

4.3.3 Discussion and comparison to simulation-results

Fig. 4.12a shows the mean velocity $\langle U\rangle$ as a function of the on- and off-rate π and ϵ_0, respectively. A qualitative accordance with the analog 2D and 3D simulation results (cf. Fig. 4.4a, Fig. 4.9a.) can be easily seen: $\langle U\rangle$ goes through a transition from $\langle U\rangle \approx 1$ to $\langle U\rangle \approx 0$ with decreasing off-rates. The transition-range is shifted to smaller off-rates with decreasing on-rates. Within this transition σ_U has a maximum with respect to ϵ_0 which is the larger the smaller the on-rates are.

In the following we argue that this qualitative description of Fig. 4.12a holds in general for arbitrary $N_m \in \{1,2,3,\ldots\}$. In the limit $\epsilon_0 \to 0$, i. e., when a closed bond will never rupture, the stationary probability of i closed bonds becomes zero for $i = 0,\ldots,N_m-1$ and one for $i = N_m$, see Eq. (4.26). Then, also the coefficients $a(i,j)$ are zero except for $a(N_m,0)$ which is one. Therefore, in this limit, the moments of the velocity become

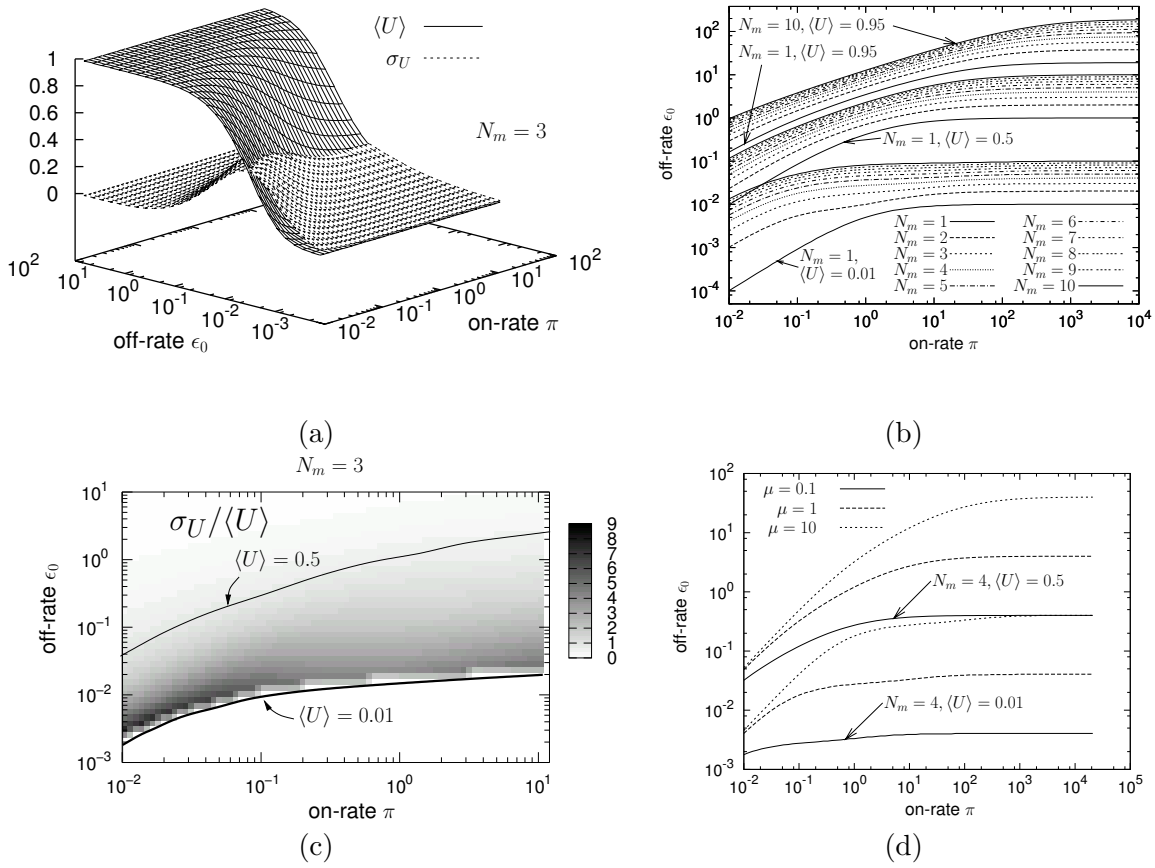

Figure 4.12: Results from the *on-off model*. (a) Mean velocity $\langle U\rangle$ and its variance σ_U as a function of the on-rate π and the off-rate ϵ_0 analog to Fig. 4.4a and Fig. 4.9a. (b) Lines of constant $\langle U\rangle$ with $\langle U\rangle = 0.01, 0.5, 0.95$ for different maximum numbers of tethers N_m. (c) For $N_m = 3$, density plot of $\sigma_U/\langle U\rangle$ for $\langle U\rangle > 0.01$. (d) Lines of constant $\langle U\rangle$ for $\langle U\rangle = 0.01, 0.5$, $N_m = 4$ and different values of the mobility coefficient μ: $\mu = 0.1, 1, 10$.

$\langle U^m\rangle \to \delta_{m0}$. Especially for $m = 1$, $\langle U\rangle = 0$, i. e., the object under consideration is not moving at all. In the other limit $\epsilon_0 \to \infty$, i. e., when closed bonds will rupture instantaneously, the probability for i closed bonds becomes $P_i = \delta_{i0}, i = 0, \ldots, N_m$. Therefore, $\langle U^m\rangle = 1, \forall m \in \{0, 1, 2, \ldots\}$ and the object moves as if no receptors were existing. The same is true in the limit $\pi \to 0$. For $\pi \to \infty$, $P_i = \delta_{iN_m}$ as for $\epsilon_0 = 0$. In contrast to the case of zero off-rate, $\langle U\rangle$ is not zero in general but still a function of the off-rate:

$$\lim_{\pi\to\infty}\langle U^m\rangle = \prod_{k=0}^{N_m-1}\frac{\epsilon_0 + k\mu}{\epsilon_0 + (k+m)\mu} = \frac{\Gamma(\epsilon_0/\mu + N_m)\Gamma(\epsilon_0/\mu + m)}{\Gamma(\epsilon_0/\mu)\Gamma(\epsilon_0/\mu + m + N_m)}, \tag{4.27}$$

with the gamma-function $\Gamma(x+1) = x\Gamma(x)$ [7]. For the variance $\sigma_U^2 = \langle U^2\rangle - \langle U\rangle^2 \geq 0$ and $\sigma_U^2 \leq 1$ holds true for all π, ϵ_0. With the statements given above, we get $\sigma_U^2 = 0$ in the limits $\epsilon_0 \to 0, \epsilon_0 \to \infty$. Therefore, the standard deviation σ_U exhibits a maximum along the transition from $\langle U\rangle = 1$ to $\langle U\rangle = 0$.

The definition of all five states of motion given in Sec. 4.2.2 cannot be applied to the

results of this model, as we deal with only one degree of freedom here, and rolling is not well defined. Fig. 4.12b shows lines of constant $\langle U \rangle$ for $N_m = 1, \ldots, 10$. The asymptotic limit for large π of these lines is implicitly given by Eq. (4.27). The region of ϵ_0 larger than the implicitly defined value $\epsilon_0(\langle U \rangle = 0.95, \pi)$ can be identified with the state *free motion*. Similar, in the region $\epsilon_0 < \epsilon_0(\langle U \rangle = 0.01, \pi)$ the object under consideration is in state *firm adhesion*. In between, along the line $\epsilon_0 = \epsilon_0(\langle U \rangle = 0.5, \pi)$, are the states rolling and transient adhesion located. Fig. 4.12c shows a density plot of $\sigma_U/\langle U \rangle$ for $\langle U \rangle > 0.01$. It can be seen that the smaller the on- and off-rates are, the larger $\sigma_U/\langle U \rangle$ which indicates the existence of the state *transient adhesion II* in the bottom-left corner of the simulation state diagrams.

Larger N_m result in a shift of the lines of constant $\langle U \rangle$ to larger off-rates. The same qualitative behavior was observed in Fig. 4.8a,b and Fig. 4.10a,b, where the impact of ligand density and receptor number in 2D and 3D was illustrated. For $m = 1$, Eq. (4.27) can be solved for ϵ_0:

$$\lim_{\pi \to \infty} \langle U^m \rangle = \frac{\epsilon_0}{\epsilon_0 + \mu N_m} \Rightarrow \epsilon_0(\langle U \rangle = U)|_{\pi \to \infty} = \frac{\mu U N_m}{1 - U}.$$

Thus, for $N_m \to \infty$ the asymptotic lines of constant $\langle U \rangle$ are shifted to $\epsilon_0 \to \infty$. That means for an infinite number of bonds the mean velocity is zero for all finite off-rates.

The influence of the fourth parameter of our model μ is shown in Fig. 4.12d. According to the definition of μ it depends on viscosity η and spring constant $\kappa^{(1D)}$ as $\mu \propto \kappa^{(1D)}/\eta$. For example for the viscosity of water and soft bonds with $\kappa^{(2D)} = 10^{-5}$ N/m, one has $\mu = 0.25$, for the same viscosity but stiff bonds $\kappa^{(2D)} = 10^{-1}$ N/m one gets $\mu = 5.5$ (both at $\dot{\gamma} = 100$ Hz) using the relation given in Fig. 4.11. Fig. 4.12d shows that the lines of constant $\langle U \rangle$ are shifted to larger off-rates with increasing μ. Comparing this to the influence of viscosity in the 2D simulations (cf. Fig. 4.7a) we note that there the line of $\langle U \rangle = 0.01$ is shifted to smaller off-rates with increasing viscosity (i. e., decreasing μ), too. However, in Fig. 4.7a this effect occurred due to a completely different reason, which we identified as a consequence of the Bell model. Also the shift of lines of constant $\langle U \rangle$ in Fig. 4.7b due to changes in the spring constant is different from the one predicted by the model. The failure of our simplified on-off model to give qualitatively correct predictions with respect to to a change in μ is a consequence of not taking the Bell model into account. Both, viscosity (via the maximum bond force) and spring constant (via the initial loading rate) couple in the Bell equation to the off-rate. Another effect, which is not taken into account by the simplified on-off model, is that for soft tether bonds the mean number of closed bonds can be larger than the mean number of receptors located in the contact zone.

In summary, the on-off (sliding) model considered here is not able to predict rolling and neglects all non-linear effects arising from the bond force acting on a sphere. Nevertheless, the mean velocity in terms of the on- and off-rate obtained from this on-off model exhibits the same generic features as the mean velocity curves obtained from adhesive dynamics simulations.

4.4 Robustness of rolling

4.4.1 Force distribution

In contrast to the assumptions of the simple on-off model it is not equally likely for every bond to rupture. In fact, from the Bell model it follows that the more a bond is stretched the more likely it will rupture. Due to the rolling process and the curvature of the cell

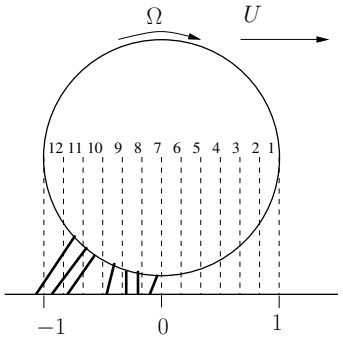

Figure 4.13: The force distribution is measured relative to the center of the cell. The bottom half circle on the cell surface is divided into L_b parts of equal length (bins) w. r. t. the wall projection of this line (e. g., in the figure $L_b = 12$). Six tether bonds are shown at some instant of time. The force from each of these bonds contributes to the bin in which the attachment point of the cell receptor lies. As the sphere moves with U, Ω a bond may contribute to another bin at the next time step.

the bonds carrying the highest load are expected to be located at the rear end of the cell. To quantitatively confirm this expectation, here, we present the results of numerical measurements of the stationary force distribution relative to the cell center using the 2D version of our adhesive dynamics algorithm.

For the force measurements we divide the projection line of the lower part of the sphere onto the boundary wall into L_b parts of equal length, see Fig. 4.13. In the following we will refer to these L_b parts as *bins*. Then, average quantities for the force are obtained as explained in the following. At each time step Δt during a simulation run the x and z-component of the bond force $F_{B,x}$ and $F_{B,z}$, respectively, are added up for each bin. This leads to the discrete version of the time integral over the bond force in each bin:

$$\sum_{\{\Delta t\}} F^i_{B,x} \approx \int_0^{T_{sim}} \mathrm{d}t F^i_{B,x}(t), \qquad \sum_{\{\Delta t\}} F^i_{B,z} \approx \int_0^{T_{sim}} \mathrm{d}t F^i_{B,z}(t), \qquad i = 1, \ldots, L_b, \tag{4.28}$$

where T_{sim} is the length of the simulation run, the superscript i stands for the ith bin, and $\{\Delta t\}$ denotes the set of all time steps during one simulation run. The force from a tether bond is accounted for a certain bin if the corresponding receptor on the cell surface lies in this bin. So, in principal (depending on the width of the bins) it is possible that more than one bond lies in a bin at a certain time. Due to curvature effects this may happen especially at the rear end of the cell.

From this the time-averaged force (denoted with a bar) in each bin is obtained as

$$\bar{F}^i_{B,x} := \frac{1}{T_{sim}} \int_0^{T_{sim}} \mathrm{d}t F^i_{B,x}(t), \quad \bar{F}^i_{B,z} := \frac{1}{T_{sim}} \int_0^{T_{sim}} \mathrm{d}t F^i_{B,z}(t), \quad i = 1, \ldots, L_b. \tag{4.29}$$

As we keep all parameters fixed, for long enough simulation times T_{sim} these averages define stationary force density distributions $f_{B,x}(x), f_{B,z}(x)$ relative to the sphere center, with

$$f_{B,x}(x) := \bar{F}^i_{B,x} \frac{2}{L_b}, \quad f_{B,z}(x) := \bar{F}^i_{B,z} \frac{2}{L_b}, \quad i = [0.5 L_b(1-x)], \quad x \in [-1, 1], \tag{4.30}$$

where the Gauss bracket $[x]$ denotes the largest integer less than x.

Results for the above defined quantities are shown in Fig. 4.14. There, the same parameters as for the state diagram in Fig. 4.5 are used. The on-rate and unstressed off-rate π and ϵ_0, respectively, are chosen such that the cell is in the stationary rolling state. Fig. 4.14a shows the stationary force distribution for the x-component of the tether force

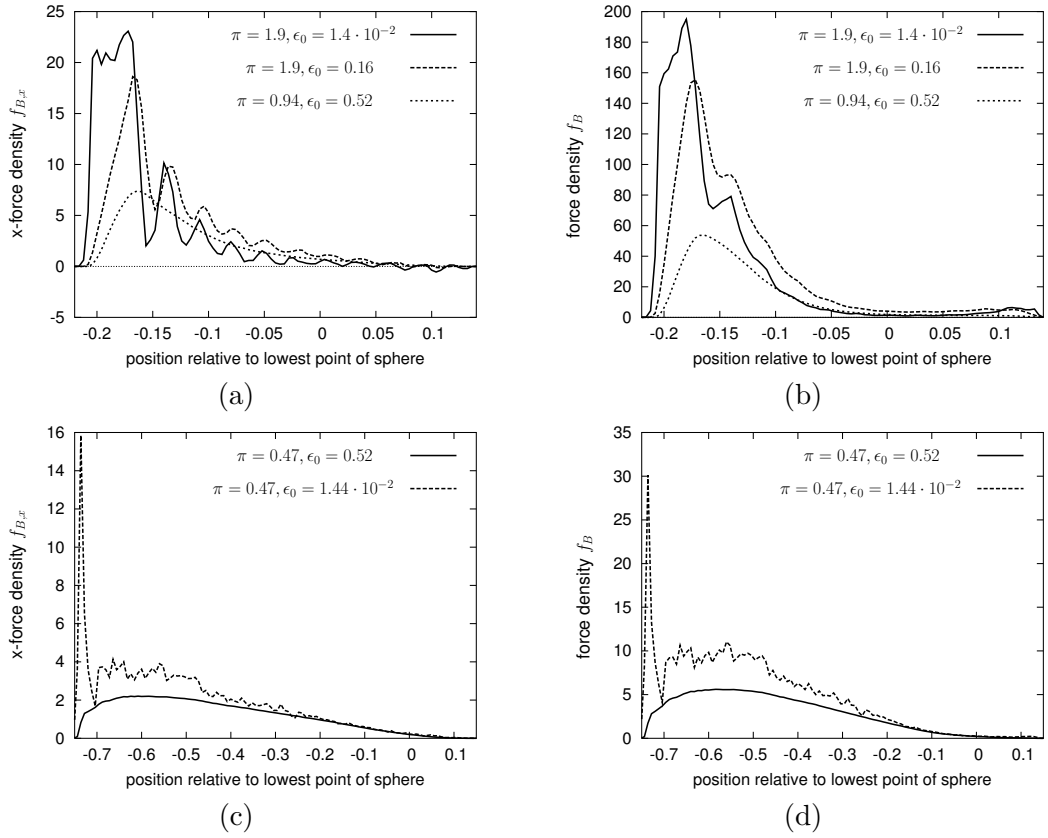

Figure 4.14: Force distributions from 2D adhesive dynamics simulations. The parameters chosen (except for the spring constant κ) are the same as for the simulations for Fig. 4.5. (a,b) Stiff bonds with spring constant $\kappa = 10^{-2}$ N/m at three different combinations of dimensionless on-rate π and unstressed off-rate ϵ_0 ($L_b = 500$). (a) Distribution density of the x-component of the bond force $f_{B,x}(x)$. (b) Distribution density of total bond force $f_B(x)$. (c,d) Soft bonds with $\kappa = 10^{-4}$ N/m at two different combinations of π, ϵ_0 ($L_b = 250$). (c) $f_{B,x}(x)$; (d) $f_B(x)$. (Numerical parameters are $T_{sim} = \dot{\gamma}2\text{s}$, $\Delta t = 10^{-4}$. Furthermore, to obtain better statistics the quantities defined in Eq. (4.29) are also averaged of 40-800 simulation runs. Length is measured in units of R, force in units of $6\pi\eta R^2\dot{\gamma}$.)

$f_{B,x}(x)$ according to Eq. (4.30) for a fairly stiff bond with spring constant $\kappa = 10^{-2}$ N/m. The integral $\bar{F}_{B,x} := \int_{-1}^{1} f_{B,x}\mathrm{d}x$ defines the x-component of the time average of the total bond force. When it has reached its maximum value (defined by the force balance at mechanical equlibrium, see Fig. 4.2) the cell is in the state of firm adhesion. For the three choices of (π, ϵ_0) shown in Fig. 4.14a,b the cell rolls and therefore the time-averaged total bond force is less than the maximum possible value. In fact, from Fig. 4.14a one can see, that the larger the off-rate and the smaller the on-rate the smaller is $\bar{F}_{B,x}$. This observation is in agreement with the result of Fig. 4.4a, where the mean velocity was found to be the larger, the smaller the on-rate and the larger the off-rate is. The curves for $\epsilon_0 = 0.014, 0.16$ in Fig. 4.14a show a regular pattern of maxima and minima which is even better pronounced for the curve with the smaller off-rate. This regular pattern corresponds to the regular ligand distribution (see Sec. 4.2.1) and the distance between two minima is approximately given by the distance between two ligands. Here, the ligand-ligand distance is $d = 0.029$ which fits well to the observed six minima between $x = -0.15$ and $x = 0$

in Fig. 4.14a. Rolling at low off-rates is not a smooth process (compare the example trajectory in Fig. 4.6(6)). It can rather be described as "stop-go" motion. This means that bonds are loaded until the cell stops and then the cell pauses in this (motionless) state until some bond ruptures. After bond rupture the cell *rolls* forward and the remaining bonds are again loaded until the x-component of their total load compensates the driving force from the shear flow. During the motion step the receptors move from one bin to the next so that (besides geometrical effects) force is rather equally distributed over the bins. If the cell moves only slowly or is even at rest the receptors stay in certain bins and therefore their bond force strongly contributes to the time-averaged force density at the position of this bin. Due to the regular ligand distribution the position of the cell center relative to the ligands is similar for all stop steps which leads to the maxima and minima of $f_{B,x}$. In addition, we note that at the front end of the cell the minima of $f_{B,x}$ are negative, which means that bonds on the front end may even pull in the direction of flow. However, this effect is weak. For the highest off-rate shown in Fig. 4.14a, $\epsilon_0 = 0.52$, only one maximum at the rear end of the cell can be identified. At this off-rate (compare the example trajectory in Fig. 4.6(5)) stops of the cell are unlikely and therefore the receptors permanently move from one bin to the other resulting in a less structured time-averaged force distribution density.

In Fig. 4.14b the total force distributions $f_B := \sqrt{f_{B,x}^2 + f_{B,z}^2}$ for the same (π, ϵ_0) pairs as in Fig. 4.14a are shown. Comparing the scales of the ordinates in Fig. 4.14a and b we see that the z-component contributes much more to the total force density than the x-component. Furthermore, the signature of the regular ligand distribution is hardly visible. This is due to the fact that the z-component of the bondforce is basically determined by the height of the receptor above the wall but not by the positions of the ligands. The total force along a tether bond leads to an exponential increase in the off-rate according to the Bell equation, Eq. (2.37). Thus, there are two competing effects that contribute to the shape of $f_B(x)$. On the one hand the bond force is the larger, the larger the receptor-wall distance is. The latter one increases with increasing distance from the cell center. On the other hand the larger the bond force, the more likely it is for the bond to rupture and therefore the smaller is its contribution to the time-averaged force density distribution. The interplay between these two effects explains the big maximum in $f_B(x)$ left to the sphere center.

In Fig. 4.14c,d the force density distributions for soft bonds, with $\kappa = 10^{-4}$ N/m are shown. In contrast to the stiff bonds discussed before, the range where the force density distribution is different from zero is now much larger. Using the same estimate as in Sec. 4.2.3 we find that for the capture radius $r_0 = 0.01$ the contact zone (the zone where bonds can be formed) is at $|x| \leq 0.14$. At the front end of the cell the end of the contact zone also marks the end of the range of active bonds. At the rear end active bonds also exist beyond the contact zone due to the rolling of the cell. The softer the bonds the more they have to be elongated to build up a certain force and therefore the more they are shifted to the rear end of the cell (see also discussion on page 69). Concerning the off-rate a similar behavior as for stiff bonds can be observed. For the larger off-rate, $\epsilon_0 = 0.52$, rupture probability is high already before the bonds are fully loaded resulting in a more uniform force distribution. On the other hand for the smaller off-rate, $\epsilon_0 = 0.014$, a narrow peak in the force density distribution exists which indicates that the left-most bond is loaded until the cell stops and ruptures on average only after some pause time. As the force distribution zone for soft tethers is much larger than the ligand-ligand distance d no signature of d in $f_{B,x}(x)$ is observed (i. e., no regular pattern of minima and maxima). Comparing again the scales of the ordinates in Fig. 4.14c and d we find that the x and

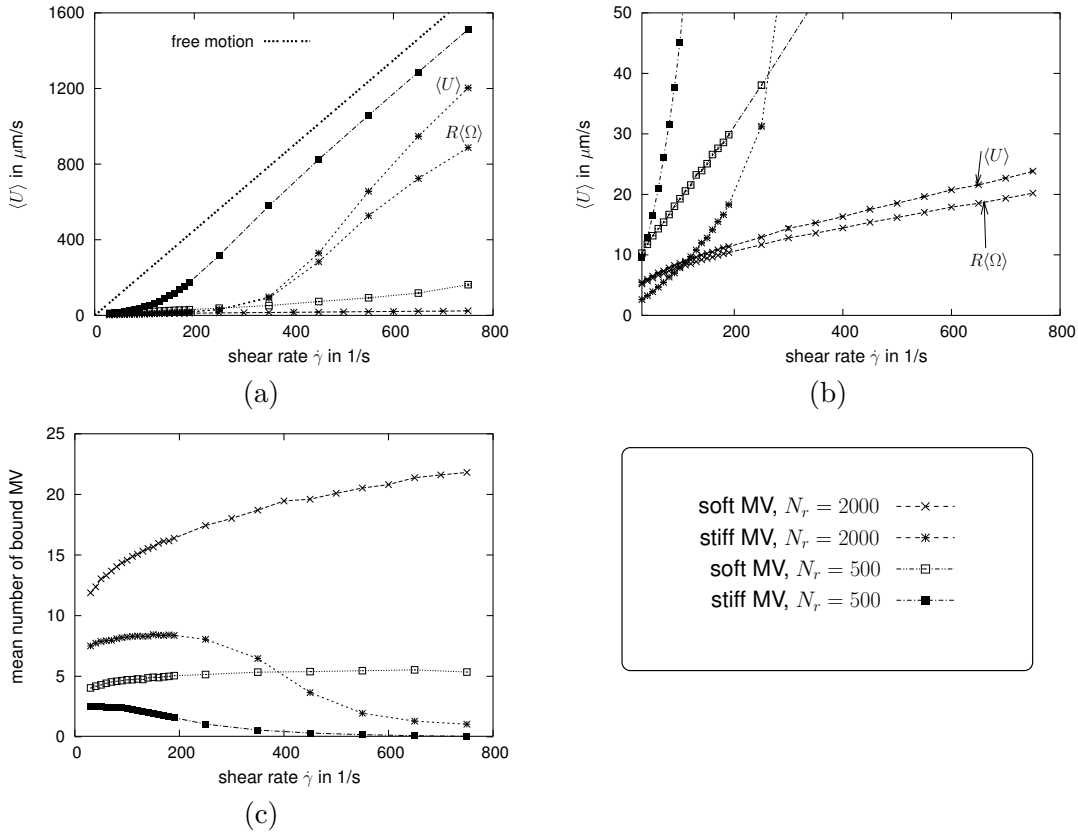

Figure 4.15: 3D adhesive dynamics simulations showing that soft microvilli (MV) increase the robustness of rolling against variations in shear rate $\dot{\gamma}$. (a) Mean velocity $\langle U \rangle$ of a cell for stiff and soft MV as a function of the shear rate. For the $N_r = 2000$ stiff MV also the mean angular velocity $R\langle\Omega\rangle$ is shown. (b) The same as in (a) with a different scale. For the case of $N_r = 2000$ soft MV also $R\langle\Omega\rangle$ is shown. (c) Mean number of bound MV as a function of the shear rate $\dot{\gamma}$. The average values have been obtained over $200 - 500$ simulation runs of $T_{sim} = 20$ s length. Other parameters used: $k_{on} = 100$ Hz, $k_0 = 5$ Hz, $R = 5$ μm, $T_a = 310$ K, $\Delta\rho = 50$ kg/m^3, $\eta = 10^{-3}$ Pa s, $d = 0.02R, r_0 = 0.01R$, $x_c = 0.2$ Å, $\Delta t = 5 \cdot 10^{-4}$.

z-components of the bond force are now of the same order of magnitude, indicating that the angle χ between the tether bond and the wall (cf. Fig. 4.2) is smaller for soft bonds than for stiff ones.

4.4.2 Shear dependence of rolling velocity

So far, all numerical rolling experiments presented in this chapter were preformed at some fixed shear rate. In this section we consider the question, how robust is rolling when the shear rate $\dot{\gamma}$ is increased? For that we use the 3D version of our adhesive dynamics algorithm to measure the mean translational velocity $\langle U \rangle$ as a function of $\dot{\gamma}$. As discussed in Sec. 4.2.1 microvilli (MV) have their own elastic constant (spring constant). Here, we consider receptor-ligand bonds with a spring constant of $\kappa_{RL} = 5.3 \cdot 10^{-3}$ N/m. In addition, we consider both, cells where the receptors are located on the tips of MV with $\kappa_{mv} = 4.3 \cdot 10^{-5}$ N/m, and beads without MV (this corresponds to the case of very stiff MV and is therefore refered to as the stiff MV case). For the on-rate and off-rate $k_{on} = 100$ Hz and $k_0 = 5$ Hz, respectively, are chosen. At $\dot{\gamma} = 100$ Hz this provides

$\pi = 1, \epsilon_0 = 0.05$ for the dimensionless reaction rates, and from Fig. 4.10a we obtain that cells with $N_r > 2000$ are in the stationary rolling state (with sample trajectories similar to that shown in Fig. 4.6(6)). Fig. 4.15a and b shows the mean velocity $\langle U \rangle$ as a function of $\dot{\gamma}$. We consider rolling to be robust against an increase in shear rate if $\langle U \rangle / \dot{\gamma}$ is not increasing with $\dot{\gamma}$. As can be seen from Fig. 4.15a for stiff MV $\langle U \rangle$ increases faster than proportional to $\dot{\gamma}$ at some range of shear rates and approximates the velocity of a freely moving cell at large shear rates. The superlinear increase of $\langle U \rangle$ with respect to $\dot{\gamma}$ occurs at higher shear rates for cells covered with $N_r = 2000$ receptors (here, each receptor corresponds to one MV) than for cells with $N_r = 500$. In addition, Fig. 4.15a also shows $R\langle \Omega \rangle$ for the cells with $N_r = 2000$ stiff MV. It can be seen that the ratio $R\langle \Omega \rangle / \langle U \rangle$ decreases, and therefore the cells no longer roll at large shear rates. Fig. 4.15b shows the mean velocities on a smaller scale, so the curves for cells with soft MV could be better resolved. One can see that $\langle U \rangle$ for cells with soft MV increases much slower with $\dot{\gamma}$ than for cells with stiff MV. For $N_r = 2000$ soft MV the increase of the mean velocity $\langle U \rangle$ with respect to $\dot{\gamma}$ is linear for large shear rates and even sublinear at small shear rates. For these cells also the $R\langle \Omega \rangle$ curve is shown. One can see that $R\langle \Omega \rangle$ also increases linearly with $\dot{\gamma}$ for large $\dot{\gamma}$, and therefore the ratio $R\langle \Omega \rangle / \langle U \rangle$ stays (approximately) constant (a value of > 0.8 for this ratio can be determined which means according to the classification given in Tab. 4.2 that the cells still roll at large shear rates).

In Fig. 4.15c the mean number of bound MV is drawn against the shear rate (it must be noted that for the data shown a MV is considered only if it is bound for more than 0.02s, thus, a vanishing mean number of bound MV means that the maximum lifetime of bound MV is less than 0.02 s). We first notice that the larger N_r, the larger is the mean number of bound MV to which we will refer to as $\bar{N}_r$ in the following. In regard to the dependence on the shear rate, we see that with increasing shear rate also $\bar{N}_r$ increases up to a (flat) maximum. For cells with stiff MV $\bar{N}_r$, decreases again at larger shear rates and approximates zero for very large $\dot{\gamma}$. This different behavior of $\bar{N}_r$ as a function of $\dot{\gamma}$ provides an explanation for the different velocity robustness observed for soft and stiff MV, respectively. However, in order to understand the different behaviors of $\bar{N}_r$ in regard to the stiffness of the microvilli, we recall the results of the last section (Sec. 4.4.1). There, we have seen that the range of force distribution is much larger for soft bonds than for stiff bonds (compare Fig. 4.14a,c). The larger the load carrying area on the cell bottom, the more MV are involved that share the total load. In addition, we saw that the largest load is carried by the bonds at the rear end of the cell. Thus, for soft bonds the zone of bond formation is well separated from the zone of highest rupture probability. Therefore, ruptured bonds are compensated by bonds formed in the contact zone and transported to the rear end. This explains the only modest (i. e., linear) increase of $\langle U \rangle$ with increasing shear rate. In contrast, stiff bonds carry an essential amount of load already in the contact zone. After their rupture, less bonds are available for compensation. If loading and rupture occurs fast (i. e., at large $\dot{\gamma}$) there is less time for new bonds to form and compensation is even less probable, resulting in an increase of $\langle U \rangle$ faster than linearly with $\dot{\gamma}$.

4.5 Summary

In this chapter we studied the motion of a cell under the action of bonds. The parameter values chosen are based on values typical for flow chamber experiments with leukocytes. However, it must be noted that the results obtained can also be applied to rolling experiments with cell free systems (i. e., with receptor bearing microspheres).

First, we saw, from the analytical analysis of the linear approximation of the deter-

ministic equations of motion and the numerical solution of the full equations that the cell starts rolling in the sense $R\Omega/U \to 1$, when functional bonds exist. Then, we defined five stationary states of leukocytes motion, including rolling, based on the mean translational and angular velocity of the cells. The appearance of these states were displayed in *on-off-state diagrams* and the influence of paramters like viscosity and ligand density to these states of motion were discussed. In addition, we could explain the generic behavior of the mean translational velocity, $\langle U \rangle$, by means of the exact solution of a simplified on-off model for motion under the action of bonds that perpetually form and rupture.

The classification of states of motion given is not directly applicable to typical leukocyte experiments done before as there only the translational and not the angular velocity is measured. So by experimantal groups typically three states of motion are defined (transient adhesion, rolling, firm arrest) all based on the measured (instantaneous) translational velocity [63, 135].

In contrast to the off-rate, it is very difficult to infer values for the on-rate of a receptor-ligand complex from flow chamber experiments. The classification of stationary states of motion according to our definition might provide a new method to obtain better estimates for the on-rate: First, one could determine the state of motion of a sphere covered with a special type of receptors, and then continously vary external parameters like viscosity and ligand density until another stationary type of motion is reached. Finally, the experimentally obtained parameters at which the state changes can be compared to our simulation results providing a value for the on-rate. This procedure of course requires the possibility to measure the angular velocity of the receptor covered sphere. Furthermore, also the ligand-ligand distance should be controllable. Both of these challenges could be accomplished in the near future using recent biotechnological developments. Receptors can be attached to micron-sized beads which are covered with anisotropic surface layers [24, 2]. If these layers are (anisotropically) reflective, rotational motion of the spheres can be recorded (in principle also rotations of leukocytes can be observed by tracking the excentric nucleus [4]). Ligand-ligand distances can be tuned using nano-patterend bio-functionalized gold dot arrays [8].

We finally studied the effect of shear rate on rolling velocity and found that rolling is much more robust against an increase in shear rate for soft bonds (soft MV) than for stiff bonds. This was explained by an increase of tethers for soft and a decrease of tethers for stiff bonds, respectively. Indeed, an increase of tethers for increased shear rates was found to stabilize rolling over a large range of shear rates (10^2 Hz $< \dot{\gamma} < 4 \cdot 10^3$ Hz) by Chen and Springer [29]. At these large shear rates an increase of tethers results probably not only from elastic deformations of the MV but also from viscous tether formation [137] and an increase of the contact zone due to elastic deformations of the whole cell [137, 29].

Chapter 5

Cargo transport by processive molecular motors

From a theoretical point of view the *active* cargo transport by processive motor proteins along filaments bears some analogies to a receptor-covered sphere moving above a ligand bearing wall. In this chapter, we apply an extended version of the *adhesive dynamics* algorithm in order to simulate the *cooperative* transport of a sphere by several kinesin-like motors along a microtubule (MT). In a recent theoretical study Klumpp and Lipowsky calculated the mean transport distance of a cargo particle as a function of the maximum number of simultaneously pulling molecular motors [83]. Here, we combine this model with Stokesian dynamics, thus accounting for effects arising from Brownian motion of a spherical cargo particle, its hydrodynamic interaction with the boundary wall and the curvature of the cargo surface. We compare our results with the theoretical predictions. A main result is that in the computer simulations (and presumably also in experiments), the maximum number of motors that can simultaneously bind cannot be considered to be a constant.

5.1 Adhesive motor dynamics

We consider spherical cargo particles uniformly covered with N_{tot} molecular motors whose generic properties are similar to those of conventional kinesin. The motor proteins are firmly attached to the cargo at their tail domains, so that N_{tot} is constant in time. The head domains of the motors can bind and unbind to special sites on the microtubule (MT). In comparison to the notation of the previous chapters the binding sites on the MT are analogous to ligands and the motor heads correspond to receptors, see Tab. 5.1. Furthermore, we consider the radius R of the cargo particle to be large compared to the diameter of the MT h_{MT} and the length of the motor protein l_0, i. e., $R \gg h_{MT}$ and $R \gg l_0$, respectively. Then, contributions from the motors and the MT to the mobility

receptor (# of $= N_r$)	motor protein attached to a cargo particle (# of $= N_{tot}$)
ligand (periodicity d)	binding site on microtubule, periodicity δ
bond	motor protein attached to MT

Table 5.1: Correspondence in notation between a rolling adhesion system (left) and a cargo that is pulled by motors (right).

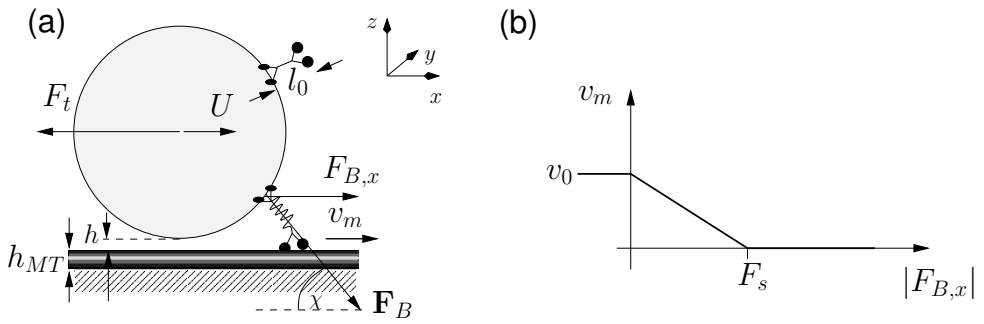

Figure 5.1: (a) Illustration of a bead (sphere) pulled by one molecular motor. The bead is subject to the motor force $\mathbf{F}_B$ and an external force F_t which results in a bead velocity U. The motor with resting length l_0 is firmly attached to the bead and can bind to and unbind from a MT and moves with velocity v_m. χ denotes the angle between motor and MT. (b) Force velocity relation for a single motor: velocity v_m as a function of load $|F_{B,x}|$ according to Eq. (5.3) with maximum velocity v_0 and stall force F_s.

matrix can be neglected. This allows us to base the simulations carried out in this chapter upon the adhesive dynamics algorithm described in Sec. 2.4.3.

Algorithm and parameters

Conventional kinesin is a polymeric dimer of total length of about 80 nm [124]. Here, we consider two variants of the simple harmonic spring model in order to have a force extension relation for this molecule. The first variant is the cable model given by Eq. (2.39), i. e., a force is only needed to extend the motor beyond its resting length l_0. The second variant is the full harmonic spring with force extension relation $F(x)$ given by

$$F(x) = \kappa(x - l_0) \tag{5.1}$$

that means, a force is needed for both compression and extension of the motor protein. Actually, it was found that kinesin exhibits a non-linear force extension relation [151], with the spring "constant" varying between $\kappa = 0.2 \cdot 10^{-4}$ N/m for small extensions and $\kappa = 0.6 \cdot 10^{-4}$ N/m for larger extensions [151, 58]. For extensions close to the contour length the molecule becomes infinitely stiff (strain stiffening) [38]. For small extensions, however, the harmonic approximation works well. Using a photonic force microscope Rohrbach et al. tracked the position of a latex bead that was attached to a single kinesin molecule. From comparison to Brownian dynamics simulations of the bead position assuming the kinesin to be a linear spring they obtained a spring constant of $\kappa \approx 0.8 \cdot 10^{-4}$ N/m. For the following simulations we use the value 10^{-4} N/m for the spring constant κ in both the cable and the full harmonic spring model.

We allow the motor head to freely rotate about the point of fixation to the cargo. In contrast to the position of the tail domain on the sphere, the head position of each motor is not explicitly traced during the simulations as long as the motor is not attached to the microtubule. The head domain is rather supposed to be located somewhere on a spherical shell around its anchorage point. The radius of this sphere is given by the resting length of the motor protein l_0, and the thickness of the shell is called r_0 (its meaning is similar to that of an encounter radius). If such a shell has some overlap with an unoccupied binding site on the MT the motor binds with rate $k_{on} = 5$ Hz [97] (i. e., with probability

Parameter → non-dimensionalized	typical value (dimensionless)	meaning	reference
$R \to 1$	1 μm (1)	bead radius	
k_0	1 Hz	unstressed off-rate	[83]
$\to \epsilon_0 = k_0/k_0$	(1)		
k_{on}	4.7 Hz	on-rate	[97]
$\to \pi = k_{on}/k_0$	(5)		[83]
$F_d \to 1$	3 pN	detachment force	[83, 126]
κ	$10^{-5} \dots 10^{-3}$ N/m	motor spring constant	[120, 38, 58]
$\to \kappa R/F_d$	(33.3)		
δ	8nm	kinesin step length	[33]
$\to \delta/R$	(0.008)		
v_0	1 μm/s(1)	maximum motor velocity	[83]
$\lambda_s^0 := v_0/\delta$	125 Hz (125)	forward step rate	
r_0	$\delta/2$	capture radius	
F_s	5.5 ... 7 pN	stall force	[158]
$\to F_s/F_d$	(2)		[83]
l_0	50 - 80 nm	(resting) length	[77, 124]
$\to l_0/R$	(0.05,0.065,0.08)		
h_{MT}	24 nm	microtubule diameter	[98]
$\to h_{MT}/R$	(0.024)		

Table 5.2: Parameters used for adhesive motor dynamics. The dimensionless values in brackets denote the values used for the simulations. For ambient temperature we use $T_a = 293$ K, for viscosity $\eta = 1$ mPa s (if not otherwise stated), furthermore $\Delta\rho = \dot{\gamma} = 0$.

$p_{on} = 1 - \exp(-k_{on}\Delta t)$ during the time step Δt). As two binding sites along the MT are $\delta = 8$ nm apart from each other, we consider the "capture radius" to be $r_0 = \delta/2$. Escape from the MT is modeled exactly as described in Sec. 2.4.3 with the Bell model parameters $k_0 = 1$ Hz and $F_d = 3$ pN for unstressed off-rate and detachment force, respectively [126, 83].

The major conceptual difference between a motor connecting a sphere with a MT and a receptor-ligand bond is that a motor can actively step forward from one binding site to the next with step length δ. The mean velocity v_0 of an unloaded kinesin motor is about $v_0 = 1$ μm/s depending on the ATP concentration of the surrounding medium [158]. If the motor protein is mechanically loaded with force opposing the walking direction, the motor velocity v_m is decreased. For a single kinesin molecule that is attached to a bead on which a trap force F_t pulls, the velocity was found to essentially linearly decrease [150, 158]:

$$v_m = v_0 \left(1 - \frac{F_t}{F_s}\right), \qquad 0 < F_t < F_s, \tag{5.2}$$

with the stall force F_s (for which we use a value of 6 pN [158, 83] in the following) and the trap force F_t acting antiparallel to the walking direction. In order to derive an expression similar to Eq. (5.2) for one of many motors pulling on the sphere which is also valid in the presence of high viscous friction, we have to identify the proper term that replaces F_t in Eq. (5.2). First, we rewrite Eq. (5.2) as $v_m = \mu_m(F_s - F_t)$, with some *internal* motor mobility coefficient $\mu_m := v_0/F_s$. This version of Eq. (5.2) allows us to interpret

the motor head as an over-damped (Stokesian) particle that constantly pulls with the stall force F_s against some external load F_t resulting in the effective velocity v_m. According to Eq. (2.38) a motor pulls with force $\mathbf{F}_B$ on the bead, so we can identify the "load" to be $-F_{B,x}$, where $F_{B,x}$ is the x-component of $\mathbf{F}_B$ and the minus sign accounts for Newton's third law (*actio = reactio*). Thus, we obtain the following linear force velocity relation for the single motor (see also Fig. 5.1b):

$$v_m = v_0 \begin{cases} 1 & \text{if} \quad \mathbf{F}_B \cdot \mathbf{e}_x \leq 0 \\ 1 - \frac{|F_{B,x}|}{F_s} & \text{if} \quad 0 < \mathbf{F}_B \cdot \mathbf{e}_x < F_s, \\ 0 & \text{if} \quad \mathbf{F}_B \cdot \mathbf{e}_x \geq F_s \end{cases} \tag{5.3}$$

where $\mathbf{e}_x$ is the walking direction of the motor, see Fig. 5.1a. Thus, if the motor pulls antiparallel to its walking direction on the bead, it walks with its maximum speed v_0. If it is loaded with force exceeding the stall force F_s, it stops. For intermediate loadings the velocity decreases linearly with load force. Eq. (5.3) defines the mean velocity of a motor in the presence of loading force. Actually, the motor walks with discrete steps of length δ. In the algorithm we account for this by defining a step rate $\lambda_s := v_m/\delta$. Then, the probability for a step during time step Δt is $p_{step} = 1 - \exp(-\lambda_s \Delta t)$. A step is rejected if the next binding site is already occupied by another motor (mutual exclusion) [100].

All parameters used for the adhesive motor dynamics simulations together with typical values are summarized in Tab. 5.2. For the algorithm and some theoretical considerations in the following we non-dimensionalize all quantities using R for the length scale, $1/k_0$ for the time scale and F_d for the force scale (see also Tab. A.1).

Single motor simulations

If an external force F_t (e. g., from an optical trap) pulls on the sphere and the motor pulls with force $F_{B,x}$, the bead velocity U is given by $U = \mu_{xx}^{tt}(F_{B,x} - F_t)$, with μ_{xx}^{tt} being a component of the mobility matrix of the sphere (cf. Eq. (2.16)) evaluated at the height of the sphere's center. On the other hand from Eq. (5.3) it follows that the motor head moves with velocity $v_m = \mu_m(F_s - F_{B,x})$ (with $\mu_m = v_0/F_s$, see above). In the stationary state of motion the two velocities are equal, $U = v_m$, and we obtain the force with which the motor pulls (in walking direction) on the bead:

$$F_{B,x} = \frac{\mu_{xx}^{tt}}{\mu_m + \mu_{xx}^{tt}} F_t + \frac{\mu_m}{\mu_m + \mu_{xx}^{tt}} F_s. \tag{5.4}$$

Thus, if the internal friction of the motor ($1/\mu_m$) is large compared to the viscous friction of the sphere, i. e., $1/\mu_m \ll 1/\mu_{xx}^{tt}$, the second term in Eq. (5.4) can be neglected and one has $F_{B,x} \approx F_t$. That means, only the trap force pulls on the motor. If $\mu_m \approx \mu_{xx}^{tt}$ both terms in Eq. (5.4) are of the same order of magnitude. Then, both external load F_t and the friction force on the bead will have visible influence on the motor velocity. Experimentally, these prediction can be checked in bead assays by varying the viscosities of the medium (e. g., by adding sugar like dextran or Ficoll [30]), or *in vivo* where the *viscoelastic* friction (i. e., scale dependent) on the cargo is high [69]. Numerically, we can vary η in the adhesive motor dynamics algorithm.

Inserting Eq. (5.4) into Eq. (5.3) provides then a prediction for the velocity of a bead subject to a pulling motor and an external force F_t. In Fig. 5.2a we compare this prediction with actual measured velocities using the adhesive motor dynamics algorithm described above. For this, we measured the mean velocity of the bead and the motor obtained from

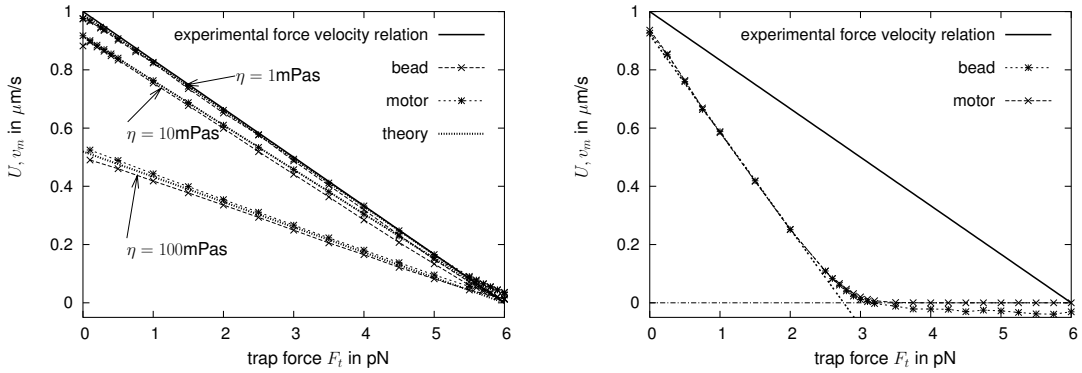

Figure 5.2: (a) Measured force velocity relation of a single motor (with $l_0 = 80$ nm) pulling a sphere of radius $R = 1$ μm for three different viscosities $\eta = 1, 10, 100$ mPa s. Shown is the relation according to Eq. (5.2), the actual measured force velocity relation of the motor head and the bead center, respectively, and the theoretical prediction according to Eq. (5.3) and Eq. (5.4). (b) The measured force velocity relation for $\eta = 1$ mPa s is shown where in Eq. (5.3) not $|F_{B,x}|$ but $\|\mathbf{F}_B\|$ is used. The dotted line emphasizes the linear decrease of the velocity. The negative velocity of the bead at large F_t results from thermal fluctuations. Fluctuations against walking direction increase the escape probability. In case of escape they cannot be compensated by fluctuations in walking direction. (Numerical parameters: $\Delta t = 10^{-5}$, number of runs $N = 2 \cdot 10^3 - 9 \cdot 10^4$.)

a large number of simulation runs (to avoid effects resulting from the initial conditions we first allowed the relative position/orientation of bead and motor to "equilibrate" before starting the actual measurement). The mean velocity is then given as the total (summed up over all simulation runs) walking distance divided by the total walking time. The good agreement between the numerical results and the theoretical predictions provides a favorable test to the algorithm. At $\eta = 1$ mPa s (the viscosity of water), friction of the bead has almost no influence on the walking speed. At hundred times larger viscosities, however, bead friction reduces the motor speed to almost half of its maximum value already at zero external load. Although the velocities of the motor and the bead are expected to be equal, Fig. 5.2a shows that the motor is slightly faster than the bead. This is due to the discrete steps of the motor and can be considered as a numerical artefact: at the moment the motor steps forward the motor stalk is slightly more stretched (loaded) than before the step, therefore, the escape probability is increased. The result of unbinding at the next time step would then be that the bead moved a distance δ less than the motor. For loads close to the stall force the observed velocity is slightly larger than the prediction, which is due to thermal fluctuations of the bead: a fluctuation in walking direction slightly reduces the load on the motor, thus increasing the step rate, whereas fluctuations against walking direction lead to zero step rate.

It was observed by Block et al. that vertical forces on the bead (i. e., in z-direction) also reduce the velocity of the motor [18]. But the same force that leads to stall when applied antiparallel to the walking direction has a rather weak effect on the motor velocity when applied in z-direction. Using nevertheless the total force of the motor $\|\mathbf{F}_B\|$ in Eq. (5.3) instead of its x-component $|F_{B,x}|$ [88], we measure a force velocity relation as shown in Fig. 5.2b. Again, the velocity decreases essentially linearly with applied external force, but stalls already at around $F_t \approx F_s/2$ due to the vertical contributions of the force $\|\mathbf{F}_B\|$.

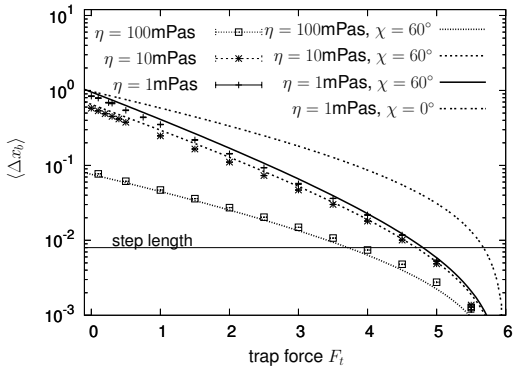

Figure 5.3: Mean walking distance $\langle \Delta x_b \rangle$ of a bead pulled by a single motor as a function of an external force on the bead F_t and for three different viscosities $\eta = 1, 10, 100$ mPa s. The lines give the theoretical predictions according to Eq. (5.5) assuming an angle of 60° between the motor and the MT. For comparison also the theoretically predicted $\langle \Delta x_b \rangle$-curve for $\chi = 0$ is shown (double dotted line).

As the effect of vertical loading reported in Ref. [18] seems to be much weaker than that shown in Fig. 5.2b, we reject this choice of force velocity relation.

From the simulations carried out for Fig. 5.2a we can also obtain the mean walking distance $\langle \Delta x_b \rangle$ for a single motor as a function of external load. The results are shown in Fig. 5.3. Using Eq. (5.3) and the Bell equation Eq. (2.37) we obtain

$$\langle \Delta x_b \rangle = \frac{v_m}{\epsilon} = \frac{v_0}{\epsilon_0} \frac{1 - |F_{B,x}|/F_s}{\exp(\|\mathbf{F}_B\|/F_d)}. \tag{5.5}$$

The numerical results shown in Fig. 5.3 fit well to the theoretical prediction of Eq. (5.5) when assuming the angle χ between the motor and the MT to be $\chi = 60°$. The angle χ depends on the bead radius R, the resting length l_0 [9] and the polymer characteristics of the motor protein, e. g., its stiffness κ.

5.2 Mean walking distance for several motors

5.2.1 Theoretical predictions

We now turn to several motors pulling on the bead. The mean walking distance in terms of the maximum number N_m of simultaneously pulling motors has been calculated by Klumpp and Lipowsky based on a one-step master equation approach [83]. In the following, we briefly summarize some of their results for the sake of later comparison to our simulation results.

Let P_i be the probability that i motors are simultaneously bound (cf. Sec. 4.3). Given sufficient data sampling, the system can be assumed to be in a stationary state. Then, the P_i can be calculated by equating forward and reverse fluxes ([83, Eq. [2]], cf. also Eq. (4.20))

$$(N_m - i)\pi P_i = (i + 1)\epsilon P_{i+1}, \qquad i = 0, \ldots, N_m - 1, \tag{5.6}$$

where it is assumed that the off-rate ϵ is a constant with respect to time. The solution to Eq. (5.6) is given by Eq. (4.26). Under the condition that at least one motor is bound the probability that i motors are simultaneously pulling is $P_i/(1 - P_0)$ for $i = 1, \ldots, N_m$. Then, the mean number of bound motors N_b (given that at least one motor is bound) is

[83, Eq. [13]]

$$N_b = \sum_{i=1}^{N_m} \frac{iP_i}{1-P_0} = \frac{(\pi/\epsilon)\left[1+\pi/\epsilon\right]^{N_m-1}}{\left[1+\pi/\epsilon\right]^{N_m}-1} N_m. \tag{5.7}$$

The effective unbinding rate ϵ_{eff}, i. e., the rate with which the system reaches the unbound state, is determined from $\epsilon_{eff}(1-P_0) = \pi P_0$. This quantity can also be identified with the inverse of the mean first passage time $T(1|0)$ for reaching the unbound state, when starting with one motor bound (Supporting Text of Ref. [83]). If the medium viscosity is small, i. e., similar to that of water, and no external force is pulling on the bead, we assume that the velocity of the bead U does not depend on the number of pulling motors. The mean walking distance, that is the mean distance the cargo is transported by the motors in the case that initially one motor was bound, is then the product of mean velocity U and mean lifetime $(1/\epsilon_{eff})$ [83, Eq. [14]]:

$$\langle \Delta x_b \rangle = \frac{U}{\epsilon_{eff}} = \frac{U}{N_m \pi} \left[\left(1 + \frac{\pi}{\epsilon}\right)^{N_m} - 1 \right]. \tag{5.8}$$

For kinesin-like motors with $\pi \gg \epsilon$ this expression can be approximated by $\langle \Delta x_b \rangle \approx (U/N_m\epsilon)(\pi/\epsilon)^{N_m-1}$, i. e., the mean walking distance grows exponentially with N_m. In the stationary state the bead velocity U and the motor velocity v_m are equal. For no external load and small viscous friction on the bead one can approximate $\epsilon \approx \epsilon_0$ in Eq. (5.7) and Eq. (5.8).

5.2.2 Simulation results

The results shown in this section are based on the following simulation procedure. In each simulation run the sphere is covered with N_{tot} motors. Initially, one motor, located at the lowest point of the sphere, is attached to the microtubule such that the minimum distance h between the sphere and the microtubule is given by the resting length of the motor, i. e., $h = l_0$. The other $(N_{tot} - 1)$ motors are uniformly distributed on the sphere's surface. When the motor starts walking it pulls the sphere closer to the MT because there is a z-component in the force exerted on the sphere by the motor stalk (which is strained after the first step). Then, other motors can bind to the MT. The system needs some time to reach a stationary state of motion, so initially the motor velocity v_m and the bead velocity U are not the same (for reasons of comparison a fixed initial position is necessary; other initial positions have been tested but initialization effects were always visible). As for the case described in Ref. [83], a simulation run lasts until no motor is bound. For each run quantities like the mean number of bound motors N_b, the walking distance Δx_b and the mean minimum distance $\overline{h}$ between sphere and MT are recorded.

In Fig. 5.4 the measured distributions of walking distances are shown for different motor coverages N_{tot} and for two different values of the resting length of the motor protein. For each value of N_{tot} the walking distance was measured about $N = 10^4$ times. The simulations turn out to be very costly, especially for large N_{tot} as the mean walking distance increases essentially exponentially with the number of pulling motors (cf. Eq. (5.8)). From Fig. 5.4 we see that the larger N_{tot}, the more probable large walking distances are, resulting in distribution functions that exhibit a flatter and flatter tail upon increasing N_{tot}. This is in qualitative accordance with distribution functions calculated in Ref. [83] for different N_m. However, it is important to note that the total number of motors on the cargo N_{tot} is not the same as the maximum number of simultaneously pulling motors N_m appearing in

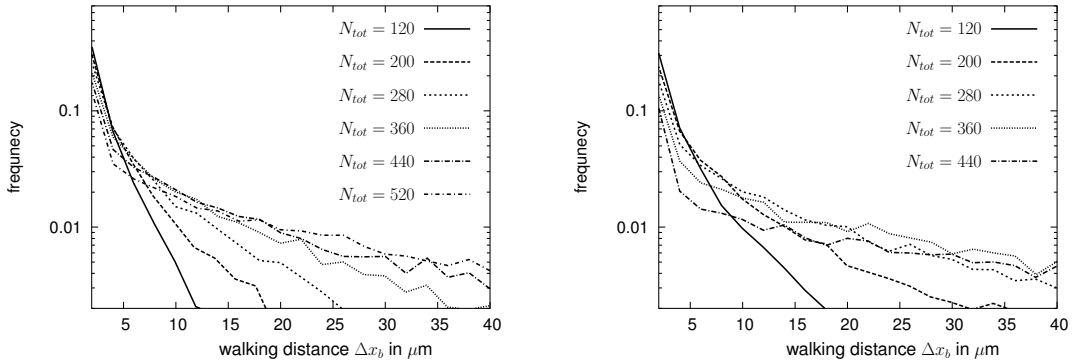

Figure 5.4: Distribution of walking distances Δx_b in semi-logarithmic scale for different values of motor coverage N_{tot}. The motor protein is modeled as a harmonic spring according to Eq. (5.1). (a) Resting length of the motor protein $l_0 = 50$ nm. (b) Resting length of the motor protein $l_0 = 65$ nm. (Numerical parameters: time step $\Delta t = 10^{-5}$, number of simulation runs $N \approx 10^4$.)

Eq. (5.7) and Eq. (5.8). For example, when we compare the distributions for the smaller resting length $l_0 = 50$ nm in Fig. 5.4a and for the larger one, $l_0 = 65$ nm, in Fig. 5.4b but for the same N_{tot}, we see that for the larger l_0 longer walking distances are more probable. This can easily be explained by the fact that the larger the motor proteins, the more motors are on average close enough to the microtubule to bind.

If A_b is the area on the sphere's surface that includes all points being less than l_0 apart from the MT (cf. Fig. 5.5a), then, we expect on average $n_b = N_{tot} a_b$ motors to be close enough to the MT for binding, with the reduced area $a_b := A_b/(4\pi R^2)$. At this point we encounter a major difference between the simulation experiment (and presumably also of the experimental situation) and the theoretical model leading to Eq. (5.8). While the model assumes a fixed N_m, in the simulations only N_{tot} is fixed as explained above. As the motors are uniformly distributed on the cargo, the probability distribution function $P(k)$ for placing k motors inside the above defined area fraction a_b is a binomial distribution. As we have $l_0 \ll R$, a_b is small and $P(k)$ is well approximated by the *Poisson distribution* function

$$P(k, n_b) = \frac{n_b^k}{k!} \exp(-n_b), \qquad n_b = N_{tot} a_b. \tag{5.9}$$

It must be pointed out that even if for every simulation run the same motor distribution is used, the number of motors a_b close enough to the MT for binding is not a constant quantity. It rather changes during the transport process as the orientation and vertical position of the sphere may change. Such fluctuations in the orientation of the sphere are most likely during periods where only one motor is bound to the MT.

Thus, in order compare the simulation results for the mean walking distance and the mean number of bound motors with the theoretical predictions Eq. (5.8) and Eq. (5.7), respectively, we have to average over different N_m. In the following we account for this in two different ways.

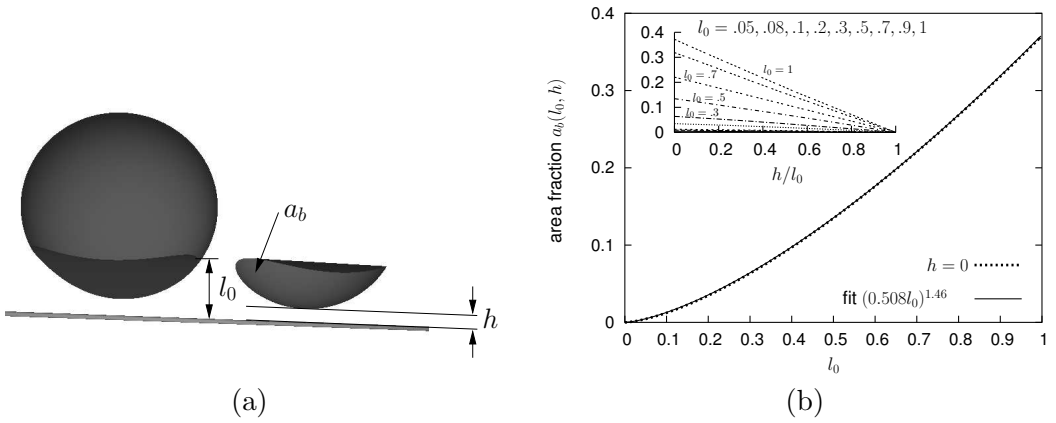

(a) (b)

Figure 5.5: (a) Illustration of the area fraction a_b of the sphere (cut and placed to the left of the sphere) on which motor proteins can reach the MT (thin cylinder). a_b depends on the minimum distance h between the sphere and the MT and on the resting length l_0. (b) Area-fraction $a_b(l_0/R)$ for $h = 0$. Using the gnuplot fit-routine a fit (solid line) to the exact result (dotted line) was obtained (cf. Eq. (5.10)). The inset shows the effect of an increase in h for different l_0.

Method 1

Here, we consider the maximum number of simultaneously pulling motors N_m to be constant during one simulation run. With respect to the ensemble of runs we consider N_m to be distributed according to Eq. (5.9). The area fraction a_b is the remaining surface area from the intersection of the sphere and a cylinder with radius l_0 that is aligned along the protofilament on which the motors are allowed to walk (see Fig. 5.5a). It can be obtained by solving the following integral which follows from geometrical considerations (all quantities are dimensionless)

$$a_b(l_0, h) = \frac{1}{4\pi} \int_0^{2\pi} \left[1 - \frac{1}{\cos^2\phi} \left(\tilde{h} - \sqrt{\tilde{h} - (1 + \tilde{h}^2 - l_0^2)\cos^2\phi + \cos^4\phi} \right) \right] \mathrm{d}\phi, \;\; \tilde{h} := h + 1,$$

a_b depends on the minimum distance h between cargo and MT and the resting length l_0 of the motor protein. By fitting to a simple ansatz it turns out that the previous expression is quite well approximated by

$$a_b(l_0, h) = 4\pi(0.53 l_0)^{1.49}(1 - h/l_0), \qquad h < l_0. \tag{5.10}$$

Fig. 5.5b displays $a_b(l_0, h = 0)$ and the dependence on h for some selected values of l_0.

Averaging the mean walking distance $\langle \Delta x_b \rangle(N_m)$ from Eq. (5.8) over all N_m with weighting factors given by Eq. (5.9) we obtain the following expression ($n_b = a_b N_{tot}$):

$$\langle\langle \Delta x_b \rangle\rangle_{Poisson} = \sum_{N_m=1}^{N_{m,max}} \frac{n_b^{N_m-1}}{(N_m-1)!} \frac{U}{N_m \pi} \left[\left(1 + \frac{\pi}{\epsilon_0} \right)^{N_m} - 1 \right] \Bigg/ \sum_{N_m=1}^{N_{m,max}} \frac{n_b^{N_m-1}}{(N_m-1)!}. \tag{5.11}$$

Note that the first motor is always placed to a_b, and therefore, $P(N_m - 1, n_b)$ denotes the probability of having in total N_m motors inside the area fraction a_b. Furthermore, we introduced a cutoff $N_{m,max}$ of maximal possible motors (N_{tot} is obviously an upper limit

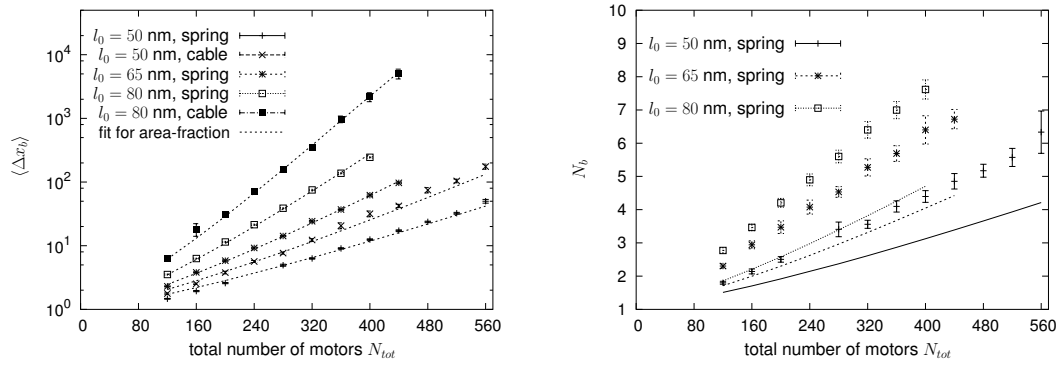

Figure 5.6: (a) Mean walking distance $\langle \Delta x_b \rangle$ (data points with error bars) as a function of motors on the bead N_{tot} obtained from adhesive motor dynamics. The lines are fits of Eq. (5.11) w. r. t. the area-fraction a_b. (b) Mean number of bound motors N_b (data points with error bars). The lines are the values obtained from the Poisson-averaged mean number of bound motors $\langle N_b \rangle_{Poisson}$ in Eq. (5.12) using for a_b the fit value from (a). (Parameters: $\pi = 5, \epsilon_0 = 1$, $\lambda_s^0 = 125$, $\Delta t = 10^{-5}$, $N \sim 10^4$.)

for $N_{m,max}$). In the limit $N_{m,max} \to \infty$ we have $\langle\langle \Delta x_b \rangle\rangle_{Poisson} = U(e^{\pi n_b/\epsilon_0} - 1)/(\pi n_b)$.

In a similar way one can calculate the Poisson-averaged mean number of bound motors $\langle N_b \rangle_{Poisson}$. Here, it is important to include the correct weighting factor: For the N simulation runs the mean number of bound motors is obtained as $\langle N_b \rangle_{sim} = \sum_i t_i n(i) / \sum_i t_i$, where t_i is a period of time during which $n(i)$ motors are bound and the sum is over all such periods of time. Assuming the bead velocity U to be a constant, the time periods t_i can also be replaced by the walking distances $\Delta x_{b,i}$ during t_i. Picking out all simulation runs with a fixed N_m, their contribution to the sum is the mean number of bound motors N_b times the total walking distance of beads with given N_m. The latter is the mean walking distance $\langle \Delta x_b \rangle_{N_m}$ times the number of simulation runs with the given N_m (for sufficiently large N). Clearly, the fraction of runs with given N_m is the probability $P(N_m - 1, n_b)$ introduced in Eq. (5.9). Consequently, we obtain

$$\langle N_b \rangle_{Poisson} = \frac{\sum_{N_m=1}^{N_{m,max}} P(N_m - 1, n_b) \langle \Delta x_b \rangle_{N_m} N_b(N_m)}{\sum_{N_m=1}^{N_{m,max}} P(N_m - 1, n_b) \langle \Delta x_b \rangle_{N_m}}. \tag{5.12}$$

In Fig. 5.6a the mean walking distance as a function of N_{tot} obtained by numerical simulations of the transport process is shown (points with error bars). For the motor stalk three different values of the resting length $l_0 = 50, 65, 80$nm are chosen and both the full-spring and the cable model are applied for the force extension relation. The larger the resting length l_0 the more motors can simultaneously bind for given N_{tot}, and therefore the larger is the mean walking distance (cf. also the distributions in Fig. 5.4). Furthermore, Fig. 5.6a also shows that it makes a clear difference whether the motor stalk behaves like a full harmonic spring or a cable. If the motor protein behaves like a cable (semi-harmonic spring, Eq. (2.39)) it exhibits force only if it is stretched. The vertical component of this force always pulls the cargo towards the MT. Thus, the mean height between the cargo and the MT (which determines how many motors can bind at maximum) results from the interplay between this force and thermal fluctuations of the bead. In contrast, if the motor also behaves like a harmonic spring when compressed, it once in a while may also push

the cargo away from the MT. This results in less motors being close enough to the MT for binding than in the case of the cable-like behavior of the motor stalk. Consequently, given the same l_0 and N_{tot}, the cargo is on average transported further when pulled by "cable-like motors".

To compare the simulation results for the mean walking distance with the theoretical prediction Eq. (5.11), we use $N_{m,max}$ equal to the maximum number of bound motors that occurred during all of the N simulation runs. For the bead velocity U we use the mean value measured during the simulations (this is up to 15 % less than the maximum motor velocity v_0; responsible are mainly geometrical effects). Then, the only unknown parameter is the area fraction a_b. The curves shown in Fig. 5.6a are obtained by fitting Eq. (5.11) to the numerical data. The fit was done using an implementation of the Marquardt-Levenberg algorithm from the numerical recipe book [117]. The resulting a_b values are summarized in Tab. 5.3. The increase in a_b for larger resting length and the cable model

l_0, motor-model	fit value for a_b	measured $\overline{h}$ $\rightarrow$ a_b (measured)
50nm, spring Eq. (5.1)	0.00211	7-14 nm $\rightarrow$ 0.0039-0.0034
50nm, cable Eq. (2.39)	0.0026	4-11 nm $\rightarrow$ 0.0041-0.0036
65nm, spring Eq. (5.1)	0.00315	7-13 nm $\rightarrow$ 0.006-0.0055
80nm, spring Eq. (5.1)	0.00403	8-14 nm $\rightarrow$ 0.0082-0.0076
80nm, cable Eq. (2.39)	0.00518	4-11 nm $\rightarrow$ 0.0085-0.0079

Table 5.3: Obtained fit values for the area fraction a_b for different l_0 and the two applied polymer models. For comparison the area fraction which is obtained from the measured mean distance $\overline{h}$ is also displayed.

is in accordance with the above discussed expectation. In the simulation also the mean distance $\overline{h}$ between cargo and MT is measured. Using $\overline{h}$ to calculate the area fraction provides about 60 % larger values for a_b than obtained from the fit (see Tab. 5.3), but shows the correct trend.

In Fig. 5.6b the mean number of bound motors (the average is obtained over all N simulation runs) is shown as a function of N_{tot} (for the same three l_0 values as in Fig. 5.6a but only for the force extension relation Eq. (5.1)). Also shown (lines) are the theoretical predictions based on Eq. (5.12) using for a_b the corresponding fit values listed in Tab. 5.3. The predicted behavior is only in qualitative accordance with simulation results. In fact, the results obtained from simulations are up to 60 % larger than the values obtained from Eq. (5.12). Indeed, from the larger *measured* area fraction (last column in Tab. 5.3) a larger number of bound motors is expected than is predicted using the smaller a_b obtained from the fit.

The observed discrepancy probably results from the basic assumption leading to Eq. (5.11) and Eq. (5.12), i. e., considering N_m to be constant during a simulation run. As already pointed out above this is not the case. For example, after the escape of one motor the pulling forces from the remaining motors may change the orientation of the spherical cargo resulting in a larger or smaller N_m. During periods where more motors are available for binding also more motors are on average bound leading to a stabilization of the cargo orientation. This effect leads to a local drift of surface areas with denser motor coverage towards the microtubule. Furthermore, we considered the off-rate ϵ to be given

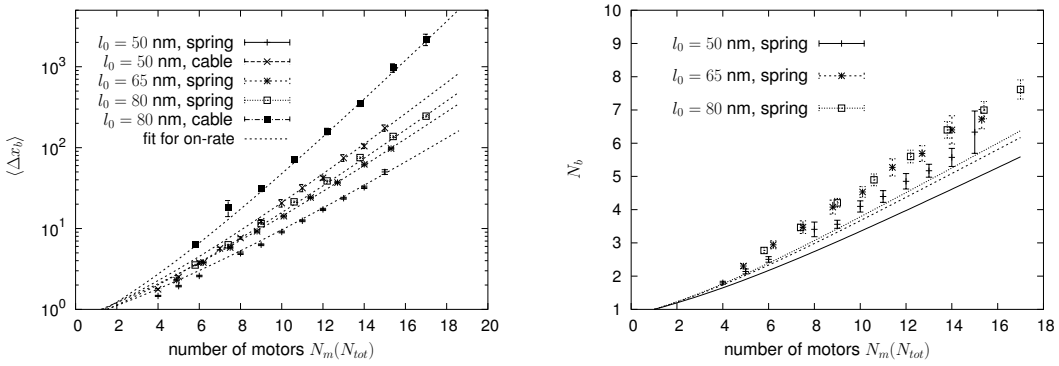

(a) (b)

Figure 5.7: The data points shown here are the same as in Fig. 5.6. Data is, however, not plotted against N_{tot} but against $N_m(N_{tot})$ according to Eq. (5.13). (a) Mean walking distance $\langle \Delta x_b \rangle$. The lines are fits of Eq. (5.8) w. r. t. an effective on-rate π_{eff}. For the fits the gnuplot fit routine was used. Resulting fit values for the full spring model: $\pi_{eff} = 0.49, 0.56, 0.60$ for $l_0 = 50, 65, 80$ nm, respectively. For the cable model: $\pi_{eff} = 0.65, 0.85$ for $l_0 = 50, 80$ nm, respectively. (b) Mean number of bound motors N_b. The lines show N_b using Eq. (5.7) with the effective on-rate π_{eff} obtained in (a).

by the unstressed off-rate ϵ_0. But in fact the off-rate is not a constant value, it rather varies permanently, with $\epsilon \geq \epsilon_0$, for each motor depending on its individual load. This results in an average off-rate rate that is larger than the unstressed off-rate.

Method 2

We now consider N_m to be a constant for fixed N_{tot}. For that we propose an estimate for N_m as a function of N_{tot} given by

$$N_m = \frac{l_0}{2R}(N_{tot} - 1) + 1 \approx \frac{l_0}{2R} N_{tot} + 1, \tag{5.13}$$

$N_{tot} l_0 / 2R$ is the mean number of motors on a spherical cap of height l_0 for N_{tot} motors uniformly distributed on the bead's surface. The additional motor count contributes for the first motor that is always distributed to be close enough for binding to the MT. The choice in Eq. (5.13) for the estimate of $N_m(N_{tot})$ is somewhat arbitrary. However, it is important that $N_m(N_{tot})$ is larger than the mean number of motors that can access the MT. This can be compensated when matching Eq. (5.8) to the data points by not using the on-rate π but some effective on-rate $\pi_{eff} < \pi$.

Fig. 5.7 shows the same simulation results as Fig. 5.6 but plotted as a function of $N_m(N_{tot})$ from Eq. (5.13). In Fig. 5.7a also fits of Eq. (5.8) for an effective on-rate π_{eff} are displayed. The resulting fit values are listed in the figure caption of Fig. 5.7. The fitted curves turn out to match the simulation data about equally well as the fitted curves in Fig. 5.6a do. The effective off-rates π_{eff} are up to a factor ten smaller than the π-value used in the simulation, indicating that most of the walking time less than the $N_m(N_{tot})$ motors proposed in Eq. (5.13) can access the MT.

In Fig. 5.7b the simulation data for the mean number of bound motors and Eq. (5.7) using π_{eff} as a function of $N_m(N_{tot})$ defined in Eq. (5.13) is shown. The theoretical prediction fits now better than the corresponding fitting method discussed above (cf.

Fig. 5.6b). But still the simulation results are up to 30 % larger than the theoretical predictions. Similarly as for the previous applied fitting method the discrepancy can partly be explained by the non-constant off-rate ϵ. Although the second method of bringing the simulation results and the theoretical prediction into accordance works slightly better, it has to be taken with a grain of salt as the proposal of N_m in Eq. (5.13) is somewhat arbitrary.

5.3 Summary and discussion

In this chapter, we introduced an extension of the adhesive dynamics algorithm presented in Sec. 2.4.3 that is capable of simulating the active transport of a spherical cargo particle by molecular motors. The important parameters and properties by which the motors are modeled are based on results of single-molecule experiments with conventional kinesin (mainly collected in [83]). The numerical measurement of the force velocity relation and the mean walking distance of the sphere for a single motor pulling in the presence of external load and high viscosities provided a favorable test to the algorithm.

Next, we computed the mean walking distance and the mean number of bound motors as a function of the total number N_{tot} of motors attached to the sphere. Klumpp and Lipowsky give theoretical predictions for these quantities as a function of the maximum number N_m of simultaneously pulling motors [83]. We pointed out that N_m is not a constant quantity neither in our simulation experiment nor in a real experiment. Thus, to account for the difference between fixed N_{tot} and N_m, respectively, we applied two methods of fitting our numerical obtained mean walking distances to the theoretical predictions from Ref. [83]. In general, these fits worked fine as the numerical data recover the same functional relation for the mean walking distance with respect to N_{tot} as the theoretical prediction does with respect to N_m. But the numerically obtained mean number of bound motors turned out to be distinctly larger (up to 60 %) than the theoretical prediction with respect to the before obtained fit values. This discrepancy possibly results from fluctuations of the cargo and the discrete steps of the motors which both lead to temporally non-constant unbinding and step rates. In addition, also the number of motors that can access the microtubule changes during the transport process. By taking these effects into account the numerically obtained values presented here provide a link between the theoretical predictions by Klumpp and Lipowsky and results obtained from *in vitro* experiments where the run length of motor-covered beads is measured (e. g., [33]).

For several motors pulling the cargo, we measured a mean separation between cargo and MT of $\overline{h} = 4 - 14$ nm. In a recent experimental study using fluorescence interference contrast microscopy it was found that kinesin holds its cargo about 17 nm away from the MT [77]. Our smaller distance probably results from neglecting any kind of volume extension (except binding site occupation) of the motor protein, the simplified force extension relation applied to model the stalk behavior, and neglecting electrostatic repulsions. Therefore, for future simulations it might be useful to account for these effects, e. g., by including a more realistic polymer model for the motor protein and by using hardcore interactions that account for the finite volume of the protein segments.

The simulations carried out so far demonstrated the applicability of the extended adhesive dynamics algorithm to active motor transport. In future simulations a couple of questions will be addressed which are difficult to treat analytically. For example Hill et al. found from *in vivo* experiments—where the *viscoelastic* friction on the cargo is about three orders of magnitude larger than that in a flow chamber—that the cargo moves with constant velocity for some period of time and then switches to another constant

velocity in a step-like fashion. The distribution of velocities is peaked at multiple values of the minimum observed velocity. It was argued that each velocity corresponds to a certain number of simultaneously pulling motors that share the load [69]. With our algorithm this situation can also be simulated *in silico* using large viscosities. Then, the instantaneous bead velocity can directly be correlated with the instantaneous number of pulling motors.

The question of 'how efficient is initial binding of a cargo particle in terms of its motor coverage' can be addressed with the method of calculating the MFPT for receptor-ligand encounter done in Chapter 3. Having many MTs aligned next to each other approximately corresponds to the situation of homogeneous ligand coverage. Then, for a cargo that is slightly denser than the surrounding medium the results for the MFPT in terms of N_r ($= N_{tot}$) in the diffusive limit (i. e., no shear flow) presented in Chapter 3 can also be applied for motor covered beads. It must be noted that in Chapter 3 it was found that the binding efficiency is especially enhanced by a large capture height r_0. For motors this roughly corresponds to the resting length $l_0/R \approx 0.05$ which turns out to be large as well.

Chapter 6

Summary and outlook

6.1 Summary

Motivated by the process of rolling adhesion of white blood cells, we investigated various aspects of specific receptor-ligand binding of a spherical particle to a wall in hydrodynamic flow. The particle was covered with receptor patches of varying density and size, and the wall was covered with a regular lattice of ligand patches of varying lattice constant. We presented an algorithm that allows to numerically simulate the motion of the spherical particle above the wall in linear shear flow by accurately taking into account the hydrodynamic interaction between the sphere and the wall, Brownian motion, and the influence of deterministic forces acting on the particle.

In Chapter 3 we numerically calculated the mean first passage time (MFPT) for the first encounter between a cell receptor and a wall ligand. Averaged over the sphere's initial orientation and initial position relative to the wall-ligands, the MFPT is a measure for the efficiency of initial binding of a sphere to a wall. We showed that the inverse of this time can be interpreted as the rate of encounter formation. For the MFPT dependence on the sphere's initial height above the wall we derived an exact expression. The MFPT in the limiting case of homogeneous receptor and ligand coverage defines the optimum efficiency of initial binding and could be solved exactly. Then, we investigated how the MFPT is modified for non-homogeneous coverage by modeling receptors as spherical patches on the sphere with capture height r_0 and ligands as spherical patches on the wall.

An important dimensionless parameter that measures the relative importance of hydrodynamic and diffusive motion is the Péclet number Pe. In the diffusive limit, i. e., for $Pe \approx 0$, we obtained a finite value for the MFPT. With increasing Pe the MFPT was always monotonically decreasing. Thus, the MFPT in the diffusive limit already defines a measure for the efficiency of initial binding. In this limit, it turned out that above a threshold value of a few hundreds, binding efficiency is enhanced only weakly upon increasing the number of receptor patches. Similarly, at very diluted ligand coverages the MFPT scales inversely with ligand density, but at ligand coverages above 1 % the MFPT deviates only weakly from the optimum value reached at 100 % coverage.

Regarding receptor geometry, increasing height increases binding efficiency much stronger than increasing lateral patch size. Our findings give an explanation why white blood cells adhere to the vessel walls through receptor patches localized to the tips of microvilli, and why malaria-infected red blood cells form elevated receptor patches, so-called *knobs*. For the case that the motion of the sphere is restricted to 2D, we were able obtain the MFPTs also by solving a reaction-diffusion equation. These analytical results allowed us to derive the proper scaling behavior for some limiting cases in terms of the strength of

the downward acting drift and the number of receptor patches, in very good agreement with our numerical findings.

In Chapter 4, we investigated the motion of white blood cells under the action of receptor-ligand bonds. For this we extended a version of Hammer's [66] adhesive dynamics algorithm by including Brownian motion and spatially resolved ligands. We first analytically demonstrated that a cell changes its motion from slipping to rolling under the action of bond forces and torques in the sense that $R\Omega/U$ becomes approximately 1, where Ω and U are angular and translational velocity of the cell, respectively. Then, we showed that depending on the parameters the cell exhibits distinct types of motion. Using the mean translational velocity $\langle U \rangle$, its standard deviation, and the mean angular velocity $\langle \Omega \rangle$, we defined five stationary states of cell motion. We systematically investigated the appearance of these stationary states with respect to the dimensionless on-rate $\pi = k_{on}/\dot{\gamma}$ (with shear rate $\dot{\gamma}$) and dimensionless unstressed off-rate $\epsilon_0 = k_0/\dot{\gamma}$ of the bonds in so-called *on-off* state diagrams. In these state diagrams the influence of different parameters was mapped to a phenomenological state of motion observable in experiments. For example for certain values of π, ϵ_0 and depending on the other parameters rolling occurred in the sense $R\langle\Omega\rangle/\langle U\rangle \to 1$. We argued that the numerically obtained state diagrams in Chapter 4 could be used to determine the on-rate of receptor-ligand bonds. This would be possible by comparing our results to flow chamber experiments based on recent nanotechnological developments that allow to control the ligand-ligand distance [8] and to observe the angular velocity by using receptor-covered beads which exhibit an optical anisotropy.

In addition to the numerical treatment, we also defined a simplified on-off model based on a master equation with non-trivial continuous drift term. By solving this model for constant off-rates, we were able to reproduce the numerically obtained general form of the mean velocity curve $\langle U \rangle$ depending on π and ϵ_0. But as the simplified model describes only motion in one dimension and as we neglected any force dependence on the off-rate, in the framework of the on-off model we were neither able to explain the appearance of rolling nor the influence of large viscosities. We concluded this chapter by showing that receptors that are located to the tips of *soft* microvilli (MV) mediate rolling in a much larger range of applied shear rates than receptors located on *stiff* MV. We could explain this increased robustness for soft MV by an increase in the number of bound MV in accordance with findings from Chen and Springer [29] and by the fact that for soft MV, the zone of bond formation is separated from the region were the tensile force on the bonds is highest.

In Chapter 5 we presented an extension of the adhesive dynamics algorithm that allows to apply our theoretical framework also to the active transport of a spherical cargo particle by molecular motors. Our algorithm includes microscopic details of this transport process, like Brownian motion of the spherical cargo, single motor actions (e. g., steps) and the effect of forces and torques exerted by a single motor on the cargo. We numerically calculated the mean run length of a sphere as a function of the total number of motors N_{tot} on the sphere. We showed that the mean run length of the sphere increases exponentially with N_{tot}. Klumpp and Lipowsky derived a similar result for the mean run length depending on the maximum number of simultaneously pulling motors N_m [83]. Our simulations showed that N_m is not a constant quantity as thermal fluctuations and torques exerted by attached motors continuously change the orientation of the sphere.

6.2 Outlook

The work presented in this thesis provides a very general framework which in the future could be used to study applications to different systems of interest in biophysics, cell

biology and biotechnology. Here, we have applied it to the initial stages of cell adhesion in shear flow (Chapter 3), rolling adhesion of white blood cells (Chapter 4) and cargo transport by several molecular motors (Chapter 5).

Regarding the initiation of cell adhesion in shear flow we considered only the encounter step of the whole receptor-ligand complex formation. In order to obtain a better comparison to experimental data, the presented analysis should be complemented by the implementation of an adhesion scenario, which in general should also include molecular determinants like residence times, receptor flexibility, and rupture probability of newly formed bonds. For example, it was argued that bonds may strengthen with increasing but small tensile force [46]. Such a catch bond behavior also affects the process of initial binding. Within our algorithm, the Bell model (which describes pure slip bonds) can be easily replaced with models that describe catch-slip bonds [12, 109]. A model extended in this way might then explain why the adhesion frequency for leukocytes first increases with increasing shear rate and then decreases again for even larger shear rates as experimentally observed in flow chamber experiments using P-selectin ligands [30]. Similarly, also the on-off state diagrams could be calculated for the case of catch bonds or other molecular adhesion scenarios.

Regarding the active cargo transport by several molecular motors it would be interesting to study also transport against the direction of an incident shear flow. This would combine the work of Chapter 4 with the ideas pursued in Chapter 5. Then, two opposing effects exist characterized by the step rate λ and the shear rate $\dot{\gamma}$, respectively. Their interplay together with the rates for binding and unbinding k_{on} and k_0, respectively, determine whether the cargo moves in walking direction or in flow direction (the latter either with hydrodynamic velocity or in a transient stop-go fashion, cf. Chapter 4). Experimentally, such a setup might provide interesting perspectives for biomimetic transport in microfluidic devices.

For the sake of computational and conceptual simplicity, in this thesis we have made several simplifying assumptions, including the assumptions of a single rigid particle in linear shear flow. In order to examine the contributions arising from deformations of the particle to the processes studied here, one could combine our simulation framework for specific adhesion with earlier work for deformable objects in shear flow, including droplets, vesicles and red blood cells [106, 92, 116]. In particular, the boundary element method could be used to account for the interactions between hydrodynamic flow and the cellular membrane [147].

Regarding the assumption of a single sphere corresponding to low cell densities, the derivation of the Euler algorithm Eq. (2.26) briefly sketched in Chapter 2 can also be extended to M rigid spheres. Then, formally Eq. (2.26) looks the same with the velocity $\mathbf{U}$ (force/torque $\mathbf{F}$) replaced by a $6M$ dimensional velocity (force/torque) vector and the mobility matrix M being a $6M \times 6M$ matrix [21]. Jones et al. give detailed descriptions of how to numerically obtain the mobility matrix for M spheres above a wall. The mobility matrix then does not only depend on the heights above the wall but also on the relative positions of the spheres to each other, which substantially increases the computational cost [32, 74]. A nice application for a two-sphere algorithm arises then in the context of active cargo transport studied in Chapter 5. For example, one could investigate synchronization effects between the stationary velocities of two cargoes pulled by motors due to hydrodynamic interactions. Furthermore, one could study the appearance of flow due to cargo transport observed in cells (*cytoplasmic streaming*) [139].

Instead of a linear shear flow one could also consider to extend our analysis to Poisseuille flow, which is relevant for experiments in narrow flow chambers and better mimics

the flow conditions in blood vessels. A numerical scheme to calculate the mobility matrix for a sphere in Poisseuille flow between two parallel walls was recently given by Jones [75].

In order to check our predictions experimentally, one can work either with biomimetic systems (e. g., latex microspheres covered with receptors) or with carefully prepared cellular systems. One especially appealing possibility is the use of malaria-infected red blood cells, which develop a fairly regular arrangement of adhesion patches on the cell surface (*knobs*). Using in addition a nanostructured substrate that forms a regular pattern of ligand patches one would obtain a very good experimental realization of our model system. Thus, one would hope to find good agreement with the MFPTs calculated in Chapter 3.

The proper knowledge of the MFPT could also be used to design cell sorting experiments. Suppose, one has a mixture of different cells each bearing some receptors and the wall is covered with one kind of ligand. Then, the cells are flowed into the chamber and flow is stopped. Certainly, only cells that bear receptors which fit to the ligands can attach to the wall. If the flow is then turned on again, the attached cells will be separated from the other cells. If the no-flow period is much shorter than the MFPT, only a few cells can attach. If the no-flow period is much longer than the MFPT, attached cells might already start to spread and are therefore difficult to remove. Only if the no-flow period is of the order of the MFPT one gets an appreciable number of weakly attached cells. In this sense the theoretical analysis presented in Chapter 3 might be essential for appropriate biotechnological applications.

Appendices

Appendix A

Varia

A.1 Units

Defining the following units: $U_M = 1/6\pi\eta R$ for mobility; $U_R = R$ for length scale, U_F for the force scale and U_T for the time scale and writing the Langevin-equation (2.21) in non-dimensionalized and time discretized form we obtain

$$\Delta\mathbf{X}_t = c_s\left(\mathbf{U}^\infty + \mathsf{M}\mathbf{F}^S\right)\Delta t + c_f\mathsf{M}\mathbf{F}^D\Delta t + c_d\nabla\mathsf{M}\Delta t + \sqrt{c_d}\Delta\mathbf{g}_t, \tag{A.1}$$

with the coefficients

$$c_s = \dot{\gamma}U_T,\ \ c_f = \frac{U_F U_T U_M}{U_R},\ \ c_d = k_B T_a \frac{U_M U_T}{U_R^2}.$$

In the following table these coefficients for different choices of U_F, U_T that are used for the different types of simulations carried out for this thesis are summarized:

	c_s	c_f	c_d	in Chapter
$U_F = 6\pi\eta R^2\dot{\gamma}$, $U_T = \frac{1}{\dot{\gamma}}$	1	1	$\frac{k_B T_a}{6\pi\eta R^3\dot{\gamma}}$	4
$U_F = 6\pi\eta R^2\dot{\gamma}$, $U_T = \frac{6\pi\eta R^3}{k_B T_a}$	$Pe = \frac{6\pi\eta R^3\dot{\gamma}}{k_B T_a}$	$Pe = \frac{6\pi\eta R^3\dot{\gamma}}{k_B T_a}$	1	2,3
$U_F = \frac{k_B T_a}{R}$, $U_T = \frac{6\pi\eta R^3}{k_B T_a}$	$Pe = \frac{6\pi\eta R^3\dot{\gamma}}{k_B T_a}$	1	1	–
$U_F = F_d$, $U_T = \frac{1}{\epsilon}$	$\dot{\gamma}/\epsilon$	$\frac{F_d}{6\pi\eta R^2\epsilon}$	$\frac{k_B T_a}{6\pi\eta R^3\epsilon}$	5

Table A.1: Coefficients for different choices of non-dimensionalizing the Langevin-equation Eq. (2.21).

A.2 Numerical time step

The numerical results presented in this thesis are based on the Euler algorithm Eq. (2.26) (see also App. B.3). Thus, the accuracy of these results depend on the used numerical time step (see also App. C). Here, we present different considerations that provide an upper limit for the time step.

For the MFPT calculations in Chapter 3 the numerical time step must be small enough to sample the trajectories at a resolution of the order of the capture height $r_0 \geq 10^{-3}$,

i. e., when the sphere is close to the wall the mean step length should be smaller than r_0. For the random update this leads to $r_0 > 0.1\sqrt{\Delta t} \Rightarrow \Delta t < 10^{-4}$ (including the effect of reduced mobility close to the wall). In addition, we obtain from the deterministic part of the update step in z-direction $\Delta t < r_0/Pe_z$. Thus, a time step of the order of 10^{-5} is reasonable for Pe_z of the order of 10^2. To keep a high spatial resolution also for large Pe a linear interpolation of the receptor's trajectory between two successive time steps is considered rather than a further decreased time step (see Sec. 3.4).

For the simulations carried out in Chapter 4 also the action of bond forces must be included for the time step estimate. Neglecting contributions from Brownian motion the sphere moves (considering the x-direction only and neglecting torques) by

$$\Delta x = U\Delta t = (\mu_{xx}^{tt} F_{B,x} + b_1)\Delta t$$

during time step Δt, where μ_{xx}^{tt} is a component of the mobility matrix (cf. Eq. (2.16)), $F_{B,x}$ is the bond force, and b_1 the hydrodynamic velocity (cf. Eq. (4.1)). Typically, the bond is stretched by the shear flow and the resulting bond force opposes the shear flow. If the bond was formed at $t = 0$ it will be stretched by $b_1\Delta t$ within the first time step. This leads to a bond force at $t = \Delta t$: $F_{B,x} = -\kappa b_1 \Delta t$. This bond force reduces the velocity of the sphere. However, if the numerical time step Δt is chosen too large the bond force may even revert the velocity. This artefact is avoided if $b_1 - \mu_{xx}^{tt}\kappa b_1 \Delta t > 0$. Thus, a reasonable numerical time step is given by

$$\Delta t \ll \frac{6\pi\eta R}{U_T \kappa} < \frac{1}{U_T \kappa \mu_{xx}^{tt}}, \tag{A.2}$$

with the time scale U_T introduced in Sec. A.1. If N_m bonds are simultaneously formed one can replace $\kappa \to N_m\kappa$ having an effectively stiffer bond. In the above analysis we neglected the effect of the bond resting length l_0. Including this effect corresponds to replacing the spring constant by $\kappa(1 - l_0/\|\mathbf{r}_l - \mathbf{r}_r\|) < \kappa$ (cf. Sec. 2.4.3). For rolling adhesion simulations at shear rates $\dot\gamma \approx 100$ Hz and for $\kappa = 10^{-3}$ N/m the estimate Eq. (A.2) gives $\Delta t \ll 5 \cdot 10^{-3}$. Similar considerations for the case of no shear flow lead the same estimate Eq. (A.2), which can therefore also be applied to the adhesive motor dynamics simulations carried out in Chapter 5.

So far, we only considered upper limits for the time step. A lower limit is given by limitations of available computing time. From a physical point of view a further limitation arises. In Sec. 2.2 we introduced a Gaussian white noise process Eq. (2.20) as an approximation for the physical noise. The approximation of uncorrelated noise is valid on time scales that are larger than $\Delta m/6\pi\eta R = 2\Delta\rho R^2/(9\eta) \approx 10^{-7}$ s (for $\Delta\rho = 50$ kg/m^3, $R = 5$ μm, $\eta = 1$ mPas) [21]. Thus, processes that involve a configuration change much faster than this time scale cannot properly be described by Eq. (2.26).

Appendix B

Stokesian dynamics

B.1 Implementation of friction and mobility matrices

For the numerical implementation of the friction and mobility tensors for a sphere in linear shear flow above a wall we use the results from Refs. [111, 31]. This implementation procedure has been described and tested in detail in Ref. [31]. In this appendix, we briefly summarize it.

Writing the friction tensors in terms of irreducible tensors formed from $\delta_{ij}, \epsilon_{ijk}, \mathbf{k}$ defines the scalar friction functions. In the case that the normal vector to the wall is $\mathbf{k} = \mathbf{e}_z$, these tensors read

$$\zeta^{tt} = \begin{pmatrix} \psi^{tt} & 0 & 0 \\ 0 & \psi^{tt} & 0 \\ 0 & 0 & \phi^{tt} \end{pmatrix}, \qquad \zeta^{tr} = \psi^{tr} \begin{pmatrix} 0 & 1 & 0 \\ -1 & 0 & 0 \\ 0 & 0 & 0 \end{pmatrix} = \zeta^{rtT},$$

$$\zeta^{rr} = \begin{pmatrix} \psi^{rr} & 0 & 0 \\ 0 & \psi^{rr} & 0 \\ 0 & 0 & \phi^{rr} \end{pmatrix},$$

$$\zeta^{td}_\alpha = \begin{pmatrix} -\frac{1}{3}\delta_{\alpha 3}\phi^{td} & 0 & \frac{1}{2}\delta_{\alpha 1}\psi^{td} \\ 0 & -\frac{1}{3}\delta_{\alpha 3}\phi^{td} & \frac{1}{2}\delta_{\alpha 2}\psi^{td} \\ \frac{1}{2}\delta_{\alpha 1}\psi^{td} & \frac{1}{2}\delta_{\alpha 2}\psi^{td} & \frac{2}{3}\delta_{\alpha 3}\phi^{td} \end{pmatrix}, \qquad \zeta^{rd}_\alpha = \frac{1}{2}\psi^{rd} \begin{pmatrix} 0 & 0 & \epsilon_{3\alpha 1} \\ 0 & 0 & \epsilon_{3\alpha 2} \\ \epsilon_{3\alpha 1} & \epsilon_{3\alpha 2} & 0 \end{pmatrix},$$

$$\zeta^{dt}_\alpha = \begin{pmatrix} \frac{1}{2}\delta_{\alpha 3}\psi^{dt} & 0 & -\frac{1}{3}\delta_{\alpha 1}\phi^{dt} \\ 0 & \frac{1}{2}\delta_{\alpha 3}\psi^{dt} & -\frac{1}{3}\delta_{\alpha 2}\phi^{dt} \\ \frac{1}{2}\delta_{\alpha 1}\psi^{dt} & \frac{1}{2}\delta_{\alpha 2}\psi^{dt} & -\frac{2}{3}\delta_{\alpha 3}\phi^{dt} \end{pmatrix}, \qquad \zeta^{dr}_\alpha = \frac{1}{2}\psi^{dr} \begin{pmatrix} 0 & \delta_{\alpha 3} & 0 \\ -\delta_{\alpha 3} & 0 & 0 \\ -\delta_{\alpha 2} & \delta_{\alpha 1} & 0 \end{pmatrix}.$$

This defines the scalar friction functions $\phi^{tt}, \psi^{tt}, \psi^{tr}, \phi^{rr}, \psi^{rr}, \phi^{td}, \psi^{td}, \psi^{dr}$. The scalar friction functions ϕ, ψ depend only on the inverse distance of the sphere from the wall, that is the dimensionless variable $s = R/z$, which takes values from the interval $[0, 1]$. The friction functions can be expanded in powers of s. The numerically obtained first 20 coefficients of such a series expansion of the dimensionless scalar friction functions

$$\hat{\phi}^{tt} = \phi^{tt}/6\pi\eta R, \qquad \hat{\psi}^{tt} = \psi^{tt}/6\pi\eta R, \qquad \hat{\phi}^{rr} = \phi^{rr}/8\pi\eta R^3,$$
$$\hat{\psi}^{rr} = \psi^{rr}/8\pi\eta R^3, \qquad \hat{\psi}^{tr} = \psi^{tr}/8\pi\eta R^2 = -\hat{\psi}^{rt}$$

are tabulated in Ref. [111]. For the other three dimensionless scalar friction functions

$$\hat{\phi}^{dt} = \phi^{dt}/6\pi\eta R^2 = \hat{\phi}^{td}, \qquad \hat{\psi}^{dt} = \psi^{dt}/6\pi\eta R^2 = \hat{\psi}^{td}, \qquad \hat{\psi}^{dr} = \psi^{dr}/8\pi\eta R^3 = -\hat{\psi}^{rd}$$

the first 32 coefficients of a series expansion in powers of s are tabulated in Ref. [31]. For small values of s the series expansion converges quite well and only a few coefficients are needed to obtain accurate results. However, for $s \to 1$, i. e., close to the wall, the friction functions are better described in a lubrication expansion, which reads

$$\hat{\phi} \approx C_1 \frac{s}{1-s} + C_2 \ln(1-s) + C_3 + C_4 \frac{1-s}{s} \ln(1-s) + \mathcal{O}(1-s). \tag{B.1}$$

The coefficients C_1, C_2, C_3, C_4 for the eight friction functions defined above can be found in Ref. [31] and are cited in Tab. B.1 (Exact expressions for C_1, C_2, C_4 for the case of lubrication flow between two unequal-sized spheres have been given before by Jeffrey and Onishi [73], the correct coefficients for a sphere above a wall then follow in the limit that one sphere becomes infinitely large.). In order to match the two limit cases, to the

	$\hat{\phi}^{tt}$	$\hat{\psi}^{tt}$	$\hat{\phi}^{rr}$	$\hat{\psi}^{rr}$	$\hat{\psi}^{tr}$	$\hat{\phi}^{dt}$	$\hat{\psi}^{dt}$	$\hat{\psi}^{dr}$
C_1	1	0	0	0	0	-1	0	0
C_2	$-\frac{1}{5}$	$-\frac{8}{15}$	0	$-\frac{2}{5}$	$\frac{1}{10}$	$-\frac{4}{5}$	$\frac{14}{15}$	$\frac{1}{5}$
C_3	0.97127	0.95429	$\zeta(3)$	0.37089	0.19295	-0.30697	1.23538	0.18719
C_3	$-\frac{1}{21}$	$-\frac{64}{375}$	0	$-\frac{66}{125}$	$\frac{43}{250}$	$-\frac{13}{21}$	$\frac{442}{375}$	$-\frac{2}{125}$

Table B.1: Coefficients of the lubrication expansion for the scalar friction function from Ref. [31]. $\zeta(x)$ is the zeta function.

asymptotic expansion of the $s \to 1$ limit is subtracted from the friction functions

$$\hat{\phi}(s) = \sum_{n=0}^{\infty} f_n s^n,$$

leading to a new series expansion:

$$\begin{aligned} &\hat{\phi}(s) - C_1 \frac{s}{1-s} - C_2 \ln(1-s) - C_4 \frac{1-s}{s} \ln(1-s) \\ &\quad = f_0 + C_4 + \sum_{n=1}^{\infty} \left(f_n - C_1 + \frac{C_2}{n} - \frac{C_4}{n(n+1)} \right) s^n =: \sum_{n=0}^{\infty} g_n s^n. \end{aligned}$$

This series is truncated at $n_{max} \equiv K$ and the coefficients g_n are calculated from the coefficients f_n, C_i. Next, the coefficients g_n $(n = 0, \ldots, K)$ are not used to calculate the Taylor sum, but rather to calculate the Padé approximant to this function. The Padé approximant is given as

$$\mathcal{P}_K(s) = \frac{a_0 + a_1 s + a_2 s^2 + \ldots + a_K s^K}{1 + b_1 s + b_2 s^2 + \ldots + b_K s^K},$$

where the coefficients a_i, b_j are the solution to

$$\sum_{n=1}^{K} b_n g_{K-n+k} = -g_{n+k}, \qquad \sum_{n=1}^{k} b_n g_{k-n} = a_k, \qquad k = 1, \ldots, K.$$

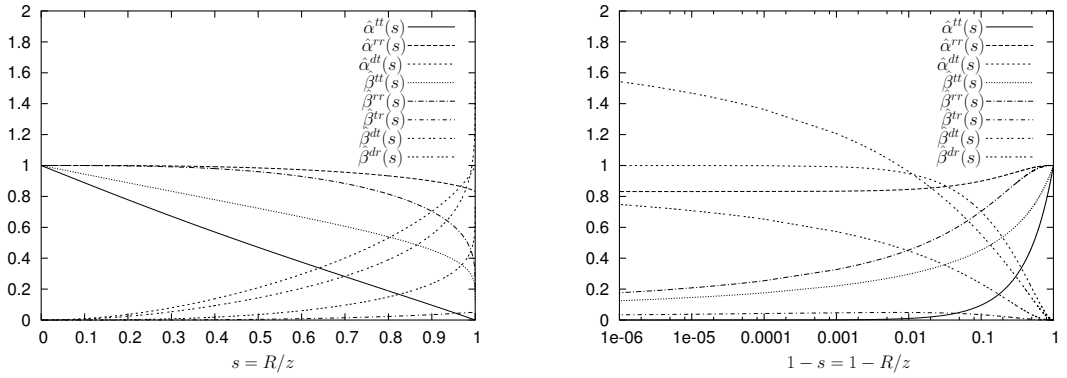

(a) (b)

Figure B.1: Dimensionless scalar mobility functions. (a) Plotted versus the dimensionless parameter s. (b) Plotted versus $1 - s$, thus better illustrating the asymptotic behavior for $s \to 1$ (in log-scale for the horizontal axis).

Finally, the numerically implemented friction functions become

$$\hat{\phi}(s) = C_1 \frac{s}{1-s} + C_2 \ln(1-s) + C_4 \frac{1-s}{s} \ln(1-s) + \mathcal{P}_K(s). \tag{B.2}$$

For the calculation of the coefficients a_i, b_j of the Padé approximant we use the algorithm provided by the Numerical Recipes [117].

As mentioned in the introduction the scalar friction functions have been calculated using a finite element method and tabulated for some selected height values by Goldman et al. [59, 60]. In Refs. [111, 31] these values are cited and compared to their own reflection series results. These tables show excellent agreement between the two numerical results. Furthermore, they provided us with the possibility to obtain favorable checks for the implementation of the scalar friction functions.

Having implemented the scalar friction functions, the implementation of the mobility tensors proceeds by substituting $\zeta \leftrightarrow \mu, \phi \leftrightarrow \alpha, \psi \leftrightarrow \beta$ in the above decomposition of the friction tensors. This defines the scalar mobility functions $\alpha^{tt}, \beta^{tt}, \alpha^{rr}, \beta^{rr}, \beta^{tr}, \alpha^{dt}, \beta^{dt}, \beta^{dr}$. Using Eq. (2.16) the dimensionless scalar mobility functions can be calculated from the scalar friction functions:

$$\begin{aligned}
&\hat{\alpha}^{tt} = 1/\hat{\phi}^{tt}, \qquad \hat{\beta}^{tt} = \frac{\hat{\psi}^{rr}}{\hat{\psi}^{tt}\hat{\psi}^{rr} - \frac{4}{3}(\hat{\psi}^{tr})^2}, \\
&\hat{\alpha}^{rr} = 1/\hat{\phi}^{rr}, \qquad \hat{\beta}^{rr} = \frac{\hat{\psi}^{tt}}{\hat{\psi}^{tt}\hat{\psi}^{rr} - \frac{4}{3}(\hat{\psi}^{tr})^2}, \\
&\hat{\beta}^{tr} = -\hat{\beta}^{rt} = -\frac{4}{3}\frac{\hat{\psi}^{tr}}{\hat{\psi}^{tt}\hat{\psi}^{rr} - \frac{4}{3}(\hat{\psi}^{tr})^2}, \qquad \hat{\alpha}^{dt} = -\hat{\alpha}^{td} = -\hat{\phi}^{dt}\hat{\alpha}^{tt}, \\
&\hat{\beta}^{dt} = -\hat{\beta}^{td} = -\hat{\psi}^{dt}\hat{\beta}^{tt} - \hat{\psi}^{dr}\hat{\beta}^{tr}, \qquad \hat{\beta}^{dr} = \hat{\beta}^{rd} = -\frac{3}{4}\hat{\psi}^{dt}\hat{\beta}^{tr} - \hat{\psi}^{dr}\hat{\beta}^{rr}.
\end{aligned} \tag{B.3}$$

The asymptotic behavior of the scalar mobility functions for $s \to 1$ follows from inserting Eq. (B.1) into Eq. (B.3) (for example for $\hat{\alpha}^{tt}$ it follows $\hat{\alpha}^{tt}(s) \approx 1 - s$ [31]). In Fig. B.1 we use our implementation to plot the eight dimensionless mobility functions.

The limit of an unbounded flow corresponds to $s \to 0$ and results in

$$\zeta^{tt} = 6\pi\eta R I, \;\; \zeta^{rr} = 8\pi\eta R^3 I, \;\; \zeta^{tr} = \zeta^{rt} = \zeta^{rd} = \zeta^{td} = 0, \tag{B.4}$$

where I is the unity matrix. Thus, Eq. (2.13) reduces to

$$\mathbf{F}^H = 6\pi\eta R \left(\mathbf{U} - \mathbf{U}^\infty\right), \qquad \mathbf{T}^H = 8\pi\eta R^3 \left(\mathbf{\Omega} - \mathbf{\Omega}^\infty\right). \tag{B.5}$$

This are the well-known Stokes laws for the friction force and torque exerted on a sphere moving in a fluid with relative velocity $\mathbf{U} - \mathbf{U}^\infty$. For the linear shear flow considered here, $\mathbf{U}^\infty = \dot\gamma z \mathbf{e}_x$ and $\mathbf{\Omega}^\infty = \dot\gamma \mathbf{e}_y/2$.

B.2 Relation to the Smoluchowski equation

The probability distribution $\Psi(\mathbf{X}, t)$ of a Brownian particle subject to external force/torque $\mathbf{F}$ satisfies a continuity equation $\partial_t \Psi + \nabla \cdot \mathbf{J} = 0$. The probability flux $\mathbf{J}$ contains a diffusive and a convective part [157]:

$$J_i = -\mathsf{D}_{ij} \partial_j \Psi + \mathsf{M}_{ij} F_j \Psi, \tag{B.6}$$

where D and M are diffusion and mobility matrices, respectively, and $\mathbf{F}$ is external force. In equilibrium, the flux has to vanish and the probability distribution has to become the Boltzmann distribution. This leads to the Einstein relation $\mathsf{D} = k_B T_a \mathsf{M}$, which is a special case of the fluctuation-dissipation theorem. Using Eq. (B.6) and the Einstein relation in the continuity equation leads to the Smoluchowski equation [36]:

$$\partial_t \Psi = \partial_i \left(\mathsf{M}_{ij} (k_B T_a \partial_j \Psi - \mathbf{F}_j \Psi)\right). \tag{B.7}$$

We now will derive the equivalent Langevin equation. In the case of constant mobility (*additive noise*), e. g., $\mathsf{M}_{ij} = \delta_{ij}$, the appropriate Langevin equation is given by

$$\partial_t \mathbf{X}_t = \mathsf{M}\mathbf{F} + \mathbf{g}_t^S, \tag{B.8}$$

where $\mathbf{g}_t^S$ is a Gaussian white noise term and the Stratonovich interpretation is used as explained in Sec. 2.2. However, if M depends on $\mathbf{X}$ (*multiplicative noise*), an additional drift term occurs in the Langevin equation

$$\partial_t \mathbf{X}_t = \mathsf{M}\mathbf{F} + k_B T_a \mathbf{Y} + \mathbf{g}_t^S. \tag{B.9}$$

The following derivation of the drift term $\mathbf{Y}$ proceeds in two steps. First, we perform a coordinate transformation which makes the noise additive. In the case of additive noise the Langevin equation (B.8) and the Fokker-Planck equation (B.7) are equivalent. Then, starting from the Fokker-Planck equation in the new coordinates we perform the transformation back to the old coordinates. Requiring the transformed Fokker-Planck equation to be of the same form as in Eq. (B.7), determines the drift term $\mathbf{Y}$.

As we use the Stratonovich interpretation for the noise process the usual rules for differentiation and integration apply and we can perform the following coordinate trans-

formation (cf. Ref. [36] for the one-dimensional case)

$$\mathbf{X}' = \int^{\mathbf{X}(t)} \mathsf{S}(\mathbf{X}'')\mathrm{d}\mathbf{X}'', \tag{B.10}$$

with some regular matrix S. The Langevin equation for the transformed coordinates then reads

$$\partial_t \mathbf{X}'_t = \mathsf{S}\partial_t \mathbf{X}_t = \mathsf{SM}\mathbf{F} + k_B T_a \mathsf{S}\mathbf{Y} + \mathsf{S}\mathbf{g}^S_t. \tag{B.11}$$

From the requirement that $\mathsf{M}'_{ij} = \delta_{ij}$, that is

$$\langle \mathsf{S}\mathbf{g}_t \mathsf{S}\mathbf{g}_t \rangle \stackrel{!}{=} 2k_B T_a \mathsf{E}, \qquad \mathsf{E}_{ij} := \delta_{ij}, \tag{B.12}$$

we can fix S to be the inverse of a matrix B with

$$\mathsf{S} = \mathsf{B}^{-1}, \qquad \mathsf{M} = \mathsf{B}\mathsf{B}^T \qquad \Leftrightarrow \qquad \mathsf{M}_{ij} = \mathsf{B}_{ik}\mathsf{B}_{jk}. \tag{B.13}$$

As M is a symmetric positive definite matrix, it is always possible to find a matrix B with $\mathsf{M} = \mathsf{B}\mathsf{B}^T$. Defining

$$\mathbf{F}' := \mathsf{B}^T\mathbf{F} + k_B T_a \mathsf{S}\mathbf{Y}, \qquad \tilde{\mathbf{g}}^S_t := \mathsf{S}\mathbf{g}^S_t = \mathsf{B}^{-1}\mathbf{g}^S_t, \tag{B.14}$$

the new Langevin equation for the primed coordinates and with additive noise reads

$$\partial_t \mathbf{X}'_t = \mathsf{M}'\mathbf{F}' + \tilde{\mathbf{g}}^S_t. \tag{B.15}$$

The corresponding probability distribution $\Psi'(\mathbf{X}', t)$ is the solution of the Smoluchowski equation

$$\partial_t \Psi'(\mathbf{X}', t) = \partial'_k \delta_{ki}(k_B T_a \partial'_i \Psi' - F'_i \Psi'). \tag{B.16}$$

Next, we transform (B.16) back to the unprimed coordinates. The preservation of probability requires that

$$\Psi'(\mathbf{X}', t) = J\Psi(\mathbf{X}, t), \tag{B.17}$$

where J is the Jacobian of the coordinate transformation [96]:

$$J := \det\left(\frac{\partial X_i}{\partial X'_j}\right) = \det(\mathsf{B}), \qquad \frac{\partial X_i}{\partial X'_j} = \mathsf{B}_{ij}. \tag{B.18}$$

Inserting (B.17) into (B.16) gives

$$\partial_t \Psi' = J\partial_t \Psi = \partial'_k(k_B T_a \partial'_k \Psi' - F'_k \Psi') = k_B T_a \partial'_k \partial'_k J\Psi - \partial'_k F'_k J\Psi. \tag{B.19}$$

Dividing by J we obtain for the first term on the right hand side of (B.19)

$$\begin{aligned} J^{-1}\partial'_k \partial'_k J\Psi &= J^{-1}(\partial'_k \partial'_k J)\Psi + 2J^{-1}(\partial'_k J)\partial'_k \Psi + \partial'_k \partial'_k \Psi \\ &= \partial_j(\mathsf{B}_{jk}\mathsf{B}_{lk}\partial_l \Psi + \mathsf{B}_{jk}(\partial_l \mathsf{B}_{lk})\Psi). \end{aligned}$$

Here, we made use of the identities

$$J^{-1}\nabla' J = \nabla \mathsf{B}^T, J^{-1}\partial_i' J = \partial_j \mathsf{B}_{ji}, \qquad \nabla' = \mathsf{B}^T\nabla, \tag{B.20}$$
$$\begin{aligned} J^{-1}\partial_i'\partial_j' J &= J^{-1}\partial_i'(JJ^{-1})\partial_j' J = J^{-1}(\partial_i' J)J^{-1}\partial_j' J + \partial_i'(J^{-1}\partial_j' J) \\ &= (\partial_k \mathsf{B}_{ki})\partial_l \mathsf{B}_{lj} + \mathsf{B}_{li}\partial_l\partial_k \mathsf{B}_{kj}. \end{aligned}$$

Again, using the identity (B.20) the second term of the right hand side of (B.19) can be evaluated to be

$$J^{-1}\partial_k' F_k' J\Psi = J^{-1}(\partial_k' J)F_k'\Psi + \partial_k' F_k'\Psi = \partial_j(\mathsf{B}_{jk}F_k'\Psi).$$

Adding both terms and inserting the definitions (B.13) and (B.14) we have

$$\partial_t\Psi = \partial_j\left(k_B T_a \mathsf{M}_{jl}\partial_l\Psi + k_B T_a \mathsf{B}_{jk}(\partial_l \mathsf{B}_{lk})\Psi - \mathsf{M}_{jl}F_l - k_B T_a Y_j\Psi\right).$$

Comparing this with the required result (B.7) we can read off $\mathbf{Y}$

$$\mathbf{Y} = \mathsf{B}\nabla\mathsf{B}^T, \qquad Y_i = \mathsf{B}_{ik}(\partial_l \mathsf{B}_{lk}).$$

Finally, shifting $\partial_t\mathbf{X}_t \to \partial_t\mathbf{X}_t - \mathbf{U}^\infty$ we obtain the Langevin equation as given by Eq. (2.21) combined with Eq. (2.22).

B.3 Euler algorithm for a sphere above a wall

In order to solve Eq. (2.23) numerically we use an Euler algorithm. As the physical situation requires to use the Stratonovich interpretation of the noise term $\mathbf{g}_t^S$, the displacement $\Delta\mathbf{X}$ of a particle from time t to time $t+\Delta t$ depends on the position of the particle at time $t + (1/2)\Delta t$, which is not known at time t. As usual, this problem is solved by rewriting the Langevin equation in the Itô-version. Then, the noise term can be evaluated at time t and as a compensation an additional drift term $\partial_l(\mathsf{B}_{ik})\mathsf{B}_{lk}$ is added to Eq. (2.23) [157]. Because $\mathsf{B}_{kl}^T\partial_l(\mathsf{B}_{ik}) + \mathsf{B}_{ik}\partial_l(\mathsf{B}_{kl}^T) = \partial_l(\mathsf{B}_{ik}\mathsf{B}_{kl}^T) = \partial_l \mathsf{M}_{il}$, we arrive at Eq. (2.25). In this equation, the random displacements $\mathbf{g}(\Delta t)$ must satisfy

$$\langle \mathbf{g}(\Delta t)\rangle = 0, \qquad \langle \mathbf{g}(\Delta t)\mathbf{g}(\Delta t)\rangle = 2\mathsf{M}\Delta t. \tag{B.21}$$

Following Ref. [44], $\mathbf{g}_i(\Delta t)$ is calculated from a weighted sum of normal deviate random numbers $\bar{x}_i \to \{x_i\}$ satisfying $\langle x_i\rangle = 0, \langle x_i x_j\rangle = 2\delta_{ij}\Delta t$. This sum is given by

$$\mathbf{g}_i(\Delta t) = \sum_{j=1}^{i} \mathsf{B}_{ij}\bar{x}_j,$$

where the weighting factors are the elements of the matrix B defined in (B.13). They can recursively be calculated according to

$$\mathsf{B}_{ii} = \left(\mathsf{M}_{ii} - \sum_{k=1}^{i-1}\mathsf{B}_{ik}^2\right)^{\frac{1}{2}}, \qquad \mathsf{B}_{ij} = \left(\mathsf{M}_{ij} - \sum_{k=1}^{j-1}\mathsf{B}_{ik}\mathsf{B}_{jk}\right)/\mathsf{B}_{jj}, i > j, \qquad \mathsf{B}_{ij} = 0, i < j.$$

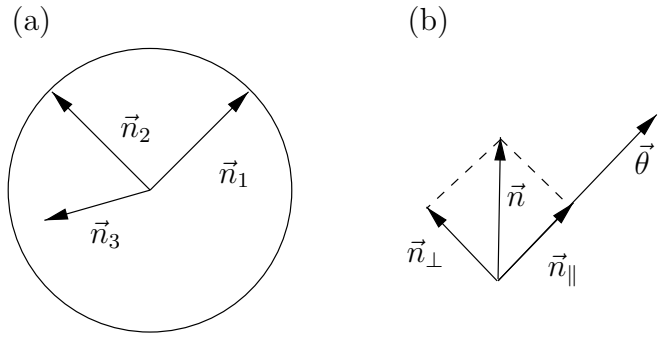

Figure B.2: (a) Shows the coordinate system fixed to the sphere. (b) Decomposition of the basis vectors $\vec{n}$ in components parallel and perpendicular to $\vec{\theta}$, $\vec{n}_\parallel$ and $\vec{n}_\perp$, respectively.

In the case of a sphere above a wall we obtain the following dimensionless weighting factors (cf. Ref. [76])

$$\hat{\mathsf{B}}_{11} = \sqrt{\hat{\beta}^{tt}}, \qquad \hat{\mathsf{B}}_{22} = \sqrt{\hat{\beta}^{tt}}, \qquad \hat{\mathsf{B}}_{33} = \sqrt{\hat{\alpha}^{tt}}, \qquad \hat{\mathsf{B}}_{42} = -\hat{\mathsf{B}}_{51} = -\frac{3}{4}\frac{\hat{\beta}^{tr}}{\sqrt{\hat{\beta}^{tt}}},$$

$$\hat{\mathsf{B}}_{44} = \hat{\mathsf{B}}_{55} = \frac{3}{4}\frac{1}{\sqrt{\hat{\beta}^{tt}}}\left(\frac{4}{3}\hat{\beta}^{tt}\hat{\beta}^{rr} - (\hat{\beta}^{tr})^2\right)^{\frac{1}{2}} \equiv \sqrt{\frac{3}{4\hat{\psi}^{rr}}}, \qquad \hat{\mathsf{B}}_{66} = \frac{1}{2}\sqrt{3\hat{\alpha}^{rr}}. \tag{B.22}$$

As pointed out in Ref. [70], using the Euler method, instead of normal deviate random variables any uncorrelated random variable $\bar{x}_i \to \{x_i, i = 1, \ldots, 6\}$ can be chosen, as long as they fulfill the required relation for the first moments $\langle x_i \rangle = 0, \langle x_i x_j \rangle = 2\delta_{ij}\Delta t$. Thus, it is much faster to generate the random numbers according to $\bar{x}_i = \sqrt{24\Delta t}(\xi_i - 0.5)$, with $\xi_i, i = 1, \ldots, 6$ being uncorrelated random variables uniformly distributed in $[0, 1]$.

Using the dimensionless constants c_s, c_f, c_d which result from a special choice of scales and have been introduced in Appendix A.1, the explicit update rules for six components of $\Delta\mathbf{X}$ in Eq. (2.26) are:

$$\begin{aligned}
\Delta\mathbf{X}_1 &= \Delta t(c_s(z - 0.5\hat{\beta}^{dt}(1/z)) + c_f(F_x\hat{\beta}^{tt}(1/z) + 0.75T_y\hat{\beta}^{tr}(1/z))) + \sqrt{c_d}\mathbf{g}_1(\Delta t)\\
\Delta\mathbf{X}_2 &= c_f\Delta t(F_y\hat{\beta}^{tt}(1/z) - 0.75T_x\hat{\beta}^{tr}(1/z)) + \sqrt{c_d}\mathbf{g}_2(\Delta t)\\
\Delta\mathbf{X}_3 &= \Delta t(c_sF_z\hat{\alpha}^{tt}(1/z) + c_d\partial_z\hat{\alpha}^{tt}(1/z)) + \sqrt{c_d}\mathbf{g}_1(\Delta t)\\
\Delta\mathbf{X}_4 &= 0.75c_f\Delta t(T_x\hat{\beta}^{rr}(1/z) - F_y\hat{\beta}^{tr}(1/z)) - \sqrt{c_d}\mathbf{g}_4(\Delta t)\\
\Delta\mathbf{X}_5 &= \Delta t(0.5c_s(1 - \hat{\beta}^{dr}(1/z)) + 0.75c_f(T_y\hat{\beta}^{rr}(1/z) + F_x\hat{\beta}^{tr}(1/z))) + \mathbf{g}_5(\Delta t)\\
\Delta\mathbf{X}_6 &= 0.75c_f\Delta tT_z\hat{\alpha}^{rr}(1/z) + \sqrt{c_d}\mathbf{g}_6(\Delta t)
\end{aligned} \tag{B.23}$$

Calculating the new configuration after each time step using (2.26) is straightforward for the spatial degrees of freedom. For the update of the orientation of the sphere we use a coordinate system spanned by three orthonormal basis vectors $\{\vec{n}_i | i = 1, 2, 3; (\vec{n}_i)_j = \delta_{ij}\}$, see Fig. B.2. The origin of this coordinate system shall be identical with the center of mass of the sphere and the relative orientation of this system and of the sphere are kept fixed. Given then an orientation update from (2.26) $\vec{\theta} := (\Delta\mathbf{X}_4, \Delta\mathbf{X}_5, \Delta\mathbf{X}_6)$, we decompose each of the basis vectors $\vec{n}_i$ into a component parallel to $\vec{\theta}$ denoted by $\vec{n}_\parallel$ and a component perpendicular to $\vec{\theta}$ denoted by $\vec{n}_\perp$ (the index i is dropped for the sake of simplicity).

These components are given by

$$\vec{n}_{\parallel} = \hat{\theta}(\hat{\theta} \cdot \vec{n}), \qquad \hat{\theta} := \vec{\theta}/\|\vec{\theta}\|$$
$$\vec{n}_{\perp} = \vec{n} - \hat{\theta}(\hat{\theta} \cdot \vec{n}).$$

Then, the orientation update affects only $\vec{n}_{\perp}$ and the updated $\vec{n}'$ is given by (with $\theta := \|\vec{\theta}\|$)

$$\vec{n}_i' = \hat{\theta}(\hat{\theta} \cdot \vec{n}_i)(1 - \cos\theta) + \vec{n}_i \cos\theta + \hat{\theta} \times \vec{n}_i \sin\theta, \qquad i = 1, 2, 3. \tag{B.24}$$

It can easily be verified that $\vec{n}_i' \cdot \vec{n}_j' = \delta_{ij}$ (Goldstein provides a similar expression with $\theta \leftrightarrow -\theta$ which corresponds to the rotation of a vector in a fixed coordinate system [62]).

In Ref. [76] it was pointed out that without external forces (torques) the following limit holds

$$\lim_{\Delta t \to 0} \frac{\langle \vec{n}_i' - \vec{n}_i \rangle}{\Delta t} = \mathsf{D}^{rr} \vec{n}_i - (\mathrm{tr}\ \mathsf{D}^{rr})\, \vec{n}_i, \tag{B.25}$$

where $\mathsf{D}^{rr}/k_B T_a$ is the rotational sector of the mobility matrix. Eq. (B.25) states that rotational diffusion causes a systematic drift in the orientation of the coordinate system fixed relative to the sphere. This is due to the fact that the group of rotations is non-Abelian. Without the wall D^{rr} is isotropic and the drift $\langle \vec{n}_i' - \vec{n}_i \rangle$ is parallel to $\vec{n}_i$. In the presence of the wall the anisotropic part of D^{rr} shifts the direction of $\langle \vec{n}_i' - \vec{n}_i \rangle$ away from that of $\vec{n}_i$ [76]. Together with Eq. (B.21) it can be shown that the update rule Eq. (B.24) obeys Eq. (B.25). In Ref. [76] a different version of the Euler algorithm is given. There, the update of the normal vectors $\vec{n}_i$ is given by $\vec{\theta} \times \vec{n}_i$ which is of first order in $\vec{\theta}$ plus an additional term which ensures that for $\langle \vec{n}_i' - \vec{n}_i \rangle$ relation B.25 is fulfilled which is a second order effect with respect to θ.

Appendix C

Reducing the systematic error in MFPT algorithm

Applying the Euler algorithm Eq. (2.26) to the mean first passage time problems (MFPT) carried out in Chapter 3 gives rise to two sorts of errors. First, there exists the statistical error, which is proportional to $1/\sqrt{N}$, where N is the number of iterations the algorithm is applied. The extent of the statistical error of the measured mean value can be calculated during the simulation. For the measurements performed in Secs. 3.3 - 3.4 typically $N \sim 10^5$ iterations where chosen resulting in statistical errors in the range of $< 1\%$. Error bars in these sections refer to the statistical error.

The systematic error for the mean first passage time calculated by use of an Euler algorithm scales with $\sqrt{\Delta t}$, although the error of the particle position is only of the order of Δt [70]. Thus, to decrease the systematic error by a factor of 10 one must increase the numerical cost by a factor of 100. One way to obtain accurate results at moderate numerical cost is to measure the mean first passage time for various intermediate numerical time steps. Fitting these results to $a + b\sqrt{\Delta t}$ allows the extrapolation to $\Delta t \to 0$. Fig. C.1 shows an example where this procedure was applied to the case of homogeneous coverage as considered in Sec. 3.1. The resulting mean first passage time then deviates by 0.2% from the value obtained from quadrature of Eq. (3.3). This is the same accuracy as we have for the implemented mobility functions themselves (cf. Appendix B.1).

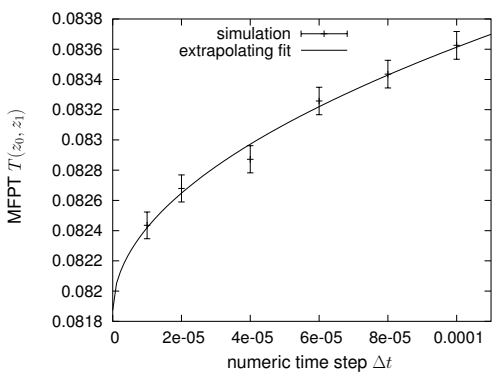

Figure C.1: Mean first passage time $T(z_0, z_1)$ with initial height $z_0 = 2$ and final height $z_1 = 1.001$ as a function of the numerical time step Δt ($Pe_z = 100$). The points are the results from simulation experiments (error bars denote their statistical error) with $N = 10^5$ iterations. The full line is a fit to $a + b\sqrt{\Delta t}$ using the gnuplot implementation of the nonlinear least-squares (NLLS) Marquardt-Levenberg algorithm. Extrapolating the fit to $\Delta t \to 0$ reduces the systematic error which is caused by the finite time step.

Appendix D

On-off model for adhesion states

In this appendix we provide a scheme how the general solution to (4.17-4.19) can be constructed. Furthermore, we give some steps explicitly which were omitted in the calculation in Sec. 4.3.2.

D.1 General solution of the on-off model

Equations (4.17-4.19) can be solved recursively starting with Eq. (4.19). First, we perform a linear orthogonal transformation O^{N_m} for the coordinates that transforms Eq. (4.19) into an first order ordinary differential equation. The transformed coordinates are given by[1]

$$x'_j = \mathsf{O}^{N_m}_{ji} x_i,$$

where O^{N_m} has the following properties $\mathsf{O}^{N_m}_{1j} = 1/\sqrt{N_m}, j = 1, \ldots, N_m$ and $\sum_{k=1}^{N_m} \mathsf{O}^{N_m}_{ik} = 0, i = 2, \ldots, N_m$. Then, the sum of partial derivatives transforms as

$$\sum_{i=1}^{N_m} \frac{\partial}{\partial x_i} = \sum_{i=1}^{N_m} \frac{\partial x'_j}{\partial x_i} \frac{\partial}{\partial x'_j} = \sum_{i=1}^{N_m} \mathsf{O}^{N_m}_{ji} \frac{\partial}{\partial x'_j} = \sqrt{N_m} \frac{\partial}{\partial x'_1}.$$

Due to the orthogonality of the transformation O and the preservation of probability, the probability density function for the transformed coordinates is $\bar{p}_{N_m}(\mathbf{x}'_{N_m}) = p_{N_m}\left(\left(\mathsf{O}^{N_m}\right)^{-1} \mathbf{x}'_{N_m}\right)$. Integrating the transformed equation Eq. (4.19) and transforming back to the original coordinates $\mathbf{x}_{N_m}$, one obtains

$$p_{N_m}(\mathbf{x}_{N_m}) = \frac{\bar{p}_{N_m}}{U(x_{b,N_m})} \exp\left(-\frac{1}{N_m} \int^{x_{b,N_m}} \frac{\sum_{j=1}^{N_m} \epsilon((x' + N_m x_j - x_{b,N_m})/N_m)}{U(x')} dx' \right), \quad \text{(D.1)}$$

with a normalization constant $\bar{p}_{N_m}$.

In a similar fashion the i-bond probability density function can be obtained for $i =$

[1] Here, the Einstein summation convention is applied. That is, an index that appears twice is summed over.

$1, \ldots, N_m - 1$. It turns out that the solution for p_i involves an integral over p_{i+1}:

$$p_i(\mathbf{x}_i) = \frac{1}{U(x_{b,i})} \left[\bar{p}_i \exp\left(-\frac{1}{i} \int^{x_{b,i}} \frac{\pi_i + \sum_{j=1}^{i} \epsilon((x' + ix_j - x_{b,i})/i)}{U(x')} dx' \right) \right.$$
$$+ \frac{1}{i} \int_{x_{b,max}}^{x_{b,i}} dx' \exp\left(-\frac{1}{i} \int_{x'}^{x_{b,i}} \frac{\pi_i + \sum_{j=1}^{i} \epsilon((x'' + ix_j - x_{b,i})/i)}{U(x'')} dx'' \right)$$
$$\left. \times \sum_{j=1}^{i+1} \int dx_j \epsilon(x_j) p_{i+1}(\mathbf{x}_i(x'), x_j) \right]. \tag{D.2}$$

The sum in the last term $\left[\sum_{j=1}^{i+1} \int dx_j \epsilon(x_j) \ldots\right]$ can be replaced by $\left[(i+1) \int dx_{i+1} \epsilon(x_{i+1}) \ldots\right]$ as the i-bond probability density function must be symmetric with respect to a permutation of its arguments. The normalization constants $\bar{p}_i, i = 1, \ldots, N_m$ have to be chosen such that Eq. (4.20) and Eq. (4.21) are fulfilled.

It must be noted that Eq. (D.2) is only a formal expression built form the general solution for an inhomogeneous first order differential equation. Using the Bell model for the escape rates $\epsilon(x) = \epsilon_0 \exp(\kappa x / F_d)$, the series of integrals in (D.1, D.2) can only be evaluated with high numerical cost which is far beyond the original intention of this on-off model.

D.2 Constant off-rates

For a constant off-rate, $\epsilon = \epsilon_0$, Eqs. (4.17 - 4.19) simplify to

$$\pi_0 p_0 = \epsilon_0 P_1 \tag{D.3}$$

$$\sum_{k=1}^{i} \partial_k \left[U(x_{b,i}) p_i(\mathbf{x}_i) \right] = -\left(\pi_i + i\epsilon_0\right) p_i(\mathbf{x}_i) + (i+1)\epsilon_0 \int dx_{i+1} p_{i+1}(\mathbf{x}_i, x_{i+1}),$$
$$i = 1, \ldots, N_m - 1 \tag{D.4}$$

$$\sum_{k=1}^{N_m} \partial_k \left[U(x_{b,N_m}) p_{N_m}(\mathbf{x}_{N_m}) \right] = -N_m \epsilon_0 p_{N_m}(\mathbf{x}_{N_m}) \tag{D.5}$$

Inserting the ansatz Eq. (4.22) for the i-bond state $p_i(\mathbf{x}_i)$ into Eq. (D.4), the term on the left-hand side becomes

$$\sum_{k=1}^{i} \partial_k \left[U(x_{b,i}) p_i(\mathbf{x}_i) \right] = -\sum_{j=0}^{N_m - i} \mu i (\nu_{i+j} + j) a(i,j) \prod_{l=0}^{i-1} \mu(\nu_{i+j} + j + l) U(x_{b,i})^{\nu_{i+j} - 1 + j}.$$

The first term on the right-hand side of Eq. (D.4) becomes

$$-\left(\pi_i + i\epsilon_0\right) p_i(\mathbf{x}_i) = -\left(\pi_i + i\epsilon_0\right) \sum_{j=0}^{N_m - i} a(i,j) \prod_{l=0}^{i-1} \mu(\nu_{i+j} + j + l) U(x_{b,i})^{\nu_{i+j} - 1 + j},$$

and the second term

$$(i+1)\epsilon_0 \int dx_{i+1} p_{i+1}(\mathbf{x}_i, x_{i+1}) = \\ (i+1)\epsilon_0 \sum_{j=1}^{N_m - i} a(i+1, j-1) \prod_{l=0}^{i-1} \mu(\nu_{i+j} + j + l) U(x_{b,i})^{\nu_{i+j}-1+j}.$$

The ansatz provides a solution if the coefficients of different powers of $U(x_{b,i})$ equal zero. From the "$j = 0$" term one obtains Eq. (4.23), the other terms lead to

$$a(i,j) = \frac{(i+1)\epsilon_0}{(\pi_i + i\epsilon_0) - \mu i(\nu_{i+j} + j)} a(i+1, j-1), \qquad j = 0, \ldots N_m - i. \tag{D.6}$$

From Eq. (4.23), it can be seen that the denominator diverges if $\nu_i = \nu_{i+j} + j$ for some j, i. e., two exponents in the ansatz Eq. (4.22) are equal. In that case we set $a(i,j) \equiv 0$. Eq. (D.6) can recursively be applied to give an expression for $a(i,0), i = 1, \ldots N_m$ as done in Eq. (4.24). If for some j, $a(i,j)$ was set equal to zero this then implies also that $a(i-k, j+k) \equiv 0$ for $k = 0, \ldots, j-1$.

In the special case of two possible bonds, $N_m = 2$, the coefficients $a(i,j)$ are:

$$\begin{aligned} a(2,0) &= P_2, \\ a(1,0) &= P_1 - P_2 \frac{2\epsilon_0}{\mu(\nu_1 - 1 - \nu_2)}, \\ a(1,1) &= P_2 \frac{2\epsilon_0}{\mu(\nu_1 - 1 - \nu_2)}. \end{aligned}$$

If now $\nu_1 = \nu_2 + 1$ the $a(1,1)$-term in the ansatz Eq. (4.22) becomes redundant and has to be abandoned. Then, the $a(i,j)$ are just given by $a(2,0) = P_2, a(1,0) = P_1, a(1,1) = 0$.

Bibliography

[1] B. Alberts, A. Johnson, J. Lewis, M. Raff, K. Roberts, and P. Walter. *Molecular Biology of the Cell*. Garland Science, fourth edition, 2002.

[2] M. Albrecht, G. Hu, I. L. Guhr, T. C. Ulbrich, J. Boneberg, P. Leiderer, and G. Schatz. Magnetic multilayers on nanospheres. *Nature Materials*, 4:203–206, 2005.

[3] R. Alon, S. Chen, K. D. Puri, E. B. Finger, and T. A. Springer. The Kinetics of L-selectin Tethers and the Mechanics of Selectin-mediated Rolling. *The Journal of Cell Biology*, 138(5):1169–1180, 1997.

[4] R. Alon and group: private communications.

[5] R. Alon, D. A. Hammer, and T. A. Springer. Lifetime of the P-selectin-carbohydrate bond and its response to tensile force in hydrodynamic flow. *Nature*, 374:539–542, 1995.

[6] R. Amino, R. Menard, and F. Frischknecht. In vivo imaging of malaria parasites - recent advances and future directions. *Curr. Opin. Microbiol.*, 8(4):407–414, 2005.

[7] G. Arfken. *Mathematical Methods for Physicists*. Academic Press, Inc., third edition, 1985.

[8] M. Arnold, E. A. Cavalcanti-Adam, R. Glass, J. Blümmel, W. Eck, M. Kantlehner, H. Kessler, and J. P. Spatz. Activation of Integrin Function by Nanopatterned Adhesive Interfaces. *ChemPhysChem*, 5:383–388, 2004.

[9] C. L. Asbury, A. N. Fehr, and S. M. Block. Kinesin Moves by an Asymmetric Hand-Over-Hand Mechanism. *Science*, 302:2130–2134, 2003.

[10] M. Asfaw, B. Różycki, R. Lipowsky, and T. R. Weikl. Membrane adhesion via competing receptor/ligand bonds. *Europhysics Letters*, 76(4):703–709, 2006.

[11] L. Bannister and G. Mitchell. The ins, outs and roundabouts of malaria. *Trends in Parasitology*, 19(5):209–213, 2003.

[12] V. Barsegov and D. Thirumalai. Dynamics of unbinding of cell adhesion molecules: Transition from catch to slip bonds. *PNAS*, 102(6):1835–1839, 2005.

[13] G. I. Bell. Models for the Specific Adhesion of Cells to Cells. *Science*, 200:618–627, 1978.

[14] G. I. Bell, M. Dembo, and P. Bongrand. Cell Adhesion: Competition Between Nonspecific Repulsion and Specific Bonding. *Biophysical Journal*, 45:1051–1064, 1984.

[15] H. C. Berg. *Random Walks in Biology*. Princeton University Press, 1993.

[16] H. C. Berg and E. M. Purcell. Physics of Chemoreception. *Biophysical Journal*, 20:193–219, 1977.

[17] S. K. Bhatia, M. R. King, and D. A. Hammer. The State Diagram for Cell Adhesion Mediated by Two Receptors. *Biophysical Journal*, 84:2671–2690, 2003.

[18] S. M. Block, C. L. Asbury, J. W. Shaevitz, and M. J. Lang. Probing the kinesin reaction cycle with a 2D optical force clamp. *PNAS*, 100(5):2351–2356, 2003.

[19] K. J. Böhm, R. Stracke, P. Mühlig, and E. Unger. Motor protein-driven unidirectional transport of micrometer-sized cargoes across isopolar microtubule arrays. *Nanotechnology*, 12:238–244, 2001.

[20] P. Bongrand. Ligand-receptor interactions. *Rep. Prog. Phys.*, 62:921–968, 1999.

[21] J. F. Brady and G. Bossis. Stokesian Dynamics. *Ann. Rev. Fluid Mech.*, 20:111–157, 1988.

[22] I. N. Bronstein, K. A. Semendjajew, G. Musiol, and H. Mühlig. *Taschenbuch der Mathematik*. Verlag Harri Deutsch, third edition, 1997.

[23] R. Bruinsma. Physical aspects of adhesion of leukocytes. In T. Riste and D. Sherrington, editors, *Physics of Biomaterials: Fluctuations, Selfassembly and Evolution*, pages 61–101. Kluwer Academic Publishers, 1996.

[24] F. Burmeister, C. Schäfle, B. Keilhofer, C. Bechinger, J. Boneberg, and P. Leiderer. From Mesoscopic to Nanoscopic Surface Structures: Lithography with Colloid Monolayers. *Advanced Materials*, 10(6):495–497, 1998.

[25] K. E. Caputo and D. A. Hammer. Effect of Microvillus Deformability on Leukocyte Adhesion Explored Using Adhesive Dynamics Simulations. *Biophysical Journal*, 89:187–200, 2005.

[26] K.-C. Chang and D. A. Hammer. Influence of Direction and Type of Applied Force on the Detachment of Macromolecularly-Bound Particles from Surfaces. *Langmuir*, 12:2271–2282, 1996.

[27] K.-C. Chang and D. A. Hammer. The Forward Rate of Binding of Surface-Tethered Reactants: Effect of Relative Motion between Two Surfaces. *Biophysical Journal*, 76:1280–1292, 1999.

[28] K.-C Chang, D. F. J. Tees, and D. A. Hammer. The state diagram for cell adhesion under flow: Leukocyte rolling and firm adhesion. *PNAS*, 97(21):11262–11267, 2000.

[29] S. Chen and T. A. Springer. An Automatic Braking System That Stabilizes Leukocyte Rolling by an Increase in Selectin Bond Number with Shear. *The Journal of Cell Biology*, 144(1):185–200, 1999.

[30] S. Chen and T. A. Springer. Selectin receptor-ligand bonds: Formation limited by shear and dissociation governed by the Bell model. *PNAS*, 98(3):950–955, 2001.

[31] B. Cichocki and R. B. Jones. Image representation of a spherical particle near a hard wall. *Physica A*, 258:273–302, 1998.

[32] B. Cichocki, R. B. Jones, R. Kutteh, and E. Wajnryb. Friction and mobility for colloidal spheres in Stokes flow near a boundary: The multipole method and applications. *Journal of Chemical Physics*, 112(5):2548–2561, 2000.

[33] D. L. Coy, M. Wagenbach, and J. Howard. Kinesin Takes One 8-nm Step for Each ATP That It Hydrolyzes. *The Journal of Biological Chemistry*, 274(6):3667–3671, 1999.

[34] M. de Château, S. Chen, A. Slas, and T. A. Springer. Kinetic and Mechanical Basis of Rolling through an Integrin and Novel Ca^{2+}-Dependent Rolling and Mg^{2+}-Dependent Firm Adhesion Modalities for the $\alpha 4\beta 7$-MAdCAM-1 Interaction . *Biochemistry*, 40:13972–13979, 2001.

[35] M. Dembo, D. C. Torney, K. Saxman, and D. Hammer. The Reaction-Limited Kinetics of Membrane-to-Surface Adhesion and Detachment. *Proceedings of the Royal Society of London*, B 234:55–83, 1988.

[36] M. Doi and S. F. Edwards. *The Theory of Polymer Dynamics*. Oxford Science Publications, 1986.

[37] E. R. Dufresne, D. Altman, and D. G. Grier. Brownian dynamics of a sphere between parallel walls. *Europhysics Letters*, 53(2):264–270, 2001.

[38] T. Duke and S. Leibler. Motor Protein Mechanics: A Stochastic Model with Minimal Mechanochemical Coupling. *Biophysical Journal*, 71:1235–1247, 1996.

[39] O. Dwir, A. Solomon, S. Mangan, G. S. Kansas, U. S. Schwarz, and R. Alon. Avidity enhancement of L-selectin bonds by flow: shear-promoted rotation of leukocytes turn labile bonds into functional tethers. *The Journal of Cell Biology*, 163(3):649–659, 2003.

[40] M. Eigen. Diffusion control in biochemical reactions. In S. L. Minz and S. M. Wiedermayer, editors, *Quantum Statistical Mechanics in the Natural Sciences*, pages 37–61. Plenum NY, 1974.

[41] T. J. English and D. A. Hammer. Brownian Adhesive Dynamics (BRAD) for Simulating the Receptor-Mediated Binding of Viruses. *Biophysical Journal*, 86(6):3359–3372, 2004.

[42] T. Erdmann. *Stochastic dynamics of adhesion clusters under force*. PhD thesis, Potsdam University, 2005.

[43] T. Erdmann and U. S. Schwarz. Adhesion clusters under shared linear loading: A stochastic analysis. *Europhysical Letters*, 66(4):603–609, 2004.

[44] D. L. Ermak and J. A. McCammon. Brownian dynamics with hydrodynamic interactions. *J. Chem. Phys.*, 69(4):1352–1360, 1978.

[45] E. Evans. Probing the relation between force –Lifetime– and chemistry in single molecular bonds. *Annu. Rev. Biophys. Biomol. Struct.*, 30:105–128, 2001.

[46] E. Evans, A. Leung, V. Heinrich, and C. Zhu. Mechanical switching and coupling between two dissociation pathways in a P-selectin adhesion bond. *PNAS*, 101(31):11281–11286, 2004.

[47] E. Evans and K. Ritchie. Dynamic Strength of Molecular Adhesion Bonds. *Biophysical Journal*, 72:1541–1555, 1997.

[48] B. U. Felderhof. Force density induced on a sphere in linear hydrodynamics. *Physica A*, 84:569–576, 1976.

[49] B. U. Felderhof, B. Cichocki, and R. Schmitz. Hydrodynamic interactions between two spherical particles. *PhysicoChemical Hydrodynamics*, 10(3):383–403, 1988.

[50] B. U. Felderhof and R. B. Jones. Hydrodynamic scattering theory of flow about a sphere. *Physica A*, 136:77–98, 1986.

[51] B. U. Felderhof and R. B. Jones. Displacement theorems for spherical solutions of the linear Navier-Stokes equations. *J. Math. Phys.*, 30(2):339–342, 1989.

[52] A. E. Filipov, J. Klafter, and M. Urbakh. Friction through Dynamical Formation and Rupture of Molecular Bonds. *Physical Review Letters*, 92(13):135503, 2004.

[53] E. B. Finger, K. D. Puri, R. Alon, M. B. Lawrence, U. H. von Andrian, and T. A. Springer. Adhesion through L-selectin requires a threshold hydrodynamic shear. *Nature*, 379:266–269, 1996.

[54] M. Forero, W. E. Thomas, C. Bland, L. M. Nilsson, E. V. Sokurenko, and V. Vogel. A Catch-Bond Based Nanoadhesive Sensitive to Shear Stress. *Nano Letters*, 4(9):1593–1597, 2004.

[55] D. Frenkel and B. Smit. *Understanding Molecular Simulation*. Academic Press, 2002.

[56] J. Fritz, A. G. Katopodis, F. Kolbinger, and D. Anselmetti. Force-mediated kinetics of single P-selectin/ligand complexes observed by atomic force microscopy. *PNAS*, 95:12283–12288, 1998.

[57] O. D. Genbacev, A. Prakobphol, R. A. Foulk, A. R. Krtolica, D. Ilic, M. S. Singer, Z. Q. Yang, L. L. Kiessling, S. D. Rosen, and S. J. Fisher. Trophoblast L-selectin-mediated adhesion at the maternal-fetal interface. *Science*, 299:405–408, 2003.

[58] F. Gibbons, J.-F. Chauwin, M. Despósito, and J. V. José. A Dynamical Model of Kinesin-Microtubule Motility Assays. *Biophysical Journal*, 80:2515–2526, 2001.

[59] A. J. Goldman, R. G. Cox, and H. Brenner. Slow viscous motion of a sphere parallel to a plane wall—I, Motion through a quiescent fluid. *Chemical Engineering Science*, 22:637–651, 1967.

[60] A. J. Goldman, R. G. Cox, and H. Brenner. Slow viscous motion of a sphere parallel to a plane wall—II, Couette flow. *Chemical Engineering Science*, 22:653–660, 1967.

[61] R. A. Goldsby, T. J. Kindt, B. A. Osborne, and J. Kuby. *Immunology*. W. H. Freeman, fifth edition, 2003.

[62] H. Goldstein. *Classical Mechanics*. Addison Wesley, second edition, 1980.

[63] V. Grabovsky, O. Dwir, and R. Alon. Endothelial chemokines destabilize L-selectin-mediated lymphocyte rolling without including selectin shedding. *Journal of Biological Chemistry*, 227(23):20640–20650, 2002.

[64] P. S. Grassia, E. J. Hinch, and L. C. Nitsche. Computer simulations of Brownian motion of complex systems. *J. Fluid Mech.*, 282:373–403, 1995.

[65] A. W. Greenberg, D. K. Brunk, and D. A. Hammer. Cell-Free Rolling Mediated by L-Selectin and Sialyl Lewis^x Reveals the Shear Threshold Effect. *Biophysical Journal*, 79:2391–2402, 2000.

[66] D. A. Hammer and S. M. Apte. Simulation of cell rolling and adhesion on surfaces in shear flow: general results and analysis of selectin-mediated neutrophil adhesion. *Biophysical Journal*, 63:35–57, 1992.

[67] D. A. Hammer and D. A. Lauffenburger. A dynamical model for receptor-mediated cell adhesion to surfaces. *Biophysysical Journal*, 52:475–487, 1987.

[68] P. Hänggi, P. Talkner, and M. Borkovec. Reaction-rate theory: fifty years after Kramers. *Reviews of Modern Physics*, 62(2):251–341, 1990.

[69] D. B. Hill, M. J. Plaza, K. Bonin, and G. Holzwarth. Fast vesicle transport in PC12 neurites: velocities and forces. *European Biophysics Journal*, 33:623–632, 2004.

[70] J. Honerkamp. *Stochastic Dynamical Systems*. VCH Publishers, Inc., 1994.

[71] W. Hortshemke and R. Lefever. *Noise-Induced Transitions*. Springer-Verlag, 1984.

[72] J. D. Jackson. *Classical Electrodynamics*. John Wiley & Sons, Inc., third edition, 1999.

[73] D. J. Jeffrey and Y. Onishi. Calculation of the resistance and mobility functions for two unequal rigid spheres in low-Reynolds-number flow. *Journal of Fluid Mechanics*, 139:261–290, 1984.

[74] R. B. Jones. Stability of colloidal clusters in shear flow near a wall: Stokesian dynamics simulation studies. *Journal of Chemical Physics*, 115(11):5319–5330, 2001.

[75] R. B. Jones. Spherical particle in Poiseuille flow between planar walls. *Journal of Chemical Physics*, 121(1):483–500, 2004.

[76] R. B. Jones and F. N. Alavi. Rotational diffusion of a tracer colloid particle. IV. Brownian dynamics with wall effects. *Physica A*, 187:436–455, 1992.

[77] J. Kerssemakers, J. Howard, H. Hess, and S. Diez. The distance that kinesin-1 holds its cargo from the microtubule surface measured by fluorescence interference contrast microscopy. *PNAS*, 103(43):15812–15817, 2006.

[78] D. B. Khismatullin and G. A. Truskey. Three-dimensional numerical simulation of receptor-mediated leukocyte adhesion to surfaces: Effects of cell deformability and viscoelasticity. *Physics of Fluids*, 17:031505, 2005.

[79] M. R. King and D. A. Hammer. Multiparticle adhesive dynamics: Hydrodynamic recruitment of rolling leukocytes. *PNAS*, 98(26):14919–14924, 2001.

[80] M. R. King and D. A. Hammer. Multiparticle Adhesive Dynamics. Interactions between Stably Rolling Cells. *Biophysical Journal*, 81:799–813, 2001.

[81] M. R. King, V. Heinrich, E. Evans, and D. A. Hammer. Nano-to-Micro Scale Dynamics of P-Selectin Detachment from Leukocyte Interfaces. III. Numerical Simulation of Tethering under Flow. *Biophysical Journal*, 88:1676–1683, 2005.

[82] M. R. King, S. D. Rodgers, and D. A. Hammer. Hydrodynamic Collisions Suppress Fluctuations in the Rolling Velocity of Adhesive Blood Cells. *Langmuir*, 17(14):4139–4143, 2001.

[83] S. Klumpp and R. Lipowsky. Cooperative cargo transport by several molecular motors. *PNAS*, 102(48):17284–17289, 2005.

[84] S. Knutton, M. C. B. Sumner, and C. A. Pasternak. Role of microvilli in surface changes of synchronized P815Y mastocytoma-cells. *The Journal of Cell Biology*, 66(3):568–576, 1975.

[85] C. Korn and U. S. Schwarz. Efficiency of Initiating Cell Adhesion in Hydrodynamic Flow. *Physical Review Letters*, 97:138103, 2006.

[86] C. Korn and U. S. Schwarz. Mean first passage times for bond formation for a Brownian particle in linear shear flow above a wall. Accepted for publication in *Journal of Chemical Physics*, January 2007.

[87] G. Koster, M. VanDuijn, B. Hofs, and M. Dogterom. Membrane tube formation from giant vesicles by dynamic association of motor proteins. *PNAS*, 100(26):15583–15588, 2003.

[88] P. Kraikivski. *Non-equilibrium Dynamics of Adsorbed Polymers and Filaments*. PhD thesis, University of Potsdam, 2005.

[89] P. Kraikivski, R. Lipowsky, and J. Kierfeld. Enhanced Ordering of Interacting Filaments by Molecular Motors. *Physical Review Letters*, 96:258103, 2006.

[90] H. A. Kramers. Brownian motion in a field of force and the diffusion model of chemical reactions. *Physica*, 7:284–304, 1940.

[91] E. F. Krasik and D. A. Hammer. A Semianalytic Model of Leukocyte Rolling. *Biophysical Journal*, 87:2919–2930, 2004.

[92] M. Kraus, W. Wintz, U. Seifert, and R. Lipowsky. Fluid Vesicles in Shear Flow. *Physical Review Letters*, 77(17):3685–3688, 1996.

[93] S. C. Kuo, D. A. Hammer, and D. A. Lauffenburger. Simulation of Detachment of Specifically Bound Particles from Surfaces by Shear Flow. *Biophysical Journal*, 73:517–531, 1997.

[94] D. A Lauffenburger and J. J. Linderman. *Receptors*. Oxford University Press, 1993.

[95] M. B. Lawrence and T. A. Springer. Leukocytes Roll on a Selectin at Physiologic Flow Rates: Distinction from and Prerequisite for Adhesion through Integrins. *Cell*, 65:859–873, 1991.

[96] M. Lax. Classical Noise IV: Langevin Methods. *Reviews of Modern Physics*, 38(3):541–566, 1966.

[97] C. Leduc, O. Campàs, K. B. Zeldovich, A. Roux, P. Jolimaitre, L. Bourel-Bonnet, B. Goud, J.-F. Joanny, P. Bassereau, and J. Prost. Cooperative extraction of membrane nanotubes by molecular motors. *PNAS*, 101(49):17096–17101, 2004.

[98] L. Limberis, J. J. Magda, and R. J. Stewart. Polarized Alignment and Surface Immobilization of Microtubules for Kinesin-Powered Nanodevices. *Nano Letters*, 1(5):277–280, 2001.

[99] R. Lipowsky. Adhesion of Membranes via Anchored Stickers. *Physical Review Letters*, 77(8):1652–1655, 1996.

[100] R. Lipowsky, S. Klumpp, and T. M. Nieuwenhuizen. Random Walks of Cytoskeletal Motors in Open and Closed Compartments. *Physical Review Letters*, 87(10):108101, 2001.

[101] B. T. Marshall, M. Long, J. W. Piper, T. Yago, R. P. McEver, and C. Zhu. Direct observation of catch bonds involving cell-adhesion molecules. *Nature*, 423:190–193, 2003.

[102] C. Migliorini, YH. Qian, H. Chen, E. B. Brown, R. K. Jain, and L. L. Munn. Red Blood Cells Augment Leukocyte Rolling in a Virtual Blood Vessel. *Biophysical Journal*, 83:1834–1841, 2002.

[103] K. L. Moore, K. D. Patel, R. E. Bruehl, L. Fugang, D. A. Johnson, H. S. Lichenstein, R. D. Cummings, D. F. Bainton, and R. P. McEver. P-Selectin Glycoprotein Ligand-1 Mediates Rolling of Human Neutrophils on P-Selectin. *The Journal of Cell Biology*, 128(4):661–671, 1995.

[104] L. L. Munn, R. J. Melder, and R. K. Jain. Analysis of Cell Flux in the Parallel Plate Flow Chamber: Implications for Cell Capture Studies. *Biophysical Journal*, 67:889–895, 1994.

[105] E. Nagao, O. Kaneko, and J. A. Dvorak. Plasmodium *falciparum*-Infected Erythrocytes: Qualitative and Quantitative Analyses of Parasite-Induced Knobs by Atomic Force Microscopy. *Journal of Structural Biology*, 130:34–44, 2000.

[106] N. A. N'Dri, W. Shyy, and R. Tran-Son-Tay. Computational Modeling of Cell Adhesion and Movement Using a Continuum-Kinetics Approach. *Biophysical Journal*, 85:2273–2286, 2003.

[107] C. E. Orsello, D. A. Lauffenburger, and D. A. Hammer. Molecular properties in cell adhesion: a physical and engineering perspective. *TRENDS in Biotechnology*, 19(8):310–316, 2001.

[108] K. D. Patel, M. U. Nollert, and R. P. McEver. P-selectin Must Extend a Sufficient Length from the Plasma Membrane to Mediate Rolling of Neutrophils. *The Journal of Cell Biology*, 131(6):1893–1902, 1995.

[109] Y. V. Pereverzev, O. V. Prezhdo, M. Forero, E. V. Sokurenko, and W. E. Thomas. The Two-Pathway Model for the Catch-Slip Transition in Biological Adhesion. *Biophysical Journal*, 89:1446–1454, 2005.

[110] G. S. Perkins and R. B. Jones. Hydrodynamic interaction of a spherical-particle with a planar boundary. I. Free-surface. *Physica A*, 171:575–604, 1991.

[111] G. S. Perkins and R. B. Jones. Hydrodynamic interaction of a spherical-particle with a planar boundary. II. Hard-wall. *Physica A*, 189:447–477, 1992.

[112] A. Pierres, A.-M. Benoliel, C. Zhu, and P. Bongrand. Diffusion of Microspheres in Shear Flow Near a Wall: Use to Measure Binding Rates between Attached Molecules. *Biophysical Journal*, 81:25–42, 2001.

[113] A. Pierres, H. Feracci, V. Delmas, A.-M. Benoliel, J.-P. Thiery, and P. Bongrand. Experimental study of the interaction range and association rate of surface-attached cadherin 11. *PNAS*, 95:9256–9261, 1998.

[114] A. Pierres, J. Vitte, A.-M. Benoliel, and P. Bongrand. Dissecting individual ligand-receptor bonds with a laminar flow chamber. *Biophysical Reviews and Letters*, 1(3):231–257, 2006.

[115] C. Pozrikidis. *Introduction to Theoretical and Computational Fluid Dynamics*. Oxford University Press, 1997.

[116] C. Pozrikidis. Numerical Simulation of the Flow-Induced Deformation of Red Blood Cells. *Annals of Biomedical Engineering*, 31:1194–1205, 2003.

[117] W. H. Press, S. A. Teukolsky, W. T. Vetterling, and B. P. Flannery. *Numerical Recipes in C*. Cambridge University Press, second edition, 1994.

[118] E. M. Purcell. Life at low Reynolds number. *American Journal of Physics*, 45(1):3–11, 1977.

[119] S. Redner. *A guide to first passage time processes*. Cambridge University Press, 2001.

[120] A. Rohrbach, E.-L. Florin, and E. H. K. Stelzer. Photonic Force Microscopy: Simulation of principles and applications. *Proceedings of SPIE*, 4431:75–86, 2001.

[121] H. Rossiter, R. Alon, and T. S. Kupper. Selectins, T-cell rolling and inflammation. *Molecular Medicine Today*, pages 214–222, May 1997.

[122] A. Schallamach. A theory of dynamic rubber friction. *Wear*, 6:375–382, 1963.

[123] A. Schallamach. How does rubber slide? *Wear*, 17:301–312, 1971.

[124] M. Schliwa, editor. *Molecular Motors*. Wiley-VCH, 2003.

[125] R. Schmitz and B. U. Felderhof. Creeping flow about a spherical particle. *Physica A*, 113:90–102, 1982.

[126] M. J. Schnitzer, K. Visscher, and S. M. Block. Force production by single kinesin motors. *Nature Cell Biology*, 2:718–723, 2000.

[127] G. Schreiber. Kinetic studies of protein-protein interactions. *Curr. Opin. Struct. Biol.*, 12:41–47, 2002.

[128] U. S. Schwarz. *Forces and elasticity in cell adhesion*. Habilitationsschrift, University of Potsdam, 2004.

[129] U. S. Schwarz and R. Alon. L-selectin-mediated leukocyte tethering in shear flow is controlled by multiple contacts and cytoskeletal anchorage facilitating fast rebinding events. *PNAS*, 101(18):6940–6945, 2004.

[130] U. S. Schwarz, S. Komura, and S. A. Safran. Deformation and tribology of multi-walled hollow nanoparticles. *Europhysics Letters*, 50(6):762–768, 2000.

[131] T. W. Secomb. Mechanics of red blood cells and blood flow in narrow tubes. In C. Pozrikidis, editor, *Modeling and Simulation of Capsules and Biological Cells*, pages 163–196. Chapman & Hall/CRC Press, 2003.

[132] U. Seifert. Configurations of fluid membranes and vesicles. *Advances in Physics*, 46(1):13–137, 1997.

[133] U. Seifert. Hydrodynamic Lift on Bound Vesicles. *Physical Review Letters*, 83(4):876–879, 1999.

[134] K. Sekimoto and L. Leibler. A Mechanism for Shear Thickening of Polymer-Bearing Surfaces: Elasto-Hydrodynamic Coupling. *Europhysics Letters*, 23(2):113–117, 1993.

[135] R. Shamri, V. Grabovsky, J.-M. Gauguet, S. Feigelson, E. Manevich, W. Kolanus, M. K. Robinson, D. E. Saunton, U. H. von Andrian, and R. Alon. Lymphocyte arrest requires instantaneous induction of an extended LFA-1 conformation mediated by endothelium-bound chemokines. *Nature Immunology*, 6(5):497–505, 2005.

[136] H. Shankaran and S. Neelamegham. Hydrodynamic Forces Applied on Intercellular Bonds, Soluble Molecules, and Cell-Surface Receptors. *Biophysical Journal*, 86:576–588, 2004.

[137] J.-Y. Shao, H. P. Ting-Beall, and R. M. Hochmuth. Static and dynamic lengths of neutrophil microvilli. *PNAS*, 95:6797–6802, 1998.

[138] J. Shillcock and U. Seifert. Escape from a metastable well under a time-ramped force. *Physical Review E*, 57(6):7301–7304, 1998.

[139] T. Shimmen and E. Yokota. Cytoplasmic streaming in plants. *Current Opinion in Cell Biology*, 16:68–72, 2004.

[140] V. R. Shinde Patil, C. J. Campbell, Y. H. Yun, S. M. Slack, and D. J. Goetz. Particle Diameter Influences Adhesion under Flow. *Biophysical Journal*, 80:1733–1743, 2001.

[141] D. Shoup and A. Szabo. Role of diffusion in ligand-binding to macromolecules and cell-bound receptors. *Biophysical Journal*, 40(1):33–39, 1982.

[142] J. M. Skotheim and L. Mahadevan. Soft Lubrication. *Physical Review Letters*, 92:245509, 2004.

[143] M. v. Smoluchowski. Versuch einer mathematischen Theorie der Koagulationskinetik kolloidaler Lösungen. *Zeitschrift f. physikalische Chemie*, 92:129–168, 1917.

[144] T. A. Springer. Traffic signals for lymphocyte recirculation and leukocyte emigration: The multistep paradigm. *Cell*, 76:301–314, 1994.

[145] T. A. Springer. Traffic signals on endothelium for lymphocyte recirculation and leukocyte emigration. *Annu. Rev. Physiol.*, 57:827–872, 1995.

[146] H. Stöcker. *Taschenbuch der Physik*. Verlag Harri Deutsch, 1998.

[147] S. Sukumaran and U. Seifert. Influence of shear flow on vesicles near a wall: A numerical study. *Physical Review E*, 64:011916, 2001.

[148] C. Sun, C. Migliorini, and L. L. Munn. Red Blood Cells Initiate Leucocyte Rolling in Postcapillary Expansions: A Lattice Boltzmann Analysis. *Biophysical Journal*, 85:208–222, 2003.

[149] S. Suresh, J. Spatz, J. P. Mills, A. Micoulet, M. Dao, C. T. Lim, M. Beil, and T. Seufferlein. Connections between single-cell biomechanics and human disease states: gastrointestinal cancer and malaria. *Acta Biomaterialia*, 1:15–30, 2005.

[150] K. Svoboda and S. M. Block. Force and velocity measured for single kinesin molecules. *Cell*, 77(5):773–784, 1994.

[151] K. Svoboda, C. F. Schmidt, B. J. Schnapp, and S. M. Block. Direct observation of kinesin stepping by optical trapping interferometry. *Nature*, 365:721–727, 1993.

[152] A. Szabo, K. Schulten, and Z. Schulten. First passage time approach to diffusion controlled reactions. *J. Chem. Phys.*, 72(8):4350–4357, 1980.

[153] W. E. Thomas, E. Trintchina, M. Forero, V. Vogel, and E. V. Sokurenko. Bacterial Adhesion to Target Cells Enhanced by Shear Force. *Cell*, 109(7):913–923, 2002.

[154] H. P. Ting-Beall, D. Needham, and R. M. Hochmuth. Volume and Osmotic Properties of Human Neutrophils. *Blood*, 81:2774–2780, 1993.

[155] A. Tözeren and K. Ley. How do selectins mediate leukocyte rolling in venules? *Biophysical Journal*, 63:700–709, 1992.

[156] R. D. Vale. The Molecular Motor Toolbox for Intracellular Transport. *Cell*, 112:467–486, 2003.

[157] N. G. van Kampen. *Stochastic Processes in Physics and Chemistry*. Elsevier, 1992.

[158] K. Visscher, M. J. Schnitzer, and S. M. Block. Single kinesin molecules studied with a molecular force clamp. *Nature*, 400:184–189, 1999.

[159] C. Wofsy and B. Goldstein. Effective Rate Models for Receptors Distributed in a Layer above a Surface: Application to Cells and Biacore. *Biophysical Journal*, 82:1743–1755, 2002.

[160] T. Yago, A. Leppänen, H. Qiu, W. D. Marcus, M. U. Nollert, C. Zhu, R. D. Cummings, and R. P. McEver. Distinct molecular and cellular contributions to stabilizing selectin-mediated rolling under flow. *The Journal of Cell Biology*, 158(4):787–799, 2002.

[161] T. Yago, J. Wu, C. D. Wey, A. G. Klopocki, C. Zhu, and R. P. McEver. Catch bonds govern adhesion through L-selectin at threshold shear. *The Journal of Cell Biology*, 166(6):913–923, 2004.

[162] T. Yago, V. I. Zarnitsyna, A. G. Klopocki, R. P. McEver, and C. Zhu. Transport governs flow-enhanced cell tethering through L-selectin at threshold shear. *Biophysical Journal*, 92:330–342, 2007.

Acknowledgments

Ich möchte allen, die zum Gelingen dieser Arbeit beigetragen haben, herzlich danken.

Bei Herrn Prof. Dr. Reinhard Lipowsky bedanke ich mich dafür, dass ich meine Arbeit an seinem Institut anfertigen konnte. Das hervorragende Klima in seiner Abteilung und das reichhaltige Angebot an Vorlesungen, Seminaren und Vorträgen habe ich sehr genossen.

Mein besonderer Dank gilt Herrn PD Dr. Ulrich Schwarz für die Vergabe eines sehr interessanten Themas. Ulrich Schwarz war für mich ein immer erreichbarer Betreuer und half mir mit vielen richtungsweisenden Ideen. Durch ihn und die von ihm organisierten Veranstaltungen (Konferenzen, Seminare) habe ich viel über biologische Physik gelernt.

Ich danke Herrn Prof. Dr. Ronen Alon für die Einladung ans Weizmann-Institut in Israel und die herzliche Aufnahme in seiner Arbeitsgruppe. Seiner Arbeitsgruppe danke ich dafür, dass ich an Flußkammerexperimenten mit weißen Blutkörperchen teilhaben konnte und mir geduldig die Fragen eines Theoretikers beantwortet wurden. Insbesondere möchte ich auch Jenia Manevich danken, die mir den Norden Israels rund um den See Genezareth und das Leben in einem Kibbuz gezeigt hat.

Herrn Prof. Dr. Samuel Safran danke ich für hilfreiche Anregungen meine Arbeit betreffend und die Bereitstellung eines Büroplatzes während meines Aufenthalts am Weizmann Institut.

Herrn Dr. Stefan Klumpp gilt mein Dank für die vielen wertvollen Beiträge, die mir bei der Simulation molekularer Motoren sehr hilfreich waren. Ebenso danke ich Melanie Müller und Janina Beeg für viele interessante Diskussionen über molekulare Motoren.

Ich danke Jakob Schluttig, Achim Besser und Melanie Müller für das sorgfälltige Korrekturlesen einzelner Teile meiner Arbeit.

Den Arbeitskollegen in Potsdam und Heidelberg gilt mein Dank für viele interessante Diskussionen über alle möglichen Themen in der traditionellen 'Kaffeerunde' nach dem Mittagessen.

Meiner Freundin Christiane Sperr danke ich für ihre Unterstützung und die sehr schöne Zeit, die wir gemeinsam in Potsdam verbracht haben.

Meinen Eltern und Großeltern danke ich für ihre immer vorhandene Unterstützung, die mich immer in meinem Weg bekräftigt hat.